Bioprinting and characterization of medium viscosity alginate scaffold for nerve tissue regeneration

A Thesis Submitted to
the College of Graduate and Postdoctoral Studies
in Partial Fulfillment of the Requirements for
the Degree of Doctor of Philosophy in
the Division of Biomedical
Engineering
University of Saskatchewan

By
Md Ariful Islam Sarker

PERMISSION TO USE

In presenting this thesis in partial fulfilment of the requirements for a postgraduate degree from the University of Saskatchewan, I agree that the Libraries of this University may make it freely available for inspection. I further agree that permission for copying of this thesis in any manner, in whole or in part, for scholarly purpose may be granted by the Prof. Daniel Chen and Prof. David Schreyer who supervised my thesis work, or in their absence, by the Head of the Department or the Dean of the College in which my thesis work was done. It is understood that any copying or publication or use of this thesis or part thereof for financial gain shall not be allowed without my written permission. It is also understood that due recognition shall be given to me and to the University of Saskatchewan in any scholarly use which may be made of any material in my thesis.

Requests for permission to copy or to make other use of material in this thesis in whole or part should be addressed to:

College of Graduate and Postdoctoral Studies

116 Thorvaldson Building

110 Science Place

University of Saskatchewan

Saskatoon, Saskatchewan (S7N 5C9)

Canada

OR

Head of the Division of Biomedical Engineering

College of Engineering

57 Campus Dr.

University of Saskatchewan

Saskatoon, Saskatchewan (S7N 5A9)

Canada

ABSTRACT

Injured peripheral nerves with a gap >2mm often demonstrate poor regeneration ability, where scaffolds made from biomaterials are possibly used to bridge the gap for functional recovery. To fabricate such scaffolds, extrusion-based three dimensional (3D) printing technique shows promising due to its ability to precisely extrude biomaterial solution and build 3D structures by a layer-by-layer fashion. However, the 3D printing technique faces several challenges in fabricating scaffolds for nerve tissue regeneration. Among them, the printability, structural integrity, and biological performance of scaffolds printed from sodium alginate (SA) (a biomaterial widely used in nerve tissue regeneration) are the key issues. To address the issues, this thesis aims to develop SA scaffolds for potential application in peripheral nerve regeneration. Three specific objectives are set so as to investigate (1) the effect of fluid (i.e., SA solution) flow behavior, printing parameters, and concentration of ionic crosslinkers on the printability of SA scaffolds, (2) the influence of SA precursor and ionic crosslinker concentrations on the mechanical and biological properties of scaffolds, and (3) the influence of peptide conjugation with SA molecules on the biological performance of the scaffolds for nerve tissue regeneration.

The flow rate in the printing process is critical to the scaffold structure and printability. The first part of dissertation is to examine the flow rate of SA solution or precursor extruded through a tapered needle in the scaffold fabrication process by developing a novel model for its representation. Specifically, the flow rate of the medium viscosity SA precursor was modeled by taking into account of both slip and shear flow from a tapered needle. Since the flow rate of SA precursor depends on its flow behavior, model predicting the flow behavior of the hydrogel precursor was also developed from regression of experimental data. For different extrusion pressures (e.g. 20, 25, 30, and 40 kPa) and concentrations (e.g. 2, 3, and 4%) of SA precursor, the flow rate model predicted with reasonable accuracy (coefficient of determination, $R^2 = 0.98$). Further, at various needle diameters (0.2, 0.25, 0.41, and 0.61 mm) and temperatures (25, 35, 45, and 55°C) the flow rate model predicted more accurately for low dispensing pressure (20 kPa, $R^2=0.99$) compared to high pressure (30 kPa, $R^2=0.98$).

The mechanical and biological properties of SA scaffold largely depend on the ionic crosslinker used in bioprinting of scaffolds from SA. The second part of dissertation is to conduct a comparative study of three ionic crosslinkers including calcium chloride ($CaCl_2$),

barium chloride (BaCl₂), and zinc chloride (ZnCl₂) on the mechanical and biological properties of 3D printed SA scaffolds. Multiple regression equations were developed to predict the mechanical properties of SA scaffolds; and the printability of SA precursor was evaluated at varying concentrations of both ionic crosslinkers and SA precursor. Experimental results revealed that the elastic modulus of the hydrogels decreasing in the order $BaCl_2 > CaCl_2 > ZnCl_2$ over 42 days while Schwann cell (SC) viability decreased in the order $CaCl_2 > BaCl_2 > ZnCl_2$ over 7 days. The predictions of multiple regression equations show reasonable agreement with experimental data, while the 3% (w/v) SA precursor demonstrates acceptable printability in $CaCl_2$ and $BaCl_2$ solution. The experimental and predicted results obtained in this part of work would be useful in selecting the appropriate ionic crosslinkers and concentration of SA precursor for bioprinting of tissue scaffolds.

Notably, SA precursor lacks of cell binding motifs in the molecular structure, which significantly limits its applications in nerve tissue regeneration. For improvement, the third part of dissertation is to conjugate peptide molecules into SA, resulting in peptide conjugated SA (PCSA) and to further examine the effect of single and composite PCSA scaffolds on axon regeneration *in vitro*. In particular, a 2% (w/v) SA precursor was conjugated with either arginine-glycine-aspartate (RGD) or tyrosine-isoleucine-glycine-serine-arginine (YIGSR) peptides, or mixture of RGD and YIGSR (1:2), and was bioprinted into cuboid structures. The printability of the composite PCSA precursor was evaluated in terms of the strand width, pore geometry, and angle-formation accuracy at varying concentration of $CaCl_2$ (i.e. 50 - 150 mM); and the mechanical stability of scaffolds was examined over 3 weeks in terms of swelling, degradation, and compression modulus; and surface morphology of the degraded scaffolds. Axon regeneration ability of PCSA scaffolds were assessed by quantifying the viability, morphology, amount of secreted brain derived neurotrophic factor (BDNF) of incorporated SCs, and directional neurite outgrowth in a 2D culture. Experimental results reveal that composite PCSA precursor extruded in 50 mM $CaCl_2$ has good printability and that PCSA scaffolds remains porous over 3 weeks with the elastic modulus decreased by ~70%. Also, the results illustrates that composite PCSA scaffolds facilitate better the viability and morphology of SCs, as well as support greater directional neurite outgrowth as compared to those of single PCSA scaffolds.

Taken together, the thesis develops methods to fabricate SA and PCSA scaffolds with results illustrating their potential applications in the regeneration of damaged peripheral nerves.

ACKNOWLEDGMENTS

concentrations of 100 mM (A, C, E) and a fixed alginate concentration of 3% (w/v) (B, D, F).

LIST OF ABBREVIATIONS

Abbreviation	Elaboration
aFGF	Acidic fibroblast growth factor
ASC	Adipose stem cell
Ba^{2+}	Barium ion
$BaCl_2$	Barium chloride
BDNF	Brain-derived neurotrophic factor
bFGF	Basic fibroblast growth factor
BMSC	Bone marrow stem cell
BSA	Bovine serum albumin
Ca^{2+}	Calcium ion
CAB	Cellulose acetate butyrate
$CaCl_2$	Calcium chloride
CCH	Collagen-chitosan
CMAP	Compound muscle action potential
CMS	Chitosan microspheres
CNAPs	Compound nerve action potentials
CO_2	Carbon dioxide
COOH-	Carboxyl group
DAPI	4', 6-diamidino-2-phenylindole
DMEM	Dulbecco's modified eagle medium
DNA	Deoxyribonucleic acid
DPMD	Direct polymer melt deposition
DRG	Dorsal root ganglion
ECM	Extracellular matrix
EDC	(N-(3-dimethylaminopropyl)-N'-ethylcarbodiimide hydrochloride)
EDTA	Ethylene diamine tetra acetic acid
ES	Electrospinning
FBS	Fetal bovine serum
FN	Fibronectin

GAG	Glycosaminoglycan
GDNF	Glial cell derived neurotrophic factor
GelMA	Gelatin methacrylate
GMW	Gastrocnemius muscle weight
GTMC	Glycolide trimethylene carbonate
HUVEC	Human umbilical vein endothelial cells
LIFT	Laser-induced forward transfer
Mg^{2+}	Magnesium ions
MW	Molecular weight
MWNT	Multi-walled carbon nanotubes
Na^+	Sodium ions
NCAP	Nerve compound action potentials
NCV	Nerve conduction velocity
NGC	Nerve guidance conduit
NGF	Nerve growth factor
NHS	N-hydroxysuccinimide
NSCs	Neural stem cells
PA	Peptide amphiphiles
PAN-MA	Poly-acrylonitrile methylacrylate
PBS	Phosphate buffered saline
PCLEEP	Poly (e-caprolactone-co-ethyl ethylene phosphate)
PCSA	Peptide-conjugated sodium alginate
PDLLA	Poly-DL-lactic acid
PDS	Polydioxanone
PEG	Polyethylene glycol
PEI	Polyethyleneimine
PES	Polyethersulfone
PGA	Poly-glycolic acid
PHB	Poly (3-hydroxybutyrate)
PHBV	Poly (3-hydroxybutyrate-co-3-hydroxyvalerate)
PHEMA-MMA	Poly (hydroxyethyl methacrylate)-methyl methacrylate

PI	Propidium iodide
PLCL	Poly (L-lactide-co-caprolactone)
PLGA	Poly (lactic-co-glycolic acid)
PLLA	Poly-L-lactic acid
PNS	Peripheral nervous system
PO_4^{3-}	Phosphate ions
PPC	Poly (propylene carbonate)
PPy	Polypyrrole;
PRSC	Primary rat Schwann cells
PU	Polyurethane
R_a	Mean roughness values
RGD	Arginyl-glycyl-aspartic acid
RP	Rapid prototyping
RPSCs	Rat primary SCs
SA	Sodium alginate
SAPNS	Self-assembling nanofibre scaffold
SC	Schwann cell
SEM	Scanning electron microscopy
SEP	Somatosensory evoked potential
SF	Silk fibroin
SWNT	Single walled carbon nanotubes
TBST	Tris-buffered saline + 0.1% Tween 20
VEGF	vascular endothelial growth factor
YIGSR	Tyrosine-isoleucine-glycine-serine-arginine
Zn^{2+}	Zinc ion
$ZnCl_2$	Zinc chloride
3D	Three dimensional

CHAPTER 1

Introduction

1.1 Tissue scaffolds and nerve tissue regeneration

In the events of injury, the scar tissue forms around the wound causes poor tissue regeneration in human body. It is an established fact that tissue regeneration is likely in most cases while the wound thickness is below 2 mm [1]. Tissue injury more than 2 mm requires structural support to regenerate which eventually lead to the formation of tissue engineering discipline. Tissue engineering has opened up the vast possibility in regenerating tissue or organ artificially in order to meet up the enormous demand worldwide to date. Tissue engineering is a multidisciplinary area of material science, cell biology, engineering, and biochemistry and aims to mimic and reproduce biological or native tissues/organs. In engineering a specific tissue, scaffold, a three-dimensional (3D) temporary structure, is implanted at the targeted anatomical site to regrow the damaged or injured tissue. The scaffolds consisting of biopolymer, cells, growth factors, peptide, or proteins facilitate tissue regeneration upon implantation, and eventually get degraded and replaced by newly grown tissues. In fact, a functional scaffold should have enough mechanical strength to sustain the structural integrity during tissue regeneration [2], sufficient porosity to facilitate nutrient transfer between cells and surroundings [3], reasonable biodegradability to be able to get replaced by newly grown tissue [4], cytocompatibility to alleviate immune reaction and inflammation in host body [5], and ECM-like property to facilitate cell survival, proliferation, differentiation, migration and tissue regeneration.

Peripheral nervous system (PNS) connects tissues, limbs and organs to central nervous system, and thus assists to regulate the sensory and motor functions of the associated tissues. Several incidents including traumatic, non-traumatic, and surgical activities have been identified as a potential reason of PNS damage that lead to poor sensational reflexes, painful neuropathies and muscles movement complexities in patient's body [6]. Approximating two nerve segments with suture is viable while the gap is small (~2 mm). If the gap is larger than 2 mm reconnecting two nerve stumps with suture generates excessive tension and causes poor regeneration [7]. To address this issue, autografts (such as; vein grafts) were investigated and implanted to bridge a large nerve gap, clinically. However, several shortcomings related to autografts, such as donor site morbidity, size inconsistency and requirements of multiple surgery limit their applications [8]. Allogenic or xenogeneic grafts were also explored to find an alternative to autografts, while

immunological complexities and eventual rejection problems restrict their application in nerve tissue regeneration [9]. To overcome these limitations, in the past decades numerous studies were conducted to explore alternative of autografts by using tissue engineered scaffolds.

In nerve tissue regeneration, cylindrical shaped conduits have been used over the past decades to bridge two damaged nerve segments. Because hollow conduit can't promote functional nerve regeneration [10], a number of studies have used filler material in the conduit to guide the growing axons [11,12]. Polysaccharide and protein based hydrogel, nano/micro filaments, magnetically/cell aligned fibrils, unidirectional freeze-dried biopolymer, and rolled up nano/micro pattern have been reported as a potential polymer in different studies [13]. While these filler materials demonstrated remarkable success in promoting axon growth, nerve regeneration across a large nerve gap remains challenging. Since SCs play a key role in maintaining and regenerating axons after in vivo injury [14], studies have been conducted to incorporate SC in the filler materials or scaffolds during fabrication [15]. Studies revealed that SCs show better viability and proliferation in a porous scaffold compared to a nonporous one. Besides, scaffold fabricating polymer should have ECM-like property to facilitate the biological activity of SCs [16].

Over the last decades, conventional (e.g. phase separation, freeze-drying, gas foaming, solvent casting and particulate leaching, etc.) [17] and additive manufacturing (AM) techniques (e.g. extrusion-based, laser-based, etc.) have been evolved for fabricating nerve tissue scaffolds [18]. The pores of the scaffolds fabricated with conventional approaches are non-uniform and partially interconnected which inhibit tissue growth. In contrast, AM approaches can fabricate scaffolds with embedded cells as per predefined computer-aided design (CAD) data. Moreover, the AM techniques support the fabrication of scaffolds with any custom-made design while maintaining uniform and interconnected porous structure [19]. This thesis aims to biofabricate tissue scaffolds using extrusion-based technique being inspired by the attractive features of AM technique.

Bioprinting of nerve tissue scaffolds requires hydrated biopolymer and mild fabrication condition to keep the SCs viable during and after 3D fabrication. To fulfill the requirement, different types of hydrogels (e.g. protein based, polysaccharide based, synthetic, etc.) have been used over the years in preparing bio-ink for extrusion-based system [20]. SA, a polysaccharide

based biopolymer and forms hydrogel under the influence of crosslinker, has frequently been explored in scaffold bioprinting due to the low production cost, availability, rapid gel formation ability, non-toxicity, biocompatibility, and biodegradability [21]. Besides, bulk SA hydrogel was identified as a promoter of axon growth reported elsewhere [22]. Being inspired by the positive perspectives, SA precursor has been used in this thesis to biofabricate scaffolds for the probable application in nerve tissue regeneration.

1.2 Extrusion-based bioprinting

It is well accepted that inclusion of a large cell population in scaffolds facilitates tissue regeneration producing growth factors and extra cellular matrix proteins [23]. Extrusion-based (EB) scaffold fabrication process has made possible to dispense cell population at a high density along with biopolymer. In an extrusion-based bioprinting system, biopolymers are extruded in a layer-by-layer fashion to create a 3D construct as per computer-aided design (CAD). Often piston, screw, or air-pressure-driven mechanism is used for dispensing biopolymer or cell-biopolymer mixture (Fig.1.1). Since the screw or piston-driven mechanism might cause shear-induced cell damage, an air-pressure-driven bioprinter was chosen in this research work. Hydrogel precursor particularly SA has been identified as a suitable polymer in EB fabrication due to their availability, cell incorporation ability, hydrated nature, gelation property and biocompatibility [24]. However, SA precursor lacking cell binding sites require peptide conjugation to enhance the biological function [25].
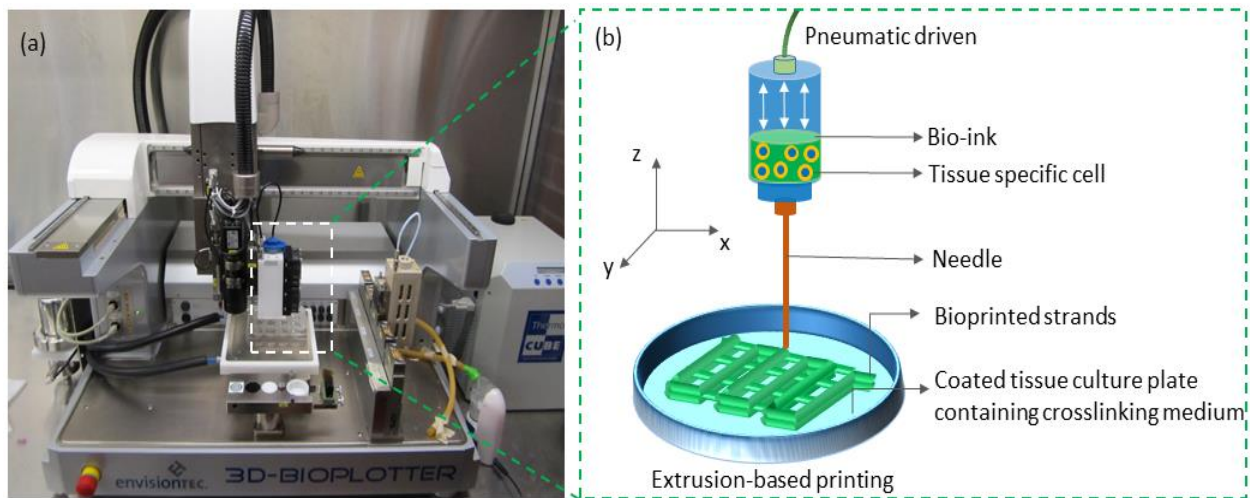
Fig. 1.1 Scaffold bioprinting with an extrusion -based bioprinting technique; (a) air pressure driven 3D bioplotter, (b) schematic of bioprinting mechanism of a 3D bioplotter

3

In the EB scaffold fabrication process the viscosity of alginate precursor affects the flow rate from needle or nozzle, thus affecting the printability of extruded strands, pore and complex 3D structure [26]. The term printability refers to how close the printed structure is in relation to the designed one. The viscosity of alginate precursor is sensitive to concentration of hydrogel precursor and extrusion temperature. A number of studies reported that low viscosity alginate precursor (100-300 cP, 2 % w/v at 25 °C) at low concentration facilitates reasonable cell viability, while shows poor printability and mechanical strength. In contrast, alginate precursor at elevated concentration reduces cell viability, but demonstrate improved printability and mechanical strength [27,28]. To tackle the issue, application of MVSA precursor (≥2,000 cP, 2 % w/v at 25 °C) in the bioprinting could be a compromised solution, where both reasonable printability and cell viability could be maintained even at low alginate precursor concentration. Mathematical modeling could be useful in selecting the diameter and speed of extrusion needle, the extrusion pressure of bio-ink, and the concentration of SA precursor that are crucial to obtain a desired flow rate of SA precursor from extrusion needle. To predict the flow of MVSA precursor from extrusion needle, rheological characterization (i.e. apparent viscosity, yield stress, and flow index) is required prior to bioprinting. A flow behavior model may predict the rheological properties of SA precursor that could further influence the outcome of flow rate model at different SA precursor concentration and operating temperatures. Such mathematical modeling in predicting the rheological property of MVSA precursor might reduce the experimental time and biopolymer wastage. However, model equations predicting the flow behavior of MVSA precursor remains unreported to date.

Flow model equations are useful in predicting strand width, and needle speed which is necessary to have reasonable printability. Such model equations are helpful to reduce the number of trials prior to bioprinting, thus eliminating the required time for trials, material and cell wastages. In bioprinting, generally micro-needles are preferred, since strand width in the microscale range facilitates mass transfer (nutrients, oxygen, etc.) between embedded cells and culture media [29]. In capillary flow, slip at the wall is likely with the elevated shear stress as reported elsewhere [30]. In particular, the slip flow becomes significant in case of non-Newtonian fluid flowing through micro channels [31]. Skipping slip flow in the model equation, might cause prediction uncertainty in the flow of hydrogel precursor from capillary needle at different extrusion pressure. Till to date, several studies modeled the fluid flow from cylindrical

and taper needle assuming shear flow condition [32]. It is mention worthy that taper needle is favorable in the bioprinting as they do less cell damage than cylindrical one. Although potential, model equations predicting the fluid from taper needle considering both shear and slip flow remains unreported till now. To address the issue, in this thesis a flow rate model was also developed for MVSA precursor considering shear and slip flow from a tapered needle. Since bioprinted scaffold can provide necessary biochemical and biophysical cues in guiding growing axons after nerve injury, the characterization of MVSA precursor in terms of flow behavior and flow rate evaluation would facilitate the bioprinting of scaffolds that could further be investigated to assess the directional outgrowth of axons in vitro.

1.3 Effect of crosslinkers in bioprinting

In the bioprinting process, extruded hydrogel precursor needs to be crosslinked or solidified to retain the shape developed in CAD program. Hydrogel precursors undergo gelation process by the influence of ionic crosslinkers, covalent crosslinkers, pH, temperature or ultraviolet light [33]. In 3D fabrication, the extruded hydrogel precursors should have rapid gelation property to facilitate successive layers fabrication along with reasonable printability [19]. Crosslinking in hydrated crosslinkers is always preferable to maintain the viability of incorporated cell population during bioprinting. However, the cytotoxicity of the crosslinkers is also a major concern that requires to be considered in the selection of ionic crosslinkers [34]. While ionic crosslinkers seems to be essential in the bioprinting process, a comparative study of 3D scaffold fabrication using different ionic crosslinkers remains unstudied to date. Since alginate hydrogel/beads crosslinked with calcium (Ca^{2+}), barium (Ba^{2+}), or zinc (Zn^{2+}) ions facilitated the release of growth factors and tissue regeneration in a number of studies [35,36], in this dissertation the ionic crosslinkers (i.e. $CaCl_2$, $BaCl_2$, and $ZnCl_2$) have been chosen in scaffold bioprinting for the possible application in nerve tissue engineering. To this end, the evaluation of printability of MVSA precursor in the ionic crosslinkers is needed to fabricate complex 3D structure without compromising predefined design data. While several studies reported the crosslinking rate of ionic crosslinker and concentration of hydrogel precursor affect scaffold printability [37], a comparative study of MVSA precursor printability into different ionic crosslinkers is lacking. Therefore, in this thesis the strand and pore shape printability of MVSA precursor were evaluated at varying alginate precursor and ionic crosslinker concentration.

Implanted scaffolds might undergo compression forces, surface and bulk degradation in *in vivo*. Therefore, to sustain biofabricated geometry in tissue regeneration process, the scaffolds should have sufficient mechanical strength [38]. To date, while several studies have reported the mechanical strength (*i.e.* swelling, degradation, and elastic modulus) of bulk hydrogel incubated in the physiologic buffer [39], the mechanical stability of biofabricated MVSA scaffolds crosslinked with varying concentration of $Ca^{2+}/Ba^{2+}/Zn^{2+}$ ions remains unexplored. Generally, hydrogel swells in a media due to ion exchange, polymer chain relaxation, and water uptake mechanism [40]. Excessive swelling of hydrogel causes tissue compression, pore blockage and uncontrolled degradation [41]. However, absorption of surrounding fluid at implantation site also causes swelling that might assist tissue regeneration [42]. Hydrogels particularly MVSA swells and loses mechanical strength exchanging Na^+/Ca^{2+} ions with physiologic buffer upon *in vivo* implantation [43]. The swelled hydrogel eventually undergo surface and bulk degradation by the combined interaction of wound fluid and physiologic buffer. In alginate hydrogel, divalent cations make bond with guluronate (G) blocks of the polysaccharide chains. Upon implantation, alginate scaffold encounter exogenous Na^+ ions supplied by wound fluid or physiological buffer. Na^+ ions release the divalent cations from gel structure that result in non-crosslinked G blocks. The free negatively charged and non-crosslinked sequences repel each other, therefore, water molecule penetrate the structure, and alginate scaffold swells and is degraded [44].

Therefore, both swelling and degradation study of bioprinted alginate scaffolds are essential for their likely application in tissue regeneration. Moreover, assessments of elastic modulus demonstrate the amount of compressive force a hydrogel can sustain avoiding plastic deformation [45]. Hydrogels having a reasonable high compression modulus can retain their structure for a certain period of time upon *in vivo* implantation[46]. Cells in regenerating tissues might be sensitive to the elastic modulus of different hydrogels at different stages of development and remodeling. Further, the tissue regeneration period and tissue response to the elastic modulus of hydrogels might vary at different anatomical territory. For example, bone tissue grow wells in a stiff hydrogel, while nerve tissue regenerates well in soft hydrogel [47]. Therefore, the assessment of elastic modulus of scaffolds at different time interval is necessary to evaluate their probable applicability at specific anatomical territory. Like printability, a comparative study is required to evaluate the bioprinted MVSA scaffolds crosslinked with $Ca^{2+}/Ba^{2+}/Zn^{2+}$ ions in terms of mechanical and biological property. Unfortunately, such

comparative study remains unreported to date. To address the issues, alginate scaffolds biofabricated at varying concentration of ionic crosslinkers and alginate precursors were evaluated mechanically and biologically at predefined time points. In particular, the mechanical strength of alginate scaffolds bioprinted in the three different ionic crosslinkers was evaluated maintaining physiologically relevant conditions up to 42 days. Since evaluation of mechanical strength of a scaffold is necessary for *in vivo* application, in this dissertation multiple regression equations have been developed to predict the swelling, degradation, and Young's modulus of scaffolds fabricated using various concentrations of alginate and ionic crosslinker after they have been incubated under physiological conditions.

1.4 Peptide modified hydrogel and PNS regeneration

Some hydrogel (e.g. collagen, gelatin, Matrigel, fibrin, etc.) contains cell binding motifs in the molecular structures while other hydrogels (alginate, chitosan, agar, etc.) don't possess [48]. Hydrogels particularly MVSA lacking cell binding motifs demonstrate poor cell-biopolymer interaction, and couldn't assist cell attachment, differentiation and survival [49]. Admixed protein or peptide molecules (such as; arginine-glycine-aspartate (RGD), tyrosine-isoleucine-glycine-serine-arginine (YIGSR), etc.) into MVSA hydrogel improves the tissue regeneration capability somewhat due to the gradual release of the admixed molecules in the surrounding fluid [50]. In contrast, covalently linked peptide sequence remains in the molecular structure of MVSA over the tissue regeneration period and interact with cell population [51]. Being promising, several studies have prepared single peptide conjugated MVSA (PCSA) bulk hydrogel and studied axon regeneration [52]. However, axon regeneration study on the biofabricated single or composite PCSA strands remains unexplored to date. To deal with the issue, in this dissertation single PCSA precursor was prepared conjugating 1 mg of RGD or YIGSR to 1 gram of MVSA, while composite PCSA precursor was prepared conjugating RGD and YIGSR peptide (1:2 molar ratio) to 1 gram of MVSA. RGD, a peptide sequence seen in fibronectin, binding with integrin receptors of cell surface facilitates cellular attachment. Besides, laminin derived peptide YIGSR plays a key role in axon regeneration [53], since a significant amount of laminin protein is seen in the basal lamina of peripheral nerves [54]. The RGD peptide was reported to affect the adhesion and proliferation of PC12 cells, while the YIGSR peptide was found to regulate neuronal differentiation at an elevated density [55].

Therefore, in this thesis RGD and YIGSR peptide sequences have been covalently linked with alginate hydrogel maintaining a 1:2 molar ratio to enhance the axon outgrowth.

The mechanical property of the PCSA hydrogel might be compromised in the preparation process since the conjugation protocol is associated with several chemical treatments. Therefore, the mechanical strength of the scaffolds fabricated with PCSA precursor requires to be characterized in terms of swelling, degradation and elastic modulus for the possible application in specific anatomical territory. Moreover, to obtain reasonable printability of PCSA precursor, needle speed and extrusion pressure requires to be tuned likewise. While a number of study measured the printability and mechanical strength of MVSA or hybrid MVSA scaffolds [28,37], the characterization of single or composite PCSA scaffold has not been conducted yet by evaluating mechanical property and printability. To address the issue, in this thesis the printability of composite PCSA strands extruded in $CaCl_2$ solution were assessed by comparing the strand width, pore shape, and angular structure with theoretical values. Mechanical strength of the scaffolds was determined by measuring the swelling, degradation, and elastic modulus data over a 3 week period.

In vivo, Schwann cells (SCs) play a significant role in regenerating damaged nerves by providing guidance cues and growth factors [56]. Therefore, inclusion of SCs in the biofabricated strands would be a promising strategy to enhance neurite out growth. However, the reasonable viability of SCs is required during the axon regeneration period. The assessment of viability of SCs at different time points in the PCSA strands is required to characterize the bioprinted strands. Besides, the interaction between PCSA and SCs requires to be evaluated with respect to cell processes length, cell morphology, and quantity of released growth factor for a specific time period. Although several studies reported the 3D viability, morphology, and proliferation of SCs in the RGD conjugated SA strands or bulk hydrogel [50], the outcome of 3D culture of SCs in the YIGSR or RGD/YIGSR conjugated MVSA strands remain unreported till now. Therefore, a comparative study has been conducted in this thesis to access the biological performance of single or composite PCSA scaffolds by measuring the viability, morphology, attachment, and BDNF secretion ability of SCs in culture.

Growing neurites through a large gap in PNS caused by injury requires physical, topographical and biochemical cues to reach the distal target and invade appropriate anatomical

territory [57]. While biofabricated pattern could provide directional guidance cues to the developing neurites, PCSA scaffolds might provide necessary biochemical cues for the attachment, proliferation, and differentiation of neuron cells. Since *in vivo* injured axon regenerates through natural ECM that contains multiple peptide sequences, it can be hypothesized that composite PCSA precursor might result in better neurite regeneration compared to single PCSA hydrogel. In addition, neuron cells harvested from stimulated dorsal root ganglia (DRGs) better represent the status of neuron cells after PNS injury. However, axon regeneration from stimulated neuron cells seeded on the single and composite PCSA strands remain uninvestigated until now. Therefore, in this dissertation axon regeneration on biofabricated PCSA strands in terms of length and directionality have been assessed.

1.5 Research goals

This dissertation aims to develop the bioprinting process of MVSA scaffolds that were characterized both mechanically and biologically for peripheral nerve tissue regeneration. The particular research objectives of this thesis are:

- To develop methods to evaluate the effect of viscosity on the flow rate of MVSA precursor extruded from 3D bioplotter. Accordingly, the flow behavior model was developed from rheological data of MVSA precursor, while the flow rate model was developed considering the flow of MVSA precursor from taper needle based on the assumption of shear and slip flow.

- To examine and identify the appropriate ionic crosslinkers in the bioprinting process of MVSA scaffolds. On this basis, the effect of various ionic crosslinkers (e.g. $Ca^{2+}/Ba^{2+}/Zn^{2+}$) on the mechanical strength and biological performance of bioprinted MVSA Scaffolds were evaluated. Varying the concentrations, the combined effect of MVSA precursor and crosslinkers is also investigated to find optimum mechanical strength and biological performance suitable for nerve tissue regeneration.

- To examine the nerve regeneration ability of hydrogel scaffolds bioprinted with PCSA precursor. Accordingly, the printability, mechanical stability, and neurite regeneration ability of PCSA scaffolds were studied. In particular, the printability of composite PCSA precursor was assessed in terms of strand, pore, and angle printability, while the mechanical strength was evaluated in terms of swelling, degradation, Young's modulus, and morphology assessment. The neurite regeneration was determined from directional

outgrowth of axons cultured on PCSA scaffolds. The efficacy of PCSA scaffolds was further evaluated by measuring the viability, growth factor release ability and morphological changes of incorporated SCs.

1.6 Organization of this thesis

This dissertation contains six chapters including this chapter, four chapters adapted from the four manuscripts that have been published or submitted for possible publication, a chapter of conclusions and suggested future research directions.

Chapter 2 presents a brief review on the recent progresses in the design and fabrication of nerve guidance conduits (NGCs) for damaged PNS regeneration. In particular, a number of design approaches including hollow, porous, multi-channel, ECM loaded, filaments incorporated, and magnetically aligned fibrils loaded NGCs were focused and the influence of the approaches on axon regeneration was reviewed. The application of rapid prototyping (i.e. extrusion- and laser-based) and nanoscale technique (i.e. electrospinning- and direct polymer melt deposition) in NGC fabrication have been described and the functional axon regeneration ability of the NGCs was discussed both for *in vitro* and *in vivo* applications. Besides, the attractive features and shortcomings of each design and fabrication approaches were highlighted and discussed, as well as the future research direction were recommended.

Chapter 3 investigates the effect of flow behavior of MVSA precursor and bioprinting variables (*i.e.* temperature, needle geometry, and dispensing pressure) on the precursor flow rate from extrusion needle. Particularly, flow rate model of MVSA precursor was developed considering both shear and slip flow from taper needle. Since the flow rate model was developed from flow behavior information, the flow behavior of MVSA precursor was characterized and modeled using non-linear regression approach. Notably, the flow behavior model was developed from rheological data collected at varying temperatures ($25–55\,°C$) and alginate concentrations (1–4%). The flow behavior and flow rate model was verified against 2.5%, and 2, 3, and 4% MVSA precursor, respectively. The flow rate model was further verified against the flow of MVSA precursor from various needle openings (0.2, 0.25, 0.41, and 0.61 mm) at varying temperatures (25, 35, 45, and $55\,°C$).

In chapter 4, the effect of three different ionic crosslinkers (e.g. $CaCl_2$, $BaCl_2$, and $ZnCl_2$) on the mechanical and biological performance of MVSA scaffolds was presented. The printability, and mechanical properties (e.g. swelling, degradation, and Young's modulus) of MVSA scaffolds were measured maintaining 2, 3, and 4% MVSA precursor concentration, while the 50, 100, and 150 mM concentration were maintained for the three ionic crosslinkers. In particular, the mechanical properties were conducted between 0-6 weeks incubating the scaffolds in the 10 mM phosphate buffered saline. The surface morphology of the degraded scaffolds collected at different points was studied using scanning electron microscopy (SEM). Multiple regression equations were derived and presented to predict the swelling, degradation, and elastic modulus of MVSA scaffolds varying the type and concentrations of ionic crosslinkers. Besides, varying the concentration of MVSA precursor and ionic crosslinkers, the viability of rat primary SCs in biofabricated MVSA strands were investigated.

Chapter 5 examines the directional axon growth ability of hydrogel scaffolds bioprinted with either single or composite PCSA precursor. In particular, the single (i.e. RGD or YIGSR) or composite (RGD: YIGSR = 1:2) PCSA precursor was characterized evaluating printability, mechanical strength, and biological performance of the scaffolds. The 2D printability of the 2% composite PCSA precursor was assessed by comparing the theoretical strand width, pore shape and angle between strands with experimental values. In addition, the printability of the precursor was examined in three different concentrations of $CaCl_2$ solution (i.e. 50, 100, and 150 mM). Moreover, the morphology of the degraded surface of composite PCSA scaffolds was evaluated with SEM imaging. The mechanical strength of the composite scaffolds was evaluated in terms of swelling, degradation, and elastic modulus over a 3 week period. Besides, the biological performance of the single or composite PCSA precursor was evaluated by studying the viability, morphology, and BDNF generation of SCs. In addition, the directional neurite growth from stimulated neuron cells seeded on PCSA scaffolds was assessed.

In chapter 6, the methods developed and results obtained from the present study are summarized and on this basis, conclusions are drawn and presented. Besides, suggestions of future research directions are presented and discussed in the chapter.

1.7 Contributions of the primary investigator

The published articles included in this thesis have multiple co-authors. However, the first author, Md. Ariful Islam Sarker, is the primary investigator of the research work as per the mutual understanding of all co-authors. In this dissertation, the co-authors are greatly appreciated and acknowledged for their valuable contributions.

1.8 References

[1]   Wilgus TA. Regenerative healing in fetal skin: a review of the literature. Ostomy Wound Manag. 2007;53:16.

[2]   Tsang VL, Bhatia SN. Three-dimensional tissue fabrication. Adv. Drug Deliv. Rev. 2004;56:1635–1647.

[3]   Loh QL, Choong C. Three-dimensional scaffolds for tissue engineering applications: role of porosity and pore size. Tissue Eng. Part B Rev. 2013;19:485–502.

[4]   O'brien FJ. Biomaterials & scaffolds for tissue engineering. Mater. today. 2011;14:88–95.

[5]   Naahidi S, Jafari M, Logan M, et al. Biocompatibility of hydrogel-based scaffolds for tissue engineering applications. Biotechnol. Adv. 2017;35:530–544.

[6]   Fonseca PRB da, Gatto BEO, Tondato VA. Post-trauma and postoperative painful neuropathy. Rev. Dor. 2016;17:59–62.

[7]   Terzis J, Faibisoff B, Williams HB. The nerve gap: suture under tension vs. graft. Plast. Reconstr. Surg. 1975;56:166–170.

[8]   Ray WZ, Mackinnon SE. Management of nerve gaps: autografts, allografts, nerve transfers, and end-to-side neurorrhaphy. Exp. Neurol. 2010;223:77.

[9]   Lu L-J, Sun J-B, Liu Z-G, et al. Immune responses following mouse peripheral nerve xenotransplantation in rats. Biomed Res. Int. 2009;2009.

[10]   Muheremu A, Ao Q. Past, present, and future of nerve conduits in the treatment of peripheral nerve injury. Biomed Res. Int. 2015;2015.

[11]   Ngo TB, Waggoner PJ, Romero AA, et al. Poly (L-Lactide) microfilaments enhance peripheral nerve regeneration across extended nerve lesions. J. Neurosci. Res. 2003;72:227–238.

[12]   Sufan W, Suzuki Y, Tanihara M, et al. Sciatic nerve regeneration through alginate with tubulation or nontubulation repair in cat. J. Neurotrauma. 2001;18:329–338.

[13]   Sarker MD, Naghieh S, McInnes AD, et al. Regeneration of peripheral nerves by nerve guidance conduits: Influence of design, biopolymers, cells, growth factors, and physical stimuli. Prog. Neurobiol. 2018; 171:125-150.

[14]   Menorca RMG, Fussell TS, Elfar JC. Peripheral nerve trauma: mechanisms of injury and recovery. Hand Clin. 2013;29:317.

[15]   Evans GRD, Brandt K, Katz S, et al. Bioactive poly (L-lactic acid) conduits seeded with

Schwann cells for peripheral nerve regeneration. Biomaterials. 2002;23:841–848.

[16] Du J, Chen H, Qing L, et al. Biomimetic neural scaffolds: a crucial step towards optimal peripheral nerve regeneration. Biomater. Sci. 2018;6:1299–1311.

[17] Annabi N, Nichol JW, Zhong X, et al. Controlling the porosity and microarchitecture of hydrogels for tissue engineering. Tissue Eng. Part B Rev. 2010;16:371–383.

[18] An J, Teoh JEM, Suntornnond R, et al. Design and 3D printing of scaffolds and tissues. Engineering. 2015;1:261–268.

[19] Wüst S, Müller R, Hofmann S. Controlled Positioning of Cells in Biomaterials—Approaches Towards 3D Tissue Printing. J. Funct. Biomater. 2011;2:119–154.

[20] Derakhshanfar S, Mbeleck R, Xu K, et al. 3D bioprinting for biomedical devices and tissue engineering: A review of recent trends and advances. Bioact. Mater. 2018;3:144–156.

[21] Lee KY, Mooney DJ. Alginate: properties and biomedical applications. Prog. Polym. Sci. 2012;37:106–126.

[22] Matyash M, Despang F, Mandal R, et al. Novel soft alginate hydrogel strongly supports neurite growth and protects neurons against oxidative stress. Tissue Eng. Part A. 2011;18:55–66.

[23] Hölzl K, Lin S, Tytgat L, et al. Bioink properties before, during and after 3D bioprinting. Biofabrication. 2016;8:32002.

[24] Sun J, Tan H. Alginate-Based Biomaterials for Regenerative Medicine Applications. 2013;1285–1309.

[25] Rowley JA, Mooney DJ. Alginate type and RGD density control myoblast phenotype. J. Biomed. Mater. Res. Part A. 2002;60:217–223.

[26] Tian XY, Li MG, Cao N, et al. Characterization of the flow behavior of alginate/hydroxyapatite mixtures for tissue scaffold fabrication. Biofabrication. 2009;1:045005.

[27] Rajaram A, Schreyer D, Chen D. Bioplotting alginate/hyaluronic acid hydrogel scaffolds with structural integrity and preserved schwann cell viability. 3D Print. Addit. Manuf. 2014;1:194–203.

[28] You F, Wu X, Zhu N, et al. 3D Printing of Porous Cell-Laden Hydrogel Constructs for Potential Applications in Cartilage Tissue Engineering. ACS Biomater. Sci. Eng.

2016;2:1200–1210.

[29] Sarker M, Chen XB, Schreyer DJ. Experimental approaches to vascularisation within tissue engineering constructs. J. Biomater. Sci. Polym. Ed. 2015;26:683–734.

[30] Yilmazer U. Slip Effects in Capillary and Parallel Disk Torsional Flows of Highly Filled Suspensions. J. Rheol. (N. Y. N. Y). 1989;33:1197.

[31] Kamerkar PA, Edwards BJ. An experimental study of slip flow in capillaries and semihyperbolically converging dies. Polym. Eng. Sci. 2007;47:159–167.

[32] Li M, Tian X, Schreyer DJ, et al. Effect of needle geometry on flow rate and cell damage in the dispensing-based biofabrication process. Biotechnol. Prog. 2011;27:1777–1784.

[33] Chai Q, Jiao Y, Yu X. Hydrogels for biomedical applications: Their characteristics and the mechanisms behind them. Gels. 2017;3:6.

[34] Irvine SA, Venkatraman SS. Bioprinting and differentiation of stem cells. Molecules. 2016;21:1188.

[35] Jay SM, Saltzman WM. Controlled delivery of VEGF via modulation of alginate microparticle ionic crosslinking. J. Control. Release. 2009;134:26–34.

[36] Wee, Gombotz. Protein release from alginate matrices. Adv. Drug Deliv. Rev. 1998;31:267–285.

[37] Ouyang L, Yao R, Zhao Y, et al. Effect of bioink properties on printability and cell viability for 3D bioplotting of embryonic stem cells. Biofabrication. 2016;8:35020.

[38] Prasadh S, Wong RCW. Unraveling the mechanical strength of biomaterials used as a bone scaffold in oral and maxillofacial defects. Oral Sci. Int. 2018;

[39] Rajaram A, Schreyer DJ, Chen DXB. Use of the polycation polyethyleneimine to improve the physical properties of alginate–hyaluronic acid hydrogel during fabrication of tissue repair scaffolds. J. Biomater. Sci. Polym. Ed. 2015;26:433–445.

[40] Holback H, Yeo Y, Park K. Hydrogel swelling behavior and its biomedical applications. Biomed. Hydrogels. Elsevier; 2011. p. 3–24.

[41] El-Sherbiny IM, Yacoub MH. Hydrogel scaffolds for tissue engineering: Progress and challenges. Glob. Cardiol. Sci. Pract. 2013;38.

[42] Chiu Y-C, Cheng M-H, Engel H, et al. The role of pore size on vascularization and tissue remodeling in PEG hydrogels. Biomaterials. 2011;32:6045–6051.

[43] Bajpai SK, Sharma S. Investigation of swelling/degradation behaviour of alginate beads

crosslinked with Ca^{2+} and Ba^{2+} ions. React. Funct. Polym. 2004;59:129–140.

[44] Matyash M, Despang F, Ikonomidou C, et al. Swelling and mechanical properties of alginate hydrogels with respect to promotion of neural growth. Tissue Eng. Part C Methods. 2013;20:401–411.

[45] Ahearne M, Yang Y, El Haj AJ, et al. Characterizing the viscoelastic properties of thin hydrogel-based constructs for tissue engineering applications. J. R. Soc. Interface. 2005;2:455–463.

[46] Wang T, Lai JH, Yang F. Effects of hydrogel stiffness and extracellular compositions on modulating cartilage regeneration by mixed populations of stem cells and chondrocytes in vivo. Tissue Eng. Part A. 2016;22:1348–1356.

[47] Matyash M, Despang F, Mandal R, et al. Novel soft alginate hydrogel strongly supports neurite growth and protects neurons against oxidative stress. Tissue Eng. Part A. 2012;18:55–66.

[48] Tibbitt MW, Anseth KS. Hydrogels as extracellular matrix mimics for 3D cell culture. Biotechnol. Bioeng. 2009;103:655–663.

[49] Rowley JA, Madlambayan G, Mooney DJ. Alginate hydrogels as synthetic extracellular matrix materials. Biomaterials. 1999;20:45–53.

[50] Ning L, Xu Y, Chen X, et al. Influence of mechanical properties of alginate-based substrates on the performance of Schwann cells in culture. J. Biomater. Sci. Polym. Ed. 2016;27:898–915.

[51] Yu Y, Guo L, Wang W, et al. Dual-peptide-modified alginate hydrogels for the promotion of angiogenesis. Sci. China Chem. 2015;58:1866–1874.

[52] Dhoot NO, Tobias CA, Fischer I, et al. Peptide-modified alginate surfaces as a growth permissive substrate for neurite outgrowth. J. Biomed. Mater. Res. Part A. 2004;71:191–200.

[53] Itoh S, Takakuda K, Samejima H, et al. Synthetic collagen fibers coated with a synthetic peptide containing the YIGSR sequence of laminin to promote peripheral nerve regeneration in vivo. J. Mater. Sci. Mater. Med. 1999;10:129–134.

[54] Mammadov B, Sever M, Gecer M, et al. Sciatic nerve regeneration induced by glycosaminoglycan and laminin mimetic peptide nanofiber gels. Rsc Adv. 2016;6:110535–110547.

[55]   Lee JW, Lee KY. Dual peptide-presenting hydrogels for controlling the phenotype of PC12 cells. Colloids Surfaces B Biointerfaces. 2017;152:36–41.

[56]   Wong KM, Babetto E, Beirowski B. Axon degeneration: make the Schwann cell great again. Neural Regen. Res. 2017;12:518.

[57]   Simitzi C, Ranella A, Stratakis E. Controlling the morphology and outgrowth of nerve and neuroglial cells: The effect of surface topography. Acta Biomater. 2017;51:21–52.

[58]   Laura MY, Leipzig ND, Shoichet MS. Promoting neuron adhesion and growth. Mater. today. 2008;11:36–43.

CHAPTER 2

Strategic Design and Fabrication of Nerve Guidance Conduits for Peripheral Nerve Regeneration

(All the literature review was conducted by me. Saman Naghieh and Adam D McInnes helped me in preparing Tables and Figures. Professor Xiongbiao Chen and David Schreyer guided and supervised the whole review work.)

2.1 Abstract

Nerve guidance conduits (NGCs) have been drawing considerable attention as an aid to promote regeneration of injured axons across damaged peripheral nerves. Ideally, NGCs should include physical and topographic axon guidance cues embedded as part of their composition. Over the past decades, much progress has been made in the development of NGCs that promote directional axonal regrowth so as to repair severed nerves. This paper briefly reviews the recent designs and fabrication techniques of NGCs for peripheral nerve regeneration. Studies associated with versatile design and preparation of NGCs fabricated with either conventional or rapid prototyping (RP) techniques have been examined and reviewed. The effect of topographic features of the filler material as well as porous structure of NGCs on axonal regeneration has also been examined from the previous studies. While such strategies as macroscale channels, lumen size, groove geometry, use of hydrogel/matrix, and unidirectional freeze-dried surface were seen to promote nerve regeneration, shortcomings such as axonal dispersion and wrong target reinnervation still remain unsolved. On this basis, future research directions are identified and discussed.

2.2 Introduction

Peripheral nerve injuries occur through traumatic, non-traumatic, and iatrogenic events, and cause painful neuropathies and neuromas, poor sensation, and weakness and paralysis for

patients due to the loss of function in damaged motor and sensory axons [1]. Successful regeneration of injured nerves is important for improving patient quality of life, and preventing complications that can result from the repair process gone wrong.

Over the past decades, regeneration of damaged peripheral nerves using nerve tissue grafts has been extensively studied and significant progress has been made. Early work investigated the clinical use of autografts, allografts, and xenografts in cases where severed nerve ends could not be rejoined with sutures. However, shortcomings of the use of grafts, including limited availability, donor site morbidity, and immunological rejection, inspired the development of alternative, artificial nerve guidance conduits (NGCs) [2]. The preliminary approach of promoting nerve repair with a hollow cylindrical conduit had limited success due to a lack of physical and topographical axon guidance cues [3]. Although hollow conduits could help in reconnecting injured nerve over a short distance (< 20 mm) [4], conduits with micro- and nanostructure fabricated by advanced techniques has recently been shown to promote the regeneration of axons across a much longer nerve gap [5]. Furthermore, placement of micro- and nanofibres at high density within the core of the NGC is helpful in generating high surface area within the conduit, while maintaining high porosity.

The distal portion of an injured peripheral nerve undergoes Wallerian degeneration [6], and the support cells known as Schwann cells (SCs) begin to reorganize and secrete growth factors and extracellular matrix (ECM) molecules that can guide regenerating axons back toward their appropriate peripheral targets through the persisting distal endoneurial tube. During axonal regeneration, SCs migrate and form "bands of Büngner" that provide a favourable, linear growth substrate for axons. During Wallerian degeneration, a variety of biological factors promotes SC proliferation, migration, differentiation, and linear organization [7]. The growth cone formed at the proximal end of each severed axon follows these bands of Büngner to reach the distal target [8]. Biological cues that promote linear axon growth may be in the form of attachment sites on the SC surface, adhesion molecules in the SC-produced ECM, or SC-secreted diffusible growth factors. However, severed axons that face a gap between the proximal and distal nerve stumps lose access to the natural physical and biochemical cues that promote and guide their growth. Misguided axons eventually advance and enter inappropriate anatomical territory, which prevents restoration of appropriate function in denervated tissues [9]. The use of NGCs can

minimize the axonal dispersion and cross target reinnervation, but more must be done to compensate for the loss of positive guidance cues that help axons grow across a gap.

Several studies report the incorporation of macro-, micro- and nanoscale filler materials within the NGC to facilitate axon regeneration. These methods have included using macroscale multilumen/multichannel structures, hydrogel matrix filler materials, magnetically-aligned fibrils, conduits rolled up from sheets of material, and unidirectional freeze-dried structures. Significant success obtained by introducing macroscale interior topography in promoting axon regeneration has led researchers to further explore micro- and nanoscale approaches.

There are two main approaches to fabricating NGCs with interior structure, i.e., conventional and rapid prototyping (RP) approaches. Conventional approaches of fabrication of conduits and filler materials result in variable pore size and geometry, with randomly oriented structure. NGCs fabricated by the conventional approaches show limited success in axon regeneration due to mass transfer complexities and disarrangement of the geometries. In contrast, precise and uniform geometry can be obtained by using RP approaches. Thus, NGCs can be fabricated with interconnected pores that facilitate vascular network formation and diffusional mass transfer for delivering nutrients to growing axons [10,11]. RP approaches also offer the promise of including more sophisticated design elements that function to guide axon growth in the right direction.

In this paper, a brief literature review has been conducted to explore RP techniques, including both extrusion and laser- and nanoscale-based assembly for NGCs fabrication. Further, this paper reviews the recent advances in the design and fabrication of NGCs embedded with topographic and biophysical cues for peripheral nerve regeneration. Such NGCs have shown promise in reducing the axonal dispersion and off-target reinnervation, and promoting the guided axonal growth *in vitro* and *in vivo*.

2.3 Strategic design of NGC

Hollow cylindrical NGCs were initially developed to bridge a nerve gap and confine axon regeneration to an appropriate channel. Unfortunately, the hollow NGCs resulted in poor axon regeneration across nerve injury gaps exceeding ~20 mm. To overcome this limitation, researchers have investigated various strategies to enhance the physical and biological cues within hollow NGCs (Fig. 2.1) and thereby improve axon growth across large nerve gaps.

Regenerating axons develop distal tip expansions called growth cones that explore and recognize growth and guidance cues within the surrounding milieu. Growth cones extend membranous protrusions called filopodia and lamellipodia that interact with the extracellular environment on the nanoscale range. Growth cone adhesion and attachment to a solid surface is necessary for axon growth. Thus, the microarchitecture of the NGC interior is likely to be a crucial factor for achieving effective axon growth across an injury-induced peripheral nerve gap.
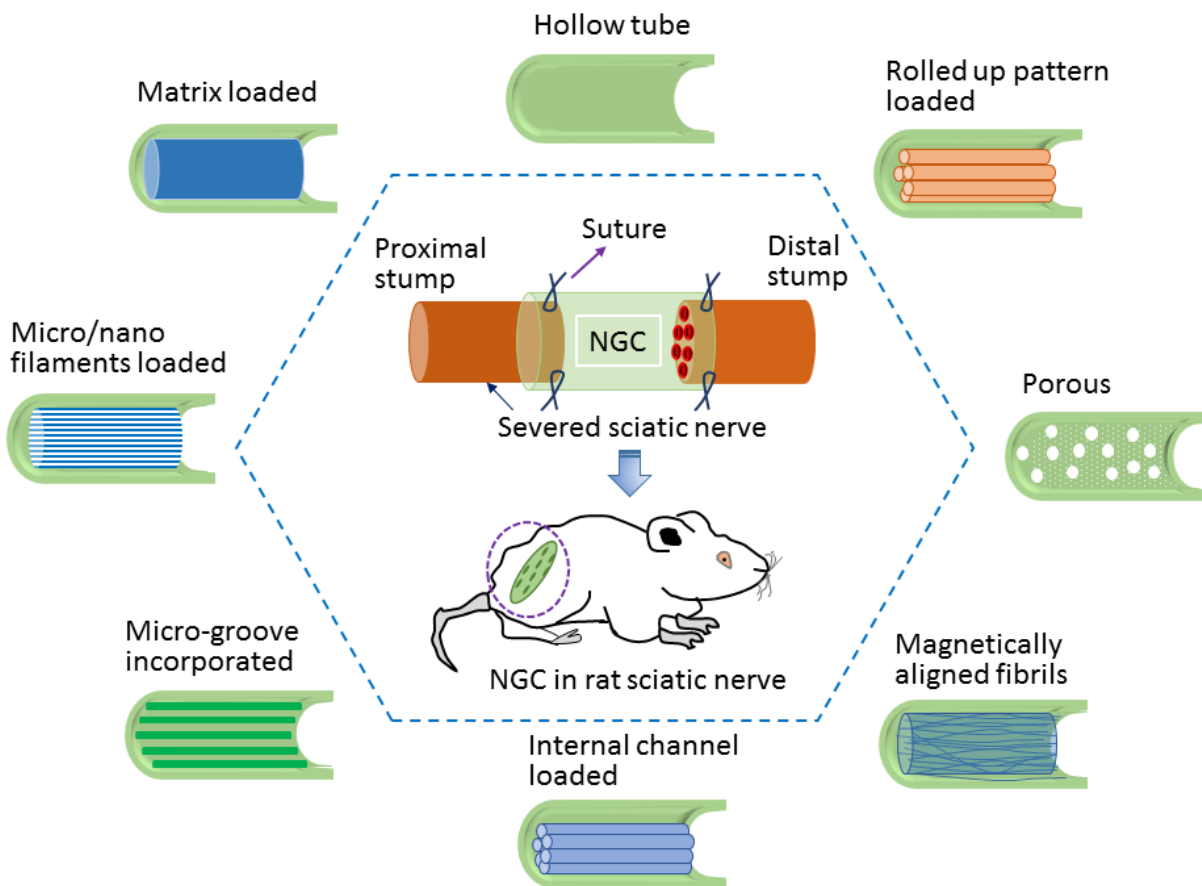
Fig. 2.1 Schematic of strategic design of NGC to promote directional axon growth and regeneration

2.3.1 Hollow NGCs

Hollow cylindrical tubes (Fig. 2.1) can be fabricated with natural or synthetic biomaterials typically by using melt extrusion, injection molding, physical film rolling, crosslinking, braiding, and electrospinning methods, [12–14]. The mechanical, physicochemical, and biological interactive properties of the prepared hollow tubes depend on both the preparation method and

the type of biomaterial. *In vivo*, hollow NGCs promote the formation of fibrin networks engendered by the blood clotting process, migration of various cells (e.g., SCs, endothelial cells, fibroblasts, etc.), and accumulation of neurotrophic growth factors from surrounding tissues. Further, several studies reported that hollow NGCs decrease neuroma and scar formation, collateral axon sprouting and myofibroblast infiltration [9,15]. However, hollow nerve conduits themselves lack biological, biochemical, and biophysical cues that are essential for directional neurite outgrowth. This may be why implanted hollow NGCs demonstrate inferior functional recovery compared to autografts [16]. The clinical and animal model study of single hollow tube NGCs are limited to cases of ≤ 30 mm nerve gap (Table 2.1), correlating with inappropriate and disorganized dispersion of the regenerating axons growing through the NGC lumen [17].

2.3.2 Porous NGCs

Porous NGCs (Fig. 2.1) were evaluated for their potential to support regenerating peripheral nerves over the past decades. Porous NGCs allow for blood vessels, nutrients, oxygen, and growth factors to permeate the structure [22]. Moreover, they permit migration of Schwann cells from adjacent nerve tissue that can form aligned structures similar to bands of Büngner [6]. In contrast, nonporous conduits do not permit such mass transfer [18] and can lead to nerve compression due to the accumulation of extracellular fluid [19]. Between these two extremes are semipermeable NGCs, which allow blood vessels, nutrients, oxygen, and growth factors to enter the conduits while excluding fibroblasts [20] that may inhibit nerve regeneration by depositing chondroitin sulfate within the NGC [21]. Asymmetric porous structures allow for the drainage of debris and other wastes in the early inflammatory period, preserve neurotrophic growth factors, and prevent the infiltration of inhibitor cells during axon regeneration (Table 2.1) [22]. Proper selection of the degree of NGC porosity is thus important in promoting optimal nerve regeneration.

2.3.3 Matrix loaded NGCs

In the case of a nerve gap > 20 mm, a hollow NGC cannot promote good nerve regeneration even with the formation of an internal fibrin network [23]. Schwann cells fail to form sufficient bands of Büngner at the lesion site and the nerve regeneration process remains ineffective due to insufficient topographical guidance cues [24]. Porous matrices could be incorporated into

22

hollow conduit or hollow NGC having wall porosity to incorporate physical cues in the NGCs. Incorporation of a matrix, typically made from hydrogel, into hollow conduits can promote directional growth of neuron cells (Fig. 2.1). Polysaccharides, ECM molecules, proteins, and peptides have been used in different studies to prepare a hydrogel matrix for use in hollow NGCs. ECM proteins such as collagen, fibronectin and laminin contain attachments sites that are recognized by advancing axonal growth cones, and inclusion of these proteins leads to better nerve regeneration in several *in vivo* studies (Table 2.1). For example, collagen- chondroitin-6-sulfate-filled collagen nerve conduits implanted in a 10-mm sciatic nerve defect in rats could recover the nerve function, and the recovery was close to that of the autograft implanted group [25]. Diluted ECM material used as filler can facilitate superior axon regeneration than concentrated ECM materials can. This effect has been proved when diluted collagen- or laminin-gel-filled silicon tubes promoted better nerve regeneration through 6 mm sciatic nerve gaps in mice than saline solution [26]. The combined effect of various ECM molecules has also been investigated in axon regeneration to mimic the *in vivo* situation. Laminin combined with fibronectin was found to be very effective for bridging a larger nerve gap compared to cytochrome-c, fibronectin, laminin, or nerve growth factor loaded conduit when silicon chambers filled with fibronectin and laminin were implanted into a 18 mm severed sciatic nerves ends of rats [27]. Including growth factors within the ECM molecule have been seen to favour axon regeneration compared to only ECM-molecule-loaded NGCs. NT-3, BDNF, or aFGF-1 included in a collagen matrix enhances better axon growth in the rat compared to plain collagen-gel-filled porous PHEMA-MMA NGCs. Notably, aFGF-1 promotes angiogenesis within the NGCs, and can facilitate similar nerve regeneration to autografts [28]. Besides, incorporating polysaccharide molecules within the NGC have been seen to aid axon regeneration. Although the polysaccharide molecules do not contain cell binding peptides, absorption of fluids produced in the wound at the implantation site improves their biological performance. PGA mesh tubes filled with alginate sponges caused functional nerve regeneration three months postoperatively when implanted in a 50 mm gap in the right sciatic nerve of cats [29].

2.3.4 Multichannel NGCs

Surface energy distribution, nanoscale chemical heterogeneities, and roughness are some of the factors in NGC design that may be important for promoting axon extension. Different methods

have been used to manufacture scaffolds with multiple channels and patterns. Several studies have used molding techniques to introduce macroscale multichannels within NGCs that potentially provide a permissive pathway for axon growth (Fig. 2.1). Multiple channels facilitate attachment of Schwann cells, release of growth factors, and lessen the dispersion of regenerating axons. Multilumen collagen conduits were observed to reduce axonal dispersion and facilitate functional nerve regeneration when implanted in a 10 mm sciatic nerve defects in rats [30]. However, while multichannel scaffolds are useful in reducing axonal dispersion, macro-sized lumens could not provide sufficient physical cues for directional outgrowth of axons. Over the past decades, researchers have explored various approaches and fabrication methods to develop microchannels within the NGCs. Microchannels offer topographical and physical cues that better mimic the microchannels of an endoneurium tube. *In vivo*, collagen-chitosan (CCH) scaffolds having longitudinally-orientated, parallel microchannels showed nerve regeneration and functional recovery similar to autografts when used to repair a 15 mm sciatic nerve gap in rats [31]. Such micropatterns affect Schwann cell migration and axon regeneration at the microlevel where these cells interact with them.

2.3.5 Rolled-up pattern/micro-groove incorporated NGCs

A number of studies have used rolled up micro- or nanopatterned two dimensional surfaces, or patterned micro- or nanomaterials as a filler material for NGCs (Fig. 2.2G and 2N) [32]. It was demonstrated that silicon nitride microtubes (Fig. 2.2E) prepared with conventional planar processing technique could provide a pathway for neuron cells [33]. Fabrication of microgrooves has been explored (Fig. 2.1), which has shown that while microgrooves facilitate cell attachment and growth, the size of the grooves should be designed with regards to cell diameter to obtain the desired performance. Experimental data suggest that narrow microgrooves (5-10 µm) constrain the development of cells (12 ± 3 µm) and axon outgrowth compared to wider grooves (20-60 µm). However, the smaller microgrooves were found to better align axon growth, minimize the number of axon branches per cell, and reduce wrong target reinnervation [34]. Electrospun cellulose acetate butyrate nanofibers having longitudinal nanogrooves (200 nm) supported better functional recovery of sciatic nerves in rats compared to controls [35]. Electrospinning of high molecular weight cellulose acetate butyrates resulted in grooves on nanofibres. Incorporation of

nanogrooves (Fig. 2.2J and 2.2K) in NGCs increases the available surface area to volume ratio, and thus enhance cell and growth cone attachment and proliferation [36].

Another method that has been evaluated is anisotropic micropillar arrays. These patterns are created by fabricating arrays of micro- and nanoscale columns using methods such as capillary force lithography and photolithography (Fig. 2.2I). The research has shown that both the size of the pillars and the distance between the pillars has important effects on the resulting axon growth. [37,38]. Moreover, gradients of the topographic features in the nanoscale range cause directional topotaxis of neurons. Arrays of nanocolumns (diameter 600 nm) in a graded fashion (Fig. 2.2F) caused migration of neurons *in vitro* in the direction of sparser column after 12 hours of seeding [37]. Nanoscale roughness of the substrate has also been investigated for its effect on axon extension (Fig. 2.2M). Higher value of mean roughness (R_a ~80–100 nm) were associated with lower levels of cell adhesion on the substrate and higher levels of cellular necrosis. Conversely, a lower value of R_a (36 nm) was associated with much higher levels of cell attachment and lower levels of cellular necrosis [39]. The diameter of the nanoparticles used to form packed features on the nanosurface was also studied (Fig. 2.2L). Well-packed silica beads (>200 nm) on a glass substrate were reported to accelerate neurite out growth *in vitro* [40]. Packing density and size of the nanoparticles were shown to have an influence on the rate of axon outgrowth.

In order to better mimic the physiologic environment, rolled-up sheet was prepared by compiling a micro-patterned surface containing nerve cells and a flat membrane having a gradient concentration of neurotrophic factors (Fig. 2.2D) [41]. Besides, several studies have incorporated nerve growth factor (NGF) loaded microspheres into patterned microstructures to prepare NGCs. For example, a collagen-chitosan (CCH) conduit, having longitudinally oriented microchannels and NGF loaded chitosan microspheres, resulted in superior nerve generation in a 15-mm-long sciatic nerve gap in rats compared to NGF loaded CCH or CCH conduit alone 16 weeks postoperatively [42]. In these studies, microspheres were identified as an effective carrier for NGF to achieve controlled release.
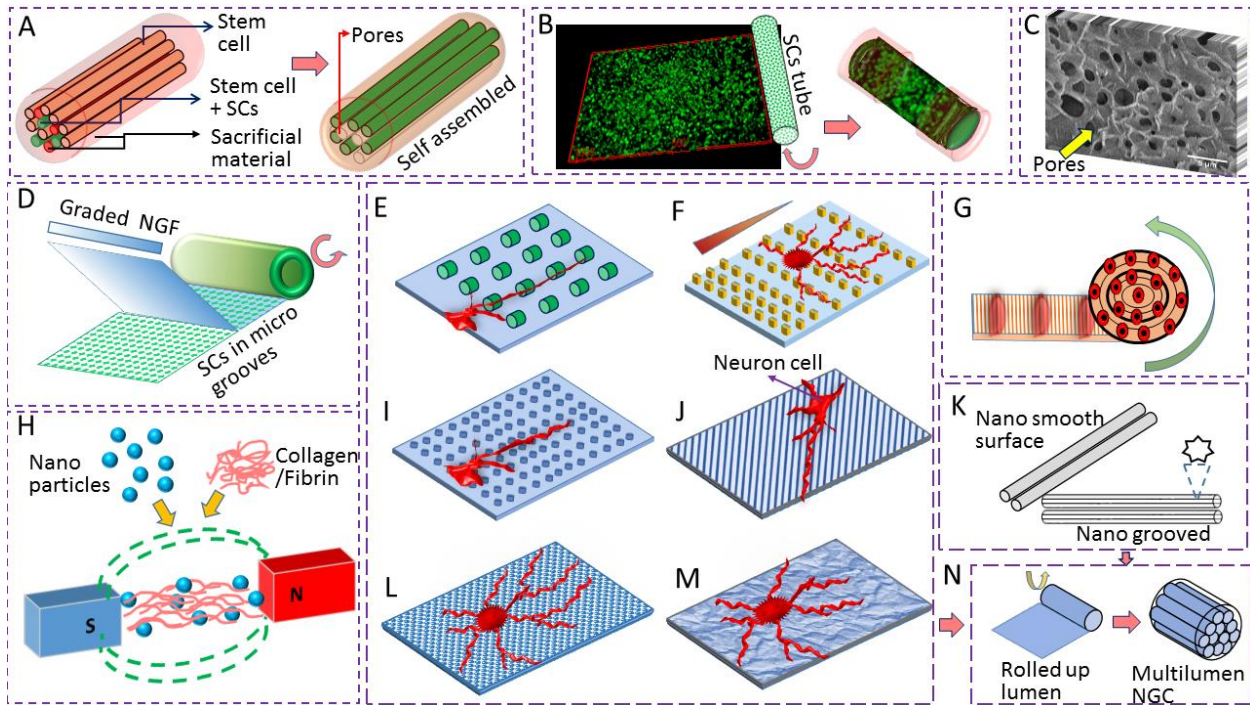
Fig. 2.2 Schematic of versatile conduit design for peripheral nerve regeneration, (A), self-assembled NGC; (B), rolled up Schwann cell sheet; (C), unidirectional freeze dried surface; (D), rolled up sheet containing Schwann cells and NGF in a graded fashion ; (E), microtubes prepared with planar processing; (F), graded nanoscale feature; (G), rolled up microscale pattern; (H), magnetically aligned fibrils; (I), surface having nanoscale column; (J), surface with nanoscale gratings; (K), nanofilaments with nanoscale grooves; (L), surface with nanoscale packed beads; (M), surface having nanoscale roughness; (N), rolled up multilumen NGC.

2.3.6 NGCs loaded with filaments

Unidirectionally aligned microfilaments assist axonal growth cones in recognizing and responding to the microenvironment in order to follow a path (Fig. 2.1). Simultaneously, SC migration could be affected by the stiffness gradient of microfilaments [43]. As a consequence, axon growth towards the distal part of a severed nerve is improved. Besides helping direct axonal growth, micropatterned substrates lessen the inflammatory response and foreign body reaction [44]. To mimic the autologous nerve graft, studies were conducted incorporating a large number of microfilaments within NGCs. These studies demonstrated that the number of microfilaments in NGCs had a significant effect on axonal regeneration [45] and that more microfilaments were

associated with improved nerve regeneration. However, while a larger number of microfilaments promoted better axon regeneration, excess microfilaments were found to inhibit axonal growth. The degree of successful nerve regeneration and the number of axons that ultimately matured to become myelinated were found to be improved with lower, rather than higher packing densities [46]. Synergistic effect of porous conduit and microfilaments on axon regeneration was also evaluated *in vivo*. A microporous chitosan conduit loaded with oriented PGA micro filaments could functionally recovered a 30-mm dissected sciatic nerve trunk in Beagle dogs six months post operatively [47].

2.3.7 Magnetically/cell aligned fibres

ECM hydrogels containing entangled 50 – 500 nm protein fibrils (collagen, fibrin, and laminin) can promote axonal growth across a long nerve gap (> 6 mm) [26]. However, axons that grew in such conduits were often misguided by the randomly oriented fibrils and this lead to poor nerve regeneration [48]. Fibrin deposition occurring as part of the normal blood clotting process is seen to form a bridge across a nerve defect and thus promote axon regeneration. However, the size and orientation of fibrils, and the required fibrin formation time significantly affect the axon regeneration process [49]. To overcome the random distribution of fibrils, efforts were conducted in several studies to prepare unidirectional fibrils with external forces (Fig. 2.2H), which have shown improved axon outgrowth. These studies suggest that both direction and size of protein fibrils influence the axon regeneration.

Since fibrin doesn't have enough mechanical stability, researchers have explored alternative biomaterials that can be aligned through applying external forces. High-strength magnetic fields were used to align type I collagen monomers into fibrils. Increases in the magnetic field strength were associated with improved axon growth and alignment, both *in vitro* and *in vivo*, compared to both lower-strength fields and no alignment [50,51]. Magnetically aligned type I collagen gel loaded collagen NGCs promoted better nerve regeneration compared to non-aligned collagen gel group while implanted into 4-6 mm sciatic nerve gap of mice 60 days after implantation [51].

Other methods of preparing aligned fibrils have been evaluated, including electrical gradients, gravity-driven flow and polymerization, etc. Of the different methods assessed, magnetic alignment of the fibrils was superior [52–54]. Besides application of external forces,

alignment of protein fibrils using cell-induced forces has been explored. Incorporation of appropriate cell types, notably SCs and fibroblasts embedded within the gel, generate contraction forces due to attachment and migration. These cell-aligned fibril NGCs showed improved nerve regeneration compared to empty NGCs [55]. In search of other substitute biomaterials, NGCs consisting of unidirectional-shear-oriented strands of fibronectin have also been evaluated. These conduits demonstrated levels of regeneration and SC migration comparable to autologous nerve grafts, and were superior to freeze-dried muscle [56].

Table 2.1 Conduit designs for nerve regeneration

Conduit/ coating material	Scaffold Details/ filler material	Fabrication method	*In vitro/ In vivo*	Study period	Results	Ref.
PLGA	Hollow fibre membranes	Wet phase inversion	*In vitro*		Selective permeability was lost at 3 weeks, and degraded completely at 8 weeks.	[57]
Glycolide trimethylene carbonate (GTMC) and collagen	Hollow NGC, tube and crimped form		2- and 5-cm nerve gaps in primates	14 months	GTMC conduit showed better axon regeneration in a 5 cm nerve gap than collagen conduit, but inferior axon growth in a 5 cm gap compared to a 2 cm gap.	[58]
PLGA and pluronic F127	Asymmetrically porous (pore size: 50 nm inside, and 50 µm outside)	Immersion precipitation	10 mm sciatic nerve gap in rat	6 months	Better axon regeneration than controls, inside of the NGC prevented the connective tissue infiltration and NGF accumulation, while the outside aided vascular ingrowth	[59]
PGA tube coated with collagen	Filled with NGF, bFGF and Matrigel	Cylindrically woven	25 mm sciatic nerve gap in cats.	16 months	Latency and SEPs were almost normal, walking pattern did not recover.	[60]
Silicone rubber	Keratin hydrogel	Hydrogel by rehydration	5 mm tibial nerve gap in mice	6 months	Keratin hydrogel showed similar CMAP, but there was greater axon density and diameter in autograft controls.	[61]
PGA/ Collagen	Collagen sponge	Tubular braiding	15 mm peroneal nerve gap in dogs	6 months	CNAPs and SEPs for the PGA-collagen NGC had a smaller latency and higher peak voltage than those on the autograft.	[62]
PGA/ Collagen	Laminin soaked collagen sponge		80 mm peroneal nerve gap in dogs	12 months	CMAPs showed complete recovery, SEPs indicated substantial recovery, and walking patterns reached near-normal.	[63]
PLLA/PCL and PU/PLLA	Two-ply conduit, outer pore 30–70 µm, inner pore 0.5–1µm	Immersed extrusion	7 mm sciatic nerve gap in rats	2 month	Nerve regeneration was similar to autograft.	[19]
PLLA	Porous NGC, porosity 83.5% and pore size 12.1 µm	Extrusion	10 mm sciatic nerve gap in rats	16 weeks	Walking track analysis and gastrocnemius muscle weight was better in isograft than PLLA conduit.	[64]
PLA	Microporous NGC,	Transfer	15 mm sciatic	8 weeks	SCs with ASCs or DPSCs seeded	[65]

	ASCs , DPSCs, and SCs seeded	molding	nerve gap in rats		conduit promoted better peripheral nerve regeneration than ASCs or DPSCs alone.	
PLA	Microporous NGC, GDNF or BDNF gene transfected NSCs seeded	Solvent/ nonsolvent process	15 mm gap in rat sciatic nerve	8 weeks	More myelinated axons and improved functional recovery was seen in GDNF- and BDNF-transfected NSCs than nontransfected NSCs.	[66]
Acrylic and silicon	Semipermeable and impermeable tubes		4 mm sciatic nerve gap in rats	27 weeks	More myelinated fibres and better endoneurium surface was seen in the impermeable NGC.	[67]
PLLA conduits	NGC loaded with SCs and collagen matrix	Solvent casting, extrusion, particulate leaching	12 mm sciatic nerve gap in rats.	4 months	Gastrocnemius muscle weight was similar, but axon density was inferior to isograft controls.	[68]
PLA	Microporous asymmetric conduit	Immersion precipitation	20 mm sciatic nerve gap in rabbit	18 months	Functional recovery was ∼82%, but morphologies were different from normal sciatic nerve.	[69]
Silicone rubber	Collagen, laminin, and fibronectin gel		10 mm gap in rat sciatic nerve	6 weeks	28% more cross-sectional area and myelinated axons in the extracellular gel group than the controls.	[70]
PGA–collagen	Laminin coated collagen fibres	Cylindrically woven PGA mesh	80 mm gap in dog peroneal nerve	12 months	Numerous unmyelinated and myelinated nerve fibres grew, dogs showed normal walking pattern.	[71]
PGA mesh	Freeze dried alginate gel	Cylindrically woven	50-mm gap in cat sciatic nerve	7 months	Functional reinnervation of motor and sensory nerves occurred as per CMAP and SEP.	[72]
Gelatin methacryloyl (cryoGelMA)	Multichannel NGC	3D printing	10 mm sciatic nerve gap in rats	16 weeks	Regeneration is comparable to autografts as per functional and histological evaluations.	[73]
PEG	Single and multi-lumen	Stereolithography	10 mm sciatic nerve gap in rats	5 weeks	Numbers of regenerated axons in single lumen was close to normal nerve, and higher than multilumen NGC.	[74]
P(LLA-CL)	Multichannel with aligned nanofibres	Electrospun	In vitro, seeded with Schwann cell	14 days	Schwann cells grew on nanofibres, and cell growth was increased in high channel density than the lower one.	[75]
PDLLA	Schwann cell seeded on micropatterned inner lumen	Transfer molding	10 mm sciatic nerve gap in rats	8 weeks	Sciatic function index and walking track analysis was enhanced in the conduit implanted groups.	[76]
PCL-PLA	Microgrooves with geometries (V shaped, sloped walls, and square shaped)	Solvent casting	In vitro, neural cell line	1 week	Nerve cells responded to the shape of the longitudinal grooves and the slope angle of the groove walls.	[77]
Silicone	Collagen gel (G), fibres (F), 100 − 150μm collagen fibres coated with laminin (L) or YIGSR (Y)	Elongation with a weight	10 mm sciatic nerve gap in rats	8 weeks	Myelinated axons density in the L- and Y-group were higher than F-group, regeneration didn't happen in G group.	[78]
Silicone	PLLA microfilaments, Packing density (3.75, 7.5, 15, and 30%)	Wet-spun	10 mm gap in the rat sciatic nerve	10 weeks	Lower packing densities grew more myelinated axons than highest packing density groups, regenerated nerve up to 18 mm gap.	[46]
No external conduit coating	Collagen filaments, diameter 20 μm		20 mm rat sciatic nerve defects	25 weeks	Number and diameter of grown axons were 6,900 and 3.1 μm in autograft, and 6,300 and 3.3 μm in filament groups.	[79]

| No external conduit coating | Collagen hydrogels with magnetic nanoparticles | External magnetic field | *In vitro* with primary neuron cells | 7 days | Neurons showed normal electrical activity, viability, and formed elongated morphology. | [80] |

2.4 RP NGC fabrication techniques

RP refers to techniques used to quickly create 3D parts or constructs based on the layer-by-layer manufacturing technology. Among various RP techniques, extrusion-based and Laser-based techniques have been widely used to fabricate constructs or scaffolds for a wide range of tissue engineering applications [78-90].

2.4.1 Extrusion-based techniques

In extrusion-based techniques, extruders/printers are used to deposit/print biomaterial solutions, where the biomaterials may also be augmented with living cells or biologically active proteins (referred as to bioprinting) [81]. For instance, Pati *et al.* have reported the bioprinting of decellularized ECM protein using a multi-head tissue/organ building system [82]. Such novel bioink resulted in high cell viability and functionality in the *in vitro* experiments. An extrusion-based printer mainly consists of a small nozzle for dispensing the biomaterial solution and an automatic robotic mechanism which is capable of moving in x, y, and z directions [83–86]. This technique uses mechanical (piston/screw-based) or pneumatic mechanisms to extrude the biomaterial (Fig. 2.3A). The flow behaviour of the biomaterial, especially its viscosity, plays a central role on the accuracy of deposition with these techniques [87]. Mechanically-operated 3D bioprinting systems can print biomaterials with relatively high viscosities, which is a main benefit of this technique over pneumatic systems. Moreover, this technique might be coupled with medical imaging techniques to create custom-made constructs [88]. Biomaterials with higher viscosities can support their own weight during the printing process and thus prevent any collapse during fabrication of a porous scaffold. However, damage to any encapsulated cells during extrusion due to large shear forces is a problem with this type of bioprinter [89]. It should also be noted that pneumatic methods may introduce delays in dispensing biomaterials owing to the use of a compressed gas volume and, thus, the mechanical methods can provide better control over the flow of biomaterials [90]. However, pneumatic 3D bioprinters have a simpler mechanism compared to mechanical bioprinters.

As a general rule, biomaterial selection for extrusion-based bioprinting should be based on satisfying requirements for both the mechanical stability of the material and preservation of cell viability and functionality [91,92]. It has been reported that 3D bioprinting techniques are capable of printing biomaterials with viscosity from 0.03 Pa/s to more than 30000 Pa/s [93]. Low-viscosity materials are generally good candidates for maintaining cell viability during and after printing, but materials with higher viscosity can provide better support and fidelity during the printing process.

Hydrogels are favoured biomaterials in extrusion-based bioprinting because of their high water content and their ability to mimic the properties of ECM [94]. Hydrogels are grouped as natural or synthetic in origin. Polysaccharides, such as alginate and chitosan, are considered natural hydrogels, and are noted for exhibiting good printability (Table 2.2). However, they do not have cell adhesion sites, which are necessary for cells to attach to the biomaterial [95,96]. On the other side, synthetic hydrogels facilitate the fabrication of scaffolds with modulated properties, but they do not participate in natural cell interactions and do little to promote cell functionality [97].

There are several factors that need to be considered in selecting suitable hydrogels for extrusion bioprinting. In extrusion-based bioprinting, hydrogels with shear-thinning behavior have drawn attention from researchers because these hydrogels show both self-healing properties and have reduced viscosity at higher shear rates [98]. Although promising, shear-thinning biomaterials offer relatively lower cell viability during extrusion compared to other methods (such as inkjet) due to shear-induced cell damage [99]. While the use of lower dispensing pressures and larger bore needles has proven effective in reducing cell damage, this comes at the expense of lower resolution of printing [100]. Considering that nanoscale features are required to mimic the native tissue, while the available extrusion-based bioprinters on the market can offer maximum 5 µm printing resolution at low speeds, research on developing and selecting biomaterials suitable for nanoscale fabrication is an important topic [101,102].

With more advanced 3D bioprinters, multiple nozzles can be used to dispense different materials, both as separate print heads as well as with coaxial nozzles (Fig. 2.3B). For example, Schwann cells and scaffold material can be printed separately to fabricate cell-encapsulating microlumen structures for axon regeneration [101]. Extrusion-based 3D bioprinting yields cell viability ranging from 40% to 97% depending on the types of biomaterial and extrusion-based

system used [103]. Some approaches have been developed that improve cell viability by using extrusion, then cross-linking, in a two-steps process [104]. Since cells cannot degrade some hydrogels (e.g. alginate) by enzymatic degradation, or form adhesive contacts, encapsulated cells in these hydrogels show circular morphology and poor proliferation in culture [105]. As a result, the poor cell-cell and cell-biomaterial interactions within an NGC fabricated using these hydrogels will inhibit nerve regeneration. To tackle this issue, composite scaffolds have been printed using multiple biomaterials, where mechanically stable materials were used to ensure structural support over time, while co-dispensed soft or enzymatically degradable materials were used to incorporate cells at higher densities. For instance, in a recent study, Gao et al. have shown how to functionalize alginate so that it can promote the proliferation, differentiation, and neovascularization of endothelial progenitor cells while maintaining the 3D coaxial printability [106].

In an extrusion-based system, the dispensing material remains in a liquid state in the nozzle, and then turns into a solid phase after being printed. Deposited material undergoes sol-gel transition via photoconversion, thermal conversion, or pH-induced, enzymatic, or chemical crosslinking [107]. Slow or fast sol-gel transition of the dispensed material has been explored for different cell-seeding techniques in different studies. Scaffolds can be prepared with harsh condition (e.g. high temperature, toxic crosslinker, acidic or alkaline chemicals, etc.) for post-bioprinting cell seeding, whereas cell-incorporation in a biomaterial requires optimum conditions to maintain cell viability during the entire biofabrication process [108]. In addition, hydrogel materials used in extrusion systems need to be crosslinked quickly to preserve structure, prevent cell damage, and facilitate printing complexity [109]. Nontoxic ionic crosslinkers have been used in many studies to crosslink hydrogel precursors immediately upon being dispensed under biologically mild conditions. The type and concentration of ionic crosslinkers must be considered carefully in light of other variables associated with the fabrication process (e.g. nozzle diameter, dispensing speed, viscosity of the biomaterial, temperature, pneumatic pressure, etc.) in order to achieve good printing resolution and mechanical stability of scaffold over time [110]. Although extrusion-based systems are quite convenient in generating high cell density within hydrogel scaffolds, the lack of mechanical stability of hydrogel materials limits their application in nerve tissue engineering [111].

Extrusion-based bioprinters have a major advantage in that they are capable of printing cells at high densities. To capitalize on this benefit, efforts have been made to bioprint nerve cells in high density without any biopolymers in order to induce cell fusion [112]. Such an approach, called a self-assembling spheroid, can facilitate the organization of tissues.

In the recent years, the extrusion-based system has been modified to print different types of cells/biopolymer mixtures simultaneously with multi-robotic arms printing complex structures that mimic native tissue composed of multiple types of cells (e.g. nervous system, vascular networks, or lymphatic systems) [113]. Since neuron cells grow well in microchannels, application of coaxial nozzles in extrusion-based systems has made it possible to print microlumen scaffolds for nerve regeneration. Coaxial printing of materials can take several approaches that vary the shell and core structure of the printed strands, such as sacrificial material or the cross-linker as the core material, cell aggregates or hydrogel as the shell material, and can be combined with using a print bath. Some parameters, for example the flow rheology and concentration of hydrogel precursor and ionic cross-linker, dictate the nozzle diameter and shell thickness of the bioplotted strand extruded from a coaxial nozzle [114]. Generally, SCs are either incorporated into the shell structure during bioplotting, or post-seeded with microfluidic techniques onto the bioplotted acellular microluminal surface, and then perfused with culture medium to facilitate the formation of bands of Büngner. In recent years, researchers have put emphasis on the biofabrication of tissue constructs with cell aggregates to increase the cell-cell interactions. In this context, the coaxial systems could be implemented to extrude the cell aggregates in the shell structure while keeping the sacrificial material in the core.
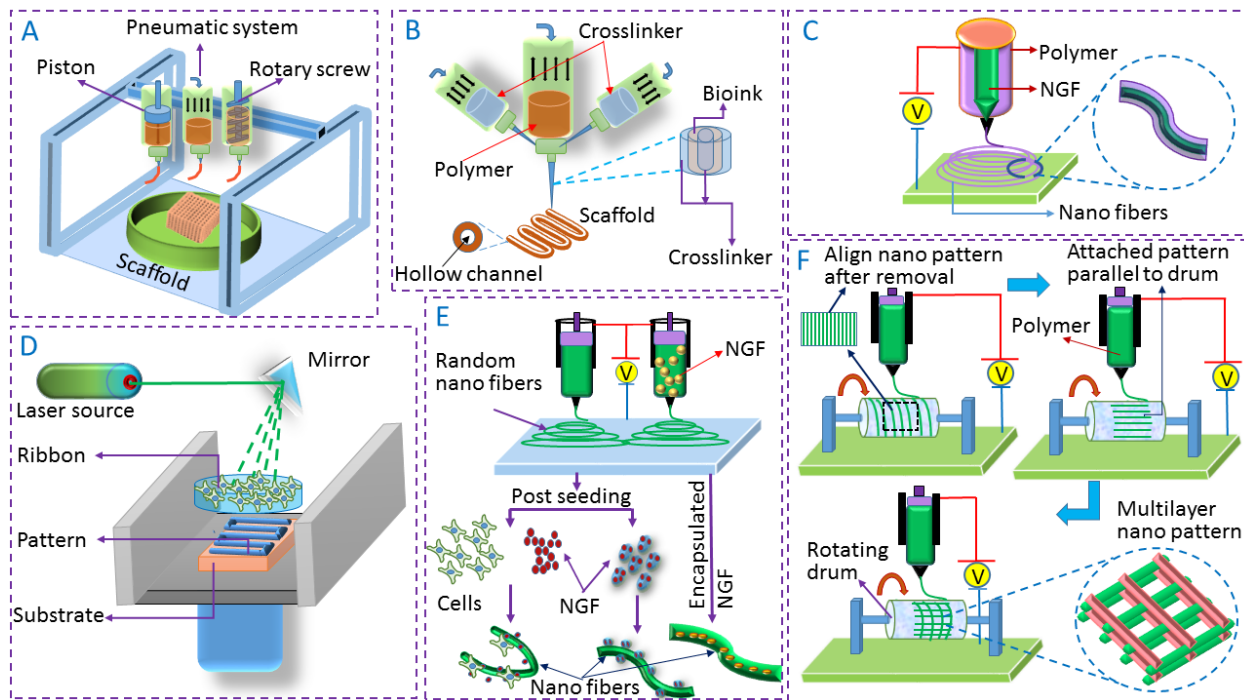
Fig. 2.3 Schematic of rapid prototyping and nanoscale techniques for 3D scaffold fabrication. (A), extrusion-based system; (B), coaxial nozzle system for 3D bioplotting; (C), coaxial nozzle system for nanoscale fabrication; (D), laser-based system; (E), growth factors and cell incorporation approach in randomly-oriented nanofibres; (F), fabrication approach of aligned nanofibers.

2.4.2 Laser-based Techniques

Laser-induced forward transfer (LIFT) is a 3D bioprinting technique that has been successfully implemented for biological materials, like peptides, DNA, and cells [100,115–117] and has been utilized to fabricate NGCs for nerve tissue regeneration [118]. LIFT uses a pulsed laser beam, directed at a focusing mirror and lens, which is then focused on a tri-layer ribbon (Fig. 2.3D). The ribbon consists of a carrier for the biomaterial, a sacrificial layer in the middle that absorbs the laser energy, and donor layer that consists of cells and other related biological materials. The laser energy is absorbed by the sacrificial layer where it rapidly vaporises a small area, which in turn ejects the donor layer overlying that area. This process transfers cells and other biological materials on the ribbon to a receiver/acceptor substrate where it is collected.

Since LIFT is a nozzle-free technique, nozzle clogging and shear-induced cell damage do not occur, and much higher resolution is possible. Using the LIFT technique, materials with

variable viscosities ranging from 1 to 300 mPa/s can be printed with acceptable cell viability [119,120]. The resolution of this technique depends on factors such as the amount of energy received, the distance between the receiver and ribbon, the viscosity of the cells/biological materials, and surface tension [121].

Despite the benefits, the LIFT technique is challenging. Preparation of the ribbon for every material is quite time-consuming and the accurate positioning of cells cannot always be guaranteed due to problems with the ribbons (however, using a scanning system has been proposed to tackle this issue by selecting only one cell associated with each pulse of laser [100]). Moreover, it has been reported that bioprinted constructs fabricated using LIFT can be contaminated by the small amounts of metallic parts associated with the absorbing layer [122,123]. There is also a potential for cells to be damaged by direct exposure of laser energy. Finally yet importantly, LIFT technology is expensive.

The LIFT approach has shown potential for fabricating high-density cell layers in applications such as cellularized skin constructs and custom bioresorbable tracheal splints [124]. In regenerating peripheral nerve, a number of *in vitro* and *in vivo* studies have been conducted to evaluate the performance of NGCs fabricated with LIFT technology (Table 2.2), and some of these showed results comparable to autografts [125,126]. However, translation of LIFT to large-scale tissue production is still out of reach [127].

Table 2.2 Nerve regeneration with scaffolds fabricated with RP scaffold technique for nerve regeneration

Biomaterial	Details	Fabrication method	*In vivo/ in vitro*	Study period	Results	Ref.
Agarose, BMSCs and SCs, self-assembled (Fig. 2.2A)	Multi-luminal channels, ~500 μm diameter cellular cylinders	Extrusion-based	10 mm sciatic nerve gap in rats	40 weeks	Motor function recovery similar to controls, presence of agarose within the channel prevented nerve growth	[128]
Agarose, BMSCs and SCs, self-assembled	Bioink made of SC (10%), and BMSC (90%), strand width was 500 μm, conduit diameter was 2 mm	Extrusion-based	10 mm sciatic nerve lesion in rats	3 weeks	Axons(40%) at the proximal stump reached the distal segment of the sciatic nerve through the scaffold	[129]
Fibrin	Dimension 14 ×5 ×2 mm³, Strand angle of each layer alternated between 85°, 90°, and 95°	Extrusion-based	Schwann cell were incorporated, DRG seeded and cultured *in vitro*	7 days	Schwann cells were aligned and DRG extended ~800 μm long neurites	[130]
Gelatin methacrylamide	Porous scaffolds with and without graphene were	Extrusion-based	Neural stem cells were	2 weeks	Graphene promoted neuronal differentiation, low concentrated	[131]

hydrogel with graphene nanoplatelets	mixed with neural stem cells to create a cell density of 2×10^6 cell/mL		encapsulated and cultured *in vitro*		GelMA showed good cell viability, stem cells extended their neurites	
Polyurethane (PU) PCL and PDLLA ratio was 4:1	Dimension $1.5 \times 1.5 \times .15$ cm^3, contained 4×10^6 NSCs/ml	Extrusion-based	*In vitro/in vivo*	8 days	Encapsulated NSCs showed excellent proliferation and differentiation, brain injured zebrafish was rescued	[132]
Collagen and gelatin gels	8 Collagen layers (10×10 mm^2), spatial resolution was 600 µm, and incorporated cell density was 3.0×10^6 cells/mL	Extrusion-based	Rat embryonic (day 18) neurons	7 days	Effective way for creating a unique cell patterned 3D structure in a high throughput manner	[133]
PEGylated hydrogels made of fibrinogen and collagen	Micro-patterned structure	Photo-lithography and photo-ablation	Chick dorsal root ganglion	4 day	Directed neurite outgrowth of DRG through the channels	[134]
PLA substrates Symmetric/asymmetric microporous	Micro-grooved structure	Photo-lithography	10 mm sciatic nerve defects in rats	6 weeks	Asymmetrically porous microgrooved conduit grew highest degree of myelinated axons and blood vessels, and promoted functional recovery.	[135]
PLGA	Microfibrous PLGA bundle enfolded in a micro/nanostructured PLGA membrane	Photo-lithography, and nano-electroforming	2×10^4 neuron progenitor cells/mL were injected	3 days	Cell migration rate was increased 1.6-fold than a flat PLGA membrane, and 90% of the cells aligned with the designed patterns.	[136]
Poly(ethylene glycol) diacrylate	1mm (diameter) x 5mm (length) x 250 µm (wall thickness) conduit	Laser-based microstereolithography	Schwann cell, neuronal, and DRG culture and 3 mm common fibular nerve gap in mice	72 h *in vitro* and 3 weeks *in vivo*	Directional neurite growth from DRGs, axon regeneration close to that of an autograft control	[126]
PEGylated fibrinogen	Photopatterned microchannel, depth ~15-100 µm	Laser-based photoablation	*In vitro* DRGs were cultured	23 days	DRGs grew unidirectional neurites in the microchannel	[137]

2.5 Nanoscale NGC fabrication techniques

Nanotechniques have opened a new window on ways to obtain large surface areas in a small volume. The application of nanofibres to mimic ECM structures that promote tissue regeneration allows cells to interact with a 3D microenvironment composed of nanostructured collagen, laminin, fibronectin, elastin, or other ECM components. Electrospinning (ES), melt spinning, phase separation, and self-assembly are the four established techniques that can be used to prepare nanofibres, though this review will focus on ES only. These methods, especially ES, can be modified to include living cells deposited by electrospraying (Table 2.3).

2.5.1 Electrospinning

Of the four nanofiber production methods, ES is the most feasible in terms of cost and efficiency, and can be used to prepare aligned fibres, random fibres, fibrous conduits, and core-shell constructs. ES relies on an electrical charge to produce and elongate polymers into microscopic fibres, and has been used to fabricate nanofibrous scaffolds for nerve tissue engineering [138]. When these fibres are collected on a grounded plate or mandrel, the fibres will form a random, non-woven matt.

A wide spectrum of materials can be electrospun, including synthetic, natural, composite or copolymers. For example, poly(L-lactic acid) (PLLA), polycaprolactone (PCL),poly(3-hydroxybutyrate) (PHB), poly(3-hydroxybutyrate-co-3-hydroxyvalerate) (PHBV), polyethersulfone (PES), polydioxanone (PDS), methyl methacrylate-acrylic acid, poly(propylene carbonate) (PPC), collagen, silk fibroin, chitosan, and gelatin have all been electrospun to fabricate nanofibres for nerve tissue engineering (Table 2.3). While synthetic materials are superior to natural material in terms of mechanical strength and preparation flexibility, synthetic materials typically have poor hydrophilic properties and lack cell binding sites, limiting their application. Some research has evaluated the effects of modifying the surface chemistry (hydrophobicity) and morphology (roughness) of the nanofibres to achieve better cell adhesion properties [139]. In contrast, natural materials are more attractive compared to synthetic ones in terms of their hydrophilic properties and cell binding capacity. However, nanofibres composed of natural material show rapid or uncontrolled degradation rate, and poor mechanical strength. These limitations of both natural and synthetic material have led researchers to explore fabrication of nanofibres with hybrid, composite, or copolymers materials for applications in nerve tissue regeneration, and the results of those studies looks quite promising [140].

In initial research, randomly-oriented nanofibres (synthetic or natural polymers) were prepared using ES technique to study nerve tissue growth *in vitro* and *in vivo* (Fig. 2.3C and 2.3E). A number of promising studies using randomly-oriented fibres convinced researcher to go further with nanofibres. Researchers put emphasis on the fabrication of aligned nanofibres for *in vivo* nerve regeneration (Fig. 2.3F), as alignment of structures in NGCs are associated with improved directional growth of neurites [141]. Several studies have been conducted to date on regenerating nerve with aligned nanofibres, and the results are quite impressive. In different *in vitro* or *in vivo* studies, various types of pure or modified biomaterial were electrospun to

fabricate aligned nanofibres for nerve regeneration. Biomaterials were modified with copolymerization, hybridization, and incorporation of bioactive molecules or growth factors. Neuron explants cultured on electrospun nanofibres of high, intermediate, and random alignment showed axons became longer (16-20%) on highly aligned fibre compared to random and intermediate fibres [142]. To enhance the axon growth rate, researchers have looked at ES fibres loaded with growth factors and ECM components (Fig. 2.3E). Neurite extension was shown to be greatest on aligned, treated fibres having immobilized additives, as compared to combinations of soluble immobilized additives and untreated fibres. Moreover, neurite extension was shown to be much less on the random fibres for different combinations compared to the aligned one [143]. While synthetic materials show outstanding mechanical strength, often such material is resistant to biological degradation, causing nerve compression and inflammation. Synthetic fibres can be modified to create tunable degradation rates through copolymerization with other biomaterials as well as coaxial electrospinning (Fig. 2.3C).

Synergistic effect of natural and synthetic nanofibre in NGCs has also been investigated. Composite materials used in electrospun fibres may have included proteins such as silk fibroin, collagen I, and collagen III added to the synthetic biomaterials. These composite electrospun polymers showed outstanding axon regeneration, so studies were conducted to determine the optimum ratio of various polymers. Studies found that using a high weight ratio of natural materials to synthetic materials in scaffolds resulted in more rapid degradation loss, which reduced the cell proliferation [144]. The results suggest that in composite biomaterials, there exist a critical limit of weight ratio between the synthetic and natural material. Studies have also looked at using conductive material for fabricating nanofibres. These studies showed improved cell growth and differentiation compared to nonconductive fibres. In addition, application of electrical potential to conductive scaffolds stimulated greater and longer neurite generation compared to unstimulated cells on the same nanofibers [145]. Both electrical stimulation and topographical guidance proved significant for nerve regeneration.

2.5.2 Direct polymer melt deposition

Small pore sizes and random spacing are some of the major problems with electrospinning, however, they can be addressed through hybrid fabrication processes. One such hybrid approach is to combine ES with direct polymer melt deposition (DPMD) in order to fabricate scaffolds

with controlled features, including improved pore size, appropriate cell adhesion, and structural similarity to the ECM [146]. DPMD is a form of extrusion-based fabrication that is capable of fabricating microfibres. One of the limitations of this technique is that, for instance, in case of using PCL, this biomaterial needs to be heated up to approximately 150°C in order to be used for DPMD. However, at this temperature, most proteins will be denatured. In spite of these drawbacks and limitations, research in nanoscale fibre spinning continues.

Table 2.3 Synthetic and natural nanofibres for nerve regeneration

Nano fibrous material	Fabrication method	Animal model	Defect size/location	Study Period	Results	Ref.
PLGA/PCL		Rats	10 mm sciatic nerve gap	4 months	Functional reconnection, myelination, collagen IV deposition, and insignificant inflammatory response was detected	[147]
PLGA-silk fibroin		Rats	10 mm sciatic nerve defects	6 weeks	Regenerative results (morphological and functional) similar to autografts	[148]
Aligned PLGA+NGF		Rats	13 mm sciatic nerve defect	12 weeks	Similar functional (electrophysiological and muscle weight) recovery was detected for autograft and PLGA/NGF implanted group	[149]
Aligned SF/P(LLA-CL) + NGF	Coaxial electrospinning	Rats	15 mm sciatic nerve defect	12 weeks	Regenerative results (functional and histological) was significantly better than the aligned SF/P(LLA-CL) NGCs	[150]
Chitosan-PHBV	Electrospinning	Rats	10 mm sciatic nerve gap	4 months	Myelinated axons were found to bridge the gap	[151]
SC loaded PHBV	Electrospinning	Rats	30 mm sciatic nerve gap	4 months	Nerve regeneration and functional recovery (behavioral and nociceptive function) was detected	[152]
Aligned PCLEEP + GDNF	Electrospinning	Rats	15 mm sciatic nerve gap	3 months	Better nerve regeneration and functional recovery was detected than controls	[153]
Aligned/random PAN-MA	Electrospinning	Rats	17mm tibial nerve gap	16 weeks	Regenerated axons reinnervated muscles, reformed neuromuscular junctions and promoted functional recovery	[154]
Bilayered chitosan + Peptide	Electrospinning	Rats	10 mm sciatic nerve gap	10 weeks	Regenerative result (functional and histological) was similar to isograft	[155]
PLGA	Electrospinning	Rats	10 mm sciatic nerve gap	1 month	Diameter and density of the regenerated nerve fibre was lower than controls	[156]
Blood vessel + SAPNS		Rats	10 mm sciatic nerve gap	16 weeks	Better regenerative result was detected than empty conduit, but inferior to normal control in terms of NCAP and GMW	[157]
Aligned Laminin+PCL	Electrospinning	Rats	10 mm tibial nerve gap	6 weeks	Aligned PCL fibres facilitated motor function recovery, while aligned laminin + PCL fibre promoted sensory function recovery	[158]
Aligned PCL	Electrospinning	Rats	15 mm sciatic nerve gap	3 months	Higher number of myelinated axons, CMAP, and lower distal motor latency was detected compared to microfibre implanted group	[159]

MWNT + Collagen/PCL	Electrospinning	Rats	8 mm sciatic nerve defect	4 months	Successful regeneration result (CMAP, GMW, and nerve density tests) with insignificant muscle atrophy and inflammation	[160]
Laminin + PLLA conduits, NGF+PLGA lumen	Electrospinning	Rats	10 mm sciatic nerve gap	3 months	Better regeneration result (muscle reinnervation and withdrawal reflex latency tests) than autograft; inferior regeneration results in term of axon density	[23]
PLGA+ aligned PA	Gas foaming + self assembly	Rats	12 mm sciatic nerve gap	12 weeks	Regenerative results (motor and sensory function recovery) are comparable to autograft group	[161]
Aligned collagen/PLGA	Electrospinning	Rats	13 mm sciatic nerve defect		Regenerative result (histological and functional) was inferior to autografts	[162]
P(LLA-CL)+NGF	Core shell	Rats	10 mm sciatic nerve gap	12 weeks	Regenerative result (functional and histological) was similar to autograft group	[163]
Grooved CAB fibres	Electrospinning	Rats	13 mm sciatic nerve defect	12 weeks	Effectively enhanced nerve regeneration as per histological and functional analyses	[35]
Aligned SF+P(LLA-CL)	Electrospinning	Rats	10 mm sciatic nerve gap	8 weeks	Regenerative result (functional and morphological) was superior to P(LLA-CL) group	[164]
SF/SWNT/FN	Electrospinning	Rats	10 mm sciatic nerve gap	5 weeks	Regeneration result (NCV, and myelinated axon number) was inferior to normal nerve, but SC population was similar to normal nerve	[165]

2.6 Future research directions and conclusions

In peripheral nerve regeneration, the key is to have Schwann cell-guided axonal growth cones so as to form the 'bands of Büngner.' Schwann cells attach, differentiate, proliferate, and align on substrates that have favorable topographic and physical cues. Over the past several decades, a number of strategies have been implemented to incorporate appropriate physical cues within the NGCs to bridge large peripheral nerve gaps. Often, conduits were used *in vivo* to guide growing axons, inhibit the infiltration of fibrous tissues, and prevent axonal off-target reinnervation. Nerve regeneration was investigated with porous, semi-porous and nonporous conduits. Of these three, semi-porous conduits were found more suitable as they facilitate mass transport, vascular network formation, Schwann cell migration and inhibit the fibroblast cell infiltration. Though promising, such conduits were found ineffective in regenerating nerve across a large nerve gap (>40 mm) [4].

To tackle the shortcomings, researchers have incorporated various hydrogels and matrices within the hollow conduits to further add physical and biological cues for the regenerating neurons. Although this strategy brought some success, axonal dispersion and off-

target reinnervation still remained unsolved. To address this issue, conduits having multiple lumens were investigated to reduce the axonal dispersion. Within these multilumen NCGs, various materials have also been incorporated in the conduit walls and as the filler material. While neurons were seen to advance their axons through microlumens, the swelling and degradation of the bioink is a major issue that needs to be overcome. Hydrogels with uncontrolled swelling properties were identified as inappropriate for incorporating in the lumen, as they cause nerve compression upon swelling *in vivo*. Degradation rates of the hydrogel both *in vitro* and *in vivo* are also factors to determine the suitability of the material, as rapid degradation is associated with loss of structure and failure of the scaffold, whereas degrading too slowly is associated with cell death and fibrosis. The hydrogels used as bioinks were also evaluated for their biological performance and potential for cytotoxicity.

In some cases, unidirectional freeze-dried ECM material (Fig. 2.2C) was found to promote neurite growth *in vivo*, however, non-uniform pore size and poor mechanical stability limits their application [166]. Since functional nerve regeneration requires aligned architecture, strong magnetic fields have been used to align fibrils of ECM material (e.g. collagen, fibrin) to fabricate the NGC. However, poor mechanical strength of the aligned strands is a major drawback of these approaches. With the development of nanoscale fabrication technology, micro- and nanofibres were fabricated and inserted within NGCs to mimic the surface topography of ECM seen in an autograft. Filaments fabricated with rapid prototyping (e.g. extrusion, laser, etc.) technique showed great promises in axon regeneration.

In particular, extrusion-based systems have made it possible to dispense a large cell population in a controlled and precise way. Therefore, with extrusion-based techniques, a large density of Schwann cell can be provided within the printed strands. The success of extrusion-based approaches depends on the mechanical stability, biological performance, and cytotoxicity of the bioink/hydrogel precursor. Importantly, the type of crosslinking agent can provoke the cytotoxicity of the hydrogel material in *in vivo* culture. Extrusion-based methods have been further improved through the advent of coaxial dispensing systems to create micro-lumens within extruded strands.

With the progress of optics, laser-guided approaches have been investigated for scaffold fabrication and precise cell positioning. While some attractive features, such as nozzle-less, high printing speed, and resolution have made this approach superior to other approaches,

41

shortcomings limits the application of laser-fabrication. For example laser energy, resin chemistry, and photo-initiators can induce cell damage. Moreover, preparing the material for laser-guided approaches is time consuming and difficult.

Microfilaments do not contain nanoscale physical cues that cells typically respond to. This can include the binding sites on collagen, laminin, fibrin, and fibronectin do, and therefore requires the hydrogel precursor to be modified by adding peptides. Coaxial nozzles are used to incorporate NGF within the nanofibre to achieve synergistic effect of physical and biochemical cues. To eliminate the complexity of biochemical cue incorporation and increasing the filaments packing density, nanofibres were evaluated and showed favourable results in guiding axons between the proximal and distal ends of damaged peripheral nerves. In addition, efforts were made to enhance the physical and topographical cues on nanofibres by incorporating grooves. The grooved nanofibres were found more effective in promoting axonal outgrowth compared to smooth nanofibres. Rolled up nanopatterns (e.g. nanocolumn, grates, beads, roughness, graded density, tubes, etc.) were found effective in reducing axonal dispersion and enhancing neurite length. Although the use of nanofibres in a NGC seems to solve various drawbacks experienced in other approaches, there are still problems. Overlapping, misguidance, and dispersion of the growing axons were identified in nanofibre-loaded NGCs. Furthermore, the biodegradability of synthetic nanofibres *in vivo* is a major concern that requires more improvements.

To address these problems, methods of developing scaffolds to form bands of Büngner have been recently explored. Cell aggregates have been used to fabricate biopolymer-free scaffolds. In this regard, cell pellets, tissue spheroids, and tissue filaments of Schwann cells that can be bioplotted as a strand are methods that are being evaluated. However, this approach requires a huge number of cells for *in vivo* applications. Therefore, stem cells are being explored to eliminate the slow proliferation rate of primary cells. Stem cell-enriched bioinks could be used to form self-assembled microfilaments similar to that of natural autografts. However, the time delay of self-assembly and risk associated with stem cells incorporation requires more investigations.

Truly, nerve regeneration *in vivo* is a complicated process whereby axons grow by the combined effect of topographic, electric, chemotactic and haptotactic cues that guide the directional growth of the axons [167]. More investigations are needed to study the degradation, cytotoxicity, immunogenicity, and long term effect of such NGCs *in vivo*.

2.7 References

[1]   Tomassoni D, Amenta F, Di Cesare Mannelli L, et al. Neuroprotective activity of thioctic acid in central nervous system lesions consequent to peripheral nerve injury. Biomed Res. Int. 2013;2013.

[2]   Ray WZ, Mackinnon SE. Management of nerve gaps: autografts, allografts, nerve transfers, and end-to-side neurorrhaphy. Exp. Neurol. 2010;223:77.

[3]   Marquardt LM, Sakiyama-Elbert SE. Engineering peripheral nerve repair. Curr. Opin. Biotechnol. 2013;24:887–892.

[4]   de Ruiter GCW, Malessy MJA, Yaszemski MJ, et al. Designing ideal conduits for peripheral nerve repair. Neurosurg. Focus. 2009;26:E5.

[5]   Biazar E, Heidari Keshel S. A nanofibrous PHBV tube with Schwann cell as artificial nerve graft contributing to Rat sciatic nerve regeneration across a 30-mm defect bridge. Cell Commun. Adhes. 2013;20:41–49.

[6]   Rajaram A, Chen X-B, Schreyer DJ. Strategic design and recent fabrication techniques for bioengineered tissue scaffolds to improve peripheral nerve regeneration. Tissue Eng. Part B Rev. 2012;18:454–467.

[7]   Radhakrishnan J, Kuppuswamy AA, Sethuraman S, et al. Topographic cue from electrospun scaffolds regulate myelin-related gene expressions in Schwann cells. J. Biomed. Nanotechnol. 2015;11:512–521.

[8]   Stoll G, Müller HW. Nerve injury, axonal degeneration and neural regeneration: basic insights. Brain Pathol. 1999;9:313–325.

[9]   Belkas JS, Shoichet MS, Midha R. Peripheral nerve regeneration through guidance tubes. Neurol. Res. 2004;26:151–160.

[10]   Sarker M, Chen XB, Schreyer DJ. Experimental approaches to vascularisation within tissue engineering constructs. J. Biomater. Sci. Polym. Ed. 2015;26:683–734.

[11]   Sarker M, Chen XB. Modeling the Flow Behavior and Flow Rate of Medium Viscosity Alginate for Scaffold Fabrication With a Three-Dimensional Bioplotter. J. Manuf. Sci. Eng. 2017;139:081002.

[12]   Freier T, Koh HS, Kazazian K, et al. Controlling cell adhesion and degradation of chitosan films by N-acetylation. Biomaterials. 2005;26:5872–5878.

[13]   Wang HB, Mullins ME, Cregg JM, et al. Creation of highly aligned electrospun poly-L-lactic acid fibers for nerve regeneration applications. J. Neural Eng. 2008;6:16001.

[14]   Chiono V, Ciardelli G, Vozzi G, et al. Enzymatically-modified melt-extruded guides for peripheral nerve repair. Eng. Life Sci. 2008;8:226–237.

[15]   Lundborg G. A 25-year perspective of peripheral nerve surgery: evolving neuroscientific concepts and clinical significance. J. Hand Surg. Am. 2000;25:391–414.

[16]   Ribeiro-Resende VT, Koenig B, Nichterwitz S, et al. Strategies for inducing the formation

of bands of Büngner in peripheral nerve regeneration. Biomaterials. 2009;30:5251–5259.

[17]   Brushart TM, Mathur V, Sood R, et al. Dispersion of regenerating axons across enclosed neural gaps. J. Hand Surg. Am. 1995;20:557–564.

[18]   Boyd JG, Gordon T. A dose-dependent facilitation and inhibition of peripheral nerve regeneration by brain-derived neurotrophic factor. Eur. J. Neurosci. 2002;15:613–626.

[19]   Hoppen HJ, Leenslag JW, Pennings AJ, et al. Two-ply biodegradable nerve guide: basic aspects of design, construction and biological performance. Biomaterials. 1990;11:286–290.

[20]   Kim DH, Connolly SE, Zhao S, et al. Comparison of macropore, semipermeable, and nonpermeable collagen conduits in nerve repair. J. Reconstr. Microsurg. 1993;9:415–420.

[21]   Groves ML, McKeon R, Werner E, et al. Axon regeneration in peripheral nerves is enhanced by proteoglycan degradation. Exp. Neurol. 2005;195:278–292.

[22]   Chang C-J, Hsu S. The effect of high outflow permeability in asymmetric poly (dl-lactic acid-co-glycolic acid) conduits for peripheral nerve regeneration. Biomaterials. 2006;27:1035–1042.

[23]   Koh HS, Yong T, Teo WE, et al. In vivo study of novel nanofibrous intra-luminal guidance channels to promote nerve regeneration. J. Neural Eng. 2010;7:46003.

[24]   Hoffman-Kim D, Mitchel JA, Bellamkonda R V. Topography, cell response, and nerve regeneration. Annu. Rev. Biomed. Eng. 2010;12:203–231.

[25]   Lee J-Y, Giusti G, Friedrich PF, et al. The effect of collagen nerve conduits filled with collagen-glycosaminoglycan matrix on peripheral motor nerve regeneration in a rat model. J Bone Jt. Surg Am. 2012;94:2084–2091.

[26]   Labrador RO, Butí M, Navarro X. Influence of collagen and laminin gels concentration on nerve regeneration after resection and tube repair. Exp. Neurol. 1998;149:243–252.

[27]   Bailey SB, Eichler ME, Villadiego A, et al. The influence of fibronectin and laminin during Schwann cell migration and peripheral nerve regeneration through silicon chambers. J. Neurocytol. 1993;22:176–184.

[28]   Midha R, Munro CA, Dalton PD, et al. Growth factor enhancement of peripheral nerve regeneration through a novel synthetic hydrogel tube. J. Neurosurg. 2003;99:555–565.

[29]   Sufan W, Suzuki Y, Tanihara M, et al. Sciatic nerve regeneration through alginate with tubulation or nontubulation repair in cat. J. Neurotrauma. 2001;18:329–338.

[30]   Yao L, de Ruiter GCW, Wang H, et al. Controlling dispersion of axonal regeneration using a multichannel collagen nerve conduit. Biomaterials. 2010;31:5789–5797.

[31]   Hu X, Huang J, Ye Z, et al. A novel scaffold with longitudinally oriented microchannels promotes peripheral nerve regeneration. Tissue Eng. Part A. 2009;15:3297–3308.

[32]   Li J, Shi R. Fabrication of patterned multi-walled poly-l-lactic acid conduits for nerve regeneration. J. Neurosci. Methods. 2007;165:257–264.

[33] Froeter P, Huang Y, Cangellaris O V, et al. Toward intelligent synthetic neural circuits: directing and accelerating neuron cell growth by self-rolled-up silicon nitride microtube array. ACS Nano. 2014;8:11108–11117.

[34] Béduer A, Vieu C, Arnauduc F, et al. Engineering of adult human neural stem cells differentiation through surface micropatterning. Biomaterials. 2012;33:504–514.

[35] Huang C, Ouyang Y, Niu H, et al. Nerve guidance conduits from aligned nanofibers: improvement of nerve regeneration through longitudinal nanogrooves on a fiber surface. ACS Appl. Mater. Interfaces. 2015;7:7189–7196.

[36] Park SJ, Lee B-K, Na MH, et al. Melt-spun shaped fibers with enhanced surface effects: fiber fabrication, characterization and application to woven scaffolds. Acta Biomater. 2013;9:7719–7726.

[37] Park J, Kim D-H, Kim H-N, et al. Directed migration of cancer cells guided by the graded texture of the underlying matrix. Nat. Mater. 2016;

[38] Park M, Oh E, Seo J, et al. Control over neurite directionality and neurite elongation on anisotropic micropillar arrays. Small. 2016;12:1148–1152.

[39] Brunetti V, Maiorano G, Rizzello L, et al. Neurons sense nanoscale roughness with nanometer sensitivity. Proc. Natl. Acad. Sci. 2010;107:6264–6269.

[40] Kang K, Choi S, Jang HS, et al. In Vitro Developmental Acceleration of Hippocampal Neurons on Nanostructures of Self-Assembled Silica Beads in Filopodium-Size Ranges. Angew. Chemie Int. Ed. 2012;51:2855–2858.

[41] Yeh C-W, Wang L-W, Wu H-C, et al. Development of biomimetic micro-patterned device incorporated with neurotrophic gradient and supportive Schwann cells for the applications in neural tissue engineering. Biofabrication. 2017;9:15024.

[42] Zeng W, Rong M, Hu X, et al. Incorporation of chitosan microspheres into collagen-chitosan scaffolds for the controlled release of nerve growth factor. PLoS One. 2014;9:e101300.

[43] Evans EB, Brady SW, Tripathi A, et al. Schwann cell durotaxis can be guided by physiologically relevant stiffness gradients. Biomater. Res. 2018;22:14.

[44] Chen S, Jones JA, Xu Y, et al. Characterization of topographical effects on macrophage behavior in a foreign body response model. Biomaterials. 2010;31:3479–3491.

[45] Yoshii S, Oka M, Shima M, et al. Bridging a 30-mm nerve defect using collagen filaments. J. Biomed. Mater. Res. Part A. 2003;67:467–474.

[46] Ngo TB, Waggoner PJ, Romero AA, et al. Poly (L-Lactide) microfilaments enhance peripheral nerve regeneration across extended nerve lesions. J. Neurosci. Res. 2003;72:227–238.

[47] Wang X, Hu W, Cao Y, et al. Dog sciatic nerve regeneration across a 30-mm defect bridged by a chitosan/PGA artificial nerve graft. Brain. 2005;128:1897–1910.

[48] Müller MF, Ris H, Ferry JD. Electron microscopy of fine fibrin clots and fine and coarse

fibrin films: observations of fibers in cross-section and in deformed states. J. Mol. Biol. 1984;174:369–384.

[49] Williams LR, Varon S. Modification of fibrin matrix formation in situ enhances nerve regeneration in silicone chambers. J. Comp. Neurol. 1985;231:209–220.

[50] Dubey N, Letourneau PC, Tranquillo RT. Guided neurite elongation and Schwann cell invasion into magnetically aligned collagen in simulated peripheral nerve regeneration. Exp. Neurol. 1999;158:338–350.

[51] Ceballos D, Navarro X, Dubey N, et al. Magnetically aligned collagen gel filling a collagen nerve guide improves peripheral nerve regeneration. Exp. Neurol. 1999;158:290–300.

[52] Elsdale T, Bard J. Collagen substrata for studies on cell behavior. J. Cell Biol. 1972;54:626–637.

[53] Benjamin HB, Pawlowski E, Becker AB. Collagen as temporary dressing and blood vessel replacement. Arch. Surg. 1964;88:725–727.

[54] Verdú E, Labrador RO, Rodríguez FJ, et al. Alignment of collagen and laminin-containing gels improve nerve regeneration within silicone tubes. Restor. Neurol. Neurosci. 2002;20:169–180.

[55] Phillips JB, Bunting SCJ, Hall SM, et al. Neural tissue engineering: a self-organizing collagen guidance conduit. Tissue Eng. 2005;11:1611–1617.

[56] Whitworth IH, Brown RA, Dore C, et al. Orientated mats of fibronectin as a conduit material for use in peripheral nerve repair. J. Hand Surg. Br. Eur. Vol. 1995;20:429–436.

[57] Wen X, Tresco PA. Fabrication and characterization of permeable degradable poly (DL-lactide-co-glycolide)(PLGA) hollow fiber phase inversion membranes for use as nerve tract guidance channels. Biomaterials. 2006;27:3800–3809.

[58] Mackinnon SE, Dellon AL. A study of nerve regeneration across synthetic (Maxon) and biologic (collagen) nerve conduits for nerve gaps up to 5 cm in the primate. J. Reconstr. Microsurg. 1990;6:117–121.

[59] Oh SH, Kim JH, Song KS, et al. Peripheral nerve regeneration within an asymmetrically porous PLGA/Pluronic F127 nerve guide conduit. Biomaterials. 2008;29:1601–1609.

[60] Kiyotani T, Teramachi M, Takimoto Y, et al. Nerve regeneration across a 25-mm gap bridged by a polyglycolic acid-collagen tube: a histological and electrophysiological evaluation of regenerated nerves. Brain Res. 1996;740:66–74.

[61] Apel PJ, Garrett JP, Sierpinski P, et al. Peripheral nerve regeneration using a keratin-based scaffold: long-term functional and histological outcomes in a mouse model. J. Hand Surg. Am. 2008;33:1541–1547.

[62] Nakamura T, Inada Y, Fukuda S, et al. Experimental study on the regeneration of peripheral nerve gaps through a polyglycolic acid–collagen (PGA–collagen) tube. Brain Res. 2004;1027:18–29.

[63]   Toba T, Nakamura T, Lynn AK, et al. Evaluation of peripheral nerve regeneration across an 80-mm gap using a polyglycolic acid (PGA)--collagen nerve conduit filled with laminin-soaked collagen sponge in dogs. Int. J. Artif. Organs. 2002;25:230–237.

[64]   Evans GRD, Brandt K, Widmer MS, et al. In vivo evaluation of poly (L-lactic acid) porous conduits for peripheral nerve regeneration. Biomaterials. 1999;20:1109–1115.

[65]   Dai L-G, Huang G-S, Hsu S. Sciatic nerve regeneration by cocultured Schwann cells and stem cells on microporous nerve conduits. Cell Transplant. 2013;22:2029–2039.

[66]   Fu K, Dai L, Chiu I, et al. Sciatic Nerve Regeneration by Microporous Nerve Conduits Seeded With Glial Cell Line-Derived Neurotrophic Factor or Brain-Derived Neurotrophic Factor Gene Transfected Neural Stem Cells. Artif. Organs. 2011;35:363–372.

[67]   Knoops B, Hurtado H, De Aguilar PVDB. Rat sciatic nerve regeneration within an acrylic semipermeable tube and comparison with a silicone impermeable material. J. Neuropathol. Exp. Neurol. 1990;49:438–448.

[68]   Evans GRD, Brandt K, Katz S, et al. Bioactive poly (L-lactic acid) conduits seeded with Schwann cells for peripheral nerve regeneration. Biomaterials. 2002;23:841–848.

[69]   Hsu S, Chan S-H, Chiang C-M, et al. Peripheral nerve regeneration using a microporous polylactic acid asymmetric conduit in a rabbit long-gap sciatic nerve transection model. Biomaterials. 2011;32:3764–3775.

[70]   Chen Y-S, Hsieh C-L, Tsai C-C, et al. Peripheral nerve regeneration using silicone rubber chambers filled with collagen, laminin and fibronectin. Biomaterials. 2000;21:1541–1547.

[71]   Matsumoto K, Ohnishi K, Kiyotani T, et al. Peripheral nerve regeneration across an 80-mm gap bridged by a polyglycolic acid (PGA)–collagen tube filled with laminin-coated collagen fibers: a histological and electrophysiological evaluation of regenerated nerves. Brain Res. 2000;868:315–328.

[72]   Suzuki Y, Tanihara M, Ohnishi K, et al. Cat peripheral nerve regeneration across 50 mm gap repaired with a novel nerve guide composed of freeze-dried alginate gel. Neurosci. Lett. 1999;259:75–78.

[73]   Hu Y, Wu Y, Gou Z, et al. 3D-engineering of cellularized conduits for peripheral nerve regeneration. Sci. Rep. 2016;6.

[74]   Evangelista MS, Perez M, Salibian AA, et al. Single-lumen and multi-lumen poly (ethylene glycol) nerve conduits fabricated by stereolithography for peripheral nerve regeneration in vivo. J. Reconstr. Microsurg. 2015;31:327–335.

[75]   Bhutto MA, Zhang J, Sun B, et al. Development of poly (L-lactide-co-caprolactone) multichannel nerve conduit with aligned electrospun nanofibers for Schwann cell proliferation. Int. J. Polym. Mater. Polym. Biomater. 2016;65:323–329.

[76]   Rutkowski GE, Miller CA, Jeftinija S, et al. Synergistic effects of micropatterned biodegradable conduits and Schwann cells on sciatic nerve regeneration. J. Neural Eng. 2004;1:151.

[77] Mobasseri SA, Terenghi G, Downes S. Micro-structural geometry of thin films intended for the inner lumen of nerve conduits affects nerve repair. J. Mater. Sci. Mater. Med. 2013;24:1639–1647.

[78] Itoh S, Takakuda K, Samejima H, et al. Synthetic collagen fibers coated with a synthetic peptide containing the YIGSR sequence of laminin to promote peripheral nerve regeneration in vivo. J. Mater. Sci. Mater. Med. 1999;10:129–134.

[79] Yoshii S, Oka M, Akagi M, et al. Bridging a peripheral nerve defect using collagen filaments. J. Hand Surg. Am. 2001;26:52–59.

[80] Antman-Passig M, Shefi O. Remote magnetic orientation of 3D collagen hydrogels for directed neuronal regeneration. Nano Lett. 2016;16:2567–2573.

[81] Geng L, Feng W, Hutmacher DW, et al. Direct writing of chitosan scaffolds using a robotic system. 5th Eur. Conf. Int. Fed. Med. Biol. Eng. Springer Berlin Heidelberg; 2012.

[82] Pati F, Jang J, Ha D-H, et al. Printing three-dimensional tissue analogues with decellularized extracellular matrix bioink. Nat. Commun. 2014;5.

[83] Naghieh S, Badrossamay M, Foroozmehr E, et al. Combination of PLA Micro-fibers and PCL-Gelatin Nano-fibers for Development of Bone Tissue Engineering Scaffolds. Int. J. Swarm Intell. Evol. Comput. 2017;06.

[84] Naghieh S, Karamooz Ravari MR, Badrossamay M, et al. Numerical investigation of the mechanical properties of the additive manufactured bone scaffolds fabricated by FDM: The effect of layer penetration and post-heating. J. Mech. Behav. Biomed. Mater. 2016;59:241–250.

[85] Naghieh S, Foroozmehr E, Badrossamay M, et al. Combinational processing of 3D printing and electrospinning of hierarchical poly (lactic acid)/gelatin-forsterite scaffolds as a biocomposite: Mechanical and biological assessment. Mater. Des. 2017;

[86] Naghieh S, Ravari MRK, Badrossamay M, et al. Finite element analysis for predicting the mechanical properties of bone scaffolds fabricated by fused deposition modeling (FDM). Modares Mech. Eng. Proc. Adv. Mach. Mach. Tools Conf. 2015. p. 450–454.

[87] Chen XB, Schoenau G, Zhang WJ. On the Flow Rate Dynamics in Time-Pressure Dispensing Processes. J. Dyn. Syst. Meas. Control. 2002;124:693.

[88] Naghieh S, Reihany A, Haghighat A, et al. Fused Deposition Modeling and Fabrication of a Three-dimensional Model in Maxillofacial Reconstruction. Regen. Reconstr. Restor. 2016;1:139–144.

[89] Li M, Tian X, Zhu N, et al. Modeling process-induced cell damage in the biodispensing process. Tissue Eng. Part C Methods. 2009;16:533–542.

[90] Chen XB, Li MG, Ke H. Modeling of the Flow Rate in the Dispensing-Based Process for Fabricating Tissue Scaffolds. J. Manuf. Sci. Eng. 2008;130:021003.

[91] Wang X, Rijff BL, Khang G. A building-block approach to 3D printing a multichannel, organ-regenerative scaffold. J. Tissue Eng. Regen. Med. 2015;

[92]   Naghieh S, Sarker M, Izadifar M, et al. Dispensing-based bioprinting of mechanically-functional hybrid scaffolds with vessel-like channels for tissue engineering applications – A brief review. J. Mech. Behav. Biomed. Mater. 2018;78:298–314.

[93]   Jones N. Science in three dimensions: the print revolution. 2012.

[94]   Ladet S, David L, Domard A. Multi-membrane hydrogels. Nature. 2008;452:76.

[95]   Park JY, Choi J-C, Shim J-H, et al. A comparative study on collagen type I and hyaluronic acid dependent cell behavior for osteochondral tissue bioprinting. Biofabrication. 2014;6:35004.

[96]   Augst AD, Kong HJ, Mooney DJ. Alginate Hydrogels as Biomaterials. Macromol. Biosci. 2006;6:623–633.

[97]   Soman P, Kelber JA, Lee JW, et al. Cancer cell migration within 3D layer-by-layer microfabricated photocrosslinked PEG scaffolds with tunable stiffness. Biomaterials. 2012;33:7064–7070.

[98]   Guvendiren M, Lu HD, Burdick JA. Shear-thinning hydrogels for biomedical applications. Soft Matter. 2012;8:260–272.

[99]   Nair K, Gandhi M, Khalil S, et al. Characterization of cell viability during bioprinting processes. Biotechnol. J. 2009;4:1168–1177.

[100] Murphy S V, Atala A. 3D bioprinting of tissues and organs. Nat. Biotechnol. 2014;32:773–785.

[101] Zhang Z, Wang B, Hui D, et al. 3D bioprinting of soft materials-based regenerative vascular structures and tissues. Compos. Part B Eng. 2017;

[102] Bahk J-H, Fang H, Yazawa K, et al. Flexible thermoelectric materials and device optimization for wearable energy harvesting. J. Mater. Chem. C. 2015;3:10362–10374.

[103] Best C, Onwuka E, Pepper V, et al. Cardiovascular tissue engineering: preclinical validation to bedside application. Physiology. 2016;31:7–15.

[104] Arai K, Iwanaga S, Toda H, et al. Three-dimensional inkjet biofabrication based on designed images. Biofabrication. 2011;3:034113.

[105] Wu Z, Su X, Xu Y, et al. Bioprinting three-dimensional cell-laden tissue constructs with controllable degradation. Sci. Rep. 2016;6:24474.

[106] Gao G, Lee JH, Jang J, et al. Tissue Engineered Bio-Blood-Vessels Constructed Using a Tissue-Specific Bioink and 3D Coaxial Cell Printing Technique: A Novel Therapy for Ischemic Disease. Adv. Funct. Mater. 2017;27.

[107] Akhtar MF, Hanif M, Ranjha NM. Methods of synthesis of hydrogels… a review. Saudi Pharm. J. 2016;24:554–559.

[108] Wüst S, Müller R, Hofmann S. Controlled Positioning of Cells in Biomaterials—Approaches Towards 3D Tissue Printing. J. Funct. Biomater. 2011;2:119–154.

[109] Cao N, Chen XB, Schreyer DJ. Influence of Calcium Ions on Cell Survival and

Proliferation in the Context of an Alginate Hydrogel. ISRN Chem. Eng. 2012;2012:1–9.

[110] Li MG, Tian XY, Chen XB. Modeling of flow rate, pore size, and porosity for the dispensing-based tissue scaffolds fabrication. J. Manuf. Sci. Eng. 2009;131:34501.

[111] Oyen ML. Mechanical characterisation of hydrogel materials. Int. Mater. Rev. 2014;59:44–59.

[112] Marga F, Jakab K, Khatiwala C, et al. Organ printing: a novel tissue engineering paradigm. 5th Eur. Conf. Int. Fed. Med. Biol. Eng. Springer; 2012. p. 27–30.

[113] Ozbolat IT, Chen H, Yu Y. Development of 'Multi-arm Bioprinter'for hybrid biofabrication of tissue engineering constructs. Robot. Comput. Integr. Manuf. 2014;30:295–304.

[114] Zhang Y, Yu Y, Ozbolat IT. Direct bioprinting of vessel-like tubular microfluidic channels. J. Nanotechnol. Eng. Med. 2013;4:20902.

[115] Colina M, Serra P, Fernández-Pradas JM, et al. DNA deposition through laser induced forward transfer. Biosens. Bioelectron. 2005;20:1638–1642.

[116] Barron JA, Ringeisen BR, Kim H, et al. Application of laser printing to mammalian cells. Thin Solid Films. 2004;453:383–387.

[117] Bohandy J, Kim BF, Adrian FJ. Metal deposition from a supported metal film using an excimer laser. J. Appl. Phys. 1986;60:1538–1539.

[118] Hribar KC, Soman P, Warner J, et al. Light-assisted direct-write of 3D functional biomaterials. Lab Chip. 2014;14:268–275.

[119] Koch L, Kuhn S, Sorg H, et al. Laser printing of skin cells and human stem cells. Tissue Eng. Part C Methods. 2009;16:847–854.

[120] Gruene M, Deiwick A, Koch L, et al. Laser printing of stem cells for biofabrication of scaffold-free autologous grafts. Tissue Eng. Part C Methods. 2010;17:79–87.

[121] Guillemot F, Souquet A, Catros S, et al. Laser-assisted cell printing: principle, physical parameters versus cell fate and perspectives in tissue engineering. Nanomedicine. 2010;5:507–515.

[122] Duocastella M, Fernández-Pradas JM, Morenza JL, et al. Novel laser printing technique for miniaturized biosensors preparation. Sensors Actuators B Chem. 2010;145:596–600.

[123] Kattamis NT, Purnick PE, Weiss R, et al. Thick film laser induced forward transfer for deposition of thermally and mechanically sensitive materials. Appl. Phys. Lett. 2007;91:171120.

[124] Zopf DA, Hollister SJ, Nelson ME, et al. Bioresorbable airway splint created with a three-dimensional printer. N. Engl. J. Med. 2013;368:2043–2045.

[125] Koroleva A, Gill AA, Ortega I, et al. Two-photon polymerization-generated and micromolding-replicated 3D scaffolds for peripheral neural tissue engineering applications. Biofabrication. 2012;4:25005.

[126] Pateman CJ, Harding AJ, Glen A, et al. Nerve guides manufactured from photocurable polymers to aid peripheral nerve repair. Biomaterials. 2015;49:77–89.

[127] Michael S, Sorg H, Peck C-T, et al. Tissue engineered skin substitutes created by laser-assisted bioprinting form skin-like structures in the dorsal skin fold chamber in mice. PLoS One. 2013;8:e57741.

[128] Owens CM, Marga F, Forgacs G, et al. Biofabrication and testing of a fully cellular nerve graft. Biofabrication. 2013;5:45007.

[129] Marga F, Jakab K, Khatiwala C, et al. Toward engineering functional organ modules by additive manufacturing. Biofabrication. 2012;4:22001.

[130] England S, Rajaram A, Schreyer DJ, et al. Bioprinted fibrin-factor XIII-hyaluronate hydrogel scaffolds with encapsulated Schwann cells and their in vitro characterization for use in nerve regeneration. Bioprinting. 2017;5:1–9.

[131] Zhu W, Harris BT, Zhang LG. Gelatin methacrylamide hydrogel with graphene nanoplatelets for neural cell-laden 3D bioprinting. Eng. Med. Biol. Soc. (EMBC), 2016 IEEE 38th Annu. Int. Conf. IEEE; 2016. p. 4185–4188.

[132] Hsieh F-Y, Lin H-H, Hsu S. 3D bioprinting of neural stem cell-laden thermoresponsive biodegradable polyurethane hydrogel and potential in central nervous system repair. Biomaterials. 2015;71:48–57.

[133] Lee W, Lee VK, Polio S, et al. Three-dimensional cell-hydrogel printer using electromechanical microvalve for tissue engineering. Solid-State Sensors, Actuators Microsystems Conf. 2009. TRANSDUCERS 2009. Int. IEEE; 2009. p. 2230–2233.

[134] Livnat N, Sarig-Nadir O, Zajdman R, et al. A hydrogel-based nerve regeneration conduit with sub-micrometer feature control. Neural Eng. 2007. CNE'07. 3rd Int. IEEE/EMBS Conf. IEEE; 2007. p. 101–103.

[135] Hsu S, Ni H-C. Fabrication of the microgrooved/microporous polylactide substrates as peripheral nerve conduits and in vivo evaluation. Tissue Eng. Part A. 2008;15:1381–1390.

[136] Peng S-W, Li C-W, Chiu M, et al. Nerve guidance conduit with a hybrid structure of a PLGA microfibrous bundle wrapped in a micro/nanostructured membrane. Int. J. Nanomedicine. 2017;12:421.

[137] Sarig-Nadir O, Livnat N, Zajdman R, et al. Laser photoablation of guidance microchannels into hydrogels directs cell growth in three dimensions. Biophys. J. 2009;96:4743–4752.

[138] Hu J, Kai D, Ye H, et al. Electrospinning of poly (glycerol sebacate)-based nanofibers for nerve tissue engineering. Mater. Sci. Eng. C. 2017;70:1089–1094.

[139] Yang F, Xu CY, Kotaki M, et al. Characterization of neural stem cells on electrospun poly (L-lactic acid) nanofibrous scaffold. J. Biomater. Sci. Polym. Ed. 2004;15:1483–1497.

[140] Ghasemi-Mobarakeh L, Prabhakaran MP, Morshed M, et al. Electrospun poly (ε-caprolactone)/gelatin nanofibrous scaffolds for nerve tissue engineering. Biomaterials.

2008;29:4532–4539.

[141] Corey JM, Gertz CC, Wang B-S, et al. The design of electrospun PLLA nanofiber scaffolds compatible with serum-free growth of primary motor and sensory neurons. Acta Biomater. 2008;4:863–875.

[142] Corey JM, Lin DY, Mycek KB, et al. Aligned electrospun nanofibers specify the direction of dorsal root ganglia neurite growth. J. Biomed. Mater. Res. Part A. 2007;83:636–645.

[143] Patel S, Kurpinski K, Quigley R, et al. Bioactive nanofibers: synergistic effects of nanotopography and chemical signaling on cell guidance. Nano Lett. 2007;7:2122–2128.

[144] Wang G, Hu X, Lin W, et al. Electrospun PLGA–silk fibroin–collagen nanofibrous scaffolds for nerve tissue engineering. Vitr. Cell. Dev. Biol. 2011;47:234–240.

[145] Lee JY, Bashur CA, Goldstein AS, et al. Polypyrrole-coated electrospun PLGA nanofibers for neural tissue applications. Biomaterials. 2009;30:4325–4335.

[146] Park SH, Kim TG, Kim HC, et al. Development of dual scale scaffolds via direct polymer melt deposition and electrospinning for applications in tissue regeneration. Acta Biomater. 2008;4:1198–1207.

[147] Panseri S, Cunha C, Lowery J, et al. Electrospun micro-and nanofiber tubes for functional nervous regeneration in sciatic nerve transections. Bmc Biotechnol. 2008;8:39.

[148] Li S, Wu H, Hu X-D, et al. Preparation of electrospun PLGA-silk fibroin nanofibers-based nerve conduits and evaluation in vivo. Artif. Cells, Blood Substitutes, Biotechnol. 2012;40:171–178.

[149] Wang C-Y, Liu J-J, Fan C-Y, et al. The effect of aligned core–shell nanofibres delivering NGF on the promotion of sciatic nerve regeneration. J. Biomater. Sci. Polym. Ed. 2012;23:167–184.

[150] Kuihua Z, Chunyang W, Cunyi F, et al. Aligned SF/P (LLA-CL)-blended nanofibers encapsulating nerve growth factor for peripheral nerve regeneration. J. Biomed. Mater. Res. Part A. 2014;102:2680–2691.

[151] Biazar E, Keshel SH. Chitosan–cross-linked nanofibrous PHBV nerve guide for rat sciatic nerve regeneration across a defect bridge. ASAIO J. 2013;59:651–659.

[152] Biazar E, Heidari Keshel S, Pouya M. Behavioral evaluation of regenerated rat sciatic nerve by a nanofibrous PHBV conduit filled with Schwann cells as artificial nerve graft. Cell Commun. Adhes. 2013;20:93–103.

[153] Chew SY, Mi R, Hoke A, et al. Aligned Protein–Polymer Composite Fibers Enhance Nerve Regeneration: A Potential Tissue-Engineering Platform. Adv. Funct. Mater. 2007;17:1288–1296.

[154] Kim Y, Haftel VK, Kumar S, et al. The role of aligned polymer fiber-based constructs in the bridging of long peripheral nerve gaps. Biomaterials. 2008;29:3117–3127.

[155] Wang W, Itoh S, Matsuda A, et al. Enhanced nerve regeneration through a bilayered chitosan tube: the effect of introduction of glycine spacer into the CYIGSR sequence. J.

Biomed. Mater. Res. Part A. 2008;85:919–928.

[156] Bini TB, Gao S, Xu X, et al. Peripheral nerve regeneration by microbraided poly (L-lactide-co-glycolide) biodegradable polymer fibers. J. Biomed. Mater. Res. Part A. 2004;68:286–295.

[157] Zhan X, Gao M, Jiang Y, et al. Nanofiber scaffolds facilitate functional regeneration of peripheral nerve injury. Nanomedicine Nanotechnology, Biol. Med. 2013;9:305–315.

[158] Neal RA, Tholpady SS, Foley PL, et al. Alignment and composition of laminin–polycaprolactone nanofiber blends enhance peripheral nerve regeneration. J. Biomed. Mater. Res. Part A. 2012;100:406–423.

[159] Jiang X, Mi R, Hoke A, et al. Nanofibrous nerve conduit-enhanced peripheral nerve regeneration. J. Tissue Eng. Regen. Med. 2014;8:377–385.

[160] Yu W, Jiang X, Cai M, et al. A novel electrospun nerve conduit enhanced by carbon nanotubes for peripheral nerve regeneration. Nanotechnology. 2014;25:165102.

[161] Li A, Hokugo A, Yalom A, et al. A bioengineered peripheral nerve construct using aligned peptide amphiphile nanofibers. Biomaterials. 2014;35:8780–8790.

[162] Ouyang Y, Huang C, Zhu Y, et al. Fabrication of seamless electrospun collagen/PLGA conduits whose walls comprise highly longitudinal aligned nanofibers for nerve regeneration. J. Biomed. Nanotechnol. 2013;9:931–943.

[163] Liu J, Wang C, Wang J, et al. Peripheral nerve regeneration using composite poly (lactic acid-caprolactone)/nerve growth factor conduits prepared by coaxial electrospinning. J. Biomed. Mater. Res. Part A. 2011;96:13–20.

[164] Wang C-Y, Zhang K-H, Fan C-Y, et al. Aligned natural–synthetic polyblend nanofibers for peripheral nerve regeneration. Acta Biomater. 2011;7:634–643.

[165] Mottaghitalab F, Farokhi M, Zaminy A, et al. A biosynthetic nerve guide conduit based on silk/SWNT/fibronectin nanocomposite for peripheral nerve regeneration. PLoS One. 2013;8:e74417.

[166] Bozkurt A, Brook GA, Moellers S, et al. In vitro assessment of axonal growth using dorsal root ganglia explants in a novel three-dimensional collagen matrix. Tissue Eng. 2007;13:2971–2979.

[167] Chiono V, Tonda-Turo C. Trends in the design of nerve guidance channels in peripheral nerve tissue engineering. Prog. Neurobiol. 2015;131:87–104.

CHAPTER 3

Modeling the Flow Behavior and Flow Rate of Medium Viscosity Alginate for Scaffold Fabrication with a Three-Dimensional Bioplotter

This chapter has been published as "Sarker MD, and Chen XB. Modeling the flow behavior and flow rate of medium viscosity alginate for scaffold fabrication with a three-dimensional bioplotter. *J Manuf Sci Eng* 2017; 139: 081002. " According to the Copyright Agreement, "the authors retain the right to include the journal article, in full or in part, in a thesis or dissertation".

(All the experimental and modeling work was conducted by me. Professor Xiongbiao Chen guided and supervised the whole work.)

3.1 Abstract

Tissue regeneration with scaffolds has proven promising for the repair of damaged tissues or organs. Dispensing-based printing techniques for scaffold fabrication have drawn considerable attention due to their ability to create complex structures layer-by-layer. When employing such printing techniques, the flow rate of the biomaterial dispensed from the needle tip is critical for creating the intended scaffold structure. The flow rate can be affected by a number of variables including the material flow behavior, temperature, needle geometry, and dispensing pressure. As such, model equations can play a vital role in the prediction and control of the flow rate of the material dispensed, thus facilitating optimal scaffold fabrication. This paper presents the development of a model to represent the flow rate of medium viscosity alginate dispensed for the purpose of scaffold fabrication, by taking into account the shear and slip flow from a tapered needle. Because the fluid flow behavior affects the flow rate, model equations were also developed from regression of experimental data to represent the flow behavior of alginate. The predictions from both the flow behavior equation and flow rate model show close agreement with experimental results. For varying needle diameters and temperatures, the slip effect occurring at the needle wall has a significant effect on the flow rate of alginate during scaffold fabrication.

3.2 Introduction

Scaffold-based tissue engineering shows promise for meeting the growing worldwide demand for organ replacement or tissue regeneration. Scaffold geometry (e.g., porosity, pore interconnectivity, and surface topography) and the biomaterial fabricated can significantly affect the survival, growth, proliferation, and differentiation of embedded cells during scaffold-based tissue culture [1–3]. Three-dimensional (3D) bioplotters based on the compressed-air-driven rapid prototyping approach have been drawing considerable attention for scaffold fabrication due to their ability to create complex structures layer-by-layer through the extrusion of continuous filaments that may incorporate cells, growth factors, peptides, and/or extracellular matrix proteins [4–6]. Furthermore, microfluidic mass transfer and precise cell positioning can also be achieved within the scaffold by 3D bioplotting [7, 8].

Hydrogels are promising biomaterials for bioplotting due to their high water content and tissuelike properties, thus providing a 3D environment for cell attachment, proliferation, and differentiation to form the desired tissue [9]. The viscosity of polymeric hydrogels has been suggested to affect cell distribution and viability as well as printability by means of a liquid dispensing printer; for example, low-viscosity hydrogels tend to form droplets rather than strands upon deposition, which causes inhomogeneous cell distribution, whereas high-viscosity materials can clog the dispensing needle and damage cells due to the high shear stress encountered during scaffold fabrication [10, 11]. Conversely, medium viscosity alginate (400–3000 cP) offers high printability and cell viability (>90%) [12] and is a suitable and preferred biofabrication material.

Rigorous selection of fabrication speed, dispensing pressure, and scaffold strand width is important to scaffold biofabrication as these parameters regulate the viability of incorporated cells as well as the mechanical properties of the scaffold [13]. Moreover, strand width affects the pore size and porosity of the scaffold, thus affecting its mechanical properties as well as the proliferation and attachment of incorporated cells [14, 15]. Rigorous selection of scaffold printing parameters can be achieved by developing effective model equations. Without such equations, achieving the desired strand width by choosing the needle speed and dispensing pressure based on experience can be challenging. In addition, many trials may be required to determine the appropriate fabrication parameters, which are time consuming and cost ineffective.

Moreover, time delays due to numerous trials can quite significantly decrease cell viability in the loaded cell/polymer mixture in the extrusion cylinder of a 3D bioplotter.

Characterization and modeling of fluid behavior are necessary to develop a model for the flow rate of the fluid dispensed in scaffold fabrication. Several studies have modeled the flow behavior of time-dependent and -independent fluids. For example, rheological kinetic and empirical models have been used to study the thixotropic behavior (i.e. shear stress decreases with time at constant shear rate) of a time-dependent fluid [16]. While useful for representing the thixotropic behavior, lack of applicability in the steady-state of viscosity limits the utility of the empirical model. Moreover, phenomenological models have been used to predict the rheological behavior of inelastic reversible thixotropic and antithixotropic fluids [17]; Herschel–Bulkley and exponential models have been applied to predict the thixotropic behavior of a time-dependent fluid [18]; and structural models have been developed to describe the rheological properties of a time-dependent complex material [17–19]. However, these models are incompatible with time-independent materials and require shear history to predict flow behavior. The flow behavior of time-independent materials has also been investigated with models; for example, close agreement between rheological data obtained from a viscometer and the Herschel–Bulkley model has been demonstrated, and a flow behavior model developed from rheometer data provided better agreement with measured data than a flow behavior model developed from dispensing experiments [20, 21]. Because models identified from rheometer data are cost and time effective, a flow behavior model for alginate/hydroxyapatite mixtures has been developed to predict flow behavior at different concentrations and temperatures [22]. This work efficiently predicts flow behavior parameters for the alginate mixture but could not predict the flow behavior of medium viscosity alginate. Hence, a flow behavior model that can predict flow parameters (consistency index, flow index, and yield stress) and thus help to predict the flow rate of alginate at various concentrations and dispensing temperatures needs to be developed.

The flow rate of a non-Newtonian fluid (epoxy resin) from a pneumatic pressure-driven dispensing head with a cylindrical needle has been modeled with empirical equations and a fuzzy regression approach [23]. Though promising, the numerous time-consuming experiments required to develop the empirical model equations limit the application of the fuzzy approach. Several analytical models have been developed to model flow rate by ignoring the influence of

air compressibility; this includes models developed to predict the flow rate of time-dependent fluids [24]. Further, models have been developed to predict the flow rate of incompressible and time-independent fluids based on the assumption of steady laminar flow [25, 26]. The dynamic flow rate of time-independent fluids has been explored under the influence of air compressibility [27, 28]. However, none of these models can predict the flow rate of nonpower-law fluids as the models were derived from the power-law equation.

Furthermore, semi-analytical expressions have been developed for particle-laden fluids flowing through channels to predict the pressure gradient, velocity profile, and flow rate [29]. Similarly, fluid flow through capillaries has been studied considering the wall slip effect [30–32], where the model equations suggest the profound influence of the fabrication material and shear stress on the wall slip effect. Likewise, several models have been developed for capillary flow in biofabrication systems, including a shear rate model for colloidal ink assuming a nonslip boundary layer condition, a flow rate model for a time-independent material assuming steady-state and nonslip conditions, and a capillary flow model for a chitosan hydroxyapatite colloid mixture dispensed from a tapered needle [33–35]. However, these models are limited to power-law fluids and nonslip conditions. In reality, wall slip occurs more in non-Newtonian versus Newtonian fluids [36, 37], and thus consideration of wall slip must be taken into account when developing a flow rate model for non-Newtonian fluids (e.g., alginate).

In this work, a flow behavior model was developed based on rheological data collected at varying temperatures (25–55 °C) and alginate concentrations (1–4%). The hypothesis was that the mathematical model would predict the flow behavior of MVSA precursor at various precursor concentrations and temperatures. The effectiveness of the model was verified with experimental data obtained for 2.5% alginate. A flow rate model was also developed for medium viscosity alginate considering shear and slip flow from a tapered needle. The flow rate model was verified with experimental results by dispensing alginate (2%, 3%, and 4%) from a tapered needle (exit diameter $200\,\mu$m) at a temperature of 25 °C. The model-predicted strand width was compared to printed alginate (3% and 4%) strand widths. The effects of various needle diameters (0.2, 0.25, 0.41, and 0.61 mm) and temperatures (25, 35, 45, and 55 °C) on flow rate were considered, and the model equation outputs were compared to measured results.

3.3 Materials and method

3.3.1 Preparation of material

Medium viscosity alginate (sodium salt from brown algae) and calcium chloride ($CaCl_2 \cdot 2H_2O$) were purchased from Sigma Aldrich, Oakville, ON, Canada. Polyethyleneimine (PEI) (MW 60,000, 50% w/w in H_2O) was purchased from Alfa Aesar, Tewksbury, MA. Alginate solutions (1%, 2%, 3%, and 4% w/v) were prepared using water as the solvent for consequent examinations to analyze the rheological properties and flow rates of materials dispensed on a 3D bioplotter.

3.3.2 Rheological apparatus and experimental procedures

The flow behavior of the alginate solutions was characterized using a Brookfield DV-III ultra-rheometer (Brookfield Engineering Labs Inc., Middleborough, MA) with a CP-41 spindle. The spindle had a conical vertex (with a 3 deg obtuse angle) perpendicular to the flat plate of the sample loading cup (Fig. 3.1). During the experiment, the CP-41 was rotated at a constant speed (ω), while 2 mL of alginate solution were loaded into the gap between the spindle and the cup plate. A tiny gap (0.013 mm) between the cone tip and the stationary flat plate was always maintained.

Fig. 3.1 (a) Brookfield DV-III ultra-rheometer and (b) its spindle and loading cup

The rheometer measured the torque required to overcome the viscous resistance of the alginate solution. Shear rate, stress, and viscosity data were obtained for the four different alginate

solutions at a constant temperature and different rotational speeds. The rheometer was run with Rheocalc® programmable software, with the following mathematical relationships used to calculate the flow parameters:

$$\tau = \frac{T}{2/3\ \pi R_c^3} \tag{3.1}$$

$$\gamma = \frac{\omega}{Sin\varphi} \tag{3.2}$$

$$\mu = \frac{\tau}{\gamma} \times 100 \tag{3.3}$$

where T is the percentage of full scale torque (N·m), R_c is the cone radius (m), ω is the cone speed (rad/s), φ is the cone angle (radian), τ is the shear stress (N/m²), γ is the shear rate (s⁻¹), and μ is the viscosity (Pa·s). Data were collected for alginate concentrations of 1–4%, and the temperature of the solution was maintained between 25 and 55 °C using a water bath. Experimental data were fit into five different models (Casson, Bingham plastic, IPC paste, power law, and Herschel–Bulkley) available in the rheometer operating program. The Herschel–Bulkley model provided the best fit (99.5–100% confidence of fit) with the experimental data and was subsequently used to identify values of the flow index (n), yield stress (τ_0), and consistency index (K).

3.3.3 Flow rate measured on the three-dimensional bioplotter

Alginate was dispensed by using tapered needles with varying exit diameters (i.e., 0.2, 0.25, 0.41, and 0.61 mm) mounted in the dispensing head of a 3D bioplotter (Envisiontec GmbH, Germany) (Fig. 3.2). The bioplotter head is driven by pneumatic pressure and can move in the X, Y, and Z directions, as described elsewhere [38]. To measure the flow rates, 20 mL of alginate solution (2%, 3%, or 4%) were loaded into the head and dispensed over a certain time period at various temperatures (25, 35, 45, and 55 °C) and dispensing pressures (20, 25, 30, and 40 kPa). The alginate dispensed was collected and weighed on a scale, then the flow rates determined by dividing the total amount of alginate dispensed by the dispensing time. For each measurement, at least three samples were collected to obtain the average flow rate.
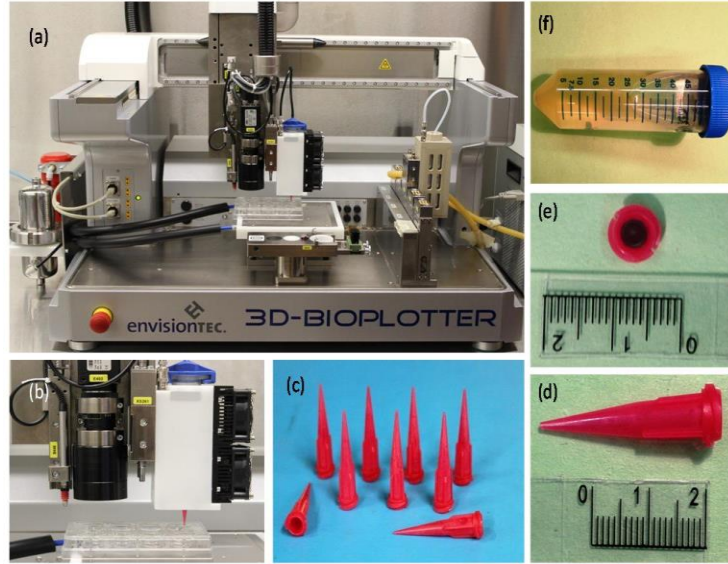
Fig. 3.2 Dispensing-based rapid prototyping machine for 3D scaffold fabrication: (a) 3D bioplotter, (b) bioplotter dispensing head, (c) tapered needle for dispensing head, (d) tapered needle with scale for length, (e) entrance diameter, and (f) 2% (w/v) alginate solution

3.3.4 Single-layer scaffold fabricated on the three-dimensional bioplotter

To measure the strand width, a single-layer scaffold pattern was printed on the 3D bioplotter. Prior to printing, CAD software was used to develop 3D virtual models of the desired scaffolds. Medium viscosity alginate solution (3% or 4% w/v) was loaded into the bioplotter head and dispensed through a tapered needle (EFD Nordson, Westlake, OH) with an extrusion diameter of $200\,\mu$m (Fig. 3.3). A linear needle speed of 6–14 mm/s was maintained in the X and Y directions during 3D fabrication, and a dispensing pressure of 0.2–0.5 bar was applied to extrude alginate into 12-well tissue culture plates containing crosslinking solution (50 mM $CaCl_2$). For each needle speed and dispensing pressure, at least three single-layer cuboid patterns ($10 \times 10 \times 0.2$ mm^3) were printed, and then the average strand width was determined. To eliminate the thermal effect on alginate viscosity, a temperature of 25 °C was maintained in the dispensing head. A right angle between the filaments of consecutive layers was maintained, and a 1 mm interstrand distance was assigned to each continuous layer.
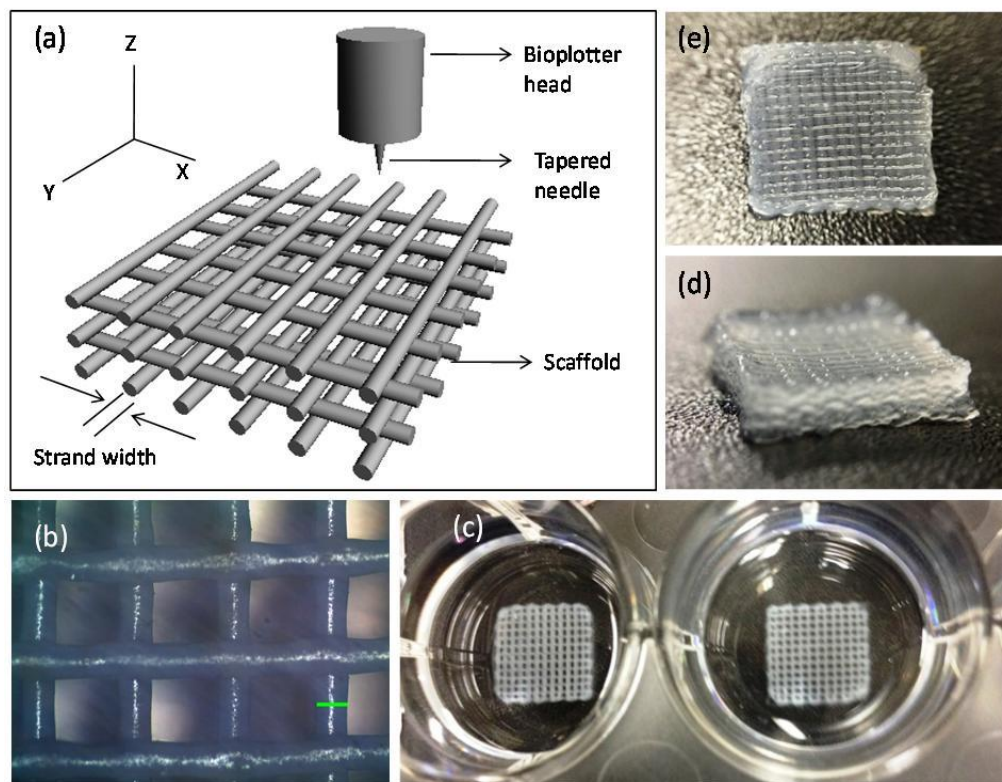
Fig. 3.3 (a) Schematic of 3D scaffold fabrication by bioplotter, (b) multiple layered alginate scaffold (scale bar = 0.2 mm), (c) printed alginate scaffold suspended in CaCl$_2$ crosslinking solution, and (d) side view and (e) top view of the printed alginate scaffold

The alginate strands were plotted into 12-well tissue culture plates containing 1 mL crosslinking solution (50 mM CaCl$_2$). Anionic alginate strands do not adhere to the negatively charged tissue culture dish and therefore float after fabrication; this does not allow for the printing of successive layers. However, coating with polycationic PEI can improve surface adhesion and crosslinking of the alginate [39, 40]. Therefore, the 12-well tissue culture plates were coated with 0.1% sterile PEI and incubated overnight at 37 °C to enhance adhesion. Excessive PEI was eliminated from the culture plate by successive washes with sterile water and 10 mM phosphate buffered saline (PBS) prior to scaffold fabrication.

3.3.5 Statistical analysis

For all experimental data, the number of replicates was three ($n = 3$), and a one-way analysis of variance (ANOVA) was used to assess statistical significance (p_b-value < 0.05). To evaluate the

61

prediction accuracy of the flow behavior and flow rate model equations with respect to experimental data, regression parameters such as coefficient of determination (R^2), residuals, root mean square error (RMSE), and mean absolute percentage error (MAPE) were assessed as per the following equations [20,41]:

$$R^2 = \frac{\{\sum_{t=1}^{n}(E_t - \bar{E})(F_t - \bar{F})\}^2}{\sum_{t=1}^{n}(E_t - \bar{E})^2 \sum_{t=1}^{n}(E_t - \bar{E})^2} \tag{3.4}$$

$$\text{Residual} = \frac{(E - F)}{E} \tag{3.5}$$

$$\text{RMSE} = \sqrt{\frac{\sum_{t=1}^{n}(E_t - F_t)^2}{n}} \tag{3.6}$$

$$\text{MAPE} = \frac{\sum_{t=1}^{n}\left|\frac{E_t - F_t}{E_t}\right|}{n} \times 100 \tag{3.7}$$

where, E, $\bar{E}$, F, and $\bar{F}$ indicate experimental data, average experimental data, predicted data, and average predicted data, respectively.

3.4 Development of model equations

3.4.1 Model development for alginate flow behavior

The Herschel–Bulkley model is quite effective at characterizing the nonlinear relationship between shear rate and shear stress of non-Newtonian fluids having yield stress. Due to its molecular architecture and high molar mass, alginate solution exhibits non-Newtonian fluid behavior [42]. Therefore, the Herschel–Bulkley model can be used to model its flow behavior:

$$\tau = \tau_o + K\gamma^n \tag{3.8}$$

where τ is the shear stress, τ_0 is the yield stress, γ is the shear rate, K is a consistency index, and n is a flow behavior index. Yield stress indicates the required amount of shear stress to start fluid flow. The flow index parameter n represents the degree of non-Newtonian flow behavior of the alginate solution. The value of n determines the pattern of velocity profile and the value of the velocity gradient for a non-Newtonian fluid. It varies for different types of non-Newtonian

62

fluids, which results in a nonlinear relationship between shear stress and velocity gradient. Interestingly, when n equals 1, the consistency index and fluid viscosity are identical. Experimental materials can show evidence of shear-thinning ($n < 1$) or shear-thickening behavior ($n > 1$) based on the value of n. The term K, known as apparent viscosity, is a function of temperature, pressure, and shear rate [43] and demonstrates the apparent viscosity of a non-Newtonian fluid with shear stress at a shear rate of $1\ \mathrm{s}^{-1}$. With increasing shear rate, K decreases for shear-thinning behavior but increases for shear-thickening behavior. The flow behavior parameters (K, τ_0, and n) of non-Newtonian fluids are a function of temperature and the concentration of solutes in solution. The effect of temperature and solute concentration on K, τ_0, and n can be expressed by the following model equations (adapted from Ref. [22]):

$$K = a\, e^{(\frac{T_0}{T} - \frac{C_0}{C})} - b\, \left(\frac{T}{T_0}\frac{C}{C_0}\right) + d\, \left(\frac{T_0}{T}\right) \tag{3.9}$$

$$\tau_0 = f e^{(\frac{T_1}{T} - \frac{C}{C_1})} + g\, \left(\frac{T_1}{T}\frac{C}{C_1}\right)^{T/T_1} + h\, \left(\frac{T_1}{T}\right) \tag{3.10}$$

$$n = i e^{(-\frac{T_2}{T} - \frac{C_2}{C})} + j\, \left(\frac{C_2}{C}\right)\left(\frac{T_2}{T}\right) + m\, \left(\frac{T}{T_2}\right) \tag{3.11}$$

where T_0, T_1, T_2, C_0, C_1, C_2, a, b, d, f, g, h, i, j, and m are constants that can be found by nonlinear regression of experimental rheological data. Fig. 3.4 is a schematic of the rheological experiment. Since the right-hand term of Eq. (9) is dimensionless, the constants (a, b, and d) are associated with the apparent viscosity of the material (alginate). Similarly, the constants (f, g, and h) of Eq. (10) are related to the yield stress, and the constants (i, j, and m) of Eq. (11) are related to the flow behavior index of alginate.
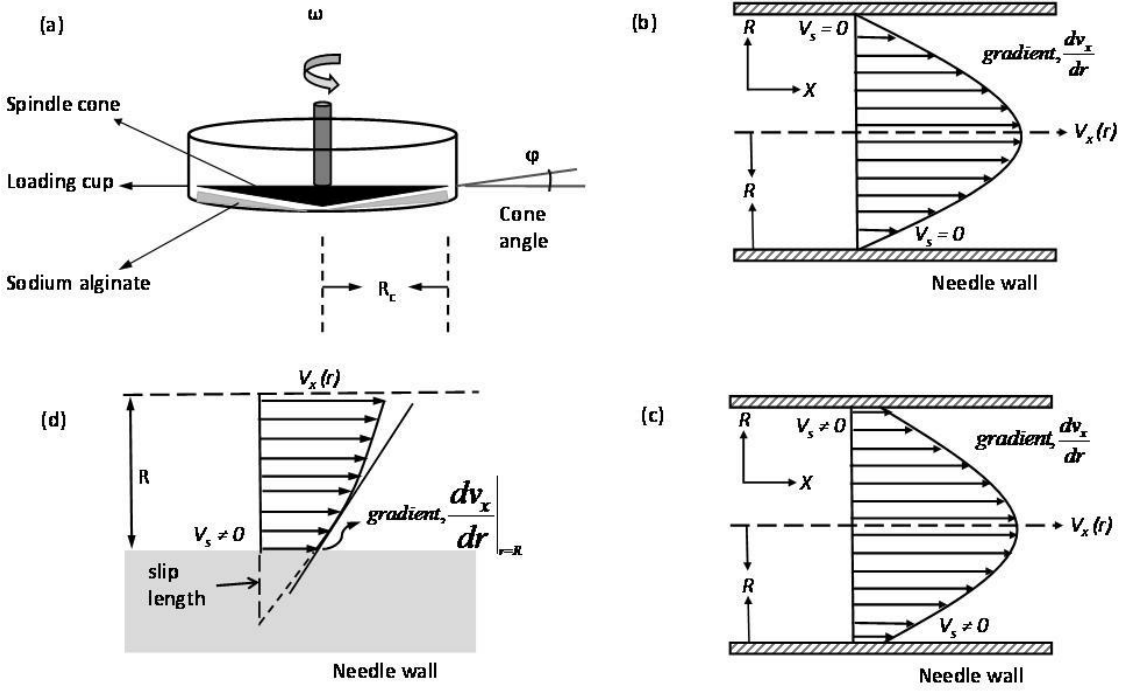
Fig. 3.4 (a) Schematic of spindle cone and loading cup of Brookfield DV-III ultra-rheometer; velocity profiles of alginate in the needle for boundary conditions (b) without slip and (c) and (d) with slip

3.4.2 Model development for the flow rate of alginate

In an air-pressure-driven dispensing system, some assumptions are made to model the flow rate: the alginate solution is incompressible; the flow of alginate in the needle is steady and fully developed; the slip between alginate and the needle wall is significant (Figs. 3.4(b)–3.4(d)); the pressure drop in the bioplotter head is insignificant; and minor losses due to entrance effects and fittings are negligible. The pressure drop and the tangent of θ can be, respectively, expressed as

$$\Delta P = P - P_e \tag{3.12}$$

$$tan\theta = \frac{r_i - r_o}{L} \tag{3.13}$$

where P is the pressure applied to the syringe/bioplotter head, P_e is the exit pressure at the needle end, r_i and r_o are the entrance and exit radius of the tapered needle, respectively, θ is the half cone angle, and L is the length of the tapered needle (Fig. 3.5).
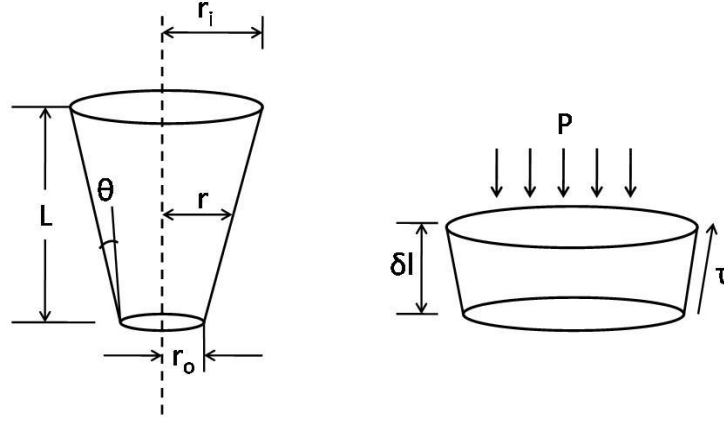
Fig. 3.5 Schematic of a tapered needle for a bioplotter head

Taking into account the reduction of viscosity near the needle wall due to fluid–wall interactions, the total flow rate equation for an alginate solution from a tapered needle [44] can be written as

$$Q_t = Q_{shear} + Q_{slip} \tag{3.14}$$

where Q_{total} is the total flow rate, Q_{shear} is the shear flow rate, and Q_{slip} is the slip flow rate. For a small needle element of length δl, force balance equations for the applied pressure and shear stress can be written as [45]

$$\delta P\, \pi r^2 = 2\pi r(\delta l\, sec\theta)(\tau cos\theta) \tag{3.15}$$

$$\gamma = \frac{4Q}{\pi r^3} \tag{3.16}$$

$$\delta l = \frac{\delta r}{tan\theta} \tag{3.17}$$

With the help of Eqs. (3.12), (3.13), and (3.15) – (3.17), the shear flow or flow without slip for a tapered needle can be expressed as [34]

$$Q_{shear} = \frac{\pi r_i^3 r_o^3}{4} \left[\frac{3n\, tan\theta\, (\Delta P + \frac{2\tau_0}{tan\theta}\, ln\frac{r_i}{r_o})}{2K\, (r_i^{3n} - r_o^{3n})} \right]^{1/n} \tag{3.18}$$

The slip flow rate can be calculated from the product of the slip velocity and cross-sectional area at the needle exit, as follows:

$$Q_{slip} = V_s\, (\pi r_o^2) \tag{3.19}$$

65

where V_s is the slip velocity, and for a slip layer thickness δ_t, the slip velocity equation is [30]

$$V_s = \frac{\delta_t \tau_w^{1/n}}{K^{1/n}}$$

(3.20)

where τ_w is the wall shear stress, and K is the apparent viscosity of alginate at the needle wall. The thickness of the slip layer ($9\,\mu$m) was taken as 15% of the mean particle size of the alginate powder ($60\,\mu$m) [31]. The shear stress at the needle wall can be obtained by integrating Eq. (3.15)

$$\tau_w = \tau_0 + \frac{3n\Delta P \tan\theta}{2\{1-(\frac{r_o}{r_i})^{3n}\}}$$

(3.21)

The slip flow rate can be obtained by combining Eqs. (3.19) – (3.21) and can be written as

$$Q_{slip} = \frac{\pi \delta_t r_0^2}{K^{1/n}}\left[\tau_0 + \frac{3n\Delta P \tan\theta}{2\{1-(\frac{r_o}{r_i})^{3n}\}}\right]^{1/n}$$

(3.22)

The total flow rate of the alginate solution from the tapered needle can be calculated by combining Eqs. (3.14), (3.18), and (3.22), and for strand width D_s, the needle moving speed V_n can be obtained as follows:

$$V_n = \frac{4Q_t}{\pi D_s^2}$$

(3.23)

3.5 Results and model equation verification

The nonlinear flow behavior of 1–4% medium viscosity alginate for temperatures ranging from 25 to 55 °C is presented as shear stress versus rate curves (Fig. 3.6). The slope of the flow behavior curves gradually decreases with increased shear rate for a given operating temperature. In addition, shear stress decreases as temperature increases for the same shear rate, which suggests a reduction in viscosity with increasing temperature. Extrapolation of the shear stress versus rate curve intersects the Y axis at a coordinate known as the yield stress. Further, the stress versus rate curve of medium viscosity alginate strongly indicates shear-thinning (yield pseudoplastic) behavior upon applied stress.
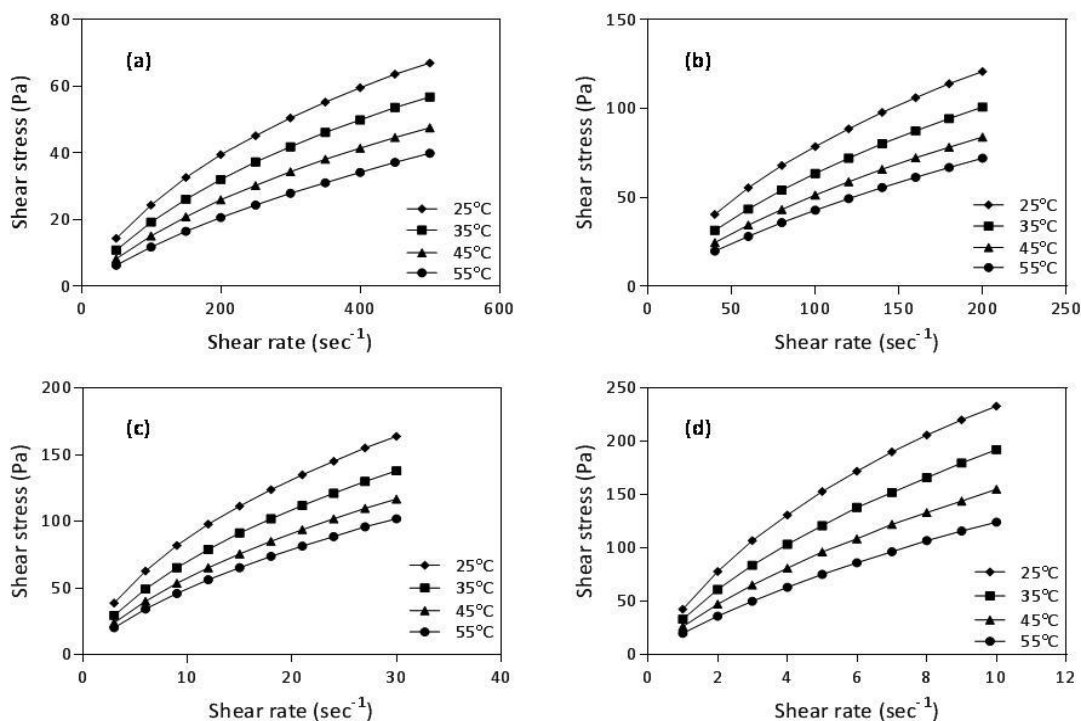
Fig. 3.6 Flow behavior curve for medium viscosity alginate: (a) 1%, (b) 2%, (c) 3%, and (d) 4%

To obtain flow behavior parameters (K, τ_0, and n), shear stress versus shear rate data were regressed against Herschel–Bulkley model equations. An increase in yield stress was noted as the alginate concentration increased from 1% to 4% (Fig. 3.7). Moreover, for a given alginate concentration, the yield stress decreased with increasing temperature, which indicates rising temperature reduces the initial flow resistance of alginate. The same phenomenon was also observed for the consistency index. However, a remarkable increase in the consistency index was noted for alginate concentrations >2%. Therefore, 2% (w/v) could be a critical concentration for medium viscosity alginate beyond which the significant entanglement of long molecular alginate chains causes radical changes in the viscosity. However, increasing temperature reduces the yield stress and consistency index due to the increased kinetic energy of the alginate molecules. Therefore, alginate demonstrates higher yield stress and consistency index values at lower temperatures and lower values at higher temperatures. For post fabrication cell incorporation, the temperature-dependent behavior of alginate facilitates 3D bioplotting while restoring mechanical strength after fabrication. In fact, dispensing materials at a higher temperature (>37 °C) ensures a superior flow rate, and addition of cells at 37 °C facilitates better cell viability. On the other hand, fabrication temperatures ≤37 °C are needed to codispense cells and alginate and

satisfactorily preserve cell viability. Furthermore, the degree of nonlinearity of the shear stress versus rate curve is regulated by the value of n, which increases with temperature and alginate concentration.
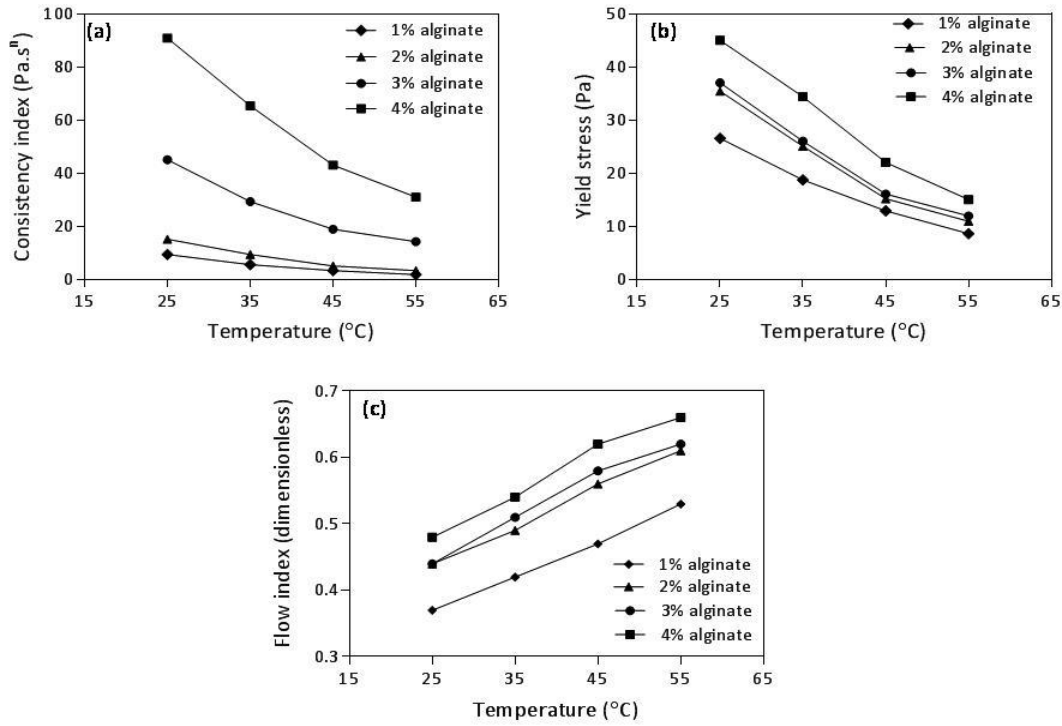
Fig. 3.7 Flow behavior parameters of medium viscosity alginate (1–4%) at various temperatures (25–55°C): (a) consistency index, (b) yield stress, and (c) flow index

3.5.1 Verification of flow behavior model

Varying the temperature and concentration affects the flow behavior of alginate. To predict the flow behavior at different temperatures and concentrations, the experimental shear stress versus shear rate data for alginate at different temperatures (25, 35, 45, and 55 °C) and concentrations (1%, 2%, 3%, and 4%) were used for regression, based on Eqs. (3.9)–(3.11).

Constant parameters for the three model equations (Table 3.1) were obtained by regressing the experimental data. For all regressions, the R^2 value obtained was between 99.2% and 99.75%. The model equations for consistency index, yield stress, and flow index (Eqs. (3.9)–(3.11)) can then be solved by substituting the constant values found in Table 3.1. The model equations were subsequently validated against rheological data measured at an alginate concentration of 2.5%.

Table 3.1 Flow behavior parameters obtained from the regression of experimental data

Equation (3.9)			Equation (3.10)			Equation (3.11)		
Constants	Value	Unit	Constants	Value	Unit	Constants	Value	Unit
a	284.09	$Pa.s^n$	f	-2.40	Pa	i	0.48	
T_0	30.11	°C	T_1	56.48	°C	T_2	5.18	°C
C_0	9.51	%(w/v)	C_1	45.02	%(w/v)	C_2	0.66	%(w/v)
b	21.89	$Pa.s^n$	g	73.13	Pa	j	0.28	
d	9.82	$Pa.s^n$	h	13.05	Pa	m	0.03	

Table 3.2 Measured and model-predicted flow behavior parameters at various temperatures

Parameters	Alginate % (w/v)	Temp. (°C)	Measured average $(Pa.s^n)$	Model with slip $(Pa.s^n)$	Residual $(Pa.s^n)$	R^2	MAPE (%)	RMSE $(Pa.s^n)$
Consistency index	2.5	25	29.86	28.16	0.06	0.98	11.51	1.69
		35	18.50	16.72	0.10			
		45	12.53	10.33	0.18			
		55	5.13	5.81	-0.13			
Yield stress	2.5	25	33.82	36.89	-0.09	0.97	6.75	2.11
		35	25.93	26.05	0.00			
		45	20.03	17.16	0.14			
		55	11.93	11.55	0.03			
Flow index	2.5	25	0.46	0.44	0.03	0.98	1.85	0.01
		35	0.51	0.51	0.01			
		45	0.56	0.57	-0.01			
		55	0.64	0.62	0.03			

Data obtained from the model equations display good agreement with experimental data, thus validating the model equations (Table 3.2). In particular, the MAPE (11.51%, 6.75%, and 1.85%) and R^2 (0.98, 0.97, and 0.98) values are quite remarkable (Figs. 3.8(d)–3.8(f)). As the temperature increases, the consistency index (Fig. 3.8(a)) and the yield stress (Fig. 3.8(b)) demonstrate decreasing trends, while the flow index (Fig. 3.8(c)) demonstrates an increasing

trend. The minute deviations between the experimental data and the model predictions are attributed to evaporative loss of water. Though the rheological apparatus is leak proof, vapor leaves the alginate solution and accumulates in the hollow space between the spindle cone and upper portion of the cup holder. This results in the concentration of the alginate solution increasing a bit with temperature. By ignoring these very minor variations, the model equations developed can be used to predict K, τ_0, and n values of alginate for different concentrations and operating temperatures.
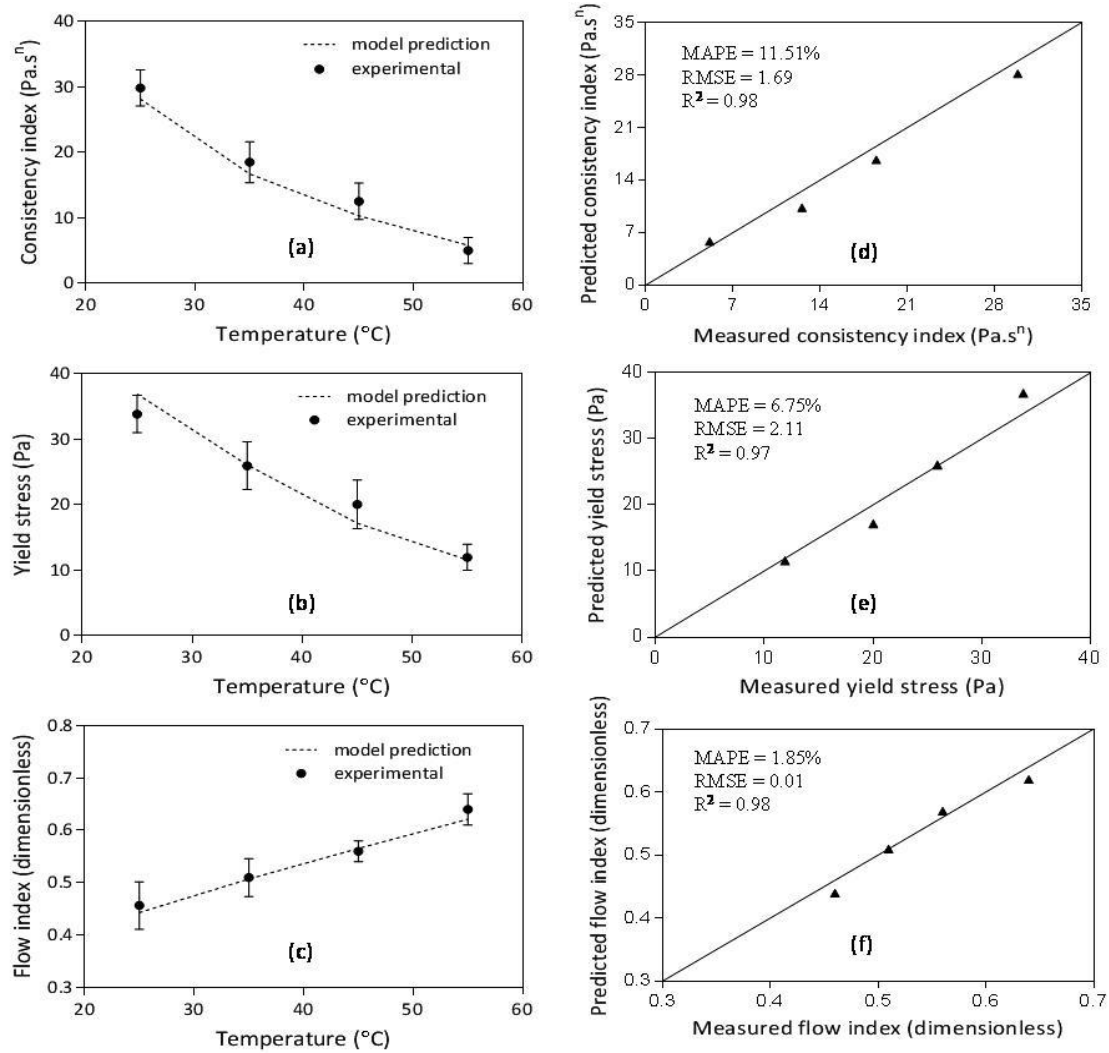
Fig. 3.8 Experimental versus model-predicted flow behavior of 2.5% (w/v) alginate at different temperatures (25, 35, 45, and 55 °C): (a) consistency index, (b) yield stress, and (c) flow index; comparison plots (with diagonal line of equality) of measured and predicted data for (d)

consistency index, (e) yield stress, and (f) flow index; experimental data are statistically

significant (n = 3, $p_b < 0.05$)

In tissue engineering, biomaterial selection is quite a challenging issue for successful scaffold outcomes after in vitro or in vivo culture. Because the viscosity of a material is one of the most important criteria for material selection, the model equations developed here will provide significant direction for biomaterial screening based on viscosity. In addition, as high viscosity causes high shear stress and metabolic complexity to incorporated cells, prefabrication and postfabrication cell damage can be reduced by taking the flow behavior information into consideration. Furthermore, as the flow behavior parameter regulates the flow rate of alginate, determination of K, τ_0, and n by model equations would reduce the time and trials required to predict the flow rate for scaffold fabrication.

3.5.2 Verification of the flow rate model with needle flow

To verify the efficiency of the flow rate model developed, experimental data were compared with those obtained from model Eqs. (3.14), (3.18), and (3.22). Flow rate was measured experimentally for pneumatic pressures of 20, 25, 30, and 40 kPa, as per the methodology discussed above, and was also calculated taking into account the slip and nonslip model equations; the results are presented graphically in Figs. 3.9(a)–3.9(c). Model prediction curves didn't follow a smooth pattern in the plots probably due to the use of a small number of data points. The model with slip shows good agreement (MAPE = 13.38%, $R^2 = 0.98$) with experimental results (Fig. 3.9(e)); however, the model without slip exhibits significant deviations (MAPE = 42.13%, $R^2 = 0.96$) from the measured data (Fig. 3.9(d)). An unbiased predictability of the flow rate model (with slip) is identified, because a random distribution of the residuals is observed (Fig. 3.9(f)). Therefore, slip clearly occurs when alginate is dispensed from the tapered needle, and consideration of the slip effect to model the flow rate equation is an appropriate assumption. Medium viscosity alginate displays shear-thinning (yield pseudoplastic) behavior with increasing shear stress. As shear stress increases with applied pneumatic pressure, the apparent viscosity of the alginate decreases at the needle wall compared to the bulk, resulting in slip flow (Table 3.3).

Table 3.3 Measured and model-predicted flow rate of alginate at different concentrations

Alginate % (w/v)	Dispensing pressure (kpa)	Alginate flow rate measured average (mg/s)	Alginate flow rate no slip (mg/s)	Alginate flow rate with slip (mg/s)	Residual with slip (mg/s)	R^2 no slip (mg/s)	R^2 with slip (mg/s)	MAPE (%) no slip	MAPE (%) with slip	RMSE no slip (mg/s)	RMSE with slip (mg/s)
2	20	9.06	4.15	7.72	0.15						
	25	15.20	9.85	15.00	0.01						
	30	25.71	13.03	21.69	0.16						
	40	39.72	29.03	44.05	-0.11						
3	20	0.81	0.33	0.64	0.21						
	25	0.99	0.71	1.30	-0.32	0.96	0.98	42.13	13.38	5.26	1.76
	30	1.84	1.06	1.82	0.01						
	40	4.20	2.31	3.70	0.12						
4	20	0.14	0.06	0.10	0.32						
	25	0.18	0.11	0.20	-0.06						
	30	0.25	0.15	0.26	-0.05						
	40	0.46	0.33	0.50	-0.10						
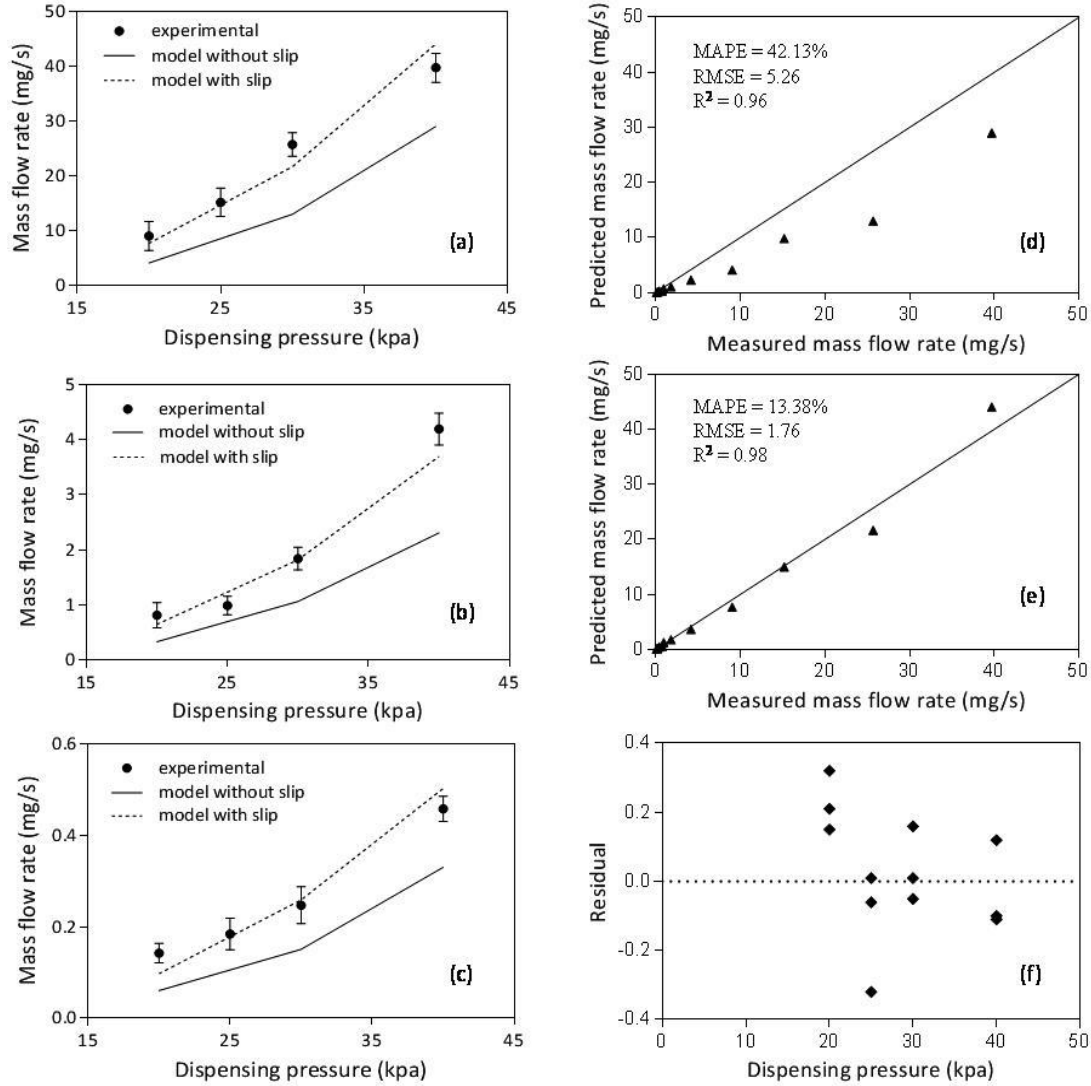
Fig. 3.9 Experimental versus model-predicted mass flow rate through a tapered needle (0.2mm exit diameter) at 25 °C and various dispensing pressures (20, 25, 30, and 40 kPa) for (a) 2%, (b) 3%, and (c) 4% (w/v) alginate; comparison plot (with diagonal line of equality) of measured and predicted mass flow rate data for models (d) without slip and (e) with slip; and (f) distribution of residual prediction errors of mass flow rate data for model with slip (f); experimental data are statistically significant (n = 3, $p_b < 0.05$)

3.5.3 Verification of flow rate model with printed strand

The printed strand width depends on the flow rate of the fabrication material and the needle speed, and therefore the validity of the model equations developed can be determined by measuring the width of printed filaments. Strand width was measured for a single-layered

73

scaffold fabricated as described above. Images of the strands were taken using a fluorescent microscope (Carl Zeiss Axiovert 100) and IMAGEJ (National Institutes of Health, Bethesda, MD) software used to measure the width of the strands. Good agreement was noted between experimental results and model predictions based on Eq. (23) (Table 3.4). The predicted strand width obtained with the model equations deviates less from the printed strand for highly viscous (4% w/v) alginate (MAPE $= 4.41\%$, $R^2 = 0.97$) than for low-viscosity (3% w/v) alginate (MAPE $= 5.33\%$, $R^2 = 0.98$) (Figs. 3.10 (b) and 3.10 (e)). Further, a random distribution pattern of the residuals suggests an unbiased predictability of the model equation (Figs. 3.10 (c) and 3.10 (f)). For the same concentration of alginate and dispensing pressure, strand width decreases with increased needle speed. In contrast, strand width increases with increased dispensing pressure for the same alginate concentration and needle speed (Figs. 3.10 (a) and 3.10 (d)). As the apparent viscosity increases with material concentration for a shear-thinning (yield pseudoplastic) material, strand width decreases with increasing alginate concentration for the same dispensing temperature, pressure, and needle speed. This information is very useful for scaffold fabrication, as optimization of dispensing pressure and needle speed is required to achieve the desired strand width with minimal cell damage. Printing strands at high dispensing pressures causes cell damage due to high shear stress [34]. On the other hand, interrupted material flow can occur during biofabrication at low dispensing pressures due to viscous clogging at the needle opening. Increasing the needle speed reduces the fabrication time, and thus affects the incorporated cell viability by shortening the exposure time to the harsh crosslinking solution. The strand width affects the porosity of the scaffold and therefore regulates the mechanical strength [46]. In addition, efficient mass transport and gaseous diffusion, which largely depend on the strand width [47], are required for better metabolic activity of the incorporated cells.

Table 3.4 Measured and model-predicted strand width of alginate at different concentrations

Alginate %(w/v)	Temp. (∘C)	Needle diameter (mm)	Needle speed (mm/s)	Dispense pressure (kpa)	Strand width measured average (µm)	model with slip (µm)	Residual (µm)	R^2	RMSE (µm)	MAPE (%)
3	25	0.2	8	20	284.35	315.88	-0.11	0.98	25.75	5.33
			10	20	261.54	282.54	-0.08			
			12	20	252.79	257.92	-0.02			
			14	20	229.10	238.78	-0.04			
			8	30	558.11	530.98	0.05			
			10	30	512.71	474.92	0.07			
			12	30	449.51	433.54	0.04			
			14	30	364.36	401.38	-0.10			
			8	40	744.77	757.60	-0.02			
			10	40	649.83	677.60	-0.04			
			12	40	659.43	618.58	0.06			
			14	40	570.16	572.70	0.00			
4	25	0.2	6	30	213.91	230.54	-0.08	0.97	12.24	4.41
			8	30	211.28	199.65	0.06			
			10	30	183.95	178.58	0.03			
			12	30	175.70	163.02	0.07			
			6	40	325.26	321.24	0.01			
			8	40	264.68	278.20	-0.05			
			10	40	229.82	248.83	-0.08			
			12	40	220.93	227.15	-0.03			
			6	50	412.54	413.04	0.00			
			8	50	360.68	357.70	0.01			
			10	50	304.16	319.94	-0.05			
			12	50	310.52	292.06	0.06			
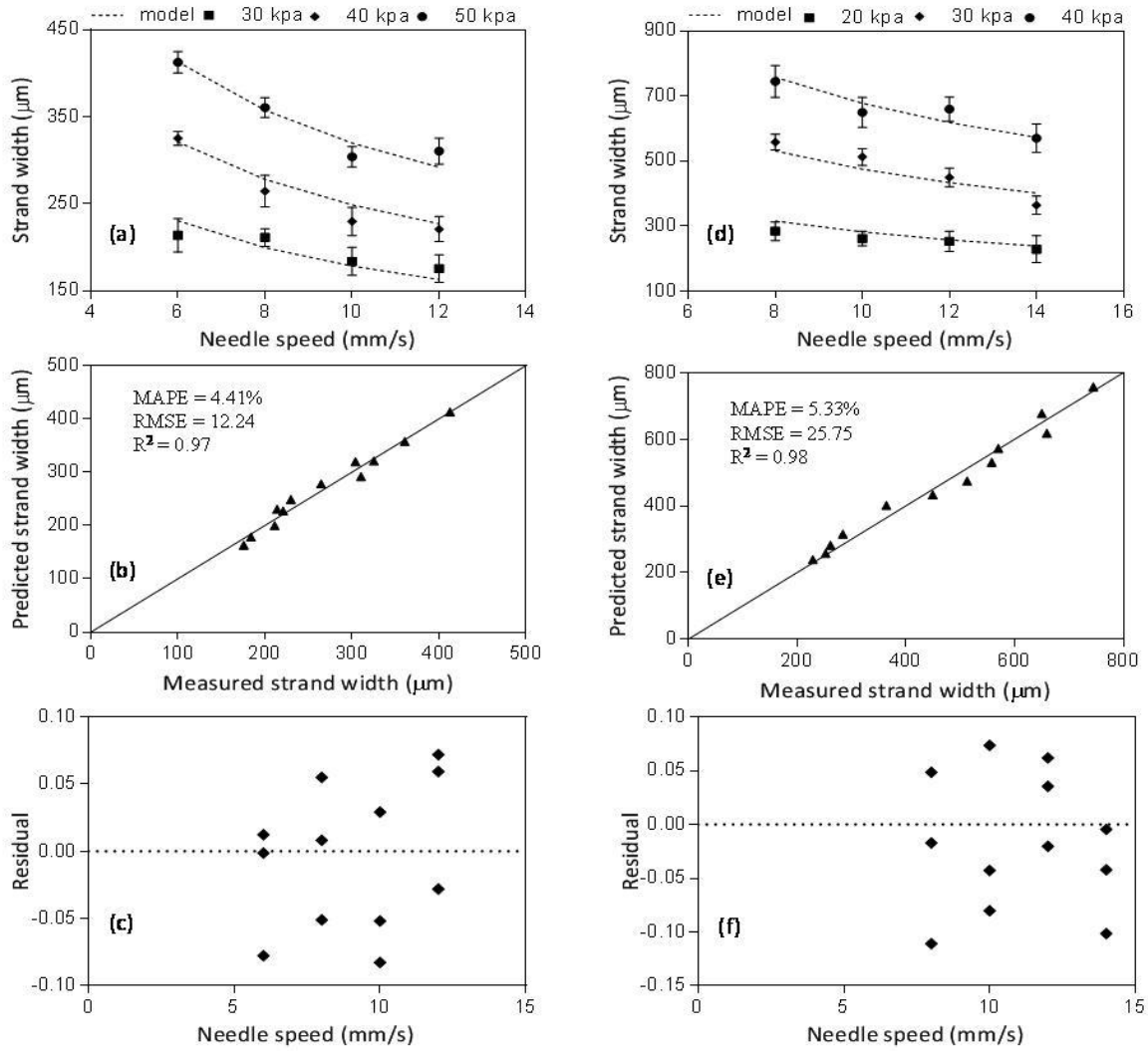
Fig. 3.10 Bioplotter printed versus model-predicted strand width (with slip) for a tapered dispensing needle (0.2mm exit diameter) at different dispensing pressures (20, 30, 40, and 50 kPa), needle speeds (6, 8, 10, 12, and 14 mm/s), and alginate concentrations of (a) 4% and (d) 3% (w/v); comparison plot (with diagonal line of equality) of measured and predicted strand width data for alginate concentrations of (b) 4% and (e) 3% (w/v); and distribution of residual prediction errors of strand width data for alginate concentrations of (c) 4% and (f) 3% (w/v). Experimental data are statistically significant for same needle speed and different dispensing pressures (n = 3; $p_b < 0.05$).

3.5.4 Combined effect of needle diameter and temperature on flow rate

In real applications, various dispensing pressures, needle diameters, and temperatures are used for the biofabrication of alginate scaffolds with rapid prototyping techniques. In this study, two different dispensing pressures (20 and 30 kPa) were maintained to study the flow rate of alginate under the collective influence of various needle diameters (0.2, 0.25, 0.41, and 0.61 mm) and temperatures (25, 35, 45, and 55 °C).

Good agreement between model predictions and experimental data was observed for dispensing pressures of 20 and 30 kPa (Table 3.5). However, model prediction is more accurate at a dispensing pressure of 20 kPa ($R^2 = 0.99$, MAPE = 11.61%) versus 30 kPa ($R^2 = 0.98$, MAPE = 12.35%) (Figs. 3.11 (b) and 3.11 (e)). The residuals demonstrate a random distribution pattern representative of an unbiased predictability of the flow rate model equation (Figs. 3.11 (c) and 3.11 (f)). At the same dispensing temperature and pressure, alginate flow rate increases with increasing needle diameter. At the same needle diameter and dispensing pressure, flow rate increases with temperature. The higher temperatures (35, 45, and 55 °C) and dispensing pressure (30 kPa) cause more deviations between model predictions and measured data compared to the lower temperature (25 °C) and dispensing pressure (20 kPa) (Figs. 3.11 (a) and 3.11 (d)). The deviations between model predictions and experimental results at different needle diameters and operating temperatures could be due to the combined effect of various considerations. For example, wall slip could take place in the cone and plate rheometric arrangement during alginate viscosity measurements [48, 49]. Because the flow behavior model was developed without considering the effect of wall slip in the rheometer, the predicted flow behavior parameters (K, τ_0, and n) would introduce error into the flow rate model. Further, the increase of needle diameter and wall shear stress results in reduced slip flow for the shear-thinning (yield pseudoplastic) fluid (alginate), and thus influences the deviations between experimental results and model predictions [48,50]. Errors were also introduced into the flow rate model predictions because surface parameters of the needle (e.g., polarity, electric charge, wettability, and roughness), which affect wall slip [48, 51], were not considered. Consequently, the error in the slip flow model further increases the uncertainty and difficulties in the prediction of total flow rate, as wall slip augments turbulence and instabilities in the fluid flow through the dispensing needle [52].
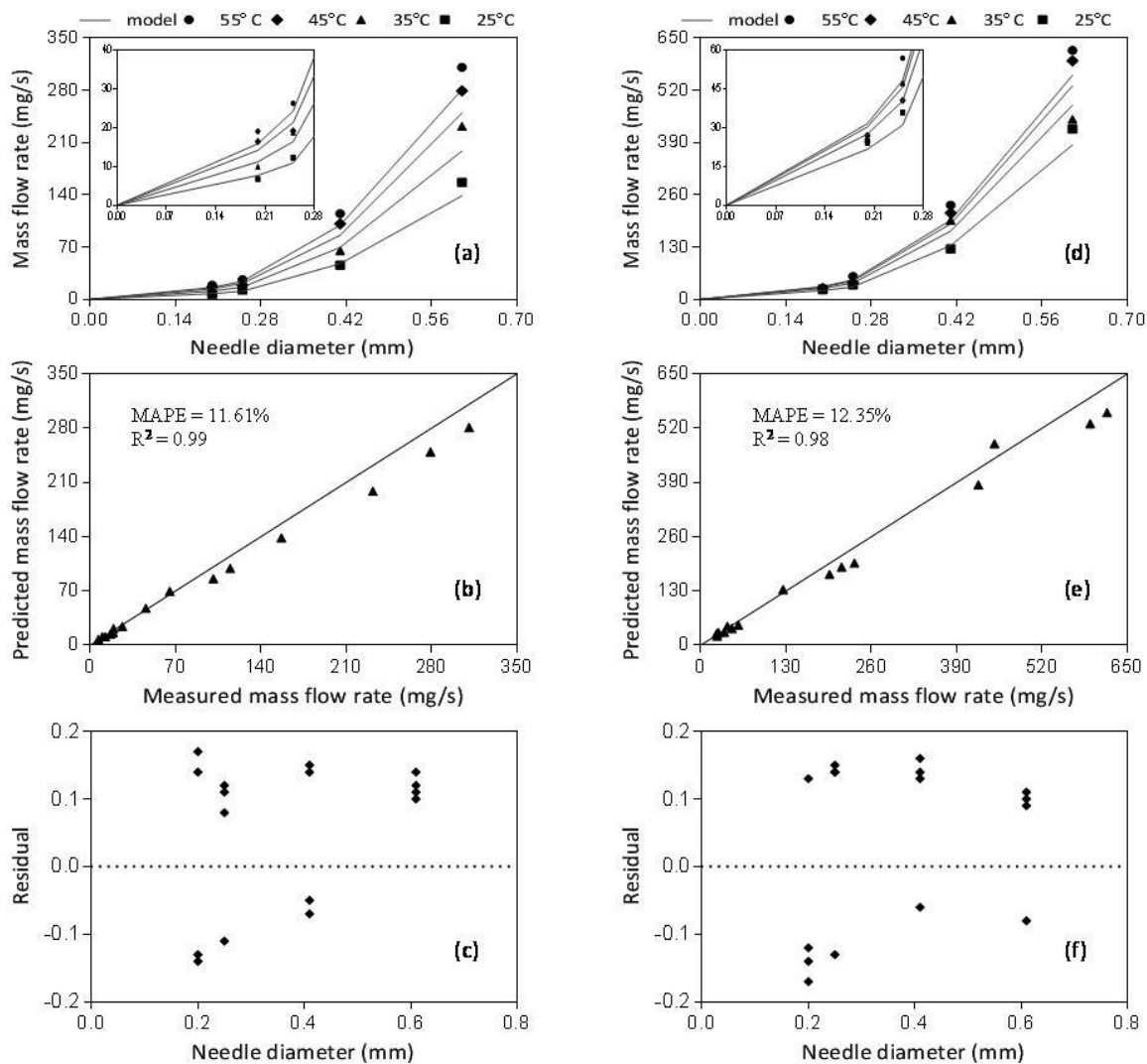
Fig. 3.11 Model-predicted versus experimental mass flow rate of alginate (2% w/v) through a tapered needle with varying exit diameters (0.2, 0.25, 0.41, and 0.61mm) at different temperatures (25, 35, 45, and 55 °C) and dispensing pressures of (a) 20 and (d) 30 kPa; comparison (with diagonal line of equality) of measured and predicted flow rates at dispensing pressures of (b) 20 and (e) 30 kPa; and distribution of residual prediction errors of flow rates at dispensing pressures of (c) 20 and (f) 30kPa

3.6 Conclusions

The present study developed model equations to predict the flow behavior and flow rate of alginate for 3D bioplotting. Experimental rheological data for alginate (1–4%) at four different temperatures (25, 35, 45, and 55 °C) were presented. Experiments to characterize the flow behavior of alginate suggest that temperature and concentration have a profound effect on the

78

consistency index, flow index, and yield stress. The model equations developed to predict flow behavior parameters at any arbitrary alginate concentration and temperature were validated against experimental values. Good agreement with experimental data indicates the ability of the model equations to predict the flow behavior of medium viscosity alginate during scaffold fabrication. Moreover, the flow rate model developed can predict the non-Newtonian flow rate of alginate from a tapered needle with remarkable accuracy and can predict the flow rate of alginate with outstanding precision under the combined effect of various needle diameters and temperatures. In addition, the assumption of the wall slip effect of alginate is reasonable because the flow behavior curve of medium viscosity alginate follows the shear-thinning (yield pseudoplastic) pattern of a Hershel–Bulkley fluid.

3.7 References

[1] den Braber ET, de Ruijter JE, Smits HT, Ginsel LA, von Recum AF, Jansen JA. Quantitative analysis of cell proliferation and orientation on substrata with uniform parallel surface micro-grooves. Biomaterials. 1996; 17:1093–9.

[2] Kruyt MC, de Bruijn JD, Wilson CE, Oner FC, van Blitterswijk CA, Verbout AJ, et al. Viable Osteogenic Cells Are Obligatory for Tissue-Engineered Ectopic Bone Formation in Goats. Tissue Eng. 2003; 9:327–36.

[3] Snyder J, Rin Son A, Hamid Q, Sun W. Fabrication of Microfluidic Manifold by Precision Extrusion Deposition and Replica Molding for Cell-Laden Device. J. Manuf. Sci. Eng. 2015; 138:041007.

[4] Wüst S, Müller R, Hofmann S. Controlled Positioning of Cells in Biomaterials—Approaches Towards 3D Tissue Printing. J. Funct. Biomater. 2011; 2:119–54.

[5] Sarker M, Chen XB, Schreyer DJ. Experimental approaches to vascularisation within tissue engineering constructs. J. Biomater. Sci. Polym. Ed. 2015; 26:683–734.

[6] Lanzotti A, Martorelli M, Staiano G. Understanding process parameter effects of reprap open-source three-dimensional printers through a design of experiments approach. J. Manuf. Sci. Eng. 2015; 137:011017.

[7] Nicodemus GD, Bryant SJ. Cell encapsulation in biodegradable hydrogels for tissue engineering applications. Tissue Eng. Part B. Rev. 2008; 14:149–65.

[8] Selmi M, Khemiri R, Echouchene F, Belmabrouk H. Enhancement of the Analyte Mass Transport in a Microfluidic Biosensor by Deformation of Fluid Flow and Electrothermal Force. J. Manuf. Sci. Eng. 2016; 138:081011.

[9] Nakamura M, Iwanaga S, Henmi C, Arai K, Nishiyama Y. Biomatrices and biomaterials for future developments of bioprinting and biofabrication. Biofabrication. 2010; 2:014110.

[10] Malda J, Visser J, Melchels FP, Jüngst T, Hennink WE, Dhert WJA, et al. 25th Anniversary Article: Engineering Hydrogels for Biofabrication. Adv. Mater. 2013; 25:5011–28.

[11] Schuurman W, Levett PA, Pot MW, van Weeren PR, Dhert WJA, Hutmacher DW, et al. Gelatin-methacrylamide hydrogels as potential biomaterials for fabrication of tissue-engineered cartilage constructs. Macromol. Biosci. 2013; 13:551–61.

[12] Jia J, Richards DJ, Pollard S, Tan Y, Rodriguez J, Visconti RP, et al. Engineering alginate as bioink for bioprinting. Acta Biomater. 2014; 10:4323–31.

[13] Rouwkema J, Rivron NC, van Blitterswijk CA. Vascularization in tissue engineering. Trends Biotechnol. 2008; 26:434–41.

[14] Murphy CM, Haugh MG, O'Brien FJ. The effect of mean pore size on cell attachment, proliferation and migration in collagen-glycosaminoglycan scaffolds for bone tissue engineering. Biomaterials. 2010; 31:461–6.

[15] Karageorgiou V, Kaplan D. Porosity of 3D biomaterial scaffolds and osteogenesis. Biomaterials. 2005; 26:5474–91.

[16] Martinez-Padilla LP, Hardy J. Quantifying thixotropy of béchamel sauce under constant shear stress by phenomenological and empirical models. J. Texture Stud. 1989; 20:71–85.

[17] Cheng DC-H, Evans F. Phenomenological characterization of the rheological behaviour of inelastic reversible thixotropic and antithixotropic fluids. Br. J. Appl. Phys. 1965; 16:1599–617.

[18] De Kee D. Flow Properties of Time-Dependent Foodstuffs. J. Rheol. (N. Y. N. Y). 1983; 27:581.

[19] Fong CFCM, Turcotte G, De Kee D. Modelling steady and transient rheological properties. J. Food Eng. 1996; 27:63–70.

[20] Taghizadeh M, Razavi SMA. Modeling Time-Independent Rheological Behavior of Pistachio Butter. Int. J. Food Prop. 2009; 12:331–40.

[21] Chen XB, Ke H. Effects of Fluid Properties on Dispensing Processes for Electronics Packaging. IEEE Trans. Electron. Packag. Manuf. 2006; 29:75–82.

[22] Tian XY, Li MG, Cao N, Li JW, Chen XB. Characterization of the flow behavior of alginate/hydroxyapatite mixtures for tissue scaffold fabrication. Biofabrication. 2009; 1:045005.

[23] Kwong CK, Bai H. Fuzzy regression approach to process modelling and optimization of epoxy dispensing. Int. J. Prod. Res. 2005; 43:2359–75.

[24] Chen XB, Zhang WJ, Schoenau G, Surgenor B. Off-line control of time-pressure dispensing processes for electronics packaging. IEEE Trans. Electron. Packag. Manuf. 2003; 26:286–93.

[25] Chen XB, Shoenau G, Zhang WJ. Modeling of time-pressure fluid dispensing processes. IEEE Trans. Electron. Packag. Manuf. 2000; 23:300–5.

[26] Razban A, Davies BL. Analytical modelling of the automated dispensing of adhesive materials. J. Adhes. Sci. Technol. 1995; 9:1435–50.

[27] Chen XB, Schoenau G, Zhang WJ. On the Flow Rate Dynamics in Time-Pressure Dispensing Processes. J. Dyn. Syst. Meas. Control. 2002; 124:693.

[28] Zhao Y-X, Li H-X, Ding H, Xiong Y-L. Integrated modelling of a time-pressure fluid dispensing system for electronics manufacturing. Int. J. Adv. Manuf. Technol. 2005; 26:1–9.

[29] Zohdi TI. On Necessary Pumping Pressures for Industrial Process-Driven Particle-Laden Fluid Flows. J. Manuf. Sci. Eng. 2015; 138:031009.

[30] Cohen Y. Apparent Slip Flow of Polymer Solutions. J. Rheol. (N. Y. N. Y). 1985; 29:67.

[31] Yilmazer U. Slip Effects in Capillary and Parallel Disk Torsional Flows of Highly Filled Suspensions. J. Rheol. (N. Y. N. Y). 1989; 33:1197.

[32] Kalyon DM. Rheological behavior of a concentrated suspension: A solid rocket fuel simulant. J. Rheol. (N. Y. N. Y). 1993; 37:35.

[33] Smay JE, Cesarano J, Lewis JA. Colloidal Inks for Directed Assembly of 3-D Periodic Structures. Langmuir. 2002; 18:5429–37.

[34] Li M, Tian X, Schreyer DJ, Chen X. Effect of needle geometry on flow rate and cell damage in the dispensing-based biofabrication process. Biotechnol. Prog. 2009; 27:1777–84.

[35] Chen XB, Li MG, Ke H. Modeling of the Flow Rate in the Dispensing-Based Process for Fabricating Tissue Scaffolds. J. Manuf. Sci. Eng. 2008; 130:021003.

[36] Kozicki W, Chou CH, Tiu C. Non-Newtonian flow in ducts of arbitrary cross-sectional shape. Chem. Eng. Sci. 1966; 21:665–79.

[37] Chang GS, Koo JS, Song KW. No Title. Wall slip vaseline steady Shear rheometry. 2003; 15:55–61.

[38] You F, Wu X, Zhu N, Lei M, Eames BF, Chen X. 3D printing of porous cell-laden hydrogel constructs for potential applications in cartilage tissue engineering. ACS Biomater. Sci. Eng. 2016; 2:1200–10.

[39] Devi DA, Smitha B, Sridhar S, Jawalkar SS, Aminabhavi TM. Novel sodium alginate/polyethyleneimine polyion complex membranes for pervaporation dehydration at the azeotropic composition of various alcohols. J. Chem. Technol. Biotechnol. 2007; 82:993–1003.

[40] Johann RM, Renaud P. Microfluidic patterning of alginate hydrogels. Biointerphases. 2007; 2:73–9.

[41] Izadifar M, Kelly ME, Haddadi A, Chen X. Optimization of nanoparticles for cardiovascular tissue engineering. Nanotechnology. 2015; 26:235301.

[42] Nichetti D, Manas-Zloczower I. Viscosity model for polydisperse polymer melts. J. Rheol. (N. Y. N. Y). 1998; 42:951.

[43] Gupta RK. Polymer and Composite Rheology, Second Edition, CRC Press. 2000;

[44] Khan AU, Briscoe BJ, Luckham PF. Evaluation of slip in capillary extrusion of ceramic pastes. J. Eur. Ceram. Soc. 2001; 21:483–91.

[45] Cogswell FN. Converging flow of polymer melts in extrusion dies. Polym. Eng. Sci. 1972; 12:64–73.

[46] Sahai N, Tewari RP. Characterization of effective mechanical strength of chitosan porous tissue scaffolds using computer aided tissue engineering. Int. J. Biomed. Eng. Sci. 2015; 2.

[47] Du Y, Ghodousi M, Qi H, Haas N, Xiao W, Khademhosseini A. Sequential assembly of cell-laden hydrogel constructs to engineer vascular-like microchannels. Biotechnol. Bioeng. 2011; 108:1693–703.

[48] Barnes HA. A review of the slip (wall depletion) of polymer solutions, emulsions and particle suspensions in viscometers: its cause, character, and cure. J. Nonnewton. Fluid Mech. 1995; 56:221–51.

[49] Franco JM, Gallegos C, Barnes HA. On slip effects in steady-state flow measurements of oil-in-water food emulsions. J. Food Eng. 1998; 36:89–102.

[50] Chen L, Duan Y, Zhao C, Yang L. Rheological behavior and wall slip of concentrated coal water slurry in pipe flows. Chem. Eng. Process. Process Intensif. 2009; 48:1241–8.

[51] Granick S, Zhu Y, Lee H. Slippery questions about complex fluids flowing past solids. Nat. Mater. 2003; 2:221–7.

[52] Graham MD. Wall slip and the nonlinear dynamics of large amplitude oscillatory shear flows. J. Rheol. (N. Y. N. Y). 1995; 39:697.

CHAPTER 4

Influence of Ionic Crosslinkers (Ca^{2+}/ Ba^{2+}/ Zn^{2+}) on the Mechanical and Biological Properties of 3D Bioplotted Hydrogel Scaffolds

This chapter has been published as "Sarker M.D., Izadifar M, Schreyer, D., and and Chen X.B. Influence of ionic crosslinkers (Ca^{2+}/ Ba^{2+}/ Zn^{2+}) on the Mechanical and Biological Properties of 3D Bioplotted Hydrogel Scaffolds. *J. Biomater. Sci. Polym. Ed.* 2018; 29: 1126-1154." According to the Copyright Agreement, "the authors retain the right to include the journal article, in full or in part, in a thesis or dissertation".

(All the experimental work was conducted by me. Izadifar M helped me to conduct compression experiements and calculaions. Professor Xiongbiao Chen and David Schreyer guided and supervised the whole research work.)

4.1 Abstract

Three dimensional (3D) bioplotting requires appropriate crosslinkers to crosslink the hydrogel precursor while simultaneously maintaining the viability of embedded cells. However, the evaluation and comparison of various types of crosslinkers in bioplotting remains underexplored to date. It was hypothesized that the mechanical strength and biological performance of medium viscosity alginate (MVSA) scaffold could be influenced by the divalent metal ions released from various ionic crosslinkers. This paper presents our study of the influence of three commonly-used ionic crosslinkers—calcium chloride (CaCl$_2$), barium chloride (BaCl$_2$), and zinc chloride (ZnCl$_2$)—on the mechanical and biological properties of 3D bioplotted alginate scaffolds. The scaffold mechanical properties characterized included the elastic modulus, swelling, and degradation while the biological properties considered included Schwann cell viability and surface morphology. The mechanical and biological properties of the bioplotted scaffolds were both dependent on the crosslinkers used for fabrication; specifically, crosslinking ions resulted in the elastic modulus of the hydrogels decreasing in the order BaCl$_2$ > CaCl$_2$ > ZnCl$_2$ over 42 days while Schwann cell viability decreased in the order CaCl$_2$ > BaCl$_2$ > ZnCl$_2$ over 7 days. Taken together, these results offer insights that are effective in terms of manipulating the 3D bioplotting process so as to tune and optimize the mechanical and biological performance of the plotted scaffolds for tissue engineering applications.

4.2 Introduction

Over the past few decades, remarkable progress has been achieved in scaffold-based tissue regeneration. The success of such scaffolds largely depends on the fabrication technique and design. Extrusion-based 3D bioplotters allow scaffolds to be printed with outstanding geometric precision compared to conventional methods [1–7]. Moreover, a large cell population can be incorporated into the scaffold to aid in tissue growth. 3D bioplotters featuring multiple nozzles further facilitate the positioning of multiple cell types layer-by-layer to mimic native tissue [1,6,8,9]. In a 3D bioplotting system, hydrogels have frequently been used due to their hydrated nature and utility for extruding cell-biopolymer mixtures [10]. In particular, fabrication of hydrogel scaffolds using a 3D bioplotter requires the simultaneous consideration of three aspects: printability, mechanical stability, and biological performance. Several hydrogel precursors have been explored to date in 3D bioplotting, including gelatin, chitosan, polyethylene glycol, fibrin, collagen, etc. [11]. In particular, sodium alginate has frequently been investigated for 3D bioplotting applications because of its availability, outstanding printability, and biocompatibility. For effective bioprinting, cells must be mixed into an alginate hydrogel precursor and the solution extruded from the bioprinter to form a hydrogel upon exposure to a crosslinker, all while maintaining cell viability within the crosslinked matrix. In this context, the crosslinker should have rapid crosslinking properties to facilitate 3D bioplotting with outstanding cell viability. Cell viability in the extrusion process depends on the printing parameters (e.g. nozzle diameter, extrusion pressure, temperature), crosslinkers (e.g. photo, ionic, enzymatic), and the properties of the hydrogel (e.g. viscosity, cytotoxicity, pH) [12–14]. Ionic crosslinkers are obviously more biocompatible compared to UV- or other cytotoxic crosslinkers (e.g., genipin, glutaraldehyde, etc.) [15,16]. In particular, alginate rapidly forms a hydrogel in the presence of divalent/trivalent cations at room temperature and mild conditions (pH~7). This property of alginate allows for the maintenance of excellent cell viability during biofabrication using an extrusion-based system [17].

Several studies have evaluated alginate microbeads crosslinked with calcium (Ca^{2+}), barium (Ba^{2+}), or zinc (Zn^{2+}) ions for their ability to promote tissue regeneration and release growth factors [18]. Ca^{2+} and Ba^{2+} ion crosslinked alginate microbeads or microparticles have also been explored for their cytocompatibility in growth factor release studies [19,20]. However, the concentration of ionic crosslinkers is a critical issue in a gelation process that requires

85

optimization to obtain enhanced cell viability. For example, excess amounts of Zn^{2+} ion provoke cytotoxicity [21] but alginate microbeads crosslinked with reasonable amount of Zn^{2+} ions improve the viability of human umbilical vein endothelial cells by releasing VEGF [22]. Besides the microbead culture, the application of ionic crosslinkers has been further extended to 3D bioprinted alginate constructs.

In *in vitro* or *in vivo* culture, the biocompatibility and mechanical properties (e.g., degradation, swelling, and elastic modulus) of bioplotted scaffold can significantly affect tissue regeneration [23]. While rapid degradation causes the loss of 3D structure and reduction in elastic modulus prior to tissue formation, non-degradable scaffolds cause inflammation and poor tissue regeneration *in vivo* [24]. Likewise, excessive swelling disrupts the harmony between native tissue and an implanted scaffold *in vivo* as a result of squeezing the surrounding healthy tissues [25]. Because uncontrolled swelling causes rapid degradation, the Young's modulus of implanted scaffolds can be significantly compromised within a short period of time. Further, if the applied compressive stress *in vivo* exceeds the elastic limit, the internal structure of the scaffold is permanently damaged. Therefore, fabricated scaffolds should have a sufficient elastic limit so as to avoid structural damage during tissue growth *in vivo*.

Several studies report that alginate hydrogels rapidly degrade *in vivo*. When alginate scaffolds were implanted in a 2-mm gap in the transected spinal cord of rodents, they degraded within 14 days and before axon regeneration [26]. However, the sequential use of dual ($CaCl_2$ and $BaCl_2$) crosslinkers for bioprinted alginate scaffolds could extend the mechanical stability from 3 d to beyond 11 d without compromising human glioma cell viability [27]. Similarly, disc-shaped alginate hydrogels crosslinked with Zn^{2+} / Ca^{2+} ions demonstrated better structural stability and water absorbency than a Ca^{2+} crosslinked alginate hydrogel [28]. Therefore, investigation of different ionic crosslinkers for hydrogel bioplotting is very important because sequential addition of various crosslinkers can simultaneously enhance mechanical stability and cell viability.

Although ionic crosslinkers are useful in alginate bioplotting, only a few studies have been conducted that investigate the mutual effect of crosslinker and hydrogel precursor percentage on the mechanical stability of alginate scaffolds over time *in vitro*. For example, a comprehensive study [29] was conducted to assess the effect of the concentration of $CaCl_2$ on the

mechanical behavior of bioplotted alginate (2% w/v) scaffolds over a 4-week period; however, the samples were incubated in distilled water instead of phosphate buffered saline (PBS), which would have simulated physiological conditions. Moreover, several studies [30–32] have evaluated the mechanical stability of bioplotted composite alginate scaffolds to inform approaches for better mechanical stability and biological performance. Their major limitation is that the non-covalently linked composite polymer (e.g., hyaluronic acid, gelatin, etc.) degrades during the incubation period and thus significantly affects the mechanical stability of the scaffolds.

In addition to mechanical properties, cell viability during the bioplotting process is a significant issue in tissue regeneration [33]. Several studies report that a large portion of the cell population experiences shear forces in the bioplotting process related to the viscosity of the alginate hydrogel which, in turn, is related to the alginate percentage in the hydrogel precursor [34,35]. Moreover, cell viability in extruded filaments is affected by the ionic crosslinker [36]. Because both the viscosity and ionic crosslinker used affect cell viability in the bioplotted scaffold, their combined effect should be considered; however, few such studies have been published.

Overall, printability, mechanical properties, and biological performance of bioplotted alginate scaffolds have not been simultaneously studied with respect to the effect of the ionic crosslinkers (Ca^{2+}/ Ba^{2+}/ Zn^{2+}) used and the percentage of alginate in the hydrogel precursor. Further, only minimal characterization of the mechanical properties (e.g., swelling, degradation, elastic modulus) of bioplotted alginate scaffolds created with an extrusion technique has been reported. This speaks to the need to perform a study to assess the influence of different ionic crosslinkers as well as alginate and crosslinker concentrations on mechanical properties of 3D-printed alginate scaffolds over time in physiologically relevant conditions. Further, because the geometrical features [37], degradation, and interconnected pores [38] play important roles in tissue regeneration, an assessment of surface morphology changes in the 3D-printed scaffold over time is also critical. Scanning electron microscopy (SEM) is frequently used to characterize and study scaffolds in nerve tissue engineering in terms of surface morphology, pore size, strand width, and pore interconnectivity [39–41]. Scaffold degradation has also been investigated with SEM imaging [42].

Here, the effects of alginate concentration (i.e. 2, 3, and 4%) and three concentrations (i.e. 50, 100, and 150 mM) of three different ionic crosslinkers (i.e. $CaCl_2$, $BaCl_2$, and $ZnCl_2$) on the physical, structural, and mechanical behavior of 3D-printed alginate scaffolds were investigated up to 42 days. A multiple regression analysis was conducted to derive predictive equations for exploring the mechanical behaviors of alginate scaffolds with respect to crosslinking conditions. The influence of these factors on Schwann cell viability in the context of 3D-bioplotted alginate scaffolds was also determined. Schwann cells were selected because they play a key role in peripheral nerve regeneration. Finally, the surface morphology of the scaffolds over 42 days of degradation *in vitro* was also assessed using SEM.

4.3 Materials and methods

Medium viscosity alginate (sodium salt from brown algae), calcium chloride, barium chloride, and zinc chloride were purchased from Sigma Aldrich (Oakville, ON, Canada). The medium viscosity alginate (product number: A2033) contained approximately 61% mannuronic (M) and 39% guluronic (G) acid for an M/G ratio of 1.56. This ratio may affect the gelling and mechanical properties of sodium alginate once crosslinked [14]. Polyethyleneimine (PEI) (MW 60,000, 50% w/w in H_2O) was purchased from Alfa Aesar (Ward Hill, MA, USA). Hoecst 33342 and propidium iodide (PI) were purchased from AnaSpec (Freemont, CA, USA). PBS (10 mM) was purchased from GE Healthcare Life Sciences (Logan, UT, USA).

4.3.1 Fabrication of 3D-bioplotted alginate scaffolds

A pneumatically controlled 3D-Bioplotter (Envisiontec GmbH, Germany) equipped with computer aided design (CAD) software was used to fabricate alginate scaffolds layer-by-layer (Figs. 4.1A-C). Medium viscosity alginate solution (4%, 3%, 2% w/v) was loaded into the material dispensing unit of the 3D bioplotter. Alginate strands were printed at a planar needle speed of 8 to 16 mm/s and pneumatic pressure of 0.1 to 0.3 bar with a taper tip dispensing needle (EFD Nordson, Westlake, OH, USA) with an extrusion diameter of 200 μm. To biofabricate alginate scaffolds with predefined dimensions (10 × 10 × 5 mm) composed of 31 successive layers, alginate precursor was dispensed into PEI-coated wells (created by incubating with 0.1% (w/v) PEI overnight at 37 °C in 5% CO_2) of a 12-well tissue culture plate (Falcon®, Corning Inc.) containing 50, 100, or 150 mM of $CaCl_2$, $BaCl_2$, or $ZnCl_2$ solution [43]. During bioprinting, the extrusion needle was kept submerged in the ionic crosslinker. The printing was conducted by

maintaining a right angle between consecutive layers of strands and a 1 to 1.5 mm interstrand distance. For each combination of alginate precursor and crosslinker concentration, at least three scaffolds were bioplotted using identical needle speeds, extrusion pressures, and temperatures.
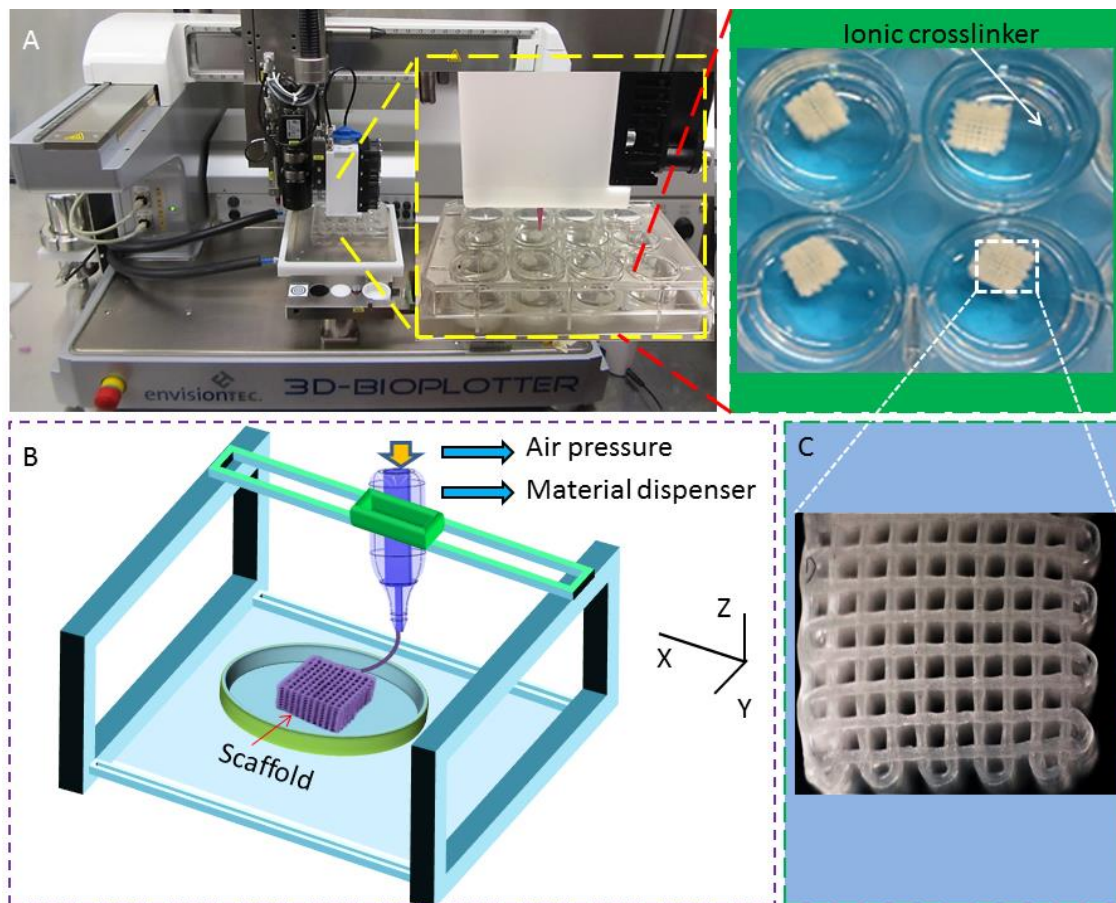
Fig. 4.1 (A) 3D bioplotting of alginate scaffold into 50 mM $CaCl_2$ solution; (B) schematic of 3D biofabrication process; and (C) stereo microscopic image of the pore structure of a scaffold bioplotted with 3% (w/v) alginate precursor in 50 mM $CaCl_2$ solution.

4.3.2 Assessment of print fidelity/ printability

The term printability indicates how close the printed scaffolds are to the intended design in terms of strand width, interstrand spacing, and pore geometry [44], which often fluctuate in practice. In 3D bioplotting, the strand width and interstrand spacing depend on the machine accuracy and properties of the hydrogel precursor. To evaluate print fidelity, scaffolds were bioplotted maintaining a given extrusion pressure (0.2 or 0.3 bar), needle speed (12 or 14 mm/s), and alginate precursor concentration (3 or 4% w/v). The expected strand width and interstrand

spacing were calculated based on the viscosity of hydrogel precursors and the printing parameters [7]. In addition to machine accuracy, ionic crosslinkers might affect the printability of a hydrogel by regulating the gelation speed of the extruded hydrogel precursor. In ideal gelation conditions, the bioplotted strands should be geometrically identical and form regular square-shaped pores if successive layers are printed maintaining a 90° angle between them. Based on the bioplotter accuracy, properties of the hydrogel precursor, and gelation speed, bioplotted strands can be under-, over-, or appropriately crosslinked in the ionic crosslinking medium. The degree of gelation can be demonstrated in terms of the printability of the alginate hydrogel, which can be calculated as per [45]:

$$\Psi = \frac{4\pi\beta}{P_r^2} \,, \tag{4.1}$$

$$P_A = \frac{\pi}{4\Psi} = \frac{P_r^2}{16\beta} \,, \tag{4.2}$$

where Ψ, β, P_r, and P_A respectively represent the circularity, area, perimeter, and printability of the bioplotted alginate strands. The printability of the 3% (w/v) hydrogel precursor was evaluated after bioplotting every 10 layers in the ionic crosslinking medium ($CaCl_2$, or $BaCl_2$, or $ZnCl_2$) at concentrations of 50, 100 and 150 mM. Images of the scaffold pores were captured with a fluorescent microscope (Carl Zeiss Axiovert 100) and a 20X *micro zoom mounted* digital camera. The images were analyzed with ImageJ software (National Institutes of Health, Bethesda, Maryland, USA) to determine the perimeter and area enclosed by a pore. A minimum of three random pores were chosen in a scaffold to characterize the printability of a given hydrogel based on Equation (4.2).

4.3.3 Degradation and swelling rate measurements

The degradation of the 3D-printed scaffolds crosslinked with 50, 100, or 150 mM $CaCl_2$, $BaCl_2$, or $ZnCl_2$ was quantified based on mass loss. The crosslinked alginate scaffolds were dipped into 3 mL of PBS solution after fabrication and their mass measured at predetermined time intervals during incubation in 10 mM PBS at 37 °C and 5% CO_2. The dry weights of the scaffolds were measured after freeze drying for 48 h after 0 (immediately after fabrication), 7, 21, and 42 d. The mass loss (M_{Loss}) (% w/w) representing the scaffold degradation was then calculated using:

$$M_{Loss} = \left(\frac{M_0 - M_t}{M_0} \right) \times 100,$$ (4.3)

where M_0 is the initial dry weight of the crosslinked scaffold (10 min in the crosslinking solution) after fabrication and M_t is the dry weight of the scaffold at the specified time intervals. Data were obtained for at least three replicates for each combination of alginate precursor concentration, crosslinker type, and crosslinker concentration.

To assess the swelling index, alginate scaffolds were immersed in 10 mM PBS solution after 3D-printing and incubated at 37 °C in 5% CO_2. At pre-determined time intervals of 0 h (immediately after fabrication), 3 h, and 1, 3, 7, and 14 d, the scaffolds were blotted to remove excess buffer using Kimwipes™ and weighed to calculate the swelling index (*SI*), defined as

$$SI = \left(\frac{W_t - W_0}{W_0} \right) \times 100,$$ (4.4)

where W_0 is the initial wet weight of the scaffold and W_t is the wet weight of the scaffold at time intervals (*t*) over 14 d. The experiments were performed in triplicate.

4.3.4 Elastic modulus testing

Compression testing was conducted on each bioplotted scaffold using a texture analyzer machine (Texture Technologies, MA, USA). Alginate precursor (2, 3, or 4% w/v) was bioplotted in the ionic crosslinker ($CaCl_2$, $BaCl_2$, or $ZnCl_2$) at concentrations of 50, 100, or 150 mM. The scaffolds were then immersed into 3 mL PBS (10 mM) solution at 37 °C in 5% CO_2 for 0, 7, 21, or 42 d. At these time points, scaffolds were removed from the 12 well plate, blotted with Kimwipes™ to eliminate excess buffer, and placed under the probe of the texture machine (Fig. 4.2). Before compression, images of the scaffolds were captured using a 20X *micro zoom mounted* digital camera to measure the dimensions (length, width, and height) with ImageJ software. During compression testing, a probe speed of 0.01 mm/s was used to compress the scaffolds to 20% of their original thickness. At least three samples were run for each combination of alginate precursor concentration, crosslinker type, and crosslinker concentration. Young's modulus was calculated from the slope of the stress versus strain curve for each scaffold in the 0-10% strain region [46].
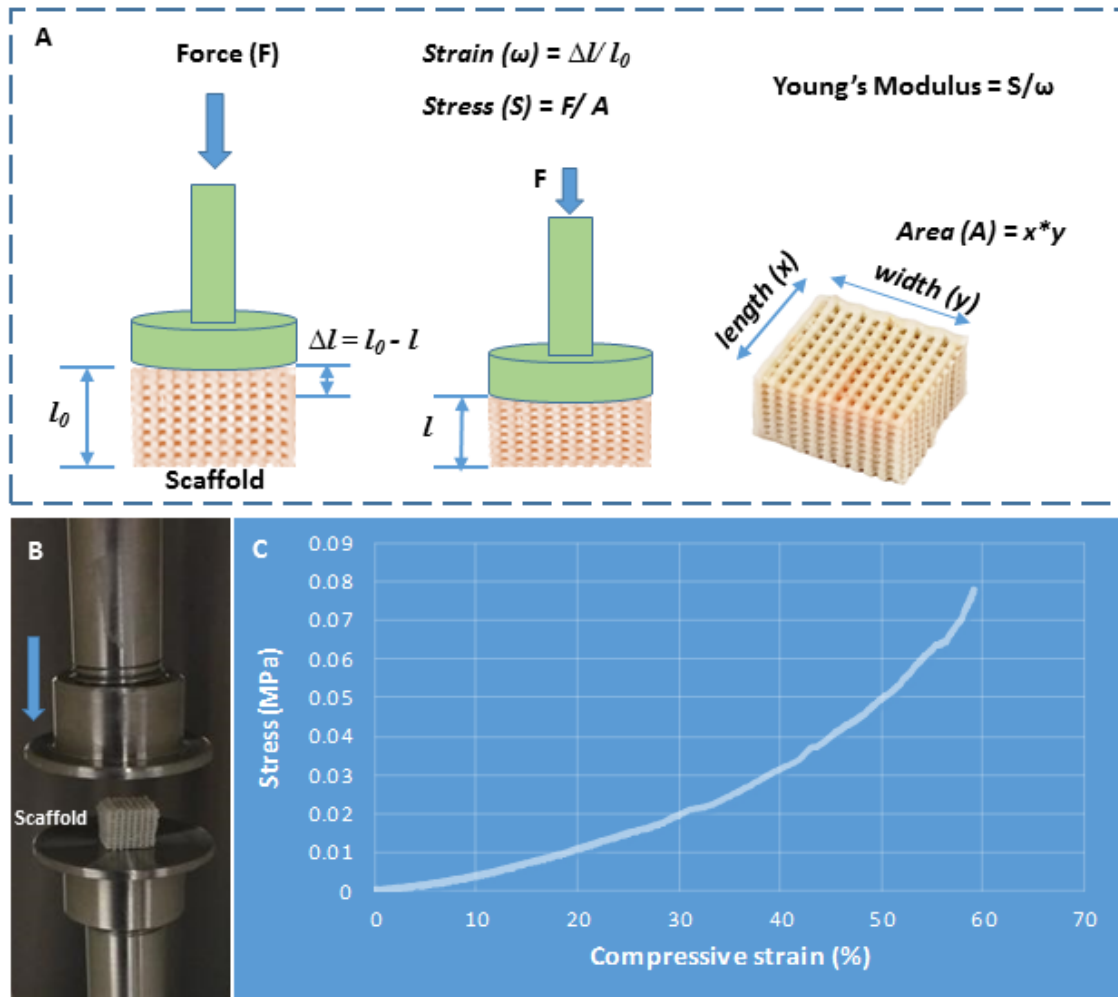
Fig. 4.2 Elastic modulus testing of alginate scaffolds: (A) schematic of experimental procedure, (B) compression probes of a texture analyzer machine, and (C) stress versus strain plot of a 3D printed alginate scaffold.

4.3.5 Biological analysis of cell-laden 3D-bioplotted scaffolds

Primary rat Schwann cells (PRSC) were used in the 3D biofabrication of alginate scaffolds. For all experiments, PRSC passage numbers were maintained between 5 and 12. The PRSCs were cultured in 10-cm tissue culture dishes containing standard Dulbecco's Modified Eagle Medium (DMEM) supplemented with 10% fetal bovine serum (FBS) (Invitrogen Co., Carlsbad, CA, USA). The culture dishes were kept in a 5% CO_2 enriched humidified incubator at 37 °C. PRSCs were cultured until 100% confluency, and then stripped with 1 mL 0.25% Trypsin/EDTA (Invitrogen) agent and suspended in 10 mL DMEM. To obtain the desired cell number per unit volume of DMEM, cell suspensions were centrifuged at 800 rpm for 5 min, counted using a

haemocytometer, and then resuspended in DMEM. To prepare the printing bioink, PRSCs were thoroughly mixed with alginate solution (prepared in Ca^{2+} free DMEM) at a density of 5×10^5 cells/mL using two syringes and a three-way stopcock.

To assess Schwann cell viability in the context of printed alginate filaments, double-layered scaffolds were printed on PEI-coated tissue culture wells. The double layers were kept in the crosslinker ($CaCl_2$, $BaCl_2$, and $ZnCl_2$) for 5 min and then washed with 10 mM PBS and DMEM to remove the excess crosslinking solution. At day 1, 4, and 7, scaffold-embedded PRSCs were stained with Hoechst 33342 (2.5 µg/mL) and propidium iodide (25 µg/mL) to count the total and dead cell populations, respectively, in the strands [47]. Images were taken from five random positions of each strand using a fluorescent microscope (Carl Zeiss Axiovert 100). ImageJ software was used to count the cells on a single projection prepared from stacking multiple images of cells captured at different planar surfaces [48]. The cell viability (*CV*, in percent) was evaluated as:

$$CV = \left(\frac{N_T - N_D}{N_T} \right) \times 100, \qquad (4.5)$$

where N_T and N_D are the total and dead cells, respectively. In all experiments, PRSC viability associated with 0.1 mg/mL poly-l-lysine (PLL)-coated plates was considered a positive control. PLL, a polycationic polymer, is often used in SC culture since PLL coated surface enhances the attachment and proliferation of SCs [49].

4.3.6 Assessments of surface morphology

The surface morphology of the degraded alginate scaffolds at different time points was studied using SEM (Hitachi SU8000, Japan). The degraded samples were first thoroughly dehydrating by freeze drying for 48 h, then placed on carbon tape attached to SEM stubs. Each sample was coated with a thin layer (10 nm) of gold (Q150T, Quorum Technologies, UK). SEM imaging was conducted at 5 kV with at least 10 images of each sample taken from random locations, and the most representative images of the surface morphology used for surface morphology assessment.

4.3.7 Derivation of multiple regression equations

Multiple regression analysis with an appropriate experimental design can be used to obtain equations that identify optimum conditions for various applications [50,51]. Multiple regression

analysis was conducted to fit regression equations to three responses (elastic modulus, degree of swelling, and degradation) as a function of three controllable factors [alginate concentration (2-4% w/v), crosslinker solution concentration (50-150 mM), and incubation time (7-42 d)]. Response variables were also measured at day 0 (after printing the scaffold) and these data included in the statistical analysis. Stepwise regression was used to select variables for inclusion in the multiple regression equations. The first order, second order, and two-factor interaction terms with significant effects (p_b-value<0.05) were included in the model. The multiple regression analysis associated with each crosslinker was performed using SPSS software (SPSS Inc., IBM).

4.3.8 Statistical analyses

An analysis of variance (ANOVA) study was carried out using SPSS and Graphpad Prism 5.0a software (GraphPad Software, San Diego, CA, USA) to identify variables significantly affecting (p_b-value < 0.05) the scaffold elastic modulus, degradation, and swelling rate as well as cell viability. Multiple regression analysis was also conducted to assess the linear, quadratic, and two-factor interaction effect of the variables on the elastic modulus and swelling of scaffolds at p_b<0.05. In addition, 'student t test' was conducted to assess the statistical significance (p_b<0.05 and p_b<0.01) of Schwann cell viability in the alginate strands crosslinked with $Ca^{2+}/Ba^{2+}/Zn^{2+}$.

4.4 Results

4.4.1 Printability/Fidelity

To quantify the printability of the alginate strands in terms of gelation efficiency, the pore shape of the bioplotted pattern was considered (Fig. 4.3B-D). In an ideal scenario, if right angles between successive layers and identical interstrand distances are assigned in the CAD program then the pores that form in the bioplotted pattern would be perfect squares (Fig. 4.3A). Experimental results show that Ca^{2+} ion crosslinked 3% (w/v) alginate strands formed square-shaped pores even after 20 consecutive layers while Ba^{2+} and Zn^{2+} ion crosslinked alginate strands generated imperfectly square-shaped pores (Figs. 4.3E-G). The printability of the alginate precursors was characterized in terms of the numerical value estimated with Equations (4.1) and (4.2). Plots of printability versus number of printed layers for the 3% alginate precursor reveal that the Ca^{2+} and Ba^{2+} ion crosslinked alginate strands have values in the region of acceptable printability (~0.9-1.1) for all concentrations of crosslinker ions considered (50-150 mM) (Figs.

4.3H-I) [45]. In contrast, Zn^{2+} crosslinked alginate strands demonstrated reasonable printability at 100 and 150 mM $ZnCl_2$ but poorer printability at 50 mM $ZnCl_2$ (Fig. 4.3J). For each concentration of $Ca^{2+}/Ba^{2+}/Zn^{2+}$ ions, the first two bioplotted layers appeared to have slightly lower printability compared to successive layers; the printability also decreased slightly after bioplotting ~20 layers of alginate strands.
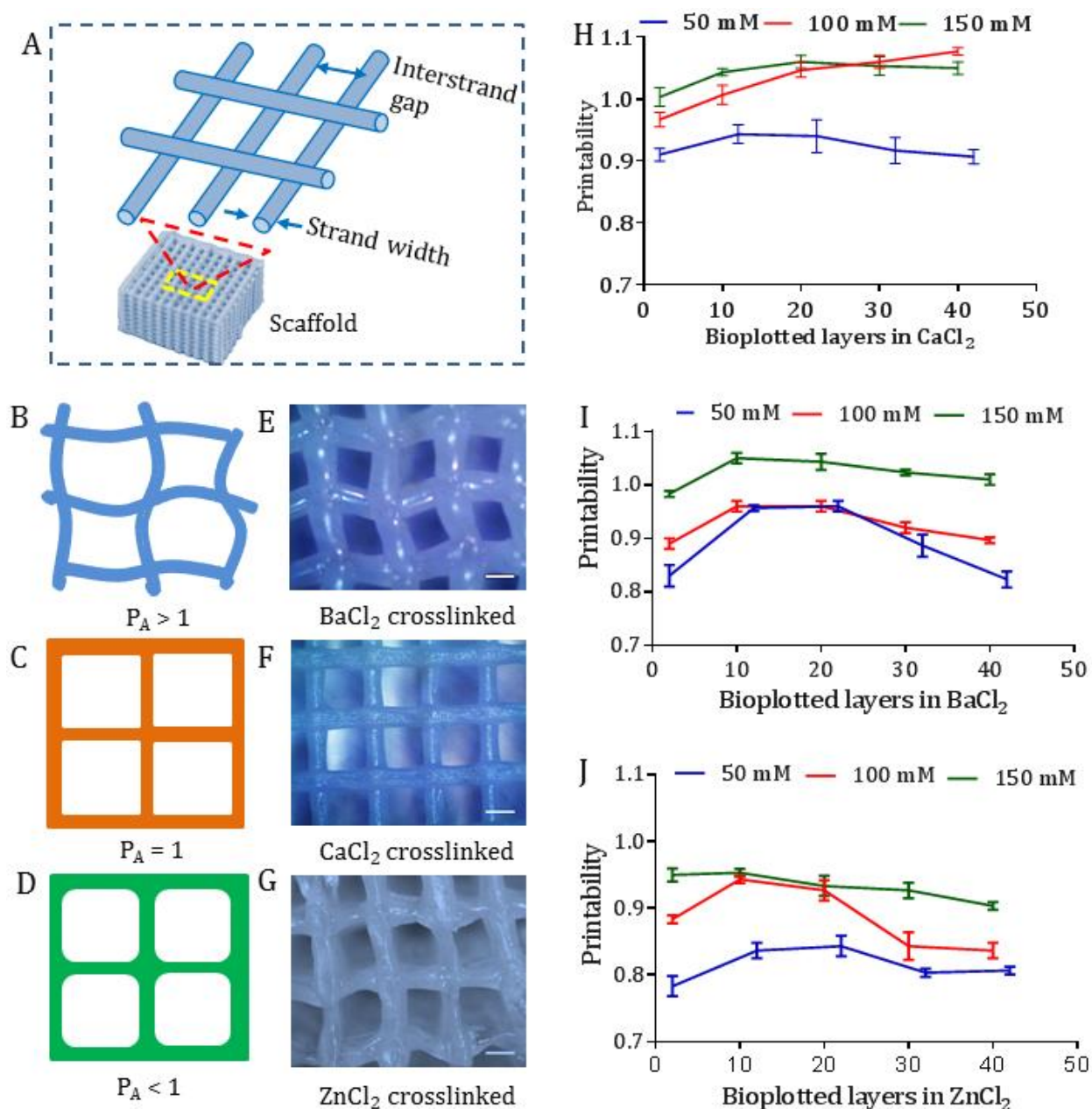
Fig. 4.3 Printability of alginate precursor in terms of gelation efficiency: (A) pore geometry of alginate scaffold; (B) over-crosslinked, (C) perfectly crosslinked, and (D) under-crosslinked

structures; top view of alginate strands bioplotted with 3% (w/v) alginate precursor into 150 mM BaCl$_2$ (E), 50 mM CaCl$_2$ (F), and 50 mM ZnCl$_2$ (G solution [scale bar = 250 µm]; and printability vs. number of printed layers for 3% (w/v) alginate precursor extruded into (H) CaCl$_2$, (I), BaCl$_2$, and (J) ZnCl$_2$ solution.

The strand widths of Ca^{2+} ion crosslinked alginate filaments bioplotted with 2-4% (w/v) hydrogel precursor were close to the predefined dimensions as per the CAD software, but the strand widths of Ba^{2+} or Zn^{2+} ion crosslinked alginate were non-uniform and varied from the predefined dimensions (Fig. 4.4A-C). The interstrand distances between the predefined geometry and bioplotted pattern for the 2% (w/v) alginate precursor in the 50 mM ionic crosslinkers (Ca^{2+}/Ba^{2+}/Zn^{2+}) were not significantly different (Fig. 4.4D). This was also the case for the Ca^{2+} ion crosslinked 3 and 4% (w/v) alginate precursor extruded strands but not those crosslinked with Ba^{2+} and Zn^{2+} ions, which featured significant non-uniformity with respect to the prescribed dimensions (Fig. 4.4E-F).
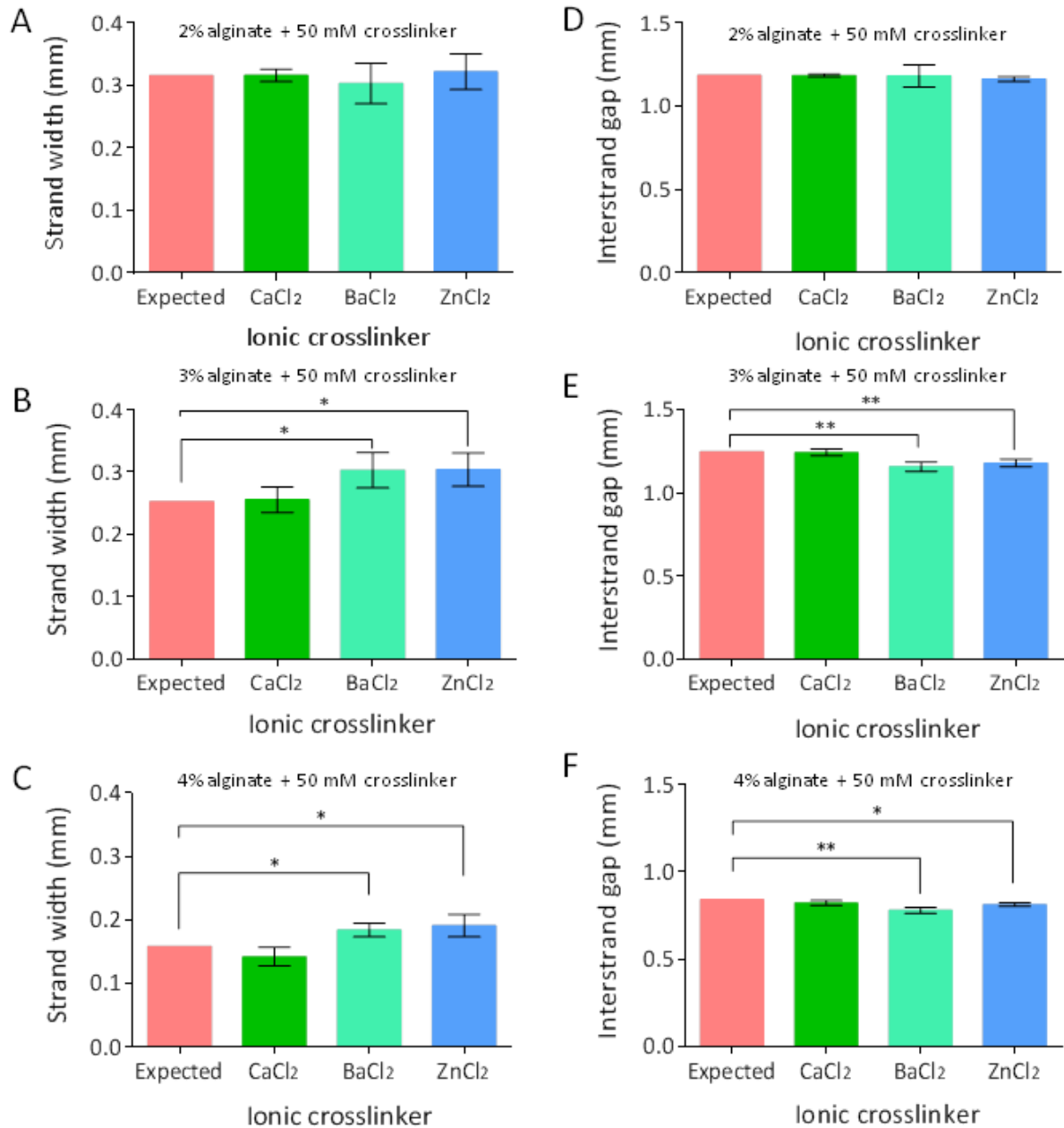
Fig. 4.4 Printability of alginate precursor in terms of strand width and interstrand gap; strand width of alginate scaffold bioplotted with (A) 2%, (B) 3%, and (C) 4% (w/v) alginate precursor [n = 3, $*p_b < 0.05$, $**p_b < 0.01$], and interstrand distance of alginate scaffolds bioplotted with (D) 2%, (E) 3%, and (F) 4% (w/v) alginate precursor [n = 3, $*p_b < 0.05$, $**p_b < 0.01$]

4.4.2 Influence of ionic crosslinkers on scaffold swelling

Images were captured on day 0 and 42 to assess swelling of the $Ca^{2+}/Ba^{2+}/Zn^{2+}$ ion crosslinked alginate scaffolds over time (Fig. 4.5CI-HIII). The day 0 scaffolds shown were crosslinked with

Ba^{2+} (Fig. 4.5CI-CIII), Ca^{2+} (Fig. 4.5EI-EIII), or Zn^{2+} (Fig. 4.5GI-GIII) ions and then incubated with 10 mM PBS. By day 42, the Ca^{2+} (Fig. 4.5FI-FIII), and Zn^{2+} (Fig. 4.5HI-HIII) ion crosslinked alginate scaffolds had notably changed dimensions due to swelling. The Ca^{2+} and Zn^{2+} ion crosslinked alginate scaffolds appeared to swell more in the PBS solution than those crosslinked with Ba^{2+} ion (Fig. 4.5DI-DIII).

Before swelling

A

SA = 4%, IC = CaCl$_2$, DI = 0 d

After swelling

Ca^{2+}

H$_2$O

Na$^+$

SA = 4%, IC = CaCl$_2$, DI = 42 d

SA = 4%, IC = CaCl$_2$, DI = 0 d   SA = 4%, IC = CaCl$_2$, DI = 42 d

BI   CI

SA = 3%, IC = CaCl$_2$, DI = 0 d   SA = 3%, IC = CaCl$_2$, DI = 42 d

BII   CII

SA = 2%, IC = CaCl$_2$, DI = 0 d   SA = 2%, IC = CaCl$_2$, DI = 42 d

BIII   CIII

SA = 4%, IC = BaCl$_2$, DI = 0 d   SA = 4%, IC = BaCl$_2$, DI = 42 d   SA = 4%, IC = ZnCl$_2$, DI = 0 d   SA = 4%, IC = ZnCl$_2$, DI = 42 d

DI   EI   FI   GI

SA = 3%, IC = BaCl$_2$, DI = 0 d   SA = 3%, IC = BaCl$_2$, DI = 42 d   SA = 3%, IC = ZnCl$_2$, DI = 0 d   SA = 3%, IC = ZnCl$_2$, DI = 42 d

DII   EII   FII   GII

SA = 2%, IC = BaCl$_2$, DI = 0 d   SA = 2%, IC = BaCl$_2$, DI = 42 d   SA = 2%, IC = ZnCl$_2$, DI = 0 d   SA = 2%, IC = ZnCl$_2$, DI = 42 d

DIII   EIII   FIII   GIII

SA = Sodium Alginate, IC = Ionic Crosslinker, DI = Days of Incubation

Fig. 4.5 Effect of various ionic crosslinkers on alginate swelling: (A) bioplotted alginate strands before and after swelling; CaCl$_2$ (50 mM) crosslinked scaffolds at day 0/42 with alginate precursor concentrations of (BI/CI) 4%, (BII/CII) 3%, and (BIII/CIII) 2% in 10 mM PBS; BaCl$_2$ (50 mM) crosslinked scaffold at day 0/42 with alginate precursor concentrations of (DI/EI) 4%,

(DII/EII) 3%, and (DIII/EIII) 2% in 10 mM PBS; and $ZnCl_2$ (50 mM) crosslinked scaffold at day 0/42 with alginate precursor concentrations of (FI/GI) 4%, (FII/GII) 3%, and (FIII/GIII) 2% in 10 mM PBS [scale bar = 5 mm].

The effect of ionic crosslinkers on scaffold swelling after immersion in 10 mM PBS solution and incubation for 2 weeks has been shown in Fig. 4.6A-C. All alginate scaffolds swelled rapidly at the start of the incubation (0-4 h) and then demonstrated little change thereafter. For the $CaCl_2$ crosslinker, the 3% (w/v) alginate precursor crosslinked with 100 mM $CaCl_2$ swelled the most, the 2% (w/v) alginate precursor crosslinked with 150 mM $CaCl_2$ the least, and the 4% (w/v) alginate precursor crosslinked with 50 mM $CaCl_2$ an intermediate amount. For the $BaCl_2$ crosslinker, the total amount of swelling was greatest in the 4% (w/v) alginate scaffold crosslinked with 100 mM $BaCl_2$, the least in the scaffold fabricated with 3% (w/v) alginate and 150 mM $BaCl_2$, and intermediate in the 2% (w/v) alginate scaffold crosslinked with 100 mM $BaCl_2$. The swelling of the 3% (w/v) alginate scaffold crosslinked with 50 mM $ZnCl_2$ and 4% (w/v) alginate scaffold crosslinked with 100 mM $ZnCl_2$ were similar after 2 days of incubation. The 2% (w/v) alginate scaffold crosslinked with 100 mM $ZnCl_2$ demonstrated the most swelling among the three combinations of alginate and $ZnCl_2$ concentration.
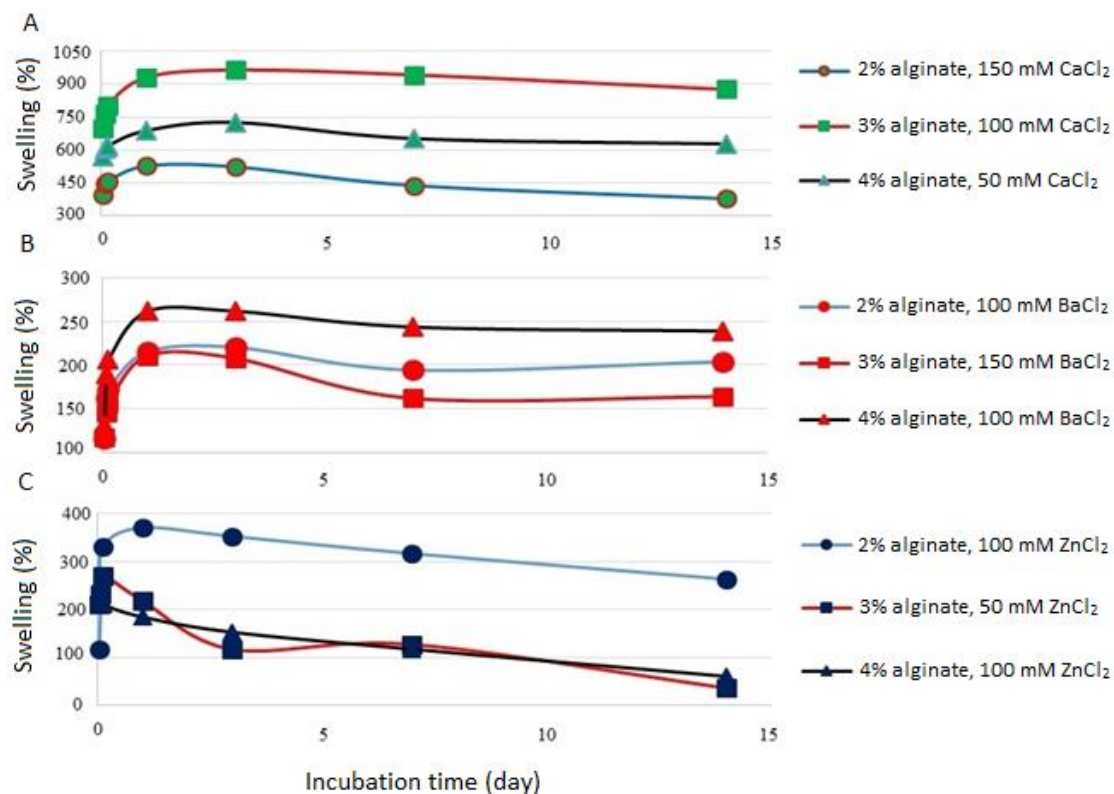
Fig. 4.6 Variation of alginate scaffold swelling (%) over 14 days of incubation at 37 °C in 10 mM PBS when (A) CaCl$_2$, (B) BaCl$_2$, or (C) ZnCl$_2$ was used as the crosslinker.

4.4.3 Influence of ionic crosslinkers on scaffold degradation

Figs. 4.7A-C are 3D representations of the cumulative degradation of alginate scaffolds crosslinked with Ca^{2+}, Ba^{2+}, or Zn^{2+} ions and incubated at 37 °C in 10 mM PBS for 42 d. Overall, scaffold degradation was significantly affected by increasing alginate and crosslinker concentrations (Fig. 4.7A-C). In particular, scaffolds fabricated from high concentration (4% w/v) alginate lost more mass per unit decrease of crosslinker concentration (Ca^{2+}/Zn^{2+}) compared to those made from low concentration (2% w/v) alginate. Such degradation was more evident in Ca^{2+}/Zn^{2+} ion crosslinked alginate scaffolds than in the Ba^{2+} ion crosslinked alginate scaffolds, which appeared less sensitive to variations in crosslinker concentration or alginate percentage. Overall, Zn^{2+} ion crosslinked alginate scaffolds showed the most degradation, Ba^{2+} ion crosslinked alginate scaffolds demonstrated the least, and Ca^{2+} ion crosslinked alginate scaffolds exhibited intermediate degradation.
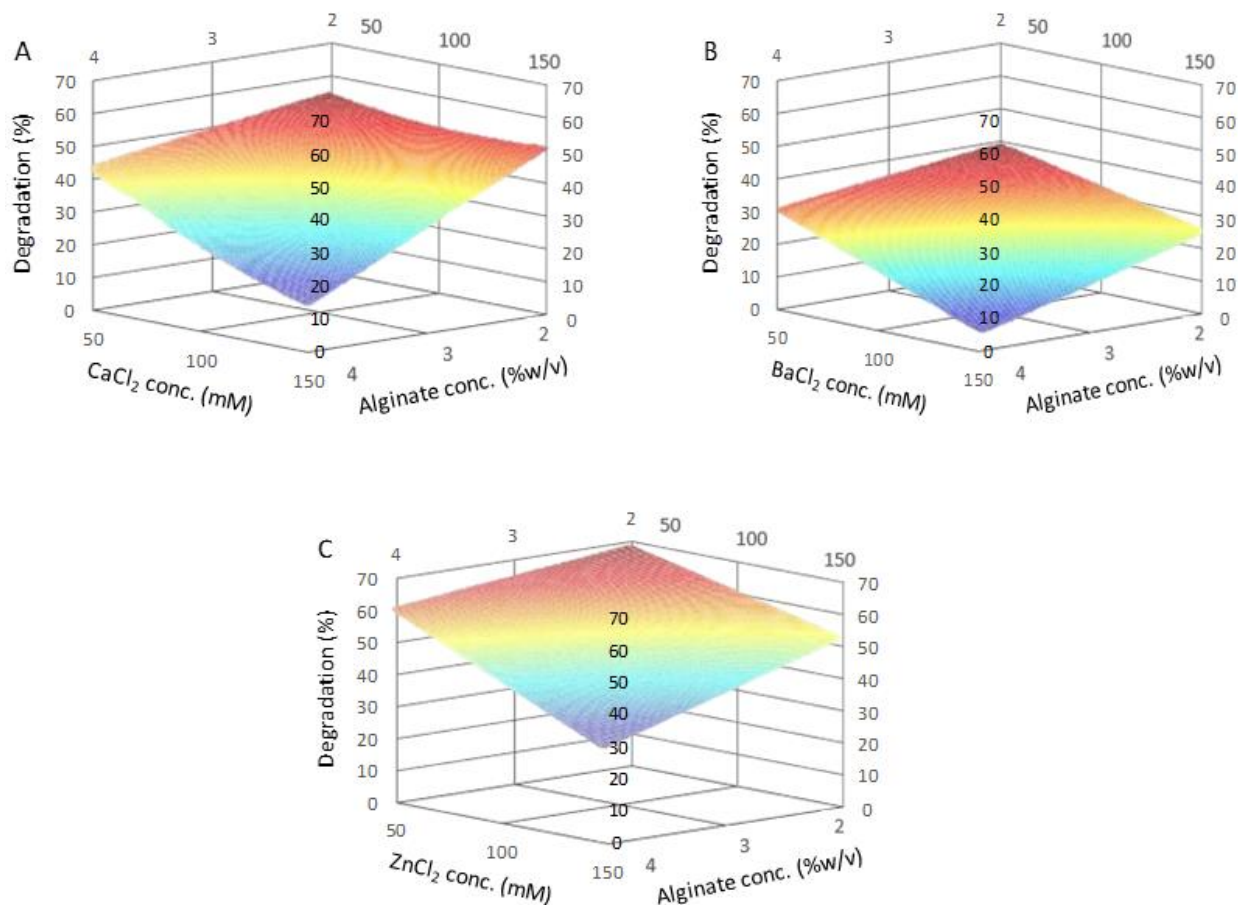
Fig. 4.7 Variation of alginate scaffold degradation (%) over 42 days of incubation at 37 °C with respect to the concentration of alginate precursor and (A) $CaCl_2$, (B) $BaCl_2$, and (C) $ZnCl_2$ solution.

4.4.4 Effects of ionic crosslinkers on mechanical strength

Figs. 4.8A-F illustrates variation of the compression elastic modulus of the alginate scaffolds with respect to alginate precursor and crosslinker concentration and incubation time for the three ionic crosslinkers considered. The compression elastic modulus of the scaffolds dramatically decreased with incubation time for all three crosslinkers but the effect of alginate precursor and crosslinker concentration varied. For scaffolds crosslinked with $CaCl_2$ (Fig. 4.8A) and $BaCl_2$ (Fig. 4.8C), decreasing the alginate precursor concentration significantly reduced the elastic modulus in the first 10-15 days of incubation in PBS; however, this effect became insignificant thereafter. In contrast, no concentration effect of hydrogel precursor on the elastic modulus of

Zn^{2+} ion crosslinked alginate scaffolds was evident (Fig. 4.8E). For the 3% alginate precursor crosslinked with lower concentrations of $CaCl_2$ (Fig. 4.8B) and $ZnCl_2$ (Fig. 4.8F), a moderate fall in the elastic modulus occurred with time; this decline was significant for $BaCl_2$, especially within the first 10-15 days (Fig. 4.8D).
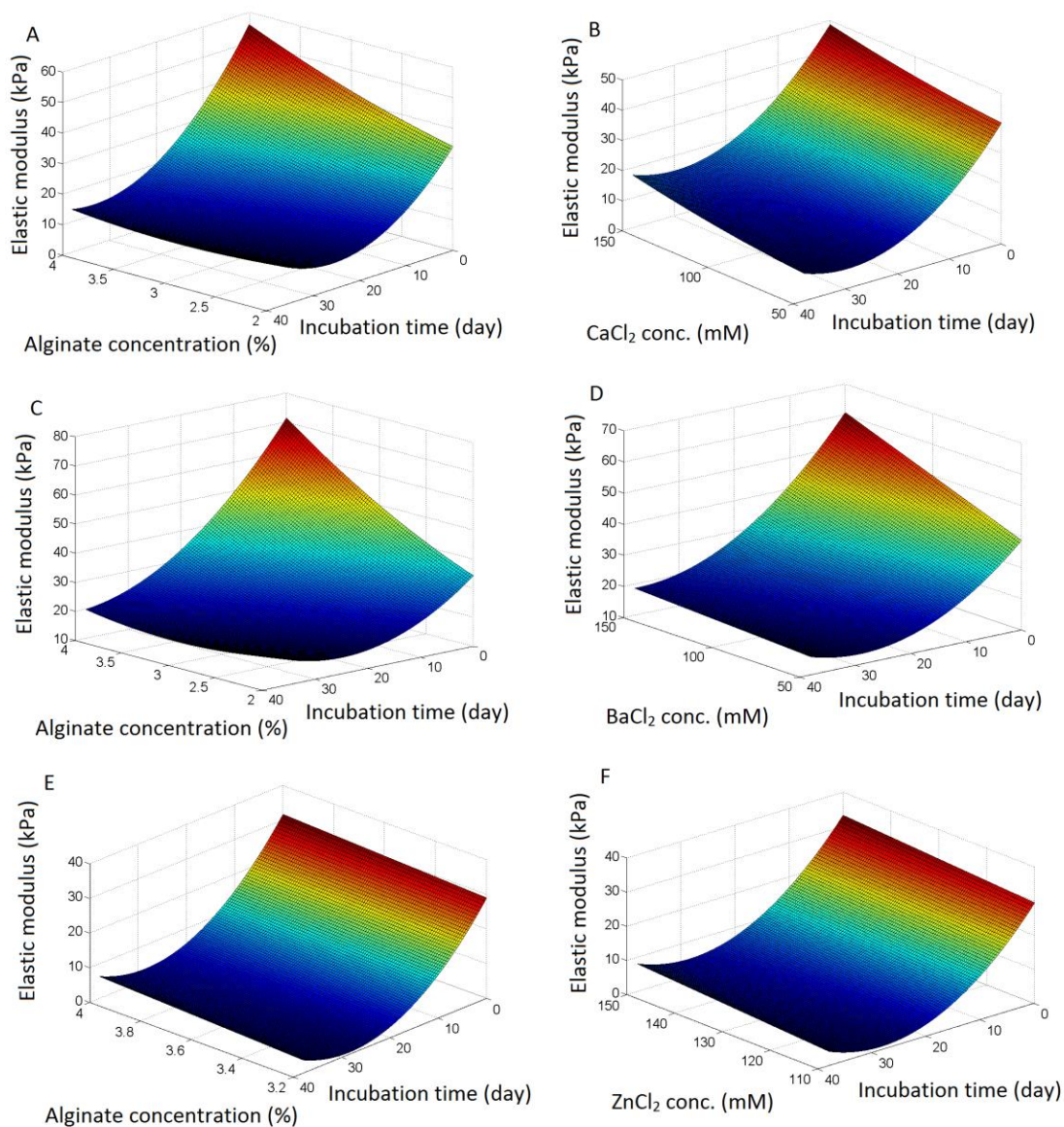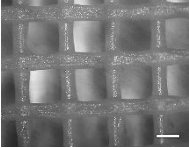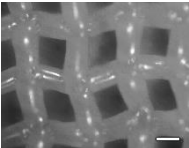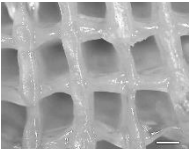
Fig. 4.8 Variation of scaffold compression elastic modulus with respect to alginate concentration, crosslinker concentration, and incubation time for crosslinking solutions containing (A, B) $CaCl_2$, (C, D) $BaCl_2$, and (E, F) $ZnCl_2$ for fixed crosslinker concentrations of 100 mM (A, C, E) and a fixed alginate concentration of 3% (w/v) (B, D, F).

4.4.5 Multiple regression analysis

Multiple regression equations were derived for the swelling, degradation, and elastic modulus of the alginate scaffolds (Table 4.1A). The swelling equation for $CaCl_2$ crosslinked alginate scaffolds features both quadratic and linear relationships to the alginate concentration, whereas the equations for $BaCl_2$ and $ZnCl_2$ crosslinked alginate scaffolds indicate a linear relationship with alginate concentration and incubation time. The swelling equation for $ZnCl_2$ crosslinked alginate scaffold also features a quadratic relationship with alginate and crosslinker concentrations. Because the multiple regression equations show good agreement with experimental values ($R^2 \sim 0.75$), the equations can be used to predict swelling in characterizing mechanical properties of alginate scaffold in a physiological environment.

Table 4.1 (A) Multiple regression equations for estimating the elastic modulus, swelling, and degradation of alginate scaffolds with respect to crosslinking variables for three ionic crosslinkers having significant effects ($p_b<0.05$); (B) summary of the crosslinking variables with significant effects on the compression elastic modulus and swelling of 3D alginate scaffold for three ionic crosslinkers.

(A)

Ionic cross-linker	Alginate scaffold	Multiple regression equations	R^2
CaCl$_2$		$S_w = 1675.34C_{Alg} - 266.49C_{Alg}^2 - 1809.63$	0.78
		$D_{Alg}^*(\%) = 66.38 - 0.13C_{Alg}C_{CaCl_2} + 0.001C_{CaCl_2}^2$	0.86
		$E_{YM}^* = 22.54 - 1.39T + 0.04T^2 + 1.82C_{Alg}^2 - 0.29C_{Alg}T + 4.19 \times 10^{-4}C_{CaCl_2}^2$	0.73
BaCl$_2$		$S_w = 147.38 + 10.69C_{Alg}T$	0.83
		$D_{Alg}^*(\%) = 44.95 - 0.06C_{Alg}C_{BaCl_2}$	0.84
		$E_{YM}^* = 3.09C_{Alg}^2 + 0.03T^2 - 0.50C_{Alg}T + 0.22C_{BaCl_2} - 0.01C_{BaCl_2}T - 0.15$	0.75
ZnCl$_2$		$S_w = 251.27 + 0.008C_{ZnCl_2}^2 - 2.74C_{Alg}T - 7.75C_{Alg}^2$	0.71
		$D_{Alg}^*(\%) = 67.11 - 0.06C_{Alg}C_{ZnCl_2} + 0.54T$	0.77
		$E_{YM}^* = 18.72 - 1.99T + 0.04T^2 + 0.03C_{Alg}C_{ZnCl_2}$	0.73

(B)

Mechanical properties	Variables	Ionic cross-linker		
		CaCl$_2$	BaCl$_2$	ZnCl$_2$
Swelling	C_{Alg}	<0.001[*, a]	0.01[*, b]	0.006[*, b]
	$C_{Cross-linker}$	0.5	0.9	0.03[*, c]
	T	0.7	0.01[*, b]	0.006[*, b]
Elastic modulus	C_{Alg}	0.534	0.538	0.675
	T	0.011[*]	0.608	<0.001[*]
	$C_{Cross-linker}$	0.908	<0.001[*]	0.750
	C_{Alg}^2	<0.001[*]	<0.001[*]	0.635
	T^2	<0.001[*]	<0.001[*]	<0.001[*]
	$C_{Cross-linker}^2$	0.033[*]	0.818	0.668
	$T \times C_{Alg}$	0.021[*]	<0.001[*]	0.394
	$T \times C_{Cross-linker}$	0.526	0.048[*]	0.218
	$C_{Alg} \times C_{Cross-linker}$	0.021[*]	0.015[*]	0.008[*]

[*] Statistically significant effect; [a] representing linear and quadratic relationship with swelling; [b] representing the effect of interaction between incubation time and alginate concentration; [c] representing quadratic relationship with swelling

The degradation of $CaCl_2$ crosslinked alginate scaffolds has a quadratic relationship with crosslinker concentration and a linear relationship with alginate and crosslinker concentrations. In contrast, the degradation equation for $BaCl_2$ crosslinked alginate scaffold features a linear relationship with alginate and crosslinker concentrations. The degradation of $ZnCl_2$ crosslinked alginate scaffolds features a linear relationship with incubation time, crosslinker concentration, and alginate concentration. The multiple regression equations presented in Table 4.1A for predicting degradation of the alginate scaffolds show good agreement with experimental values ($R^2 \sim 0.80$).

The multiple regression equations in Table 4.1A demonstrate that the elastic modulus has a linear and quadratic relationship with incubation time, and a linear relationship with the crosslinking solution concentration and/or alginate concentration or their interactions with incubation time for all crosslinker ions considered. The coefficient of determination of ~ 0.75 represents a reasonably good agreement between predicted values from equations and the measured values for the elastic modulus of the scaffolds.

Based on Fig. 4.8, multiple regression equations were developed to predict the Young's modulus of alginate scaffolds as a function of incubation time, hydrogel concentration, and crosslinker concentration. Fig. 4.9A-F illustrates the relationship between predicted and measured values of elastic modulus for the scaffolds and the distribution of residual error of prediction for the multiple regression equations given in Table 4.1A. Figs. 4.9A, C, and E indicate relatively good agreement between the experimental and predicted elastic moduli of the scaffolds, particularly below 40 kPa. For stiffer scaffolds with an elastic modulus above 55 kPa, the multiple regression equations underestimate the elastic modulus with respect to measured value. The random distribution of the prediction error, as shown in Figs. 4.9B, D, and F, represents unbiased predictability of the multiple regression equations in Table 4.1A.
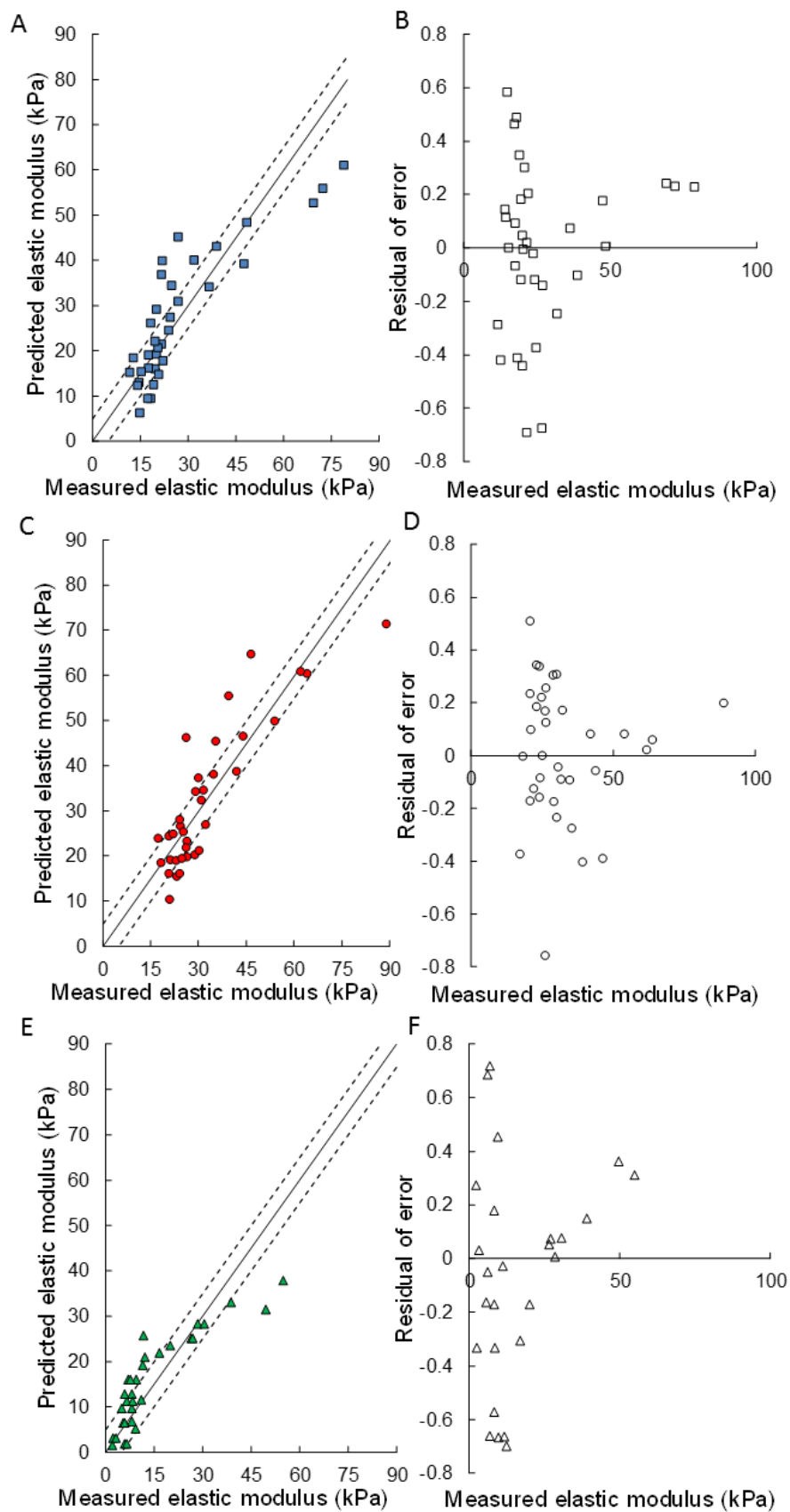
Fig. 4.9 Predictability assessment of the multiple regression equations for the 3D-printed crosslinked alginate scaffolds with respect to hydrogel and crosslinking solution variables for (A, B) $CaCl_2$, (C, D) $BaCl_2$, and (E, F) $ZnCl_2$ solutions.

Table 4.1B presents the variables involved in the hydrogel crosslinking process and their statistical significance (p_b-value) with respect to the swelling and elastic modulus (compression) of alginate hydrogels for the three ionic crosslinking solutions considered. The concentrations of alginate precursor significantly (p_b-value<0.05) affect the swelling of the alginate scaffolds crosslinked with $CaCl_2$, $BaCl_2$, or $ZnCl_2$ solutions. Notably, the incubation time of the $BaCl_2$ and $ZnCl_2$ crosslinked scaffolds significantly affects (p_b-value<0.05) the swelling of the scaffolds in PBS. In contrast, only the concentration of $ZnCl_2$ significantly (p_b-value<0.05) influences the swelling of the alginate hydrogel regardless of alginate concentration (Table 4.1B). The interaction between alginate and crosslinking agent concentrations significantly (p_b-value<0.05) affects the elastic modulus of the alginate scaffolds for $CaCl_2$, $BaCl_2$, and $ZnCl_2$. In addition, the square of the incubation time of the crosslinked hydrogel following 3D-printing has a very significant effect (p_b-value<0.001) on the compression elastic modulus. In particular, the interaction between incubation time and alginate concentration is a significant factor (p_b-value<0.05) affecting the compression elastic modulus for the $CaCl_2$ and $BaCl_2$ crosslinking solutions. Unlike the $ZnCl_2$ crosslinking solution for which alginate concentration has no significant effect on the elastic modulus, the elastic modulus is significantly influenced by the squared alginate concentration for the $CaCl_2$ and $BaCl_2$ crosslinking solutions (Table 4.1B).

4.4.6 Schwann cell viability assessments

Schwann cell viability in the double-layered alginate strands was assessed to evaluate the effect of the three divalent metal ions (Ca^{2+}/Ba^{2+}/Zn^{2+}) on cell survival over time. Fluorescent microscopy images demonstrate the highest and lowest PRSC viability in hydrogel strands printed from alginate precursors into crosslinking solutions with varied concentrations (Figs. 4.10C-N). The use of Ca^{2+} ions as a crosslinking agent resulted in the best cell viability, Zn^{2+} ions in the least, and Ba^{2+} ions in intermediate values. The lowest alginate percentage in the hydrogel precursor (2% w/v) and lowest crosslinker concentration (50 mM) resulted in the highest Schwann cell viability.
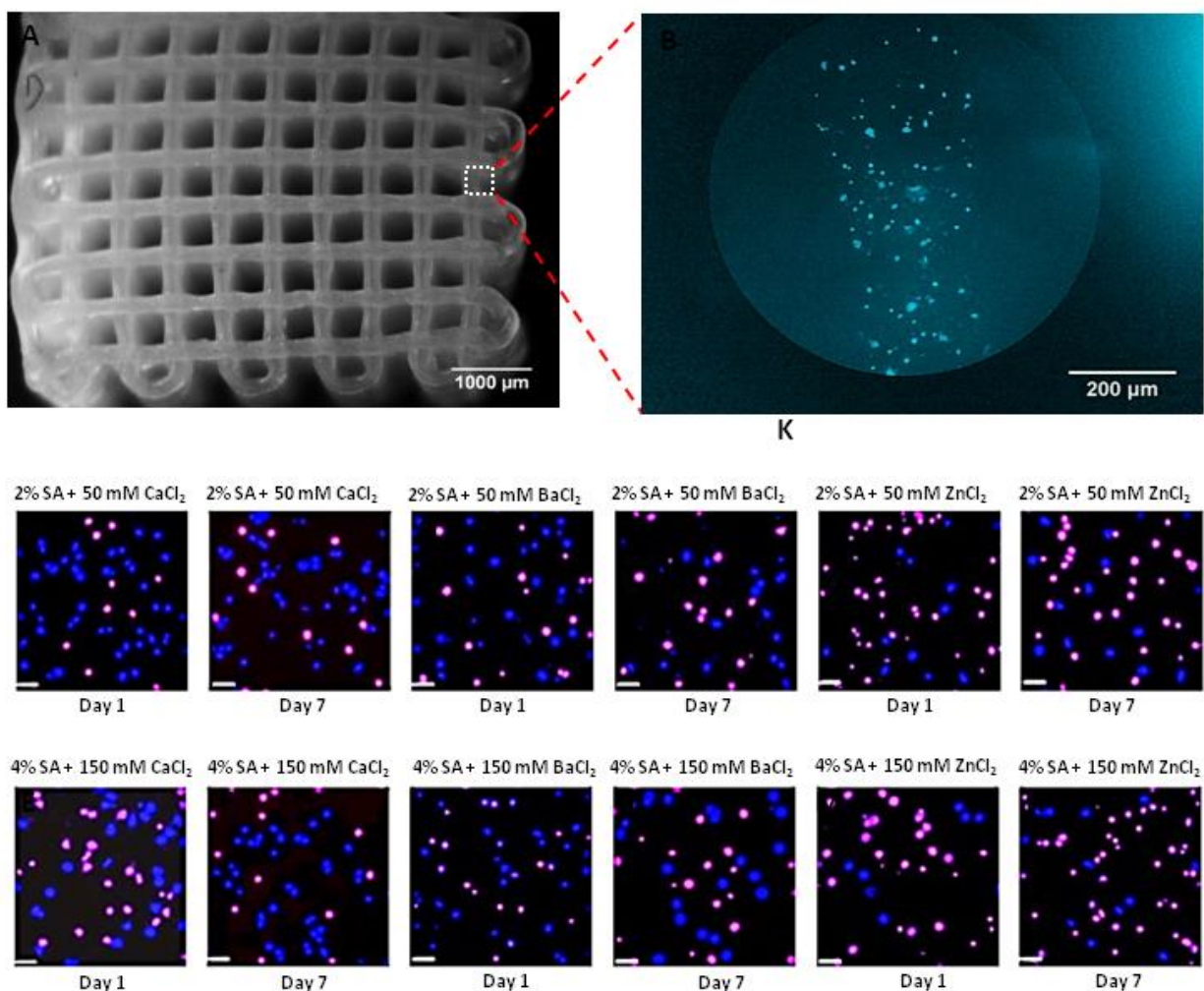
Fig. 4.10 Cell viability assessments with Hoechst 33342 and PI staining assay; (A) stereo microscopic image of bioplotted 3% (w/v) alginate precursor, (B) fluorescent image of alginate strand embedded with Schwann cells, and (C) fluorescent microscopy images representing the highest and lowest Schwann cell viability within the 2% (w/v) alginate (C, D, G, H, K, and L) strands extruded into 50 mM ionic crosslinkers and 4% (w/v) alginate (E, F, I, J, M, and N) strands dispensed into 150 mM ionic crosslinkers, respectively. Hoechst 33342 stains all Schwann cell nuclei, which appear blue in the fluorescent microscopy images, and PI stains only dead Schwann cell nuclei red; therefore, dead cells are identified as pink when both stains are present. The strands were crosslinked in $CaCl_2$ (C, D, E, and F), $BaCl_2$ (G, H, I, and J), and $ZnCl_2$ (K, L, M, and N). Cell viability results are shown for day 1 (C, E, G, I, K, and M) and day 7 (D, F, H, J, L, and N) [scale bar = 15 µm].

The viability of primary Schwann cell incorporated into the scaffolds fabricated with different alginate and crosslinker ($CaCl_2$, $BaCl_2$, and $ZnCl_2$) concentrations is shown in Fig. 4.11. Schwann cell viability declined with increasing alginate concentration for all crosslinker concentrations over the 7-day incubation period. Cell viability in the alginate strands crosslinked with $CaCl_2$ was higher or in some cases equal to that associated with $BaCl_2$ for all crosslinker concentrations (Figs. 4.11A-F); the lowest cell viability was identified in the $ZnCl_2$ crosslinked alginate strands (Figs. 4.11G-I). Scaffolds prepared from the lowest alginate precursor concentration (2% w/v) crosslinked with $CaCl_2$ demonstrated the highest cell viability (Fig. 4.11A) while those prepared from the highest (4% w/v) alginate precursor concentration crosslinked with 150 mM $ZnCl_2$ had the lowest (Fig. 4.11I).
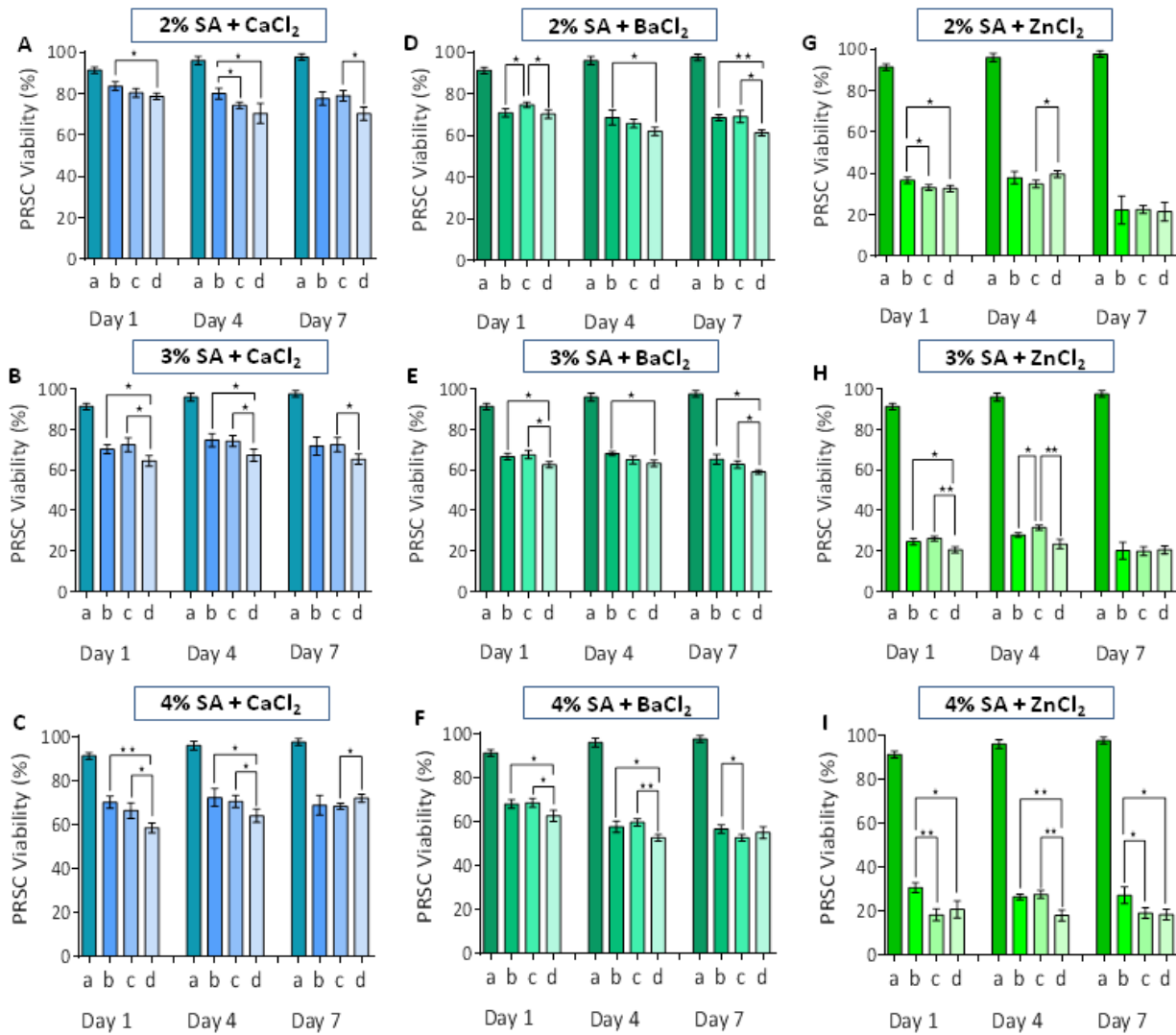
Fig. 4.11 PRSC viability in a single layered alginate pattern printed into (A-C) $CaCl_2$, (D-F) $BaCl_2$, or (G-I) $ZnCl_2$ solution. The concentration of alginate precursor was 2% (A, D, G), 3% (B, E, H), or 4% (w/v) (C, F, and I) in the bioplotted strands [n = 3, $*p_b < 0.05$, $**p_b < 0.01$].

4.4.7 Surface morphology analysis

Fig. 4.12 presents SEM images illustrating macrostructural (Figs. 12A-C) and microstructural (Figs. 4.12D-I) changes in the surface morphology of the alginate scaffolds over time. The surface morphology and structural integrity of 3% (w/v) alginate scaffolds crosslinked with 150 mM $CaCl_2$ at day 0 (before incubation; Fig. 4.12A) and at day 7 and 21 (after incubation in PBS; Figs. 4.12B and C) show that the porosity of the scaffold clearly increased with incubation time

111

due to alginate degradation. Alginate strands crosslinked with 50 mM $CaCl_2$ resulted in a more highly porous structure (Fig. 4.12D) than those crosslinked with 100 or 150 mM Ca^{2+} ions (Figs. 4.12E and F). Furthermore, the size and interconnectivity of pores significantly increased with incubation time; larger, more interconnected and exposed pores were evident at day 21 and 42 compared to day 7 (Figs. 4.12G-I). At higher crosslinker concentrations, the packing density of the alginate hydrogel is augmented and results in a tightly packed alginate matrix (Figs. 4.12D-F).
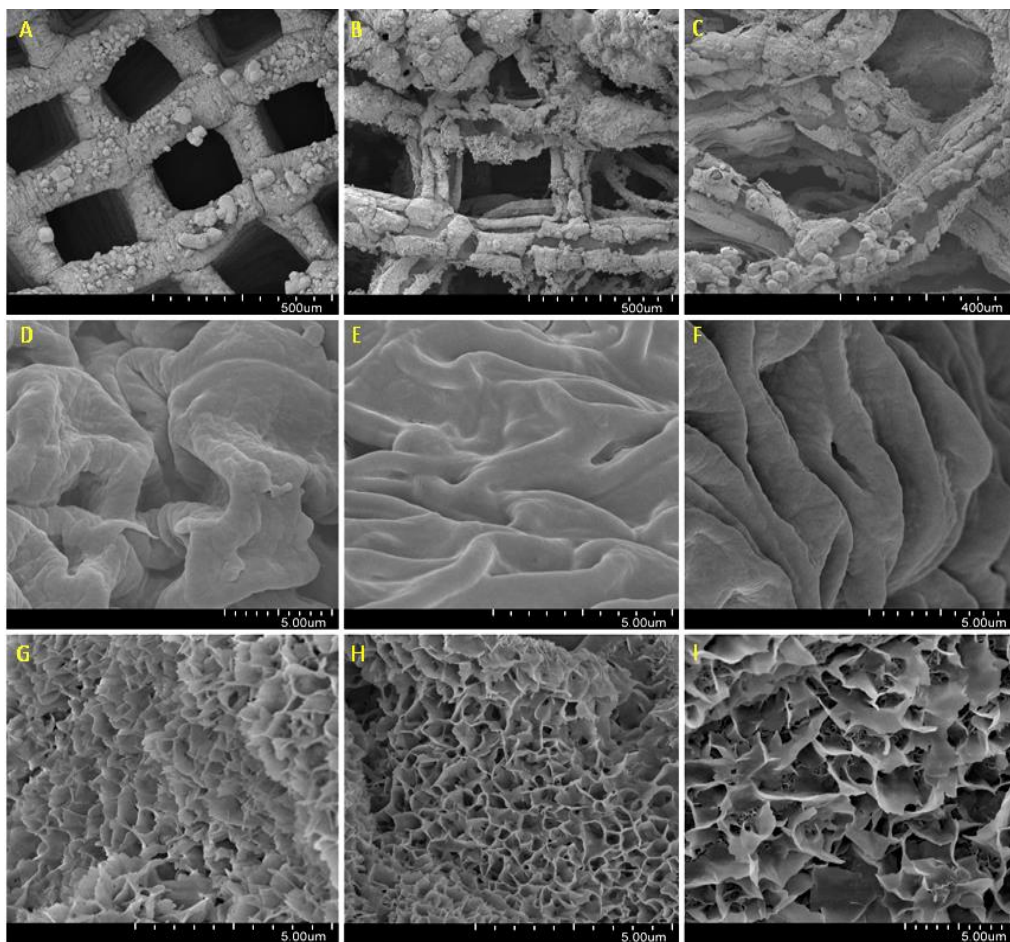
Fig. 4.12 SEM image of alginate (3% w/v) scaffolds crosslinked with 150 mM $CaCl_2$ at (A) day 0 and on (B) day 7 and (C) day 21 after incubation in 10 mM PBS [scale bar = 500 µm]; alginate scaffolds at day 0 crosslinked into (D) 50 mM, (E) 100 mM, and (F) 150 mM $CaCl_2$; and $CaCl_2$ (150 mM) crosslinked alginate scaffold incubated into 10 mM PBS at (G) day 7, (H) day 21, and (I) day 42 [scale bar = 5 µm].

4.5 Discussion

Bioplotting a 3D scaffold with a predefined architecture requires assessment of the printability of the biopolymer employed, which affects the printing resolution and geometrical accuracy. Any mismatch among bioplotting variables, biopolymer viscosity, and gelation rate might result in under- or over-gelation, non-uniform stands, and a scaffold geometry that deviates from the predefined target. Here, printability was evaluated by considering different concentrations of alginate precursor and ionic crosslinkers ($Ca^{2+}/Ba^{2+}/Zn^{2+}$). For a constant concentration of ionic crosslinkers (50 mM), the 2% alginate precursor demonstrated better printability in terms of intended strand width and interstrand gap than the 3% or 4% (w/v) alginate precursors. The poorer printability of the higher concentration precursors (i.e. 3% or 4%) is attributed to variation in the printing parameters (e.g., extrusion pressure, temperature, and needle speed), alginate viscosity, and gelation rate. For a constant alginate precursor concentration (3% w/v) and varied ionic crosslinker concentrations (50, 100, and 150 mM), Ca^{2+} and Ba^{2+} ions facilitated reasonable printability in terms of pore geometry and demonstrate their applicability in the 3D bioplotting process. Significant under-gelation was evident when 50 mM $ZnCl_2$ was employed as the precursor, with the alginate strands and building up around the intersections after bioplotting 20 successive layers (Fig. 4.3G). The slightly poorer printability noted for all crosslinkers in the first two bioprinted layers might be attributed to high surface energy caused by the flat printing surface [52]. The similar decline in printability noted after ~20 layers is attributed to the limited volume of $Ca^{2+}/Ba^{2+}/Zn^{2+}$ ions in the 12-well tissue culture plate (Figs. 4.3H-J) as discussed below.

Swelling, degradation, and elastic modulus are important mechanical properties of hydrogels that have profound effects in nerve tissue engineering. In culture, swelling affects the tissue regeneration process. While incorporated multichannels in a 3D scaffold ensure diffusional mass transfer to a larger cell population, excess swelling might inhibit the tissue growth by blocking the channels and mass transfer mechanism [38]. Upon implantation *in vivo*, the mechanical stability of scaffolds starts to decrease due to their immersion in physiological buffer and other biological activity. Therefore, scaffolds should have sufficient mechanical stability for a given period of time so that tissue regeneration can take place. Here, the Ca^{2+} ion crosslinked alginate swelled the most, Ba^{2+} crosslinked alginate the least, and the Zn^{2+} ion crosslinked alginate at intermediate levels (Figs. 4.6A-C). Because bond strength and ion diffusivity are

associated with the crosslinking plane and spatial arrangement of cations, the size and valence of cations significantly regulates the swelling behavior of alginate scaffolds [53]. The ionic radii of Ba^{2+}, Ca^{2+}, and Zn^{2+} are 1.49, 1.14 and 0.88 Å, respectively, which suggests that their bond strengths and exchange difficulty occur in the order $Ba^{2+} > Ca^{2+} > Zn^{2+}$ when ion crosslinked alginate strands are incubated in PBS. Because both bond strength and ion diffusivity determine the quantity of water uptake into divalent cation crosslinked alginate scaffolds, swelling occurs in a slightly different sequence (i.e., $Ca^{2+} > Zn^{2+} > Ba^{2+}$) (Figs. 4.6A-C). According to the bond strength, Zn^{2+} ion crosslinked alginate scaffolds should swell more than Ca^{2+} ion crosslinked alginate scaffolds; however, the Ca^{2+} ion crosslinked alginate scaffolds appear to swell more because Zn^{2+} ion crosslinked alginate scaffolds lose more mass in the incubation period.

Sodium alginate is a combination of polymannuronate and polyguluronate sequences [54]. Na^+ ions available in the PBS solution successively replace $Ca^{2+}/Ba^{2+}/Zn^{2+}$ ions bound to the $COOH^-$ groups of the polymannuronate and polyguluronate sequences of the alginate strands. As per the equations shown in Table 4.1B, alginate concentration has a significant (p-value<0.05) effect on the swelling rate of the alginate scaffolds crosslinked with the three crosslinking solutions. This is attributed to the effect of alginate concentration on the density of carboxyl groups ($COOH^-$) as well as the overall number of $Ca^{2+}/Ba^{2+}/Zn^{2+}$ ions in the alginate hydrogel. Variations in ionic density might affect the attractive forces and the ion exchange mechanism in a fixed volume of PBS. The incubation time of the $BaCl_2$ and $ZnCl_2$ (but not $CaCl_2$) crosslinked hydrogels significantly (p_b-value<0.05) affected the swelling rate of the scaffolds. This suggests that Ca^{2+} ions released from the hydrogel are replaced by surrounding Na^+ ions earlier compared to Ba^{2+} ions due to the difference in ionic radius ($Ba^{2+} > Ca^{2+}$). Zn^{2+} ions are also quickly replaced by surrounding Na^+ ions due to their small ionic radius (0.88 Å), but degradation due to ion exchange significantly affects the swelling rate. Moreover, the Zn^{2+} and Ba^{2+} ions released from alginate hydrogel might form insoluble phosphates by reacting with the PBS solution at room temperature, causing chain relaxation, water uptake, and scaffold swelling. However, Ca^{2+} ions would form partially soluble calcium phosphate; over time, free Ca^{2+} ions in the PBS solution might therefore reenter the polymer chain of alginate hydrogel [55–57]. This explains in part why the $CaCl_2$ crosslinked alginate scaffold does not swell significantly with incubation time.

Unlike $ZnCl_2$, the concentration of $CaCl_2$ or $BaCl_2$ has no significant effect on scaffold swelling. This may be because the ion exchange rate is largely dependent on the radius of crosslinked ions and the availability of Na^+ and PO_4^{3-} in the incubation medium. While a greater number of Ca^{2+} or Ba^{2+} ions in the hydrogel requires an equivalent amount of Na^+ and PO_4^{3-} ions for the ion exchange mechanism, the fixed volume (3 mL) and concentration (10 mM) of the PBS solution limits the ion exchange rate. Therefore, an increase in crosslinker ($CaCl_2$ and $BaCl_2$) concentration does not significantly affect the swelling rate. In contrast, $ZnCl_2$ crosslinked alginate underwent rapid degradation that caused significant swelling.

Moreover, higher crosslinker concentrations more effectively reduced degradation as the percentage of alginate in the hydrogels increased, particularly when Ca^{2+} and Zn^{2+} were used as the crosslinking ions. An insufficient number of $COOH^-$ ions might be available in the low concentration alginate to bond with excess Ca^{2+}/Zn^{2+} ions present in the high concentration $CaCl_2/ZnCl_2$ solution (150 mM) compared to the high concentration alginate precursor. This implies that increasing the concentration of Ca^{2+}/Zn^{2+} ions in the crosslinking media is ineffective with respect to increasing the divalent ion concentration in the molecular structure of low concentration alginate scaffolds. The high concentration alginate hydrogel might exchange more ions (Ca^{2+}/Zn^{2+}) in the PBS solution compared to the low concentration alginate hydrogel when 50-150 mM $CaCl_2/ZnCl_2$ solution is used in the gelation process. Because ion exchange is associated with polymer chain relaxation, swelling, and degradation, more mass loss per unit decrease in crosslinker concentration occurs for high concentration alginate strands crosslinked with Ca^{2+}/Zn^{2+} ions. The reduced sensitivity of degradation of scaffolds crosslinked with $BaCl_2$ is also in part attributed to the greater affinity of Ba^{2+} ions for alginate compared to Ca^{2+} or Zn^{2+} ions, as discussed above.

Furthermore, higher crosslinker concentrations increase the crosslinking density within the hydrogel, so more divalent ions are entrapped. The amount of degelation ions (Na^+) was limited in each tissue culture well due to the constant volume of PBS employed, which restricts the ion exchange mechanism in the alginate hydrogel crosslinked with higher concentration of $Ca^{2+}/Ba^{2+}/Zn^{2+}$ ions as noted above. This explains why alginate hydrogels crosslinked with 150 mM $Ca^{2+}/Ba^{2+}/Zn^{2+}$ ions show less degradation than those crosslinked with a lower concentration (50 mM) of divalent ions.

An ideal scaffold should degrade in a controlled fashion over time and simultaneously promote tissue regeneration. In general, alginate hydrogel is a soft and biocompatible material [18]. However, the degradation of alginate hydrogels can be tuned by manipulating the alginate percentage in the precursor as well as the crosslinking density. The bond strength and exchange of Ba^{2+}, Ca^{2+}, and Zn^{2+} ions follow a prescribed sequence ($Ba^{2+} > Ca^{2+} > Zn^{2+}$) when ion crosslinked alginate strands are incubated into 10 mM PBS. This sequence controls the degradation of alginate scaffolds through water uptake, polymer chain relaxation, surface erosion, and dissolution. Consequently, the alginate scaffolds considered here degrade according to the divalent cation used for crosslinking in the order $Zn^{2+} > Ca^{2+} > Ba^{2+}$. In particular, the Zn^{2+} ion crosslinked alginate hydrogel precursor underwent rapid degradation; as such, a scaffold using this crosslinking ion could cause the loss of physical cues, shape, geometry, and structural integrity over time as well as create a burst release of divalent ions.

Biomaterials used in 3D fabrication significantly affect tissue regeneration because incorporated or seeded cells can sense the mechanical properties of their surroundings [58]. In particular, the elastic modulus of biopolymers affects the differentiation, migration, and proliferation of cells [59,60]. PBS solution was used as the incubation medium in the present study for characterizing changes in the elastic modulus of alginate scaffolds over a period of 6 weeks. The elastic modulus decreased at a higher rate during the first 21 days and a slower rate thereafter, indicating that most of the ion exchange between the hydrogel and PBS took place during the first half of the experimental period. Because the scaffolds were incubated in a fixed volume of PBS, an insufficient number of Na^+ ions were available to allow further degradation after 3 weeks. However, *in vivo* renewal of physiologic buffer might result in a different trend for the elastic modulus of the alginate hydrogel [61]. All scaffolds demonstrated elastic modulus drops of ~30 to 40% within the first three weeks. This decline over time largely depends on variables including ion exchange, swelling, and degradation. Such variables are significantly affected by the affinity of divalent ions (i.e., Ba^{2+}, Ca^{2+}, and Zn^{2+}) for the alginate hydrogel.

In this study, the mechanical property (i.e. swelling, degradation, and Young's modulus) of alginate scaffolds demonstrated quadratic or linear relationship with three variables (i.e. alginate and crosslinker concentrations, and incubation time). Ideally, in a quadratic relationship with the increased value of variables, a specific mechanical property of scaffold should change

sharply for some range, and then become less responsive for other range of values of the variables. In contrast, for a linear relationship a constant change in the property is seen to take place with the increased value of variables. Unlike the linear relationship, the quadratic relationship shows the U-shaped or inverse U-shaped behavior of the material nature with respect to that particular mechanical property.

Formation of 'bands of Büngner' by Schwann cells is a prerequisite for damaged nerve regeneration [62], so the physiological conditions provided by the alginate hydrogels should include consideration of an elastic modulus sufficient to promote their formation [33]. In particular, soft alginate hydrogels have been identified as a potential biomaterial promoting vigorous neurite extension *in vitro* [63]. Moreover, neurons cultured on a soft material generate less branches compared to those cultured on a rigid material [64,65]. This suggests that both the stiff and soft properties of hydrogels are needed over time to achieve nerve regeneration. Thus, the gradual decrease in the elastic modulus of alginate hydrogels over time should be helpful for Schwann cell proliferation and axon invasion.

Calcium ions regulate the attachment, metabolism, enzyme activities, and signal transduction of neural cells [66–68]. In several studies, excellent cell viability was reported when Ca^{2+} ion crosslinked alginate was used to encapsulate the cells; however, excess Ca^{2+} ions damaged the nerve tissues [69]. Ba^{2+} ion crosslinked alginate hydrogels are more mechanically stable than Ca^{2+} ions, but long-term exposure in Ba^{2+} ions can be cytotoxic [70]. Reduced crosslinking time and Ba^{2+} ion concentration as well as thorough rinsing upon scaffold fabrication might reduce the cytotoxicity and improve cell viability. When Ba^{2+} ion crosslinked alginate microbeads were used to encapsulate Sertoli cells, excellent cell viability (90%) was observed after 9 days of encapsulation [71]. Similarly, Zn^{2+} ions crosslinked alginate hydrogel can significantly affect the bone mineralization process [72]. Reasonable cell viability was identified in the present study for the $Ca^{2+}/Ba^{2+}/Zn^{2+}$ ion crosslinked alginate strands, but optimizing the results for future applications requires the consideration of many factors.

Elevated concentrations of $Ca^{2+}/Ba^{2+}/Zn^{2+}$ ions (> 2mM) in the cytoplasm disrupts the osmotic balance (~300 mOsM) between cells and the micro milieu, and causes cell damage due to osmotic gradients [73]. In a hydrogel environment, Ca^{2+} ions remain confined and therefore do not contribute to changes in osmolality of the surrounding milieu; however, the exchange of

Ca^{2+}/Na^+ ions between the physiological buffer and the alginate hydrogel frees Ca^{2+} ions, but most react with phosphate ions (PO_4^{3-}) supplied by the PBS solution and precipitate. Minor degradation of the hydrogel scaffold might free a small number of Ca^{2+} ions, which would not be harmful to the viability of the incorporated cell population. However, intense degradation could release excess free divalent ions in a fixed volume of PBS solution. Such free divalent ions might cause cell damage due to osmotic imbalance and cytotoxicity. This phenomenon was noted in the present study for the Zn^{2+} ion in crosslinked alginate hydrogels.

In a 3D culture, cells undergo apoptosis if they lack cell-cell or cell-substrate interactions [74]. Alginate hydrogels have poor interaction with incorporated cells because no cell binding motifs are present in the molecular structure of polysaccharides   [75]. Here, the encapsulated Schwann cells demonstrated a circular morphology over the 7 days of culture period rather than an elongated morphology; as such, they failed to form any significant network with surrounding cells or the alginate substrate, which could ultimately affect their viability in a 3D scaffold. Hydrogel percentage as well as type and concentration of crosslinker affected Schwann cell viability *in vitro*, with the low percentage alginate hydrogel crosslinked with $Ca^{2+}/Ba^{2+}/Zn^{2+}$ ions demonstrating superior cell viability compared to the higher percentage alginate hydrogels. Experimental results for the elastic modulus and degradation suggest that lower alginate percentage hydrogels have inferior mechanical stability, which might facilitate Schwann cell viability through swelling and chain relaxation. In contrast, increased concentrations of divalent ions ($Ca^{2+}/Ba^{2+}/Zn^{2+}$) and/or alginate precursor enhances the crosslinking density and results in a stiffer hydrogel over the 7 days of culture period. Tightly packed hydrogels might represent a significant barrier with respect to diffusional mass (protein molecule, gas, growth factors, and metabolic waste) transfer between the incorporated cells and the culture medium, confining the cells and thus reducing cell viability. In addition, cells incorporated into the alginate hydrogel cannot proliferate and migrate concurrent with enzymatic degradation of the matrix [76]. Therefore, cells remain immobilized in their deposited position for long periods and might undergo apoptosis if an adverse environment develops. In this study, the significant drop in Schwann cell viability at higher percentages of alginate precursor in the hydrogel and higher crosslinker concentrations is attributed to the formation of stiffer hydrogels that have reduced mass diffusion. Overall, the cell viability and mechanical properties results suggest $ZnCl_2$ is a poor crosslinker with considerable cytotoxic effects in an alginate scaffold system laden with

Schwann cells, while CaCl$_2$ and BaCl$_2$ have properties that could be optimized for nerve tissue engineering applications.

SEM images were captured to study the macrostructure (500-µm scale) and microstructure (5-µm scale) of the alginate scaffolds before and after incubation in the 10 mM PBS. The macrostructure at day 0 reveals uniform geometry of the scaffold crosslinked with Ca^{2+} ions. However, scaffolds collected on day 7 and day 21 showed severe surface degradation and structural deformation due to ionic exchange between the alginate and PBS that results in polymer chain relaxation, water uptake, and swelling within the hydrogel. The scaffolds gradually degraded due to the combined effects of dissolution and bulk and surface erosion. Images captured at the 5-µm scale for alginate scaffolds crosslinked with CaCl$_2$ (50, 100, and 150 mM) illustrate how the alginate hydrogels have a more compact structure as the concentration of ionic crosslinker increases (Figs. 4.12D-F). This is attributed to the higher number of Ca^{2+} ions enhancing the attractive forces between metal ions and polymer chains and thus increasing the degree of crosslinking among polymer changes, shrinking the alginate matrix, and reducing the porosity. Notably, nano or micro pores were not identified on the surface of the alginate strands in the SEM images of scaffolds before incubation, but a large number were evident after incubation in PBS. This suggests the bulk degradation and dissolution of alginate becomes substantial over time, increasing the size and interconnectivity of pores. The major mechanism of surface and bulk degradation followed by pore formation in the alginate is the exchange of Ca^{2+}/Na$^+$ ions between the buffer (PBS) and scaffold, which causes bond relaxation between the polymer chains of the hydrogel. Indeed, calcium-sodium ion exchange at physiologically relevant conditions (PBS at 37 °C) caused significant alginate degradation and the formation of larger, more interconnected and exposed pores at day 21 and 42 compared to day 7 (Figs. 4.12G-I).

4.6 Conclusions

This study investigated the applicability of various ionic crosslinkers (CaCl$_2$, BaCl$_2$, and ZnCl$_2$) for bioplotting 3D alginate scaffolds. Bioplotting alginate strands into Ca^{2+}/Ba^{2+} crosslinker ions resulted in better printability (~0.9-1.1) than those crosslinked with Zn^{2+} ions. The mechanical (elastic modulus, swelling and degradation) and biological (cell viability) aspects of these alginate scaffolds were also explored *in vitro*. Graphical representation of the elastic modulus,

swelling, degradation, and cell viability suggests that the percentage of alginate precursor and the type and concentration of crosslinker ions have a profound effect on the mechanical stability and biological performance of the alginate constructs. Scaffolds fabricated with higher concentrations of alginate precursor and ionic crosslinkers demonstrated better mechanical stability and inferior Schwann cell viability. Moreover, SEM imagery of the surface degradation of alginate scaffolds at different time intervals demonstrates that better packing density and mechanical stability of alginate hydrogels are achieved at higher Ca^{2+} ion concentrations, with well interconnected nanopores on the bioplotted strands likely to form over time due to degradation. Scaffolds fabricated with $BaCl_2$, $CaCl_2$, and $ZnCl_2$ swell and degrade, with a concomitant decline in elastic modulus over 42 days in PBS. The mechanical performance of the bioplotted alginate scaffolds crosslinked with divalent crosslinkers declined in the order $Ba^{2+} > Ca^{2+} > Zn^{2+}$ while the biological performance declined in the order $Ca^{2+} > Ba^{2+} > Zn^{2+}$. Therefore, bioplotted alginate scaffold crosslinked with the mixture of $BaCl_2$ and $CaCl_2$ would be a prospective approach to enhance the mechanical stability and biological performance of the scaffolds *in vivo*. Such scaffolds could play a significant role in tissue regeneration applications. Multiple regression equations were generated to predict the elastic modulus, swelling, and degradation with time. Because the coefficients of determination ($R^2 \geq 0.70$) between the predicted and experimental values are quite reasonable, these equations can be used to predict the mechanical properties of alginate scaffold *in vitro* or *in vivo* in future studies.

4.7 References

[1]   Li MG, Tian XY, Chen XB. A brief review of dispensing-based rapid prototyping techniques in tissue scaffold fabrication: role of modeling on scaffold properties prediction. Biofabrication. 2009;1:32001.

[2]   Izadifar M, Chapman D, Babyn P, et al. UV-Assisted 3D Bioprinting of Nanoreinforced Hybrid Cardiac Patch for Myocardial Tissue Engineering. Tissue Eng. Part C Methods. 2017;

[3]   Izadifar Z, Chang T, Kulyk W, et al. Analyzing biological performance of 3D-printed, cell-impregnated hybrid constructs for cartilage tissue engineering. Tissue Eng. Part C Methods. 2015;22:173–188.

[4]   Izadifar M, Babyn P, Kelly ME, et al. Bioprinting Pattern-Dependent Electrical/Mechanical Behavior of Cardiac Alginate Implants: Characterization and Ex Vivo Phase-Contrast Microtomography Assessment. Tissue Eng. Part C Methods. 2017;

[5]   Olubamiji AD, Izadifar Z, Si JL, et al. Modulating mechanical behaviour of 3D-printed cartilage-mimetic PCL scaffolds: influence of molecular weight and pore geometry. Biofabrication. 2016;8:25020.

[6]   Ning LQ, Chen XB. A Brief Review of Extrusion-based Tissue Scaffold Bio-Printing. Biotechnol. J. 2017;1–47.

[7]   Sarker M, Chen XB. Modeling the Flow Behavior and Flow Rate of Medium Viscosity Alginate for Scaffold Fabrication With a Three-Dimensional Bioplotter. J. Manuf. Sci. Eng. 2017;139:081002.

[8]   Naghieh S, Badrossamay M, Foroozmehr E, et al. Combination of PLA Micro-fibers and PCL-Gelatin Nano-fibers for Development of Bone Tissue Engineering Scaffolds. Int. J. Swarm Intell. Evol. Comput. 2017;06.

[9]   Naghieh S, Reihany A, Haghighat A, et al. Fused Deposition Modeling and Fabrication of a Three-dimensional Model in Maxillofacial Reconstruction. Regen. Reconstr. Restor. 2016;1:139–144.

[10]   Naghieh S, Sarker M, Izadifar M, et al. Dispensing-based bioprinting of mechanically-functional hybrid scaffolds with vessel-like channels for tissue engineering applications – A brief review. J. Mech. Behav. Biomed. Mater. 2018;78:298–314.

[11]   Hölzl K, Lin S, Tytgat L, et al. Bioink properties before, during and after 3D bioprinting.

Biofabrication. 2016;8:32002.

[12] Tian XY, Li MG, Chen XB. Bio-rapid-prototyping of tissue engineering scaffolds and the process-induced cell damage. J. Biomimetics, Biomater. Tissue Eng. Trans Tech Publ; 2013. p. 1–23.

[13] Li M, Tian X, Zhu N, et al. Modeling process-induced cell damage in the biodispensing process. Tissue Eng. Part C Methods. 2009;16:533–542.

[14] Lee KY, Mooney DJ. Alginate: properties and biomedical applications. Prog. Polym. Sci. 2012;37:106–126.

[15] Gough JE, Scotchford CA, Downes S. Cytotoxicity of glutaraldehyde crosslinked collagen/poly (vinyl alcohol) films is by the mechanism of apoptosis. J. Biomed. Mater. Res. Part A. 2002;61:121–130.

[16] Sung H-W, Huang R-N, Huang LLH, et al. In vitro evaluation of cytotoxicity of a naturally occurring cross-linking reagent for biological tissue fixation. J. Biomater. Sci. Polym. Ed. 1999;10:63–78.

[17] Lee KY, Mooney DJ. Hydrogels for tissue engineering. Chem. Rev. 2001;101:1869–1879.

[18] Wee, Gombotz. Protein release from alginate matrices. Adv. Drug Deliv. Rev. 1998;31:267–285.

[19] Mørch YA, Donati I, Strand BL, et al. Effect of Ca2+, Ba2+, and Sr2+ on alginate microbeads. Biomacromolecules. 2006;7:1471–1480.

[20] Ghanizadeh Tabriz A, Mills CG, Mullins JJ, et al. Rapid Fabrication of Cell-Laden Alginate Hydrogel 3D Structures by Micro Dip-Coating. Front. Bioeng. Biotechnol. 2017;5.

[21] Cai L, Li X-K, Song Y, et al. Essentiality, toxicology and chelation therapy of zinc and copper. Curr. Med. Chem. 2005;12:2753–2763.

[22] Jay SM, Saltzman WM. Controlled delivery of VEGF via modulation of alginate microparticle ionic crosslinking. J. Control. Release. 2009;134:26–34.

[23] Naghieh S, Karamooz Ravari MR, Badrossamay M, et al. Numerical investigation of the mechanical properties of the additive manufactured bone scaffolds fabricated by FDM: The effect of layer penetration and post-heating. J. Mech. Behav. Biomed. Mater. 2016;59:241–250.

[24] LeRoux MA, Guilak F, Setton LA. Compressive and shear properties of alginate gel:

effects of sodium ions and alginate concentration. J. Biomed. Mater. Res. 1999;47:46–53.

[25] Wang S, Cai L. Polymer Gel Systems for Nerve Repair and Regeneration. 2010. p. 43–63. Available from: http://pubs.acs.org/doi/abs/10.1021/bk-2010-1054.ch003.

[26] Shahriari D, Koffler J, Lynam DA, et al. Characterizing the degradation of alginate hydrogel for use in multilumen scaffolds for spinal cord repair. J. Biomed. Mater. Res. Part A. 2016;104:611–619.

[27] Tabriz AG, Hermida MA, Leslie NR, et al. Three-dimensional bioprinting of complex cell laden alginate hydrogel structures. Biofabrication. 2015;7:045012.

[28] Bajpai M, Shukla P, Bajpai SK. Enhancement in the stability of alginate gels prepared with mixed solution of divalent ions using a diffusion through dialysis tube (DTDT) approach. J. Macromol. Sci. Part A. 2017;54:301–310.

[29] You F, Wu X, Zhu N, et al. 3D Printing of Porous Cell-Laden Hydrogel Constructs for Potential Applications in Cartilage Tissue Engineering. ACS Biomater. Sci. Eng. 2016;2:1200–1210.

[30] Rajaram A, Schreyer DJ, Chen DXB. Use of the polycation polyethyleneimine to improve the physical properties of alginate–hyaluronic acid hydrogel during fabrication of tissue repair scaffolds. J. Biomater. Sci. Polym. Ed. 2015;26:433–445.

[31] Rajaram A, Schreyer D, Chen D. Bioplotting alginate/hyaluronic acid hydrogel scaffolds with structural integrity and preserved schwann cell viability. 3D Print. Addit. Manuf. 2014;1:194–203.

[32] You F, Wu X, Chen X. 3D printing of porous alginate/gelatin hydrogel scaffolds and their mechanical property characterization. Int. J. Polym. Mater. Polym. Biomater. 2017;66:299–306.

[33] Ning L, Xu Y, Chen X, et al. Influence of mechanical properties of alginate-based substrates on the performance of Schwann cells in culture. J. Biomater. Sci. Polym. Ed. 2016;27:898–915.

[34] Ning L, Guillemot A, Zhao J, et al. Influence of Flow Behavior of Alginate–Cell Suspensions on Cell Viability and Proliferation. Tissue Eng. Part C Methods. 2016;22:652–662.

[35] Tian XY, Li MG, Cao N, et al. Characterization of the flow behavior of alginate/hydroxyapatite mixtures for tissue scaffold fabrication. Biofabrication.

2009;1:045005.

[36] Cao N, Chen XB, Schreyer DJ. Influence of Calcium Ions on Cell Survival and Proliferation in the Context of an Alginate Hydrogel. ISRN Chem. Eng. 2012;2012:1–9.

[37] Subramanian A, Krishnan U, Sethuraman S. Development of biomaterial scaffold for nerve tissue engineering: Biomaterial mediated neural regeneration. J. Biomed. Sci. 2009;16:108.

[38] Sarker M, Chen XB, Schreyer DJ. Experimental approaches to vascularisation within tissue engineering constructs. J. Biomater. Sci. Polym. Ed. 2015;26:683–734.

[39] Cyster LA, Grant DM, Howdle SM, et al. The influence of dispersant concentration on the pore morphology of hydroxyapatite ceramics for bone tissue engineering. Biomaterials. 2005;26:697–702.

[40] Li Z, Yubao L, Xuejiang W, et al. Studies on the porous scaffold made of the nano-HA/PA66 composite. J. Mater. Sci. 2005;40:107–110.

[41] Bhattarai N, Edmondson D, Veiseh O, et al. Electrospun chitosan-based nanofibers and their cellular compatibility. Biomaterials. 2005;26:6176–6184.

[42] Wu L, Ding J. In vitro degradation of three-dimensional porous poly(D,L-lactide-co-glycolide) scaffolds for tissue engineering. Biomaterials. 2004;25:5821–5830.

[43] Johann RM, Renaud P. Microfluidic patterning of alginate hydrogels. Biointerphases. 2007;2:73–79.

[44] Chung JHY, Naficy S, Yue Z, et al. Bio-ink properties and printability for extrusion printing living cells. Biomater. Sci. 2013;1:763–773.

[45] Ouyang L, Yao R, Zhao Y, et al. Effect of bioink properties on printability and cell viability for 3D bioplotting of embryonic stem cells. Biofabrication. 2016;8:35020.

[46] Semmling B, Nagel S, Sternberg K, et al. Long-term stable hydrogels for biorelevant dissolution testing of drug-eluting stents. J. Pharm. Technol. Drug Res. 2013;2:19.

[47] Fernandez PA, Tang DG, Cheng L, et al. Evidence that axon-derived neuregulin promotes oligodendrocyte survival in the developing rat optic nerve. Neuron. 2000;28:81–90.

[48] Cai Z, Chattopadhyay N, Liu WJ, et al. Optimized digital counting colonies of clonogenic assays using ImageJ software and customized macros: comparison with manual counting. Int. J. Radiat. Biol. 2011;87:1135–1146.

[49] Vleggeert-Lankamp CLA-M, Pêgo AP, Lakke EAJF, et al. Adhesion and proliferation of

human Schwann cells on adhesive coatings. Biomaterials. 2004;25:2741–2751.

[50] Izadifar M, Kelly ME, Haddadi A, et al. Optimization of nanoparticles for cardiovascular tissue engineering. Nanotechnology. 2015;26:235301.

[51] Kundu D, Hazra C, Chaudhari A. Statistical modeling and optimization of culture conditions by response surface methodology for 2, 4-and 2, 6-dinitrotoluene biodegradation using Rhodococcus pyridinivorans. 3 Biotech. 2016;6:1–13.

[52] Huhtamäki T, Tian X, Korhonen JT, et al. Surface-wetting characterization using contact-angle measurements. Nat. Protoc. 2018;13:1521.

[53] Bajpai SK, Sharma S. Investigation of swelling/degradation behaviour of alginate beads crosslinked with Ca^{2+} and Ba^{2+} ions. React. Funct. Polym. 2004;59:129–140.

[54] Augst AD, Kong HJ, Mooney DJ. Alginate Hydrogels as Biomaterials. Macromol. Biosci. 2006;6:623–633.

[55] Cori CF, Colowick SP, Cori GT. The isolation and synthesis of glucose-1-phosphoric acid. J. Biol. Chem. 1937;121:465–477.

[56] Walker G, Rainbow PS, Foster P, et al. Zinc phosphate granules in tissue surrounding the midgut of the barnacle Balanus balanoides. Mar. Biol. 1975;33:161–166.

[57] Barrere F, Layrolle P, Van Blitterswijk CA, et al. Biomimetic calcium phosphate coatings on Ti6Al4V: a crystal growth study of octacalcium phosphate and inhibition by Mg 2+ and HCO 3−. Bone. 1999;25:107S–111S.

[58] Discher DE, Janmey P, Wang Y-L. Tissue cells feel and respond to the stiffness of their substrate. Science. 2005;310:1139–1143.

[59] Peng X, Huang J, Deng H, et al. A multi-sphere indentation method to determine Young's modulus of soft polymeric materials based on the Johnson–Kendall–Roberts contact model. Meas. Sci. Technol. 2011;22:027003.

[60] Engler AJ, Sen S, Sweeney HL, et al. Matrix elasticity directs stem cell lineage specification. Cell. 2006;126:677–689.

[61] Hora MS, Rana RK, Nunberg JH, et al. Release of human serum albumin from poly (lactide-co-glycolide) microspheres. Pharm. Res. 1990;7:1190–1194.

[62] Faweett JW, Keynes RJ. Peripheral nerve regeneration. Annu. Rev. Neurosci. 1990;13:43–60.

[63] Matyash M, Despang F, Mandal R, et al. Novel soft alginate hydrogel strongly supports

neurite growth and protects neurons against oxidative stress. Tissue Eng. Part A. 2012;18:55–66.

[64]   Previtera ML, Langhammer CG, Firestein BL. Effects of substrate stiffness and cell density on primary hippocampal cultures. J. Biosci. Bioeng. 2010;110:459–470.

[65]   Jiang FX, Yurke B, Firestein BL, et al. Neurite outgrowth on a DNA crosslinked hydrogel with tunable stiffnesses. Ann. Biomed. Eng. 2008;36:1565–1579.

[66]   Lawler J, Weinstein R, Hynes RO. Cell attachment to thrombospondin: the role of ARG-GLY-ASP, calcium, and integrin receptors. J. Cell Biol. 1988;107:2351–2361.

[67]   Murgia M, Giorgi C, Pinton P, et al. Controlling metabolism and cell death: At the heart of mitochondrial calcium signalling. J. Mol. Cell. Cardiol. 2009;46:781–788.

[68]   Chattree V, Khanna N, Rao DN. Alterations in T cell signal transduction by M. leprae antigens is associated with downregulation of second messengers PKC, calcium, calcineurin, MAPK and various transcription factors in leprosy patients. Mol. Immunol. 2007;44:2066–2077.

[69]   Yan J-G, Agresti M, Zhang L-L, et al. Negative Effect of High Calcium Levels on Schwann Cell Survival. Neurophysiology. 2012;44:274–278.

[70]   de Vos P, Faas MM, Strand B, et al. Alginate-based microcapsules for immunoisolation of pancreatic islets. Biomaterials. 2006;27:5603–5617.

[71]   Luca G, Calvitti M, Nastruzzi C, et al. Encapsulation, in vitro characterization, and in vivo biocompatibility of Sertoli cells in alginate-based microcapsules. Tissue Eng. 2007;13:641–648.

[72]   Place ES, Rojo L, Gentleman E, et al. Strontium- and Zinc-Alginate Hydrogels for Bone Tissue Engineering. Tissue Eng. Part A. 2011;17:2713–2722.

[73]   Vest RS, Gonzales LJ, Permann SA, et al. Divalent Cations Increase Lipid Order in Erythrocytes and Susceptibility to Secretory Phospholipase A2. Biophys. J. 2004;86:2251–2260.

[74]   Wei Q, Hariharan V, Huang H. Cell-cell contact preserves cell viability via plakoglobin. PLoS One. 2011;6:e27064.

[75]   Andersen T, Auk-Emblem P, Dornish M. 3D Cell Culture in Alginate Hydrogels. Microarrays. 2015;4:133–161.

[76]   Ashton RS, Banerjee A, Punyani S, et al. Scaffolds based on degradable alginate

hydrogels and poly(lactide-co-glycolide) microspheres for stem cell culture. Biomaterials. 2007;28:5518–5525.

CHAPTER 5

Bio-Fabrication of Peptide-Modified Alginate Scaffolds: Printability, Mechanical Stability and Neurite out Growth Assessments

This chapter has been published as " MD Sarker, Saman Naghieh, Adam D McInnes, Liqun Ning, David Schreyer, and Xiongbiao Chen, Bio-fabrication of peptide-modified alginate scaffolds: Printability, mechanical stability and neurite out growth assessments. Bioprinting, 2019, e00045 (In Press)." According to the Copyright Agreement, "the authors retain the right to include the journal article, in full or in part, in a thesis or dissertation".

(All the experimental work was conducted by me. Saman Naghieh and Adam D McInnes helped me in conducting mechanical assessments, while Liqun Ning helped me in conducting DRG experiments. Adam D McInnes also helped me in English editing. Professor Xiongbiao Chen and David Schreyer guided and supervised the whole research work.)

5.1 Abstract

Peripheral nerve tissue requires appropriate biochemical and physical cues to guide the regeneration process after injury. Bioprinted peptide-conjugated sodium alginate (PCSA) scaffolds have the potential to provide physical and biochemical cues simultaneously. Such scaffolds need characterisation in terms of printability, mechanical stability, and biological performance to refine and improve application in nerve tissue regeneration. In this chapter, it was hypothesized that 3D scaffold printed with low concentrated multiple PCSA precursor would be supportive for axon outgrowth. Therefore, a 2% (w/v) alginate precursor was conjugated with either arginine-glycine-aspartate (RGD) or tyrosine-isoleucine-glycine-serine-arginine (YIGSR) peptides, or mixture of RGD and YIGSR (1:2) and was bioprinted in this study. The printability of the composite PCSA scaffolds was tested in three different concentrations of crosslinker (i.e. 50, 100, and 150 mM of $CaCl_2$), and was evaluated by measuring strand width, pore geometry, and angle-formation accuracy. Swelling, degradation, and compression experiments were conducted over a 3 week period to evaluate the mechanical stability of the composite PCSA scaffolds. Scanning electron microscopic (SEM) images were taken to study the surface morphology of the degraded scaffolds. Biological performance was assessed both for single and composite PCSA scaffolds by quantifying the viability and morphology of seeded or

incorporated Schwann cells (SCs), amount of secreted brain derived neurotrophic factor (BDNF) by incorporated SCs, and directional neurite outgrowth of neuron cells in a 2D culture. Experimental results suggest that 30 kPa extrusion pressure and 18 mm/s needle speed are suitable to fabricate composite PCSA scaffolds with reasonable strand or pore printability (~0.95-1.0), and 50 mM $CaCl_2$ facilitated better strand and pore printability than the two other concentrations. Captured SEM images demonstrate that all the composite PCSA scaffolds preserved the initial biofabricated porous structure over 3 weeks, but they lost ~70% of the initial elastic modulus. In terms of biological performance, composite PCSA scaffolds facilitated better viability and morphology of SCs, as well as supported superior directional neurite outgrowth compared to that of a single PCSA scaffolds.

5.2 Introduction

Peripheral nervous system (PNS) injuries lead to painful neuropathies, poor sensational responses, as well as reduced function in muscles and organs. Significant progress in tissue engineering research over the past decades has opened up the vast possibility to regenerate nerve tissue across a critical gap (> 2 mm) with biofabricated scaffolds [1]. In biofabrication, hydrogels, particularly sodium alginate (SA), has frequently been studied and considered as a suitable biopolymer for biocompatibility due in part to being hydrophylic [2]. However, SA lacks cell binding motifs in its molecular structure and has poor mechanical strength [3].

A number of studies investigated the printability of SA or SA composites, as well as the mechanical property (i.e. swelling, degradation, elastic modulus, etc.) of SA scaffolds incubated in DMEM or physiologic buffer over a specific time points [4–6]. Several studies have used single PCSA (i.e. RGD, YIGSR, etc.) hydrogels to investigate its biological performance in tissue regeneration [7–9]. However, studies focusing the printability of composite PCSA precursors in ionic crosslinkers and the mechanical stability of composite PCSA scaffolds remain unexplored thus far. Preparation of composite PCSA is a multistage chemical process, and there is a possibility that the chemical treatment might alter the molecular structure, orientation, and physical properties of SA. Since these properties affect the mechanical stability, viscosity, and printability of hydrogels, a systematic study is required to characterize the composite PCSA precursor for their possible application in nerve tissue regeneration.

Since Schwann cells (SCs) play a significant role in axon regeneration by upregulating numerous biochemical signals and forming 'band of Büngner', the effect of single or composite PCSA scaffolds on the biological activity of SCs needs to be evaluated. Although some studies have investigated the effect of a single PCSA hydrogel on the biological function of SCs [10], the comparative studies between a single and composite PCSA scaffolds affecting the biological activities (e.g. 3D viability, morphology, cell processes length, and growth factor secretion) of SCs remains unstudied till now. But this type of study is required to understand the effectiveness of the conjugation of multiple peptides on the molecular chain of SA for nerve tissue regeneration.

Stimulated neuron cells are more representative of *in vivo* dorsal root ganglion neurons after nerve injury compared to unstimulated neuron cells. Two-dimensional culture of stimulated neurons on PCSA strands closely simulates the *in vivo* neurite out growth through the developing growth cone. Although a number of studies have investigated neurite growth on patterned substrate [11,12], the study of stimulated neuron cell culture on a single or composite PCSA strands remains unexplored. Since nerve regeneration requires directional outgrowth of neurites, the effect of PCSA pattern on the directional growth of neurites needs to be assessed.

In this study the printability of composite peptide (i.e. RGD and YIGSR) conjugated 2% SA precursor in three different concentrations of $CaCl_2$, 50, 100, and 150 mM, were evaluated by comparing the bioprinted strand width, pore shape, and angular structure with theoretical or computer aided design (CAD) data. Mechanical stability, particularly swelling, degradation, and elastic modulus were measured by incubating the composite PCSA scaffolds in physiologic buffer (10 mM PBS) over 3 weeks. To investigate morphological changes, the degraded scaffolds were assessed by capturing SEM images. The 2D morphology of primary rat SCs (RPSCs) on RGD, YIGSR, and composite peptide-conjugated 2% SA hydrogel was studied over a 3-day culture period. The viability and morphology of RPSCs incorporated into PCSA strands was studied over a 7-day culture period. The amount of released BDNF by incorporated RPSCs in the PCSA strands over a 3-day culture period was measured using ELISA kits. To harvest stimulated neuron cells, the sciatic nerve was transected two days prior to sacrifice, and the harvested neuron cells were culture for 7 d on the PCSA strands to assess the directional neurite outgrowth.

5.3 Materials and methods

5.3.1 Materials

Medium-viscosity sodium alginate, MES buffer, NHS (N-hydroxysuccinimide), EDC (N-(3-dimethylaminopropyl)-N'-ethylcarbodiimide hydrochloride), calcium chloride (CaCl$_2$), PEI (polyethyleneimine), Tween 20, Hoechst 33342, mouse β-III tubulin and BSA (bovine serum albumin) were purchased from Sigma-Aldrich, ON, Canada. The GIBCO Life Technologies (Burlington, ON, Canada) was the supplier of calcium-free and standard DMEM media. For the immuno cytochemistry experiment, rabbit anti-S100 was purchased from Abcam (Eugene, OR, USA), whereas AF 488 anti-mouse IgG, 4', 6-diamidino-2-phenylindole (DAPI), and AF 555 anti-rabbit IgG antibodies were procured from Thermo Fisher Scientific, MA, USA. In addition, calcein-AM (1 μg/ml), propidium iodide (10 μg/ml), RGD (GGGGRGDS), and YIGSR peptides were purchased from Anaspec (Freemont, CA, USA).

5.3.2 Alginate modification

In this study, single (YIGSR or RGD) and dual peptides were linked to sodium alginate molecule using covalent chemistry reported elsewhere [13]. For single peptide conjugate reactions, 1 mg RGD or YIGSR was added to per gram alginate, while for composite peptide conjugate reactions RGD and YIGSR was added to alginate maintaining 1:2 molar ratio. The RGD peptide was reported to affect the adhesion and proliferation of PC12 cells, while the YIGSR peptide was found to regulate neuronal differentiation at an elevated density [14]. Therefore, in this thesis RGD and YIGSR peptide sequences have been covalently linked with alginate hydrogel (Fig. 5.1) maintaining a 1:2 molar ratio to enhance the axon outgrowth.
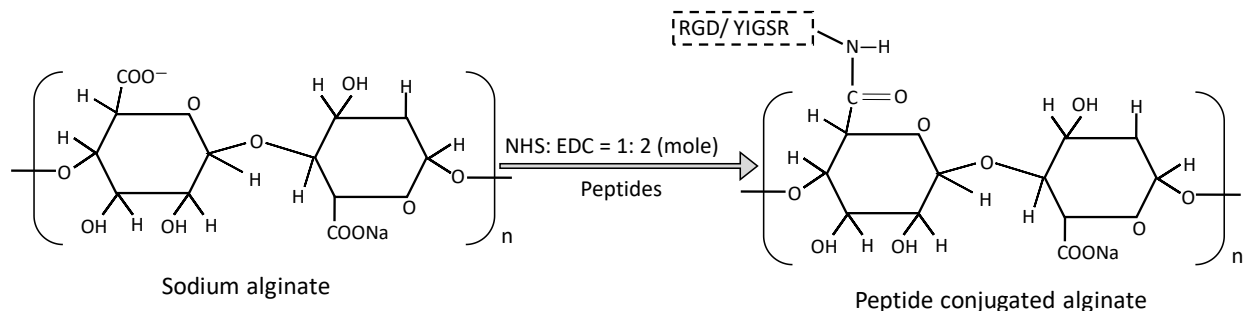
Fig. 5.1 Schematic of peptide conjugation with sodium alginate using carbodiimide chemistry

Initially, an alginate solution (1% w/v) was sterilized using 0.2 µm filter (Thermo Scientific Nalgene), and freeze dried for 48 hours. The freeze-dried alginate was dissolved in water

131

containing 0.1 M MES buffer and 0.3 M NaCl. The pH of the solution was maintained at 6.5 for optimal reaction kinetics for binding peptides to alginate molecules. Sulfo-NHS, a stabilizer for covalent reactions, was added in the solution, maintaining a ratio of 1:2 to EDC. A magnetic stirrer was used to mix the sulfo-NHS with the alginate solution for 20 minutes. EDC was added next to activate 40% of the available uronic acid residues on the alginate molecules in the solution (300 mg EDC/ g alginate), and stirred for 10 minutes. After sufficient mixing, the peptides were added to the solution, and the covalent reaction was allowed to proceed for 48 hours at 20°C under mild stirring. To eliminate the reaction by products, salt, buffer, and any unwanted molecules, the experimental solution was dialyzed with Spectra/Por dialysis tubing (MWCO 12-14000). In the dialysis process, 40 liters of deionized water was used to increase the purity of peptide-alginate conjugate over a period of 5 days. The final step was to freeze dry the dialysed solution, and resolubilize the modified alginate as required.

5.3.3 Preparation of rat primary Schwann cells (RPSCs)

To harvest RPSCs, the sciatic nerve was isolated from Sprague-Dawley rats, the epineurium was dissected off, and the denuded nerve was cut into small segments. All the surgical procedures of rodents were conducted as per the approval of the University Committee on Animal Care and Supply (University of Saskatchewan). The segments were digested in collagenase (1 μg/ml) at 37°C for 1 h, and then the digested solution was filtered to remove the ECM debris. To stimulate Schwann cell proliferation and inhibit fibroblast growth, the filtered cells were culture in Dulbecco's Modified Eagle Medium (Saint Louis, MO, USA) containing D-valine, 10% fetal bovine serum, forskolin, and bovine pituitary extract added N-2 supplement [15]. Immunofluroscent assays with S-100 and DAPI were used to evaluate the purity of the collected cells (i.e. RPSC) in culture. The cultures were incubated in a tissue culture dish (Thermo Fisher Scientific, Rochester, NY, USA) at 37 °C in a 5% CO_2-enriched humidified incubator to achieve 100% confluency.

After reaching 100% confluency, RPSCs were detached from the tissue culture plate using 1 ml 0.25% Trypsin/EDTA (Invitrogen) and suspended in 10 ml DMEM supplemented with 10% fetal bovine serum. To prepare sufficient density, the cell suspensions were transferred to 50 ml centrifuge tubes (Falcon®, Mexico) and centrifuged for 5 min at 800 rpm while maintaining 4°C. The cell pellet was resuspended in 250 µl DMEM, and the cell concentration

was determined using a haemocytometer. The cell density was adjusted by adding an appropriate amount of DMEM to achieve the desired density for 2D and 3D culture. For 2D and 3D RPSC culture, cell density was maintained as 2.5 x 10^4 cells/cm^2 and 2 x 10^5 cells/ ml hydrogel, respectively.

5.3.4 Bio-fabrication of scaffold

A pneumatic 3D Bioplotter (EnvisionTEC, Germany) was used in this study to print 2D pattern as per a predefined design. CAD software was used to develop a cuboid shape (10 mm x 10 mm x 5 mm) with 1 mm interstrand distance. To study Schwann cell viability in the bio-printed strand, double-layered grid patterns were fabricated by alternating perpendicular layers. The pattern was printed on a 12-well tissue culture using a 200 µm tapered needle. The developed flow rate model in chapter-3 was effective enough to predict the flow rate of the PCSA precursor from the extrusion needle. The needle speed and dispensing pressure were maintained as 18 mm/s and 0.3 bar, respectively, in printing alginate (2% w/v) strands. Calcium-free DMEM solution was used to prepare a 2% (w/v) solution of pure alginate or peptide conjugate alginate. To prepare alginate/cell mixture, RPSCs were trypsinized upon 100% confluency, and then thoroughly mixed with alginate (2% w/v) solution keeping cell density as 2 x 10^5 cells/ml. To study neurite extension from neuron cells, single layered patterns were bioprinted in each well of a 12 well tissue culture plate.

Alginate doesn't attach to bare tissue culture plates. To enhance the adhesion property, 1 ml PEI (0.1% w/v) was added in each well of a 12 well plate, and incubated overnight at 37°C with 5% CO_2. Before printing, the PEI solution was aspirated from the well, and three successive wash was conducted with 10 mM PBS. Then, 1 ml $CaCl_2$ (50 mM) solution was dispensed in each well to serve as a crosslinker. The 2D pattern was printed into the $CaCl_2$ solution where the Ca^{2+} rapidly crosslink the hydrogel precursor. The printed cell/alginate mixture was kept in the crosslinker solution for 2 minutes to promote uniform crosslinking. Following crosslinking, the $CaCl_2$ solution was aspirated from the well, and the pattern was washed with 10 mM PBS. One milliliter of cell culture media (90% DMEM + 10% FBS) was added to each well of the tissue culture plate, which was then placed in an incubator.

5.3.5 Assessment of printability

To evaluate 2D and 3D printability, peptide-modified alginate scaffolds were printed maintaining various extrusion pressure (i.e. 20, 30, and 40 kPa) and linear needle speed (i.e. 6, 8, 10, 12, 14, 16, 18, 20, 22, 24, and 26 mm/s). The concentration of hydrogel precursor was kept as 2% (w/v), while the concentration of $CaCl_2$ solution was varied between 50-150 mM. Printability of composite PCSA strands were evaluated in terms of strand width, interstrand distance, pore geometry, and interstrand angle. These parameters were compared with expected or CAD generated geometry. The expected strand width as per [16]:

$$D_s = \sqrt{\frac{4Q_t}{\pi V_n}} \tag{5.1}$$

where D_s, V_n and Q_t represent strand width, linear needle speed, and volumetric flow rate of hydrogel precursor, respectively. Similarly, printability of a square pore was calculated as per [17]:

$$P_A = \frac{P_r^2}{16\beta} \tag{5.2}$$

where P_A, P_r, and β represent the pore printability, perimeter of a pore, and area enclosed inside a pore, respectively. To measure the printability of alginate strands in an angular fashion, strands were printed at interstrand angles of 27°, 45°, and 60° that were assigned in the CAD program. The printability of strand width, interstrand gap and angular geometry were measured as following:

$$P_D = \frac{D_T - D_E}{D_T} \times 100\% \tag{5.3}$$

where P_D, D_T, and D_E represent dimension printability, theoretical dimension, and experimentally obtained dimension, respectively. A fluorescent microscope (Carl Zeiss Axiovert 100) was used to capture the images of printed strands from random spot and the best representative images were selected for demonstration and calculation purpose. All the dimensions were precisely measured using ImageJ software (National Institutes of Health, Bethesda, Maryland, U.S.A.) and at least three replicates were maintained for each experiment for statistical significance.

5.3.6 Swelling, degradation and compression test

To assess the swelling characteristics of composite PCSA scaffold, 10 mM phosphate buffered saline (PBS) was used in this study. Briefly, after 3D printing the scaffolds were immersed in 2 ml PBS and incubated in CO_2 at 37°C for predetermined time intervals. In particular, swelling was measured at 1, 2, 3, 24, 48, 168, and 336 hours after removing the free buffer from the scaffold pores by blotting with Kimwipes™ using the formula;

$$SI = \frac{M_t - M_0}{M_0} \text{ x } 100 \tag{5.4}$$

where SI, M_t, and M_0 represent swelling index, wet weight of scaffolds at time intervals (t), and initial wet weight of scaffolds, respectively. To obtain the initial weight, the scaffolds were taken out from crosslinker immediately after fabrication, blotted with Kimwipes™, and weighed on scale. For each time point, swelling data was collected for three replicates.

Scaffold degradation was measured by incubating them in 10 mM PBS solution for particular time points. All the scaffolds were freeze-dried for 2 days and then weighed to obtain initial mass. The freeze-dried scaffolds were immersed into 2 ml PBS and incubated at 37°C in 5% CO_2 for 3, 7, 14, and 21 days. At the scheduled time point, the scaffolds were collected, further freeze dried and weighted to obtain the final weights. The scaffold degradation in terms of percentage mass loss was calculated using:

$$M_L = \frac{M_0 - M_t}{M_0} \text{ x } 100 \tag{5.5}$$

where M_L, M_0, and M_t represent percentage (%w/w) mass loss, initial freeze-dried mass and freeze dried mass at specific time points (t), respectively. To evaluate statistical significance, degradation data was collected for three replicates.

To assess the elastic modulus of 3D printed scaffolds incubated in physiological buffer (i.e. PBS) for different time period, compressive force was applied to the scaffolds using a texture analyzer machine (Texture Technologies, MA, U.S.A.). Briefly, after 3D fabrication the scaffolds were immersed into 2 ml PBS and incubated at 37 °C in 5% CO_2 for a period of 7, 14, and 21 days. The scaffolds were taken out of the 12-well tissue culture plate at scheduled time

intervals, excess buffer solution was blotted with Kimwipes™, and the scaffolds positioned between the probes of texture analyzer machine to measure the elastic modulus. The scaffolds were compressed up to 20% of their original thickness while maintaining a uniform probe speed of 0.01 mm/s. For each time interval, compression testing was conducted on three replicates to evaluate the statistical significance. The data obtained from texture analyzer machine was of compressive force versus deformation, and dividing them by area and height result in applied stress versus strain. To obtain the area and height, the images of the associated scaffolds were captured, and processed with ImageJ software. The slope of stress versus strain curve up to yield point was considered as Young's modulus.

5.3.7 Scanning electron microscopy (SEM)

To assess the surface morphology of scaffolds at different time points (i.e. day 0, 14, and 21), scanning electron microscopic images were captured using a SEM machine (Hitachi SU8000, Japan). Briefly, the scaffolds were collected at different time intervals and freeze-dried for 2 days, then positioned on carbon tape attached SEM stubs, and coated with 10 nm gold layers (Q150T, Quorum Technologies, U.K.). Microscopic images were captured from arbitrary sites on the scaffolds at 5 kV machine voltage and the most representative images of the surface morphology are shown in this study for qualitative analysis.

5.3.8 Preparation of 2D surface and RPSC culture

The 2D alginate surface was prepared on round glass coverslips. To prepare the coverslips, 1 ml PEI (0.1% w/v) was used to coat the 2D surface overnight at 37°C in an incubator. The PEI was aspirated, and slides were washed with 10 mM PBS buffer. 100 μl (2% w/v) of RGD, YIGSR, and RGD/YIGSR-conjugated 2% alginate, and 2% pure alginate precursor were dispensed on the cover glass. The hydrogel precursor was crosslinked with 50 mM $CaCl_2$ for 1 hour to obtain a flat 2D surface. To prepare a positive control, 1 ml PLL solution was dispensed into each well of a 12-well plate and kept in an incubator (37°C) overnight to ensure coating. Prior to cell culture, PLL was aspirated from the well, and 10 mM PBS buffer was used to wash the well properly. RPSC were seeded on the top of 2D surface and cultured for 3 days at 37 °C in a 5% CO_2 enriched humidified incubator.

5.3.9 Cell viability study

Viability of Schwann cells incorporated in the bioplotted strand was assessed using a live and dead cell staining assay at day 0, 3, and 7. On the scheduled period, culture media (90% DMEM+10% FBS) was aspirated from 12-well plate, and the culture plate was washed two times with 10 mM PBS. Then 1 ml fresh culture media containing 2 µl of propidium iodide (5 µg/ml) and calcein-AM (1 µg/ml) were added in the each well of culture dish. The culture was incubated for two hours at 37°C with 5% CO_2. Prior to imaging, culture media was aspirated, and each well was washed thoroughly with 10 mM PBS three times to get rid of the free staining agent. Using a fluorescent microscope (Axiovert 100, Zeiss), multiple images were taken at different depths at selected spots in the bioplotted strands. The best representative spot of the 3D culture in the strands was chosen to evaluate the cell viability. ImageJ (National Institutes of Health, MD, USA) software was used in stacking the multiple images and measuring total dead and live cell population. The cell viability was calculated using the equation:

$$V(\%) = \frac{C_L}{C_L + C_D} \times 100, \tag{5.6}$$

where C_L, C_D, and V represent the live cells, dead cells, and viable cells, respectively.

5.3.10 BDNF-release assessment

Assaying of the release of brain-derived neurotrophic factor (BDNF) was conducted in this study with an ELISA kit (BDNF E_{max}® ImmunoAssay Systems - Promega Corporation, USA). A 96-well ELISA plate was coated with anti-BDNF mAb in carbonate buffer overnight at 4°C. The coating solution was flicked out, and the wells were washed with TBST wash buffer. To block the nonspecific binding sites on the well, blocking buffer was added in each well and incubated 1 h at room temperature. Following well blocking, the blocking solution was flicked out properly and TBST buffer was used to wash the wells. To prepare standard curve, two rows of wells were used. Diluted BDNF standard (500 pg/ml) was added to the first well of each row and 1:2 serial dilutions were conducted down to the last well of each row. To prepare test samples, printed strands of Schwann cells (2 x 10^5 cells/ml) incorporated into various alginate-peptide combination hydrogels were cultured for 3 days. For a particular sample, scaffold was fabricated dispensing 100 µl PRSC/biopolymer mixture using a 3D bioplotter. At least 3 scaffolds were printed in a 12-well tissue culture plate for a specific sample. For positive control (i.e. PLL-coated plate), 2 x 10^4 PRSCs were seeded and conducted 2D culture for 3 days. Since BDNF

demonstrates a short half-life, a long period of RPSCs culture might not significantly enhance the amount of released BDNF in the hydrogel. Accordingly, in this study a 3 day culture period of RPSCs was chosen instead of 7 days. From each culture, 100 µl of supernatant was collected and added in the nonspecific sites blocked wells of ELISA plate. BDNF-standard- and test-sample-loaded wells were incubated in a shaker at room temperature for 2 h. After 5 successive washes, diluted Anti-Human BDNF pAb in block buffer was added in each well and the ELISA plate was incubated in a shaker at room temperature for 2 h. The wells were vacated through flicking out the added solution followed by 5 consecutive washes. Then diluted Anti-IgY HRP in block buffer was added in each well and the ELISA plate was incubated in a shaker at room temperature for 1 h. Finally, after flicking out the solution and sequential washing of the wells, 100 µl TMB one solution was added to each well. The ELISA plate was incubated at room temperature in a shaker for 10 m, then the reaction was terminated by adding 100 µl 1 N hydrochloric acid to each well. The absorbance of yellow colour by the solution in each well was measured with a plate reader at 450 nm wave length.

5.3.11 Dorsal root ganglion (DRG) harvest, culture and immunocytochemistry

To stimulate the growth of the DRG neurons, the left sciatic nerves of the rats were lesioned two days prior to sacrifice (Fig. 5.2). Fifteen male Sprague-Dawley rats (weight 250-300 g) were randomly distributed into 3 groups (n = 5), and all received the following procedure. To prepare for the surgical procedure, 1.5 – 2% isoflurane was used to anesthetize the rats, and the flow rate of isoflurane and oxygen was maintained as 0.8 to 1 L/min. During the procedure, a skin incision was made along the femoral axis, then blunt dissection of the underlying muscles was conducted to reach the sciatic nerve, and then the nerve was transected. At the end of the procedure, 4-0 silk was used to close the incision in the skin. All the surgical procedures were conducted under sterile conditions. The animals were given analgesic buprenorphine injections (0.05 mg/kg) every 8 hours for 2 days post operatively. Two days after the surgery, all the animals in the groups were sacrificed.
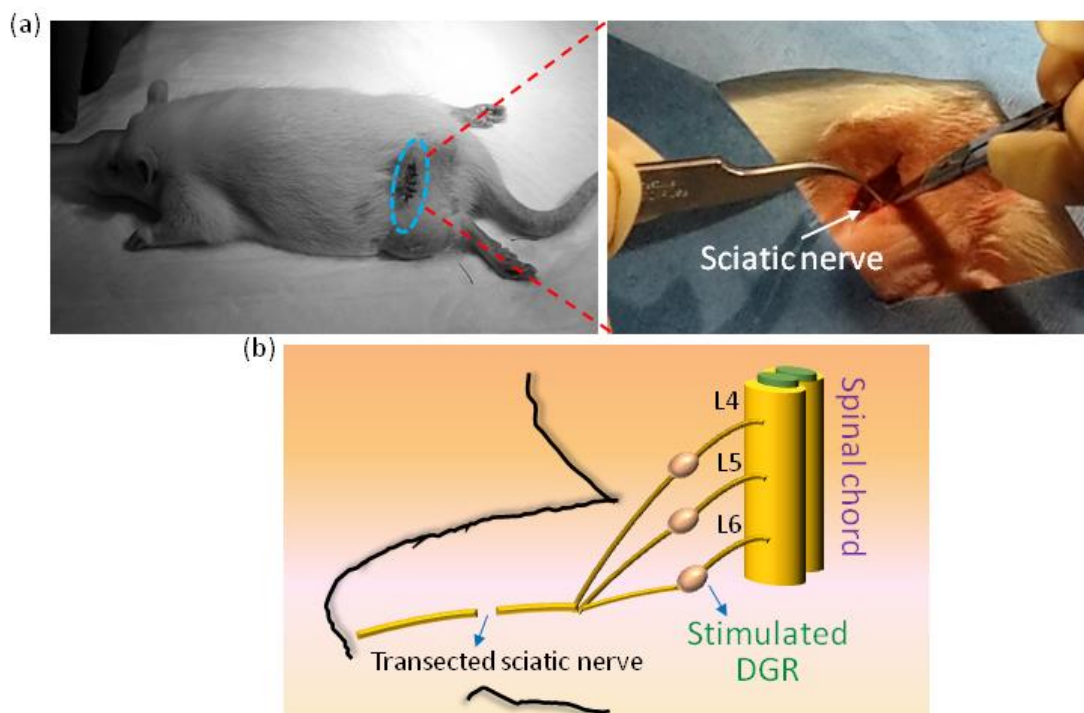
Fig. 5.2 Sciatic nerve transection to stimulate DRG neurons; (a) sciatic nerve tansection of a Sprague-Dawley rat, (b) schematic of transected sciatic nerve and associated DRGs.

The dorsal root ganglia of the sciatic nerve plexus (L4-L6) were excised from the rats, collected in L15 media, and spun at 800 rpm for 5 minutes to collect the DRG pellets. To dissociate the neurons in the DRGs, the pellets were incubated with collagenase (1 µg/ml) for 1 h at 37°C, triturated using a series of serum-coated Pasteur pipettes having large to narrow openings, and further treated with trypsin (0.75 µg/ml) for an extra 30 min. Then cold horse serum was added to quench trypsin activity, a 100 µm cell strainer was used to filter the ECM debris, and 15% bovine serum was added to form a layered cell suspension. After spinning the suspension at 850 rpm for 20 min, the supernatant was aspirated to isolate the neuron cell pellet, and DMEM was added to resuspend the neuron cell population. Finally, 1000 neuron cells were seeded on each single-layered alginate-peptide scaffold incorporated with SCs and cultured for 7 days in DMEM with 10% horse serum. PLL-coated wells seeded with neuron cells at the same density were used as a positive control. In fact, the co-culture of neuron cells and RPSCs was conducted incorporating RPSCs inside the 3D bioprinted strands and seeding neuron cells on the top of the strands.

To conduct immunocytochemistry, after 7 days, the media was aspirated from tissue culture well, and the cultures were thrice thoroughly washed with 10 mM TBS. Cold methanol (−20 °C) was used to fix the cultures for 2 h. After fixation, methanol was aspirated and the cultures were rinsed properly with TBS. Then the cultures were treated with blocking solution (10 mM TBS ,0.5% bovine serum albumin, 2% horse serum, 0.05% Tween 20) for 2 h at room temperature to prevent background staining. Primary antibody rabbit anti S-100 and mouse anti-βIII tubulin (1:1000; Sigma Aldrich) were added to the blocking solution to bind with specific proteins expressed by Schwann cells and axons, respectively, and incubated for 2 h at room temperature. To remove any remaining free antibodies, the cultures were thoroughly rinsed five times by immersing the scaffolds in TBS for 10 m each time. Blocking solution containing two secondary antibodies and DAPI (1 μM) was added next and incubated for 2 h at room temperature to fluorescently stain the Schwann cells, axons, and nuclei, respectively; specifically, Alexa Fluor 488 goat anti-mouse and Alexa Fluor 555 goat anti-rabbit immunoglobulin (1:500; Thermo Fisher Scientific) were used as secondary antibodies. Then the samples were washed thoroughly five times with TBS, and mounted on glass slides using ProLong Gold antifade mountant (Thermo Fisher Scientific). Confocal laser scanning microscopy (Leica SP5, Germany) was used to capture 2D images layer-by-layer. OrientationJ and NeuronJ were used to assess the orientation and length of neurites on the patterned scaffold.

To study Schwann cell processes in a 3D scaffold, a similar protocol was followed to conduct the immunocytochemistry, where mouse anti S-100 and Alexa Fluor 488 goat anti-mouse were used as primary and secondary antibody, respectively. A fluorescence microscope (Axio Imager M1, Zeiss) was used to capture 2D images. For a particular location, 2D images were captured successively at different height. Three-dimensional images were built by stacking multiple the 2D images with ImageJ software. For each experiment, images were captured from random locations, and the best representative images were shown in this study.

5.3.12 Statistical significance

To measure statistical significance between two sets of data, Student's t-test was conducted with Graph pad Prism 5.0a software (GraphPad Software, San Diego, CA, USA). A cut-off of $p_b <$

0.05 was used to determine statistical significance. Experimental results were presented as the mean and standard deviation (SD) of the calculated data.

5.4 Results

5.4.1 Printability of double layered pattern

Experimental results suggest that extrusion pressure and needle translation speed regulate the strand width and printability of hydrogel precursors in ionic crosslinkers. For a particular extrusion pressure, the strand width decreases with the increase of needle translation speed (Figs. 5.3(a-c)). At a particular extrusion pressure, biofabrication seems to be possible for a range of linear needle translation speed. Below or above the limit, excess accumulation or inadequate build-up of biopolymer on the printing surface results in fabrication complexities (Figs. 5.3(d-e)).

The effects of extrusion pressure and needle translation speed on strands printability in terms of the overall structure and strand width have been presented in Figs. 5.3(f- n). In this study, printed strands demonstrated nonuniformity in width along the direction of fabrication. Two-dimensional scaffold printability was measured by comparing strand width at the intersections, strand width between intersections, as well as the pore shape to the theoretical values. As the dimensions of bioprinted scaffolds approach the theoretical value, the printability value becomes 1. Since the experimental value always differs from the theoretical one, in this study the acceptable value of printability has been considered as 1 ± 0.1.

In this study, keeping the concentration of $CaCl_2$ constant (i.e. 50 mM), three different extrusion pressures (i.e. 20, 30, and 40 kPa) were applied to print 3D patterns of 2% (w/v) composite PCSA precursor using a 200 µm needle. A minimum dispensing pressure of 20 kPa was chosen to avoid fabrication problems in the 3D scaffolds. At an extrusion pressure of 20 kPa, the strand printability at the intersection was measured as ~ (0.90-0.95) for needle translation speeds of 6 and 10 mm/s, while ~ (0.8 - 0.9) printability was noticed for 8, 12, and 14 mm/s needle translation speeds (Table 5.1). However, the strand printability between the intersections was inferior ~ (0.7- 0.85) for all speeds compared to at the intersections. In contrast, the pore shape printability was superior ~ (0.95-1) to both the strand width measured at the

intersections and between intersections. At this pressure, scaffold fabrication seemed possible for needle translation speeds between 6 to14 mm/s.

At an elevated extrusion pressure (i.e. 30 kPa), reasonable strand printability ~ (0.9 - 1.1) was identified at the intersections and between intersections for 18 and 20 mm/s needle translation speeds, respectively, with 18 mm/s seeming to be ideal for all values. The scaffold pores were close to a perfect square and showed a reasonable printability value ~ (0.95 to 1.05) for 14-18 mm/s needle translation speed. However, 30 kPa pressure allowed biofabrication only for 12-20 mm/s linear needle translation speed. Further increasing the extrusion pressure to 40 kPa constricted the range of needle translation speed to 22-26 mm/s, for which 3D scaffold fabrication is possible. At this pressure, strand printability at the intersections and between intersections were calculated as ~ (0.8 -1.2) and (0.9-1.35), respectively. In particular, strand printability becomes unpredictable at elevated needle translation speeds. The pores generated at these faster speeds demonstrated unsatisfactory printability (~ 0.8-0.9).
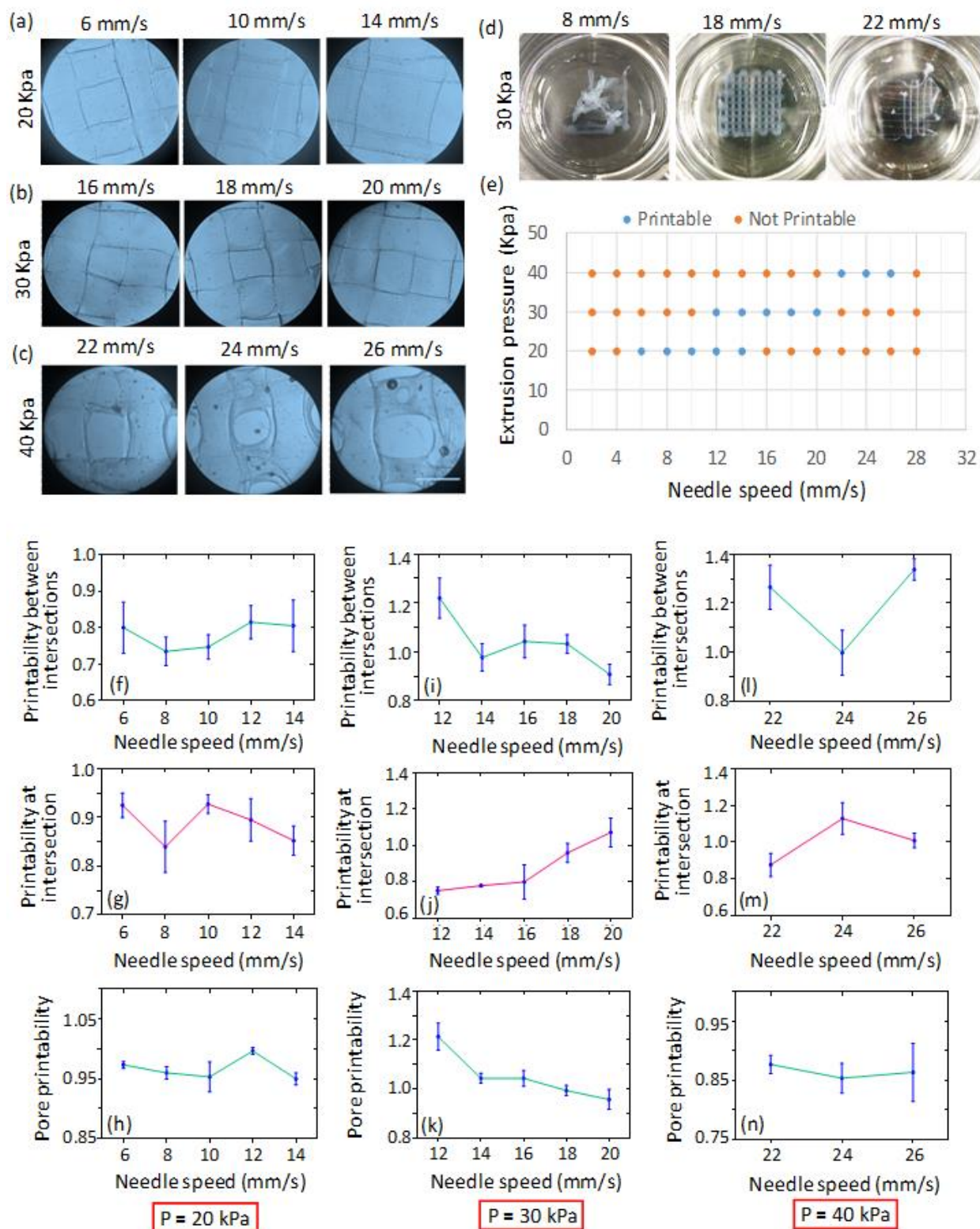
Fig. 5.3 Two-dimensional printability of RGD/YIGSR-alginate conjugate precursor: (a-c) microscopic images of alginate strands bioprinted using various pressures, (d) printable and non-

143

printable structures at 30 kpa extrusion pressure and different needle speeds, (e) plot representing the range of printable and non-printable pressures at the elevated needle speeds, (f, i, and l) strand printability between intersections at extrusion pressures 20, 30, and 40 kPa with respect to various needle translation speeds, (g, j, and m) strand printability at intersections at extrusion pressures 20, 30, and 40 kPa with respect to various needle translation speeds, and (h, k, and n) pore printability at extrusion pressures 20, 30, and 40 kPa with respect to various needle translation speeds.

Strand and pore printability at different extrusion pressures and needle translation speeds that fall in the range of reasonable printability (0.9 to 1.1) has been highlighted in the results listed in Table 5.1. For extrusion at 20 kPa, the strand width and pore shape were found to be under printed (i.e. <1) at all needle translation speeds calculated using formula (1). In contrast, at pressures of 30 and 40 kPa, the strand widths and pore shape were found either under or over printed (i.e. <1 or >1) at different needle translation speeds (Table 5.1). These results suggest that both needle translation speed and extrusion pressure affect the dimension of bioprinted strands. However, 40 kPa resulted in non-uniform strands that led to poor printability (Figs. 5.3(l-n)). Table 5.1 suggests that only extrusion pressure at 30 kPa and needle translation speed of 18 mm/s ensure outstanding strand and pore shape printability. Therefore, the pressure and needle translation speed are recommended to fabricate the composite PCSA scaffolds with 200 µm needle.

Table 5.1 Strand width printability with various extrusion pressures and needle translation speeds (highlighted data in red represents reasonable printability ranging 0.9 to 1.1)

Extrusion Pressure (Kpa)	Printability	Needle Speed (mm/s)				
		6	8	10	12	14
20	At intersections	0.925 ± 0.025	0.84 ± 0.052	0.928 ± 0.019	0.895 ± 0.044	0.853 ± 0.03
	Between intersections	0.8 ± 0.07	0.735 ± .039	0.748 ± 0.033	0.815 ± 0.045	0.805 ± 0.07
	Pore structure	0.973 ± 0.006	0.96 ± 0.01	0.953 ± 0.025	0.997 ± 0.006	0.95 ± 0.01
		12	14	16	18	20
30	At intersections	0.75 ± 0.02	0.778 ± 0.005	0.798 ± 0.095	0.958 ± 0.052	1.07 ± 0.079
	Between intersections	1.22 ± 0.082	0.978 ± 0.056	1.043 ± 0.067	1.033 ± 0.038	0.908 ± 0.042
	Pore structure	1.213 ± 0.06	1.043 ± 0.02	1.043 ± 0.03	0.993 ± 0.02	0.957 ± 0.04
		22		24		26
40	At intersections	0.878 ± 0.063		1.13 ± 0.086		1.01 ± 0.039
	Between intersections	1.265 ± 0.09		0.998 ± 0.092		1.338 ± 0.043
	Pore structure	0.877 ± 0.015		0.853 ± 0.025		0.863 ± 0.049

5.4.2 Printability of angular pattern

Biofabrication of complex structure or organ often requires extrusion of the hydrogel precursor in an angular fashion [4]. Therefore, in this study, angle printability of composite PCSA precursor was evaluated with respect to CAD data using formula (3). Since extrusion pressure at 30 kPa and needle translation speed at 18 mm/s resulted in superior strand printability, strands were printed using this pressure and speed in the 50 mM CaCl$_2$ solution. Under these conditions, no overlap or accumulation was noticed at the intersections (Figs. 5.4(a-d)). The angle printability was measured as 1.073 ± 0.12, 1.03 ± 0.03, 1.047 ± 0.06, and 1 ± 0.02 for 27°, 45°, 60°, and 90° angles that were assigned in the CAD parameters, respectively. Compared to strands at right angles, strands extruded at acute angles showed more deviation from the CAD parameters (Fig. 5.4(e)). However, all the angles printed with the alginate solution demonstrated reasonable printability (~1±0.1).
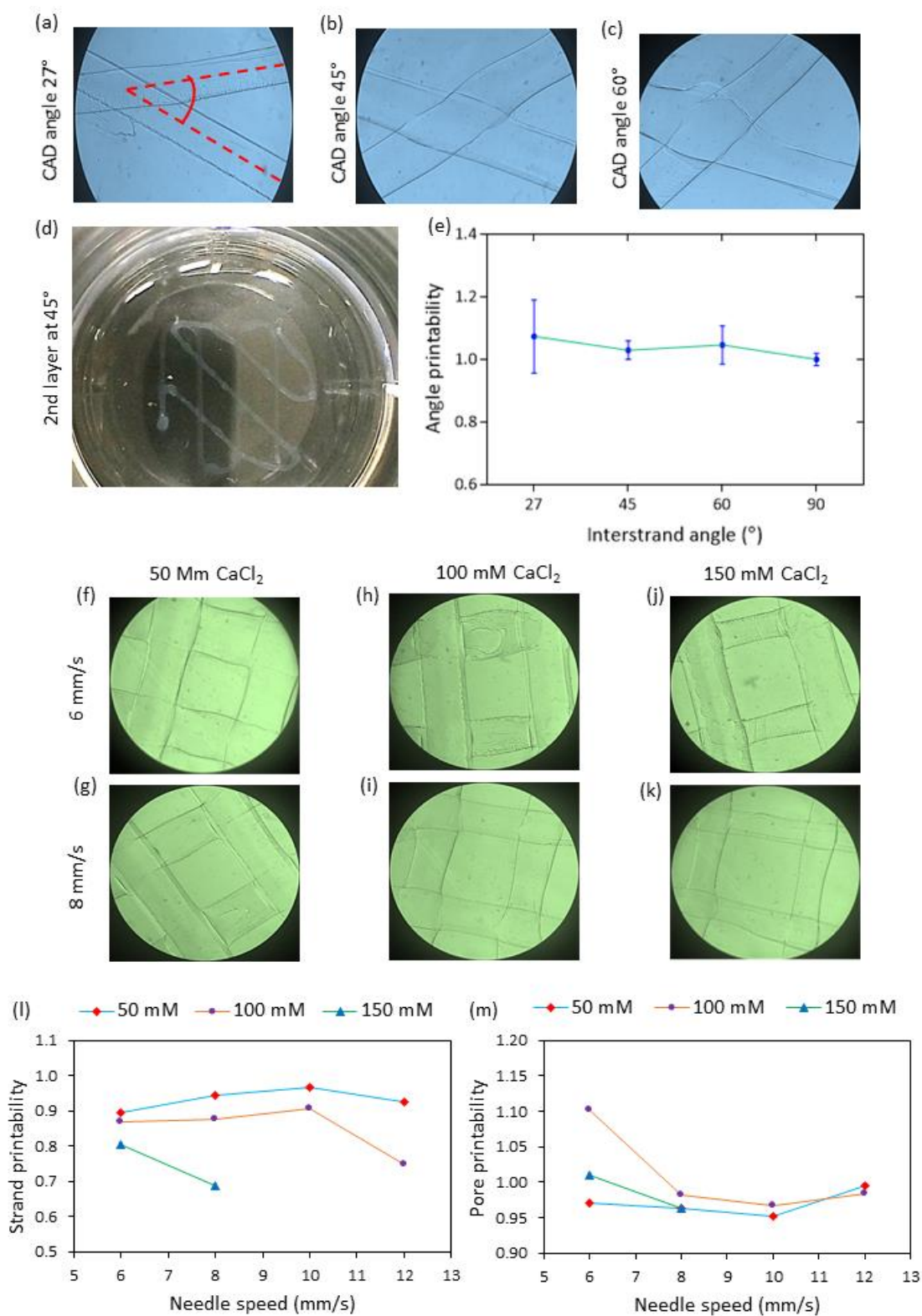
Fig. 5.4 Printability of RGD/YIGSR-alginate conjugate strands with respect to angular geometry (a-e), and varying concentration of $CaCl_2$ (f-m)

5.4.3 Printability into ionic crosslinker

Although, 30 kPa extrusion pressure and 18 mm/s needle translation speed have been identified as the ideal parameters for printing 3D pattern in the 50 mM $CaCl_2$ solution, printing the pattern in an elevated concentration of $CaCl_2$ solution requires further adjustments of the extrusion pressure and needle translation speed. It has been observed that 2% (w/v) composite PCSA precursor is printable in 50, 100, and 150 mM $CaCl_2$ solution only at 20 kPa extrusion pressure and 6-12 mm/s needle translation speed. Accordingly, to assess the strand and pore printability of the composite PCSA precursor in the three different concentration of $CaCl_2$ solution, 20 kPa extrusion pressure and 6, 8, 10, and 12 mm/s needle translation speeds were used as the printing parameter for strand fabrication.

In this section, the printability of composite PCSA precursor extruded into three different concentration of $CaCl_2$ (50, 100, and 150 mM) was evaluated by measuring pore shape and strand width and using formulas (1) and (2). Experimental results show that both the concentration of $CaCl_2$ and the needle translation speed affect the pore geometry and strand width in the biofabrication process for a given extrusion pressure (Figs. 5.4 (l, m)). In particular, strand widths were seen to reduce as a result of an increase in the needle translation speed and changes in $CaCl_2$ concentration (Figs. 5.4 (f-k)).

When the alginate solution was extruded into 50 mM $CaCl_2$, it demonstrated reasonable strand printability (~0.9-0.95) compared to both 100 and 150 mM $CaCl_2$. Bioprinting the alginate precursor into 100 mM $CaCl_2$ with a needle translation speed below 6 mm/s might enhance the strand printability. However, biofabrication of large tissue constructs at lower speeds is time consuming, and thus the viability of the incorporated cell population might be significantly compromised due to a prolonged time with no growth media. Biofabrication of alginate precursor in a 150 mM $CaCl_2$ solution seemed possible for only 6 and 8 mm/s needle translation speed. Below this limit, the extruded alginate solution was found to gel around the needle before settling down on the printing plate due to the rapid crosslinking property of the $CaCl_2$ solution.

The concentration of the $CaCl_2$ solution also affects the pore shape of the double-layered alginate scaffolds. $CaCl_2$ at different concentrations influences the dimensional uniformity of the extruded strands and thus affect the pore geometry. Of the three concentrations of ionic crosslinkers, 50 mM $CaCl_2$ facilitated the best printability ~ (0.95-1) of porous structures.

5.4.4 Printability of 3D structure

Extrusion-based systems biofabricate complex 3D structures in a layer-by-layer fashion as shown in Fig. 5.5(a). Simple to complex 3D structures were bioprinted in this study to evaluate the printability of a peptide-modified alginate solution (2% w/v). There are several challenges associated with hydrogel polymers in the biofabrication of large tissue constructs. Low viscosity alginate strands might spread upon extrusion and then shrink when crosslinking. Therefore, the distance between the tip of the needle and the previously printed strands increases with height. If the gap exceeds critical limit, then the extruded polymer floats away before settling down on the previous layer, damaging the scaffold. Further, fabrication of large tissue construct requires stable temperature and concentration of crosslinkers over the entire fabrication period to avoid viscosity and swelling-associated complexities. Simple cuboid-, cylinder-, and prism-shaped structures were bioprinted using 30 kPa extrusion pressure and 18 mm/s needle translation speed. To further evaluate the printability of complex structures, lung and kidney shapes were bioprinted using the same pressure and needle translation speed (Fig. 5.5(b)). Therefore, it seems that peptide-modified alginate precursors are a useful biopolymer in biofabricating both simple and intricate 3D structures.

Fig. 5.5 Biofabrication of scaffolds with extrusion-based technique; (a) schematic of hydrogel biofabrication, (b) biofabricated 2D and 3D structures for simple to complex structure, and the associated CAD images

5.4.5 Evaluation of mechanical stability

To evaluate the changes in mechanical performance of RGD and YIGSR peptide conjugated 2% (w/v) SA scaffolds in the physiologically relevant environment swelling, degradation and compression assessments were conducted in this section. The associated plots were presented in Figs. 5.6 (a-c). All of the composite PCSA scaffolds swelled and lost porous structure over 21 day incubation period when immersed in 10 mM PBS solution (Fig. 5.6(d)). The percentage of scaffold swelling after 1, 2, 3, and 24 hours were measured as 470.9 ± 24.2, 515.7 ± 22.07, 539.6 ± 17.86, and 584.4 ± 15.06, respectively. The data suggest that remarkable swelling took place in the first hour, and then the scaffolds swelled at a slower rate until hour 24. The swelling percentage started to fall at 48 hours (551.7 ± 17.43), and declined radically between hours 48 and 168 (551.7 ± 17.43 and 397.9 ± 23.82, respectively. The swelling rate between hours 3 to 24 and hours 168 to 336 seems to be identical but opposite in magnitude, probably indicating the saturation and drop of scaffold degradation, while the rapid loss of swelling rate between hours 48 to 168 suggests severe surface and bulk degradation of the scaffolds. The swelling graph in Fig. 5.6(a) further demonstrates that significant change in swelling took place between hours 1 to 3 and hours 3 to 24, and hours 48 to 168.

The percentage of weight loss of the scaffolds at day 3, 7, 14, and 21 was calculated as 10.45 ± 3.746, 18.33 ± 2.665, 40.64 ± 6.777, and 52.63 ± 3.689, respectively. The degradation of scaffolds over time has been presented graphically in Fig. 5.6(b). The degradation of the scaffolds from day 3 to 7 and day 14 to 21 seem to happen approximately at the same rate, while the degradation of the scaffolds between days 7 to 14 occurred at an accelerated rate. However, between day 3 to 7 and 7 to 14, statistically significant degradation took place. In particular, all the scaffolds lost approximately 20%, 40%, and 55% of their initial mass after 1, 2, and 3 weeks, respectively, when incubated in PBS.

The compression modulus was assessed over 3 weeks after incubating the scaffolds in PBS, and is presented graphically in Fig. 5.6(c). The Young's modulus was measured as 40.3 ± 2.227, 23.7 ± 3.494, 14.67 ± 3.587, and 14.47 ± 2.744 kPa at day 0 (i.e. immediately after fabrication), 7, 14, and 21, respectively. All the scaffolds seem to lose Young's modulus at a rapid rate between day 0 to 7, then the rate slowed down a bit between day 7 to 14, and finally reached equilibrium between day 14 to 21. The biofabricated scaffolds lost ~50% of their

Young's modulus in the first week, and an additional ~20% of their Young's modulus by the following week while incubating in PBS. Statistical analysis suggests that scaffolds lost elastic modulus significantly between days 0 to 7 and days 7 to 14.

(a) Swelling ratio (%) vs Time (hour / day)

(b) Degradation (%) vs Time (day)

(c) Young's modulus (kPa) vs Time (day)

(d) Side view / Top view: Day 0, Day 7, Day 14, Day 21

(e) Day 0 (f) Day 14 (g) Day 21

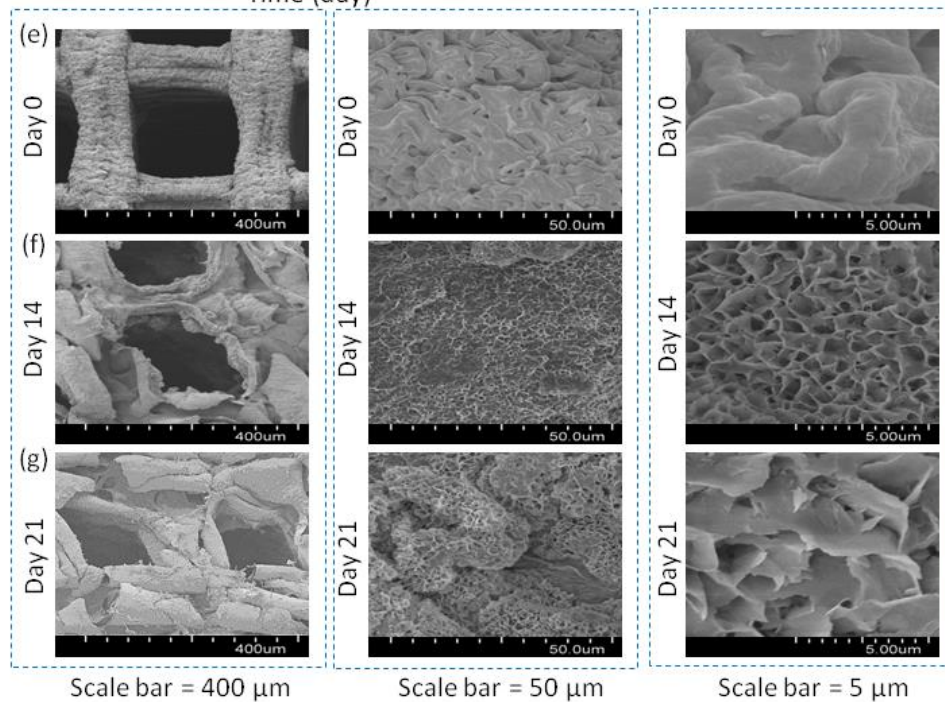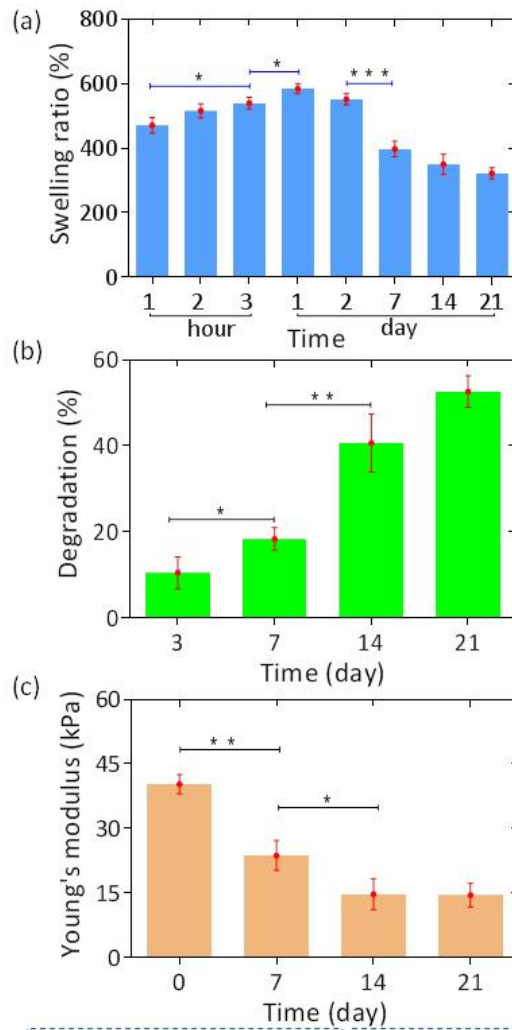Scale bar = 400 μm   Scale bar = 50 μm   Scale bar = 5 μm

152

Fig. 5.6 Assessment of mechanical stability and surface morphology of RGD/YIGSR-alginate conjugate scaffolds after PBS incubation at predetermined time points: (a) swelling ratio; (b) degradation percentage; and (c) Young's modulus; SEM images of scaffolds at (d) day 0, (e) day 14, and (f) day 21, respectively.

5.4.6 Evaluation of surface morphology

Surface morphology of RGD and YIGSR peptide conjugated 2% (w/v) SA scaffolds incubated in PBS was assessed with SEM images (Figs. 5.6 (e-g)). The Figs. 5.6(e-g) demonstrates macro- and microscale changes on the surface of the composite PCSA strands over a period of 3 weeks of incubation. The images demonstrated that over time, the strand surface became micro-porous probably due to the effect of surface and bulk degradation. Interestingly, the biofabricated pores were still evident in the scaffolds after 3 weeks of incubation in PBS. However, structural integrity seems to have been compromised over the incubation period.

5.4.7 Assessments of RPSCs morphology in 2D culture

Cell morphology was studied on prepared 2D surfaces for positive control, negative control, and experimental groups using PLL, SA, and PCSA hydrogel coatings, respectively, on round coverslips which are shown in Fig. 5.7(a). During the culture period, most of the RPSCs seeded on the SA surface maintained circular morphology and formed clusters (Fig. 5.7(c)). In contrast, RPSCs did not form clusters on PLL (Fig. 5.7(b)) and PCSA (Figs. 5.7(d-f)) surfaces, rather the cells started to spread over the 2D surface, attached well to the polymer, and developed elongated morphology. Notably, RPSCs cultured on single-PCSA-coated surfaces showed a small number of cells with unipolar, bipolar, and multipolar morphology. In contrast, RPSCs cultured on PLL- or composite PCSA-coated surfaces showed a significant number of cells with unipolar, bipolar, and a multipolar morphology. Measuring the response of RPSCs to the peptide-modified alginate demonstrated that the modified alginate was superior in promoting suitable cell morphology over unmodified alginate, and these results are shown in Figs. 5.7(g-i). The number of attached cells per 0.06 mm^2 on the composite PCSA surface was 80.33 ± 8.96, which was close to the attached cell population (i.e. 89.67 ± 4.73) on the positive control. YIGSR-alginate conjugate (YCSA) supported higher number of cell (80 ± 4) attachment compared to that of RGD-alginate conjugate (RCSA) surface (73.33 ± 4.16). Accordingly, cell attachment on the composite PCSA, YCSA, and RCSA surface was significantly higher than the

negative control. Interestingly, of the three experimental groups, cell attachment was significantly low on RCSA surface related to positive control.

The cell circularity measured on the RCSA, YCSA, and composite PCSA surface were 0.54 ± 0.04, 0.8333 ± 0.06, and 0.4333 ± 0.08, respectively, which was significantly lower than the negative control (0.9733 ± 0.02). The cell circularity value was significantly higher on YCSA surface compared to RCSA, composite PCSA, or PLL coated surface (0.46 ± 0.04). Notably, RPSCs showed identical morphology on composite PCSA surface and positive control. The cell processes grew on RCSA and YCSA surface were 10.23 ± 0.454 and 4.277 ± 0.323 µm, respectively, which were shorter than the processes grown on positive control (16.82 ± 2.396 µm). Statistically, the length of cell processes on YCSA surface was significantly shorter than both the RCSA and the composite PCSA surface (20.95 ± 2.481 µm). Remarkably, RPSCs cultured on the composite PCSA surface grew longer processes than positive control and significantly longer than RCSA surface. As Schwann cells did not develop processes in unmodified alginate, this substrate is not included in Fig. 5.7 (i).
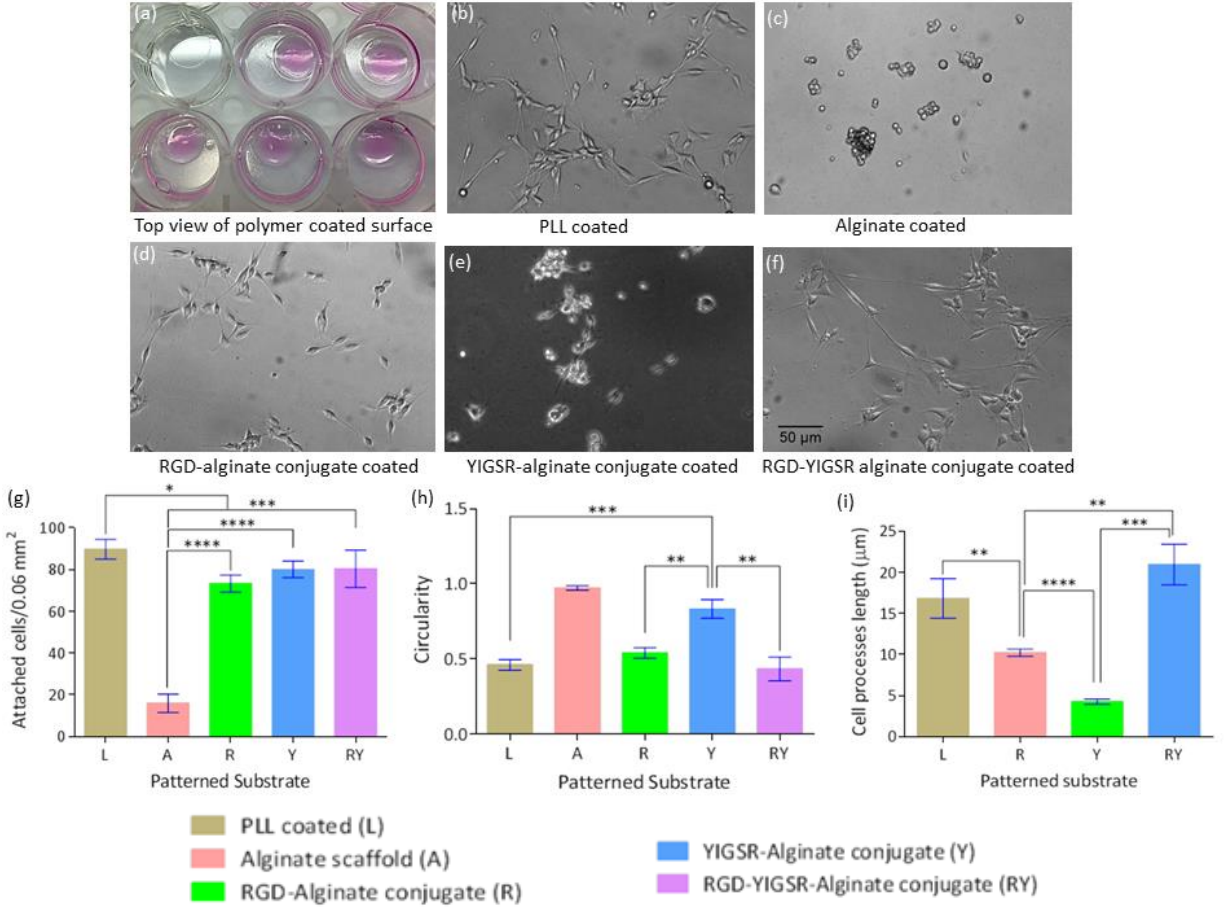
Fig. 5.7 2D culture of primary rat Schwann cells on various polymer-coated round coverslips; (a) top view of cells growing on polymer-coated surface after 3 days of culture, (b) PLL coated, (c) alginate coated, (d) RGD-alginate conjugate coated, (e) YIGSR-alginate conjugate coated, (f) RGD-YIGSR-alginate conjugate-coated surface, (g) number of attached cells, (h) circularity of the adherent cells, and (i) length of cell processes. (*p_b < 0.05; **p_b < 0.01, ***p_b < 0.001, ****p_b < 0.0001)

5.4.8 Assessments of RPSCs viability in 3D culture

The cellular biocompatibility of the substrate is important for ensuring cell viability. The cell viability assay results are illustrated in Fig. 5.8. Again, unmodified alginate was generally inferior to the other substrates, and cells often grew in clumps. RCSA strands showed favorable cell viability (90.71 ± 2.89) at day 0, but had decreased (80.81 ± 5.547) by day 3, and this trend continued (85.05 ± 5.12) on day 7. RCSA strands also had RPSCs growing in clumps, though not as frequently nor as large as unmodified alginate, and had a similar, even distribution of dead

155

cells as unmodified alginate. At day 0, 3, and, 7, the percentage of RPSCs viability in the YCSA strands was measured as 91.74 ± 3.193, 87.33 ± 4.14, and 89.47 ± 3.644, while in the composite PCSA strands was measured as 94.9 ± 0.7851, 90.63 ± 6.06, and 95.01 ± 1.954, respectively. It is obvious that RPSCs viability decreased in all experimental samples at day 3, suggesting there might be extrusion-induced cell damage or cell apoptosis in the PCSA hydrogel due to the leftover toxic byproducts of the conjugate reaction. Overtime the toxins might diffuse out from the hydrogel and enhance the viability of RPSCs. The hydrogel strands showed enhanced RPSCs viability at day 7 compared to day 3, suggesting both self-healing and proliferation of the cells. Figs. 5.8(i-k) reveal that YCSA strands showed comparable results to composite PCSA throughout the seven days. This also suggests a combined effect of composite peptides over a single peptide-alginate conjugate. However, single and composite peptide-alginate conjugate, though close in comparison, were inferior to the positive control (PLL-coated plate) and superior to the negative control (alginate) in the 7-day culture period. Moreover, experimental results indicate that RPSCs viability among the peptide-alginate conjugates were statistically insignificant at day 0 and 3, while cell viability in the composite PCSA strands was significantly different from RCSA strands at day 7. RPSCs viability in the alginate strands was significantly low compared to the peptide alginate conjugates and the PLL-coated plate over the culture period. Moreover, cell viability in the PLL-coated plate was significantly greater than RCSA strands over the 7 day culture period and YCSA strands at day 3 and 7.
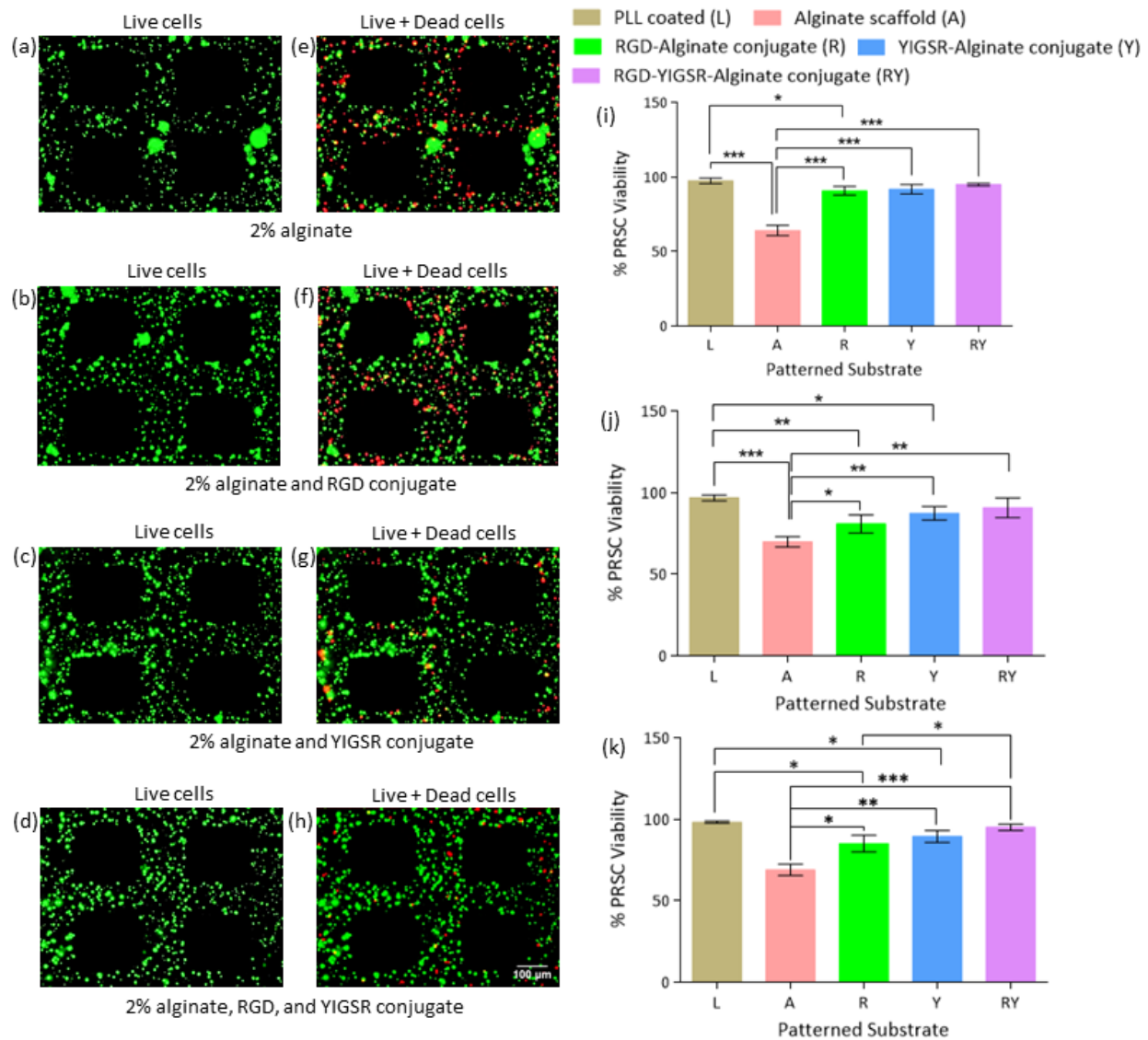
Fig. 5.8 Primary Schwann cell viability in bioplotted strands after 7 days of 3D culture where live and dead cell stains as green and red, respectively; live cells in (a) 2% alginate, (b) 2% alginate –RGD conjugate, (c) 2% alginate –YIGSR conjugate, (d) 2% alginate –RGD-YIGSR conjugate; live and dead cells in (e) 2% alginate, (f) 2% alginate –RGD conjugate, (g) 2% alginate –YIGSR conjugate, (h) 2% alginate –RGD-YIGSR conjugate (scale bar = 100 μm); cell viability graphs for (i) day 0, (j) day 3, and (k) day 7 (*$p_b < 0.05$, **$p_b < 0.01$).

5.4.9 Cell-biopolymer interactions in 3D culture

Three-dimensional printing creates an environment that embedded cells can respond to in a way that better mimics *in vivo* environments. Figs. 5.9(c-g) show both the images of the cell processes that developed and the quantification of how long the cell processes were. RPSCs are seen to distribute uniformly in the RCSA, YCSA, and composite PCSA strands. As with the 2D culture, RPSCs grew unipolar, bipolar, and multipolar processes in the hydrogel. In the peptide-alginate conjugate, cell processes combined together to promote cell-cell interaction. Culturing RPSCs in RCSA strands resulted in longer cell processes (21.54 ± 1.115 µm) than YCSA strands (14.12 ± 1.244 µm), which is similar to the results from 2D culture (Fig. 5.7(i)). Similar to 2D culture, the cell processes that developed in RCSA strands were shorter in length than those in composite PCSA strands (24.48 ± 1.047 µm). Notably, the cell processes grew in YCSA strands was significantly shorter than RCSA or composite PCSA strands. Likewise, statistically significant cell process difference was observed in the RCSA and composite PCSA strands. In contrast, most RPSCs embedded in the alginate hydrogel showed circular morphology, and though cell processes did develop in the alginate cell culture, the processes (5.57 ± 1.157 µm) were much shorter than the modified alginate cell cultures.
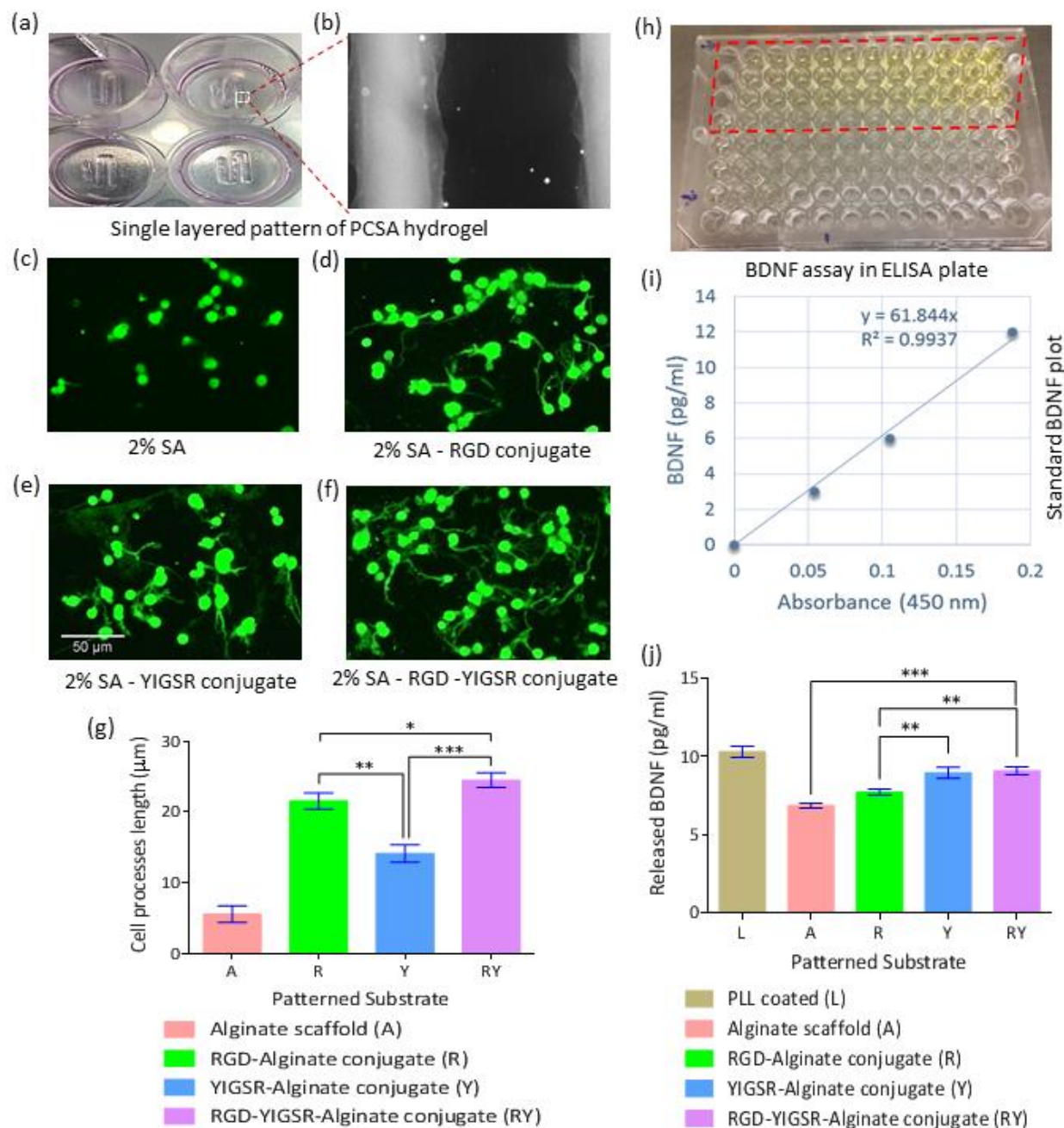
Fig. 5.9 Assessments of 3D culture of RPSCs and released BDNF in and from the bioprinted hydrogel strands with immunofluorescent assay and ELISA kit, respectively; (a and b) single layered patterns; S-100 immunocytochemistry (green) on RPSCs for 3D cultures grown in (c) alginate, (d) RGD-modified alginate, (e) YIGSR-modified alginate, and (f) RGD-YIGSR-modified alginate strands (*$p_b < 0.05$, **$p_b < 0.01$, ***$p_b < 0.001$), (g) Graphical presentation of cell processes length; (h) yellow solution in the wells of ELISA plate indicating the amount of released BDNF, (i) standard BDNF plot, (j) secreted BDNF (**$p_b < 0.01$, ***$p_b < 0.001$).

5.4.10 Assessments of BDNF secretion

To evaluate the physiological function of RPSCs in 3D culture after 3 days, the level of BDNF was quantified using an ELISA assay. The graded distribution of yellow color in the ELISA plate demonstrates the varying amount of secreted BDNF by the embedded RPSCs in the hydrogel (Fig. 5.9(h)). From the sequential dilution of standard BDNF in the ELISA plate, the correlation between known amount of BDNF and light absorbance was developed in order to calculate the amount of secreted BDNF by experimental samples (Fig. 5.9(i)). All RPSCs cultures showed a release of BDNF. In similarity to the previously-discussed experiments, cultures in alginate released the least amount of BDNF (6.847 ± 0.14 pg/ml), and cultures in RCSA hydrogel showed lower levels of BDNF (7.71 ± 0.19 pg/ml) release compared to YCSA and composite PCSA hydrogel, which was 8.943 ± 0.36 and 9.067 ± 0.25 pg/ml, respectively. Moreover, the amount of BDNF secreted by the RPSCs embedded in RCSA hydrogel was significantly lower than in YCSA and composite PCSA hydrogel. Interestingly, RPSCs embedded in YCSA and composite PCSA hydrogel had very similar levels of BDNF (Fig. 5.9(j)), which is in contrast to the length of the processes that developed in the 3D culture assay (Fig. 5.9(g)). Compared to the PLL-coated plate that served as a control, all of the modified alginate showed lower levels of BDNF release.

5.4.11 Evaluation of protein expression of RPSC

As neurons regenerate, they respond to cues in their environment, and that includes Schwann cells. In Fig. 5.10, immunocytochemistry images are shown of developing neurons from cell-seeding on a 2D culture surface that was embedded with Schwann cells. As mentioned earlier, the neurons were collected from stimulated DRGs of Sprague Dawley rats and seeded on the samples immediately after preparation. In Fig. 5.10 (a-c), the influence of Schwann cells and peptides on helping to support the growth of neurons and axons is visible by the Schwann cells aligning along the axon. In addition, the elongated morphology of the RPSCs in the peptide modified alginate strands has been demonstrated using S-100 immunofluorocytochemistry. Particularly, clusters of RPSCs are found in the close vicinity of neuron cells, suggesting the influence of chemotaxis and cell-cell interactions. DAPI staining highlights all of the nuclei of RPSCs and neuron cells in the hydrogel strands, demonstrating that RPSCs are found more uniformly distributed in the RCSA strands compared to YCSA or composite PCSA strands. Using β-3 immunofluorocytochemistry to selectively stain neurons demonstrated that neurons

grew neurites in different directions on the peptide-modified alginate surface. Since neuron cells were seeded on the PCSA strands bioprinted in the 0° direction (Fig. 5.13(f)), the neuron cells should grow their neurites in the same direction due to the presence of physical and bio-chemical cues [18]. Notably, a higher number of neurites were found aligned with the direction of 3D printing that were grown on the RCSA or composite PCSA strands than on the YCSA strands. However, neuron cells were found to grow tiny neurites on the alginate strands (i.e. negative control), the images of immunocytochemistry were presented in Fig. 5.10 (d). The growth of neurites on the PLL-coated plate (i.e. positive control) was also investigated and presented in Fig. 5.10 (e). The neurites were seen to grow in different directions and coil around neuron cell body on the PLL coated plate.
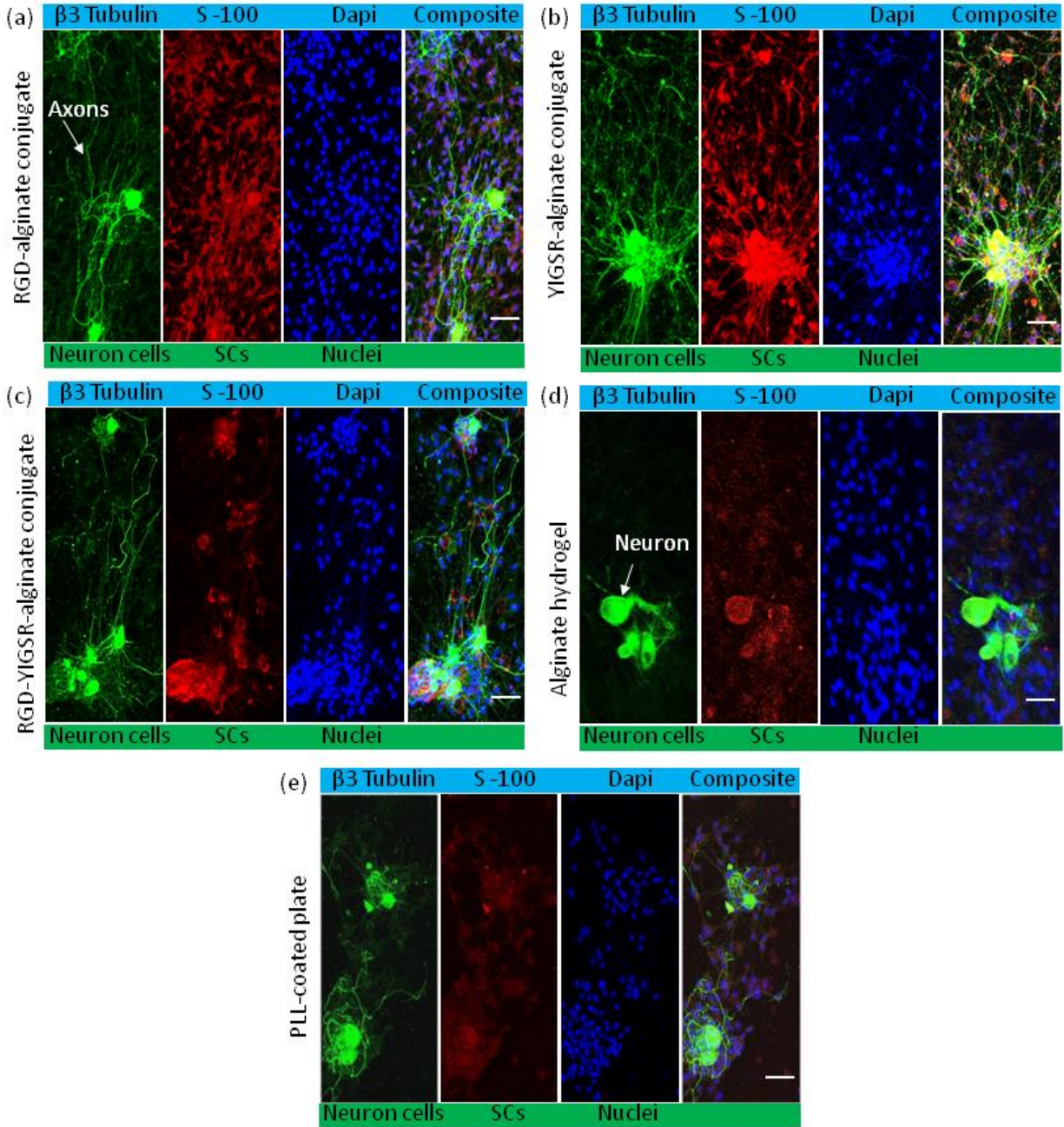
Fig. 5.10 β-3 tubulin immunocytochemistry (green) and S-100 immunocytochemistry (red) on neuron cells and Schwann cells, respectively with DAPI staining (blue) of nuclei for cultures grown on (a) RGD-alginate conjugate, (b) YIGSR-alginate conjugate, (c) RGD-YIGSR-alginate conjugate strands, (d) alginate hydrogel, and (e) PLL-coated plate; (scale bar = 100 μm).

The 3D orientation of RPSCs, neurons, and neurites has been presented for single or composite peptide alginate conjugate strands (Figs. 5.11(a-c)). The images clearly demonstrate the geometry of bioprinted strands and the directional developments of neurites on the patterned

substrate. The Figs. 5.11 (a-c) demonstrate that most of the neurites grew on the outer surface of the PCSA strands.
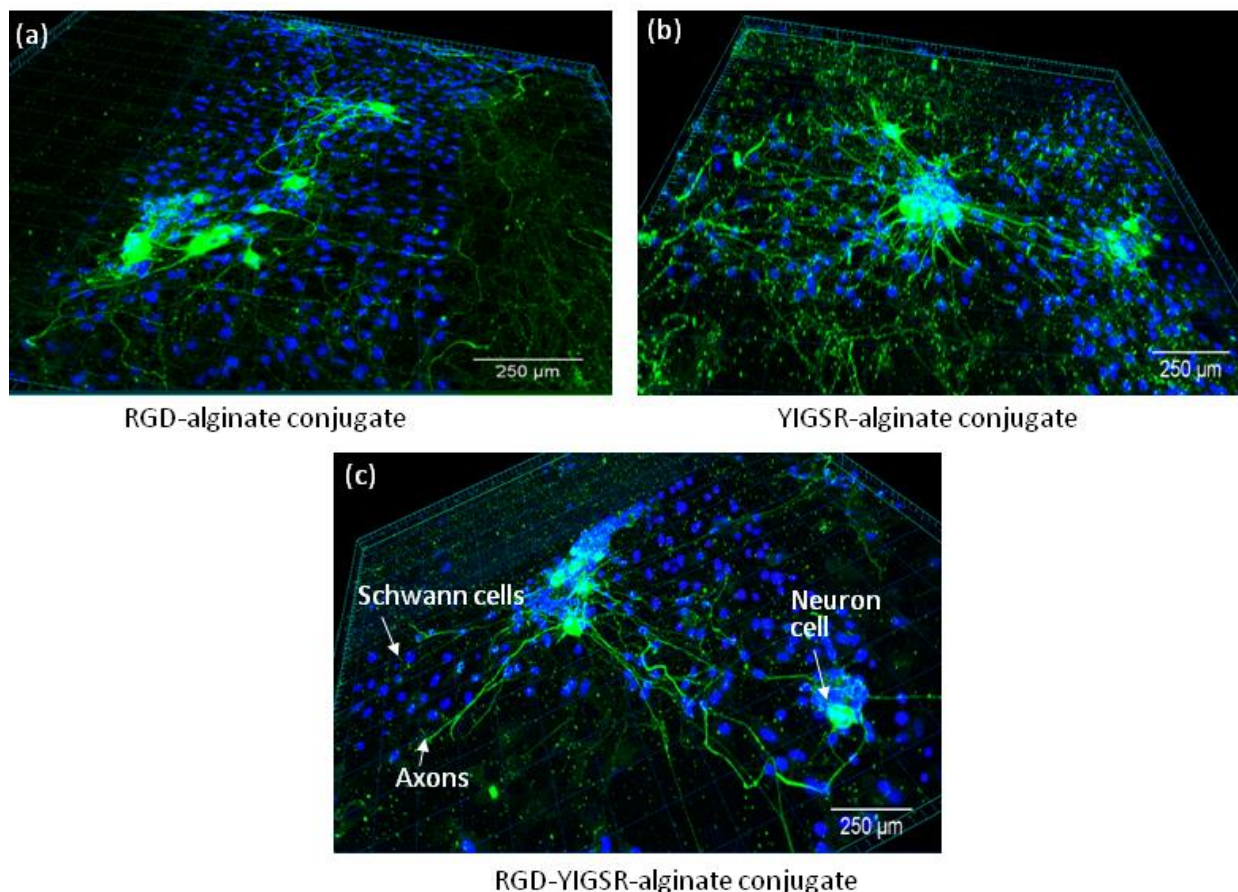
Fig. 5.11 Confocal microscopy of neuron and Schwann cells distributed three dimensionally in the (a) RGD-alginate conjugate, (b) YIGSR-alginate conjugate, and (c) RGD-YIGSR-alginate conjugate; β-3 tubulin immunocytochemistry (green) on neuron cells with DAPI staining (blue) of nuclei both for neuron and primary Schwann cells; [scale bar = 250 µm].

5.4.12 Evaluation of length and directional growth of neurites

Fig. 5.12 highlights the growth of axons from neuron cells along the strand of the bioprinted scaffold. In combination, these five figures demonstrate the combined effect of biopolymer, Schwann cells and neurons in culture on the directional growth of axons. Analogous to the effects of conjugated peptides on the growth of cell processes of Schwann cells, the length of the neurites that develop are dependent on the peptides that were used. The composite PCSA

promoted outstanding neurite growth (1548.2 ± 126.4 µm), and the neurite length on RCSA strand (1404.1 ± 361.2 µm) was superior to YCSA strand (926.8 ± 41.4 µm) or PLL coated plate (639.0 ± 103.9 µm) or alginate strand (238.0 ± 64.5 µm). Interestingly, neurite length on the PLL-coated plate was found shorter than the PCSA strands. This further highlights the probable influence of peptides and Schwann cells in helping to guide and support the growth of neurites.

Fig. 5.12 Outgrowth of neurites cultured on single layered scaffolds fabricated with (a) RGD-alginate conjugate, (b) YIGSR-alginate conjugate, (c) RGD-YIGSR-alginate conjugate, and (d) alginate hydrogel. Neuron cells cultured on (e) PLL-coated plate was considered as positive control, (pink color demonstrates the directional pathway of neurites) (*$p_b < 0.05$, **$p_b < 0.01$).

Three-dimensional printing can create microstructures that embedded cells can respond to and potentially stimulate directional growth of cell processes. The addition of compounds, such

as the peptides that were conjugated to the alginate in this experiment, can influence the ability for RPSCs to respond to those cues. The directional distribution of neurites has been evaluated by frequency versus angular orientation (Figs. 5.13(e-g)). The strands were fabricated in the direction of 0°, and a significant number of neurites have been seen to align in the 0° ± 30° direction, though for all three peptide-alginate conjugates, neurite growth was observed in the ±(75° to 90°) direction as well, which suggests the probable growth of some misguided neurites perpendicular to the strand towards culture plate. The fact that majority of the neurites grew parallel to the strand in all three PCSA samples suggests the dominant effect of peptides possibly aligned along the 0° direction. The most consistent directional growth of neurites along the longitudinal axis was on the composite PCSA strands, with a frequency of ~ 0.08 for the direction of neurite extension. Notably, the YCSA strands failed to facilitate consistent directional neurite growth of all three experimental samples, since the maximum value of frequency (~ 0.06) was found identical on both 0 and 90° directions. Likewise, the alginate strands and PLL coated plate failed to grow greater part of neurites along 0° ± 30° direction, rather both the controls grew neurons randomly between 0 and 90° directions.
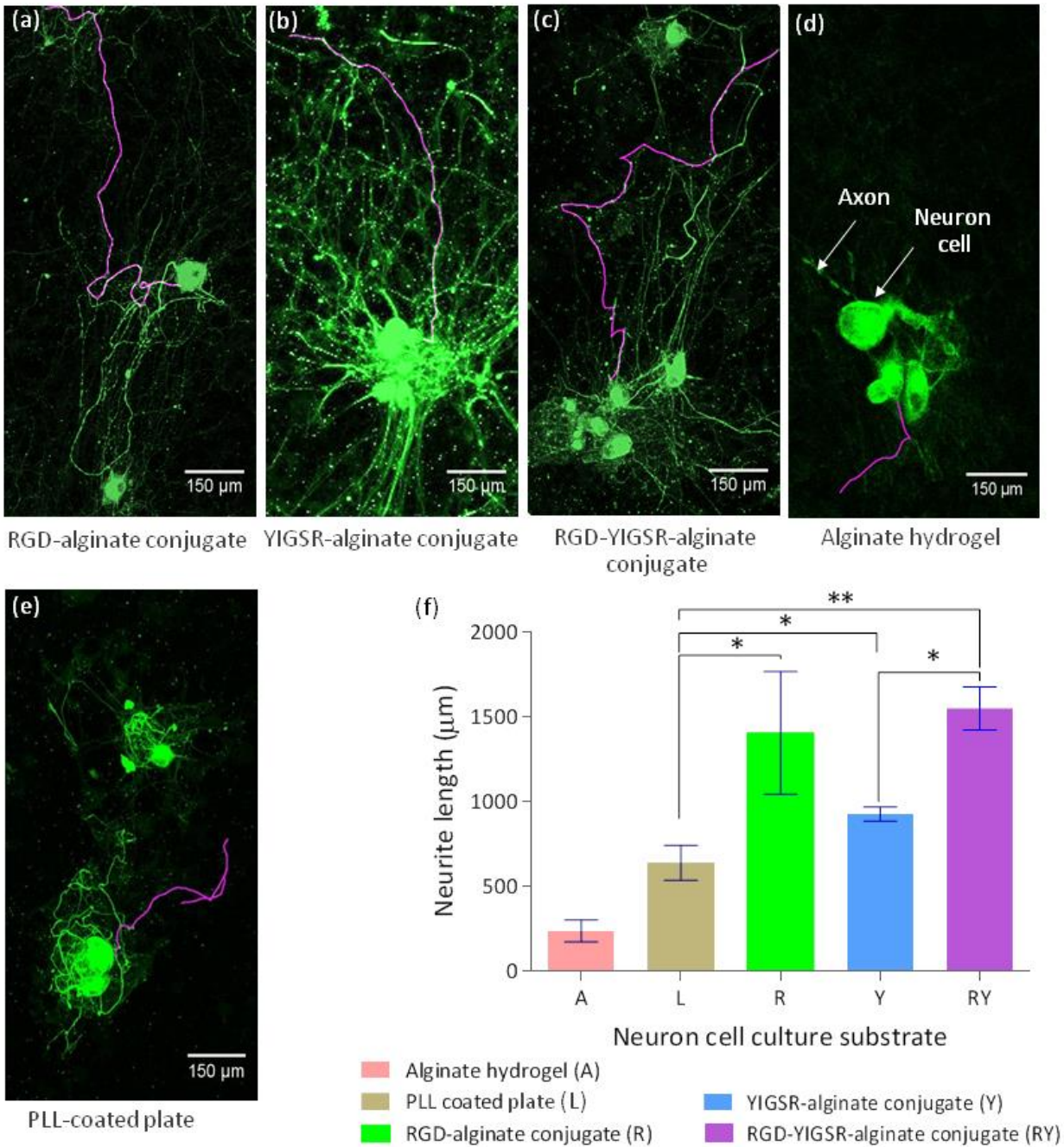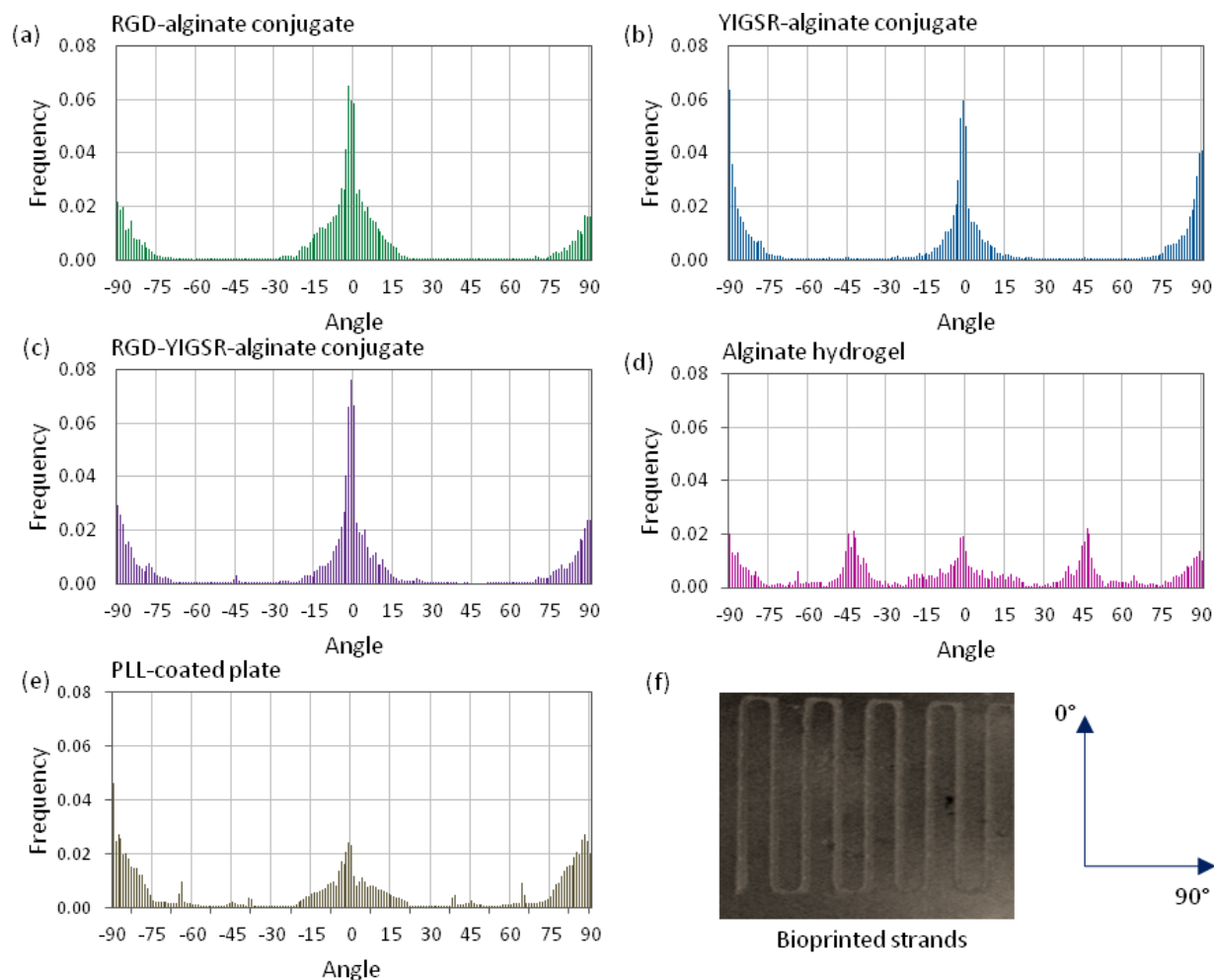
Fig. 5.13 2D distribution of neurites grown on single layered patterns fabricated with (a) RGD-alginate conjugate, (b) YIGSR-alginate conjugate, (c) RGD-YIGSR-alginate conjugate, and (d) alginate hydrogel. Neuron cells cultured on (e) PLL-coated plate was considered as positive control and (f) single layered scaffold showing 0° and 90° direction.

5.5 Discussions

In extrusion based 3D printing, the printability of hydrogel precursor largely depends on the viscosity of the precursor. The high viscous hydrogel precursor required higher extrusion pressure, while the very low viscous hydrogel precursor freely dripped from needle due to gravity (i.e. without any pneumatic pressure) [19]. Furthermore, biofabrication of scaffolds using hydrogel precursor in an ionic crosslinker might require higher extrusion pressures compared to dispensing in air if the crosslinker exhibits a rapid gelation rate. Particularly, at low dispensing

pressures the hydrogel precursor might often gets crosslinked around the needle opening prior to settling on the fabrication plate. At a particular pressure, adjusting of the needle or stage speed to faster or slower might result in the fabrication of hydrogel strands that will most closely match the theoretical values [20]. Unfortunately, biofabrication with the alginate precursor in the ionic crosslinker did not allow for a wide range of needle speeds (Fig. 5.3e). For this reason, only a few needle speeds were investigated in this article.

Several factors might cause the deviation of experimental results from the theoretical values (e.g. strand width, pore shape, and angle formations). Any mismatch between extrusion pressure, needle speed, and gelation rate might result in poor printability. In particular, inconsistency between the biopolymer flow rate and needle translation speed might lead to rupture and tearing due to under extrusion or random coiling due to over extrusion of the biopolymer strand prior to it settling down and adhering to the plate, or not allow enough time for crosslinking resulting in poorly formed scaffolds. Notably, PEI-coated tissue culture plates were used in this study to allow the extruded strands to adhere to the plate and in their predefined geometry. At higher linear speeds, the extruded strands start floating in the crosslinking solution instead of settling down probably due to the incongruity between gelation rate, surface attachment, and buoyancy force (Fig. 5.3d). This suggests that there exists a limit for the minimum and maximum linear speed for a particular needle opening with respect to biopolymer viscosity and extrusion pressure. Below and above the limit, the hydrogel precursor demonstrates poor printability. Accordingly, for three extrusion pressures and a particular needle opening, a number of linear needle speeds were identified in this study that caused moderate to outstanding printability of composite PCSA precursor.

For all measurements, the second layers were chosen as the layer to evaluate to eliminate the polymer spreading due to the wettability of the printing surface [21]. Nonuniformity in the strand width along the length of the stand was seen possibly due to the spreading and fusion of the second layer with the previous layer where they intersect. This phenomenon might result in under printability ($\sim P_D < 1$) at the intersections and between intersections for the strands fabricated with 20 or 30 kPa extrusion pressure for particular needle speeds. In contrast, for 40 kPa extrusion pressure, over printability ($\sim P_D > 1$) at the intersections and between intersections was observed probably due to excess hydrogel deposition with respect to different needle speeds.

Moreover, the concentration of $CaCl_2$ might also affect the strand and pore printability. In crosslinking the extruded strands, Ca^{2+} ions enter between the molecular chains of alginate monomers and form intermolecular ionic bonds, which induces a sol-gel transition [22]. Using $CaCl_2$ at higher concentration perhaps supplies more Ca^{2+} ions to the extruded alginate precursors and promotes fast reaction kinetics. Consequently, in this study it was noticed that strand fabrication was possible only at lower needle speeds (i.e. 6 and 8 mm/s) in the elevated concentration of $CaCl_2$ solution (i.e. 150 mM). The invasion of more Ca^{2+} ions into molecular structure causes shrinkage, which is obvious in the experimental results [23]. In particular, the shrinkage of composite PCSA precursor caused inferior strand and pore printability at elevated concentrations of $CaCl_2$ (i.e. 100 and 150 mM).

Swelling, degradation, and loss of Young's modulus of the alginate scaffolds could be attributed to ion exchange, polymer chain relaxation, and water uptake mechanism. The ion exchange (Ca^{2+}/Na^+) between hydrogel and PBS solution probably relaxes the bond between polymeric chains inside hydrogel, and facilitates the water uptake mechanism [24]. From the swelling graph (Fig. 5.6(a)), it is obvious that most of the ion exchange took place in the first 24 hours, since the incubation was conducted in a fixed volume of PBS. Because the composite PCSA scaffolds started degrading along with swelling over time, the swelling of the scaffolds was found to decline after day 1. In particular, mass loss from the scaffolds reduced the value of swelling obtained from equation (5.4). Similarly, the degradation graph (Fig. 5.6(b)) demonstrates that probably surface degradation was most prominent in the first week, while primarily bulk degradation and polymer dissolution likely took place in the following weeks. However, the lack of ion exchange might slow down the degradation process in the third week. Since both swelling and degradation affect the Young's modulus of the bioprinted scaffolds, the scaffolds lost 70% of initial elastic modulus within the first two weeks of incubation.

The changes to the surface morphology of the composite PCSA scaffold over time might have profound effects on tissue growth, particularly for nerve tissue regeneration. Since the strand surface became micro-porous over time, the scaffolds seems to be conducive for mass diffusion exchange between the incorporated cell populations and the surrounding fluids [25]. Moreover, the extended incubation period increased the roughness of the composite PCSA scaffold, which could have an influential effect on nerve regeneration [26]. The alginate

scaffolds investigated in this study contain both biochemical (i.e. conjugated peptides) and biophysical (i.e. surface roughness) cues required for axon outgrowth. Therefore, in nerve tissue regeneration the micro-porous scaffold might ensure reasonable viability of incorporated Schwann cells and facilitate neurite growth.

Biocompatible sodium alginate has been frequently studied in various tissue engineering applications due to its low cytotoxicity and excellent bio-printability [27,28]. However, alginate hydrogels are unable to regenerate tissue due to the lack of cell-binding peptides in the molecular structure [13]. Since extracellular-matrix-derived RGD and laminin-derived YIGSR peptides bind to integrin and laminin receptors of neuron cells, respectively, covalent chemistry was used to link RGD and YIGSR peptides to SA monomers in this study to enhance axon growth [29,30]. Modification of the alginate by individual single peptide-modified alginate showed favourable results, though the results from the composite peptide-modified alginate suggested that there is an interactive effect from their combination. In contrast, unmodified alginate showed very poor results in promoting cell attachment, morphology, and processes. RCSA was routinely superior to YCSA hydrogel, though composite PCSA hydrogel was generally superior to the other culture substrates being evaluated. While RGD peptides facilitated cell adhesion and process growth through interacting with integrin receptors, YIGSR peptides promoted cell proliferation by interacting with laminin receptors on neuron cells [31,32]. This was demonstrated where RCSA hydrogel influenced the RPSCs to show more elongated morphology and grow longer processes compared to YCSA hydrogel, while YCSA hydrogels induced the formation of cell clusters through cell proliferation. RPSCs attached very poorly to unmodified alginate, whereas they attached to the modified alginate culture substrates in comparable numbers to the PLL-coated tissue culture plate that served as a positive control. A sign of favorable RPSC response is the degree of polarity that the cells develop, where the composite PCSA hydrogel was superior to the other culture substrates. Another measure of the cellular polarity is the length of the processes that develops in the cell. Here again, composite PCSA was superior to all other culture substrates, and markedly so compared to the other modified alginates due to the simultaneous interaction of the composite peptides with the two cell receptors.

BDNF, a member of the neurotrophin family, supports the survival, growth, and differentiation of neuron cells [33]. In addition, BDNF stimulates the regeneration of damaged

peripheral nerves and the axon remyelination process [34]. In tissue engineering applications, the controlled release of BDNF has been shown to be beneficial for axon regeneration [35]. However, released BDNF has a short half-life and thus will lose bioactivity before axon regeneration is complete [36]. *In vivo*, Schwann cells secrete BDNF after nerve injury that regulates the growth of neurites from neuron cells [37]. Therefore, in this study RPSCs were embedded in peptide-alginate conjugates to provide a controlled and continuous release of BDNF and to evaluate the potential for future application in promoting axon regeneration. The amount of BDNF secreted by the RPSC was minimal in this study. The number of incorporated cells in one layer, the amount of taken supernatant, and the leftover BDNF in the hydrogel might cause the small amount in experimental measurements. However, the RPSC embedded in peptide-alginate conjugated strands secreted greater amount of BDNF compared to negative control and smaller amount of BDNF than positive control. In particular, RPSC incorporated in composite PCSA demonstrated superior result of the three experimental samples, suggesting the simultaneous interaction of integrin and laminin receptor on the production of BDNF.

Physical and biochemical cues are essential for guiding neurite growth after PNS injury [38]. To achieve the goal, patterned structures were biofabricated in this study using an alginate bio-ink that has been conjugated with either single or composite peptides. The seeded neuronal cells were seen to grow their neurites on the patterned substrates and responding to the cues in their microenvironment. RPSC seemed to distribute unevenly in the YCSA- and composite PCSA-strands compared to RCSA-strands, suggesting the effect of RGD peptide on cell migration within the biopolymer. The single-layer strands didn't degrade much during the 7-day culture period, and maintained their structural integrity. During the culture period, the neuronal cells grew ~1- 1.5 mm-long neurites on all three peptide-conjugated alginates, which is quite impressive. Of the five samples studied, composite PCSA strands demonstrated outstanding outcomes in terms of directional neurite growth. Therefore, alginate conjugated with multiple types of peptides should be considered as a potential superior bio-ink for nerve tissue regeneration for future study.

Composite PCSA scaffold significantly promoted better neurite growth compared to the YCSA scaffold. The difference in neurite length between composite PCSA and RCSA was insignificant probably due to the large noise for RCSA strands. Increasing the number of samples

could be useful in reducing the noise. However, composite PCSA scaffold supported better directional growth of neurite than two other peptide samples. These results support our initial hypothesis regarding the effect of composite PCSA scaffold on neurite growth. Since experimental results show that the PCSA scaffold has intermediate to poor mechanical stability, in future the scaffold could be used as NGC filler material in bridging a damaged peripheral nerve.

5.6 Conclusion

In this study, a set of experiments were conducted to characterize PCSA scaffolds in terms of printability, mechanical stability, and neurite out growth. Experimental results suggest that the selection of extrusion pressure, needle translation speed, and crosslinker concentration has profound effects on the strand printability of composite PCSA precursor. However, arbitrary selection of these parameters does not facilitate reasonable printability. Using a needle translation speed range of 12 - 20 mm/s and an extrusion pressure of 30 kPa supported better average strand width printability (~0.9 - 1) than either 20 or 40 kPa extrusion pressure. However, reasonable pore shape printability (~1 ± 0.05) was observed when pressures of 20 and 30 kPa were maintained. Only one combination of extrusion pressure (30 kPa) and needle translation speed (18 mm/s) was selected based on outstanding strand and pore printability, and was found to facilitate reasonable angle printability (~1 ± 0.05) in 50 mM $CaCl_2$. Strands extruded in 50 mM $CaCl_2$ at 20 kPa pressure maintaining 6 - 12 mm/s needle translation speed demonstrated reasonable strand and pore printability (~0.9 - 1) compared to both 100 or 150 mM $CaCl_2$. SEM images revealed that composite PCSA scaffolds incubated in 10 mM PBS maintained their structural arrangement over 3 weeks of incubation. However, the scaffolds lost 55% and 70% of initial mass and elastic modulus, respectively, during the incubation period. In addition, RPSCs incorporated in composite PCSA strands demonstrated somewhat better viability, morphology, and BDNF release compared to that of single PCSA scaffolds. Moreover, composite PCSA strands facilitated better directional neurite outgrowth of neurons compared to controls or single PCSA strands. Therefore, it can be concluded that in future, composite PCSA scaffolds would be useful to use as an artificial nerve graft in regenerating damaged PNS. Since PCSA scaffold was seen to lose 70% of the initial elastic modulus within the first two weeks of in vitro culture, for long term in vivo studies it is recommended that the composite PCSA scaffold could be used as a potential filler material in nerve graft fabricated with a mechanically stable synthetic biopolymer.

5.7 References

[1]   Terzis J, Faibisoff B, Williams HB. The nerve gap: suture under tension vs. graft. Plast. Reconstr. Surg. 1975;56:166–170.

[2]   Lee KY, Mooney DJ. Alginate: properties and biomedical applications. Prog. Polym. Sci. 2012;37:106–126.

[3]   Rowley JA, Mooney DJ. Alginate type and RGD density control myoblast phenotype. J. Biomed. Mater. Res. Part A. 2002;60:217–223.

[4]   He Y, Yang F, Zhao H, et al. Research on the printability of hydrogels in 3D bioprinting. Sci. Rep. 2016;6:29977.

[5]   Ouyang L, Yao R, Zhao Y, et al. Effect of bioink properties on printability and cell viability for 3D bioplotting of embryonic stem cells. Biofabrication. 2016;8:35020.

[6]   You F, Wu X, Zhu N, et al. 3D Printing of Porous Cell-Laden Hydrogel Constructs for Potential Applications in Cartilage Tissue Engineering. ACS Biomater. Sci. Eng. 2016;2:1200–1210.

[7]   Frampton JP, Hynd MR, Shuler ML, et al. Fabrication and optimization of alginate hydrogel constructs for use in 3D neural cell culture. Biomed. Mater. 2011;6:015002.

[8]   Khavari A, Nydén M, Weitz DA, et al. Composite alginate gels for tunable cellular microenvironment mechanics. Sci. Rep. 2016;6:30854.

[9]   Dhoot NO, Tobias CA, Fischer I, et al. Peptide-modified alginate surfaces as a growth permissive substrate for neurite outgrowth. J. Biomed. Mater. Res. Part A. 2004;71:191–200.

[10]   Ning L, Xu Y, Chen X, et al. Influence of mechanical properties of alginate-based substrates on the performance of Schwann cells in culture. J. Biomater. Sci. Polym. Ed. 2016;27:898–915.

[11]   Guenther MI, Weidner N, Müller R, et al. Cell-seeded alginate hydrogel scaffolds promote directed linear axonal regeneration in the injured rat spinal cord. Acta Biomater. 2015;27:140–150.

[12]   England S, Rajaram A, Schreyer DJ, et al. Bioprinted fibrin-factor XIII-hyaluronate hydrogel scaffolds with encapsulated Schwann cells and their in vitro characterization for use in nerve regeneration. Bioprinting. 2017;5:1–9.

[13]   Rowley JA, Madlambayan G, Mooney DJ. Alginate hydrogels as synthetic extracellular matrix materials. Biomaterials. 1999;20:45–53.

[14]   Lee JW, Lee KY. Dual peptide-presenting hydrogels for controlling the phenotype of PC12 cells. Colloids Surfaces B Biointerfaces. 2017;152:36–41.

[15]   Kaewkhaw R, Scutt AM, Haycock JW. Integrated culture and purification of rat Schwann cells from freshly isolated adult tissue. Nat. Protoc. 2012;7:1996–2004.

[16]   Sarker M, Chen XB. Modeling the Flow Behavior and Flow Rate of Medium Viscosity

Alginate for Scaffold Fabrication With a Three-Dimensional Bioplotter. J. Manuf. Sci. Eng. 2017;139:081002.

[17] Sarker M, Izadifar M, Schreyer D, et al. Influence of ionic crosslinkers (Ca2+/Ba2+/Zn2+) on the mechanical and biological properties of 3D Bioplotted Hydrogel Scaffolds. J. Biomater. Sci. Polym. Ed. 2018;1–29.

[18] Ning L, Sun H, Lelong T, et al. 3D bioprinting of scaffolds with living Schwann cells for potential nerve tissue engineering applications. Biofabrication. 2018;

[19] Malda J, Visser J, Melchels FP, et al. 25th Anniversary Article: Engineering Hydrogels for Biofabrication. Adv. Mater. 2013;25:5011–5028.

[20] Suntornnond R, Tan EYS, An J, et al. A mathematical model on the resolution of extrusion bioprinting for the development of new bioinks. Materials (Basel). 2016;9:756.

[21] Yang H-C, Chen Y-F, Ye C, et al. Polymer membrane with a mineral coating for enhanced curling resistance and surface wettability. Chem. Commun. 2015;51:12779–12782.

[22] Draget KI, Skjåk-Bræk G, Smidsrød O. Alginate based new materials. Int. J. Biol. Macromol. 1997;21:47–55.

[23] Huang S-L, Lin Y-S. The size stability of alginate beads by different ionic crosslinkers. Adv. Mater. Sci. Eng. 2017;2017.

[24] Bajpai SK, Sharma S. Investigation of swelling/degradation behaviour of alginate beads crosslinked with Ca2+ and Ba2+ ions. React. Funct. Polym. 2004;59:129–140.

[25] Sarker M, Chen XB, Schreyer DJ. Experimental approaches to vascularisation within tissue engineering constructs. J. Biomater. Sci. Polym. Ed. 2015;26:683–734.

[26] Brunetti V, Maiorano G, Rizzello L, et al. Neurons sense nanoscale roughness with nanometer sensitivity. Proc. Natl. Acad. Sci. 2010;107:6264–6269.

[27] Chung JHY, Naficy S, Yue Z, et al. Bio-ink properties and printability for extrusion printing living cells. Biomater. Sci. 2013;1:763–773.

[28] Markstedt K, Mantas A, Tournier I, et al. 3D bioprinting human chondrocytes with nanocellulose–alginate bioink for cartilage tissue engineering applications. Biomacromolecules. 2015;16:1489–1496.

[29] Ruoslahti E. RGD and other recognition sequences for integrins. Annu. Rev. Cell Dev. Biol. 1996;12:697–715.

[30] Dekkers BGJ, Bos IST, Halayko AJ, et al. The laminin β1-competing peptide YIGSR induces a hypercontractile, hypoproliferative airway smooth muscle phenotype in an animal model of allergic asthma. Respir. Res. 2010;11:170.

[31] Lin H, Sun W, Mosher DF, et al. Synthesis, surface, and cell-adhesion properties of polyurethanes containing covalently grafted RGD-peptides. J. Biomed. Mater. Res. 1994;28:329–342.

[32] Andukuri A, Minor WP, Kushwaha M, et al. Effect of endothelium mimicking self-assembled nanomatrices on cell adhesion and spreading of human endothelial cells and smooth muscle cells. Nanomedicine Nanotechnology, Biol. Med. 2010;6:289–297.

[33] Gabriele B, Enrico T. BDNF splice variants from the second promoter cluster support cell survival of differentiated neuroblastoma upon cytotoxic stress. J. Cell Sci. 2009;122:36–43.

[34] McGregor CE, English AW. The role of BDNF in peripheral nerve regeneration: Activity-dependent treatments and Val66Met. Front. Cell. Neurosci. 2018;12.

[35] Hong M-H, Hong HJ, Pang H, et al. Controlled release of growth factors from multilayered fibrous scaffold for functional recoveries in crushed sciatic nerve. ACS Biomater. Sci. Eng. 2018;4:576–586.

[36] Wurzelmann M, Romeika J, Sun D. Therapeutic potential of brain-derived neurotrophic factor (BDNF) and a small molecular mimics of BDNF for traumatic brain injury. Neural Regen. Res. 2017;12:7.

[37] Yi S, Yuan Y, Chen Q, et al. Regulation of Schwann cell proliferation and migration by miR-1 targeting brain-derived neurotrophic factor after peripheral nerve injury. Sci. Rep. 2016;6:29121.

[38] Sarker MD, Naghieh S, McInnes AD, et al. Regeneration of peripheral nerves by nerve guidance conduits: Influence of design, biopolymers, cells, growth factors, and physical stimuli. Prog. Neurobiol. [Internet]. 2018; 171: 125-150.

Conclusions and Future Recommendations

6.1 Conclusions

In tissue engineering, EB scaffold fabrication process has made possible to fabricate artificial cell laden structure mimicking the respective native tissue. In this regard, MVSA precursor has been considered as a suitable bioink due to the ability to incorporate a large cell population into 3D construct. However, the flow rate of the MVSA precursor dispensed from the extrusion needle is critical for printing the predefined scaffold structure. In particular, the flow rate of MVSA precursor, a function of polymer flow behavior, operating temperature, needle geometry, and extrusion pressure, determines the structure of scaffolds in the bioprinting process. Besides, scaffolds printed with MVSA precursor requires appropriate ionic crosslinker to maintain mechanical strength and cell viability in the culture period. Further, concentration of ionic crosslinker and MVSA precursor needs to be optimized in bioprinting scaffolds to achieve reasonable printability, mechanical strength and biological performance. While optimization of flow rate of MVSA precursor and concentration of ionic crosslinker can ensure the fabrication of predifined geometry of scaffolds, the directional axon regeneration through scaffolds remains challenging due to the lack of cell binding motifs in the molecular structure of MVSA precursor. Conjugation with peptide molecules might improve the biological performance of MVSA precursor; however the viscosity of MVSA precursors might be compromised in the preparation process, thus demanding the characterization of hydrogel in terms of printability, mechanical stability, and tissue regeneration ability. All the issues outlined have been investigated in this thesis, and the obtained conclusions have been summarized as follows:

- In predicting the flow rate of MVSA precursor from extrusion needle, model developed considering both shear and slip flow were found effective in relation to experimental values. Since the flow behavior of MVSA precursor affects the flow rate, developed regression equations of MVSA flow behavior could be used in predicting flow parameters needed to calculate the flow rate. Thus the application of the model equations in future would reduce the number of trials required prior to bioprinting of hydrogel precursor.

- The printability, mechanical strength and biological performance (i.e. cell viability) of MVSA precursor significantly depends on the type and concentration of ionic crosslinkers used in the bioprinting process. Besides, the concentration of MVSA precursor was found to affect the printability, mechanical strength and biological performance of the 3D scaffold. While some ionic crosslinkers are attractive for augmenting mechanical stability of scaffolds, others are attractive for maintaining reasonable cell viability in culture. Therefore, sequential or simultaneous crosslinking approach might be implemented to fabricate scaffolds with enhanced mechanical and biological performance.

- Developed multiple regression equations in predicting the swelling, degradation and elastic modulus demonstrate the significant influence of various independent variables (i.e. concentration of MVSA precursor, incubation time, and concentration of ionic crosslinker) on the mechanical strength of MVSA scaffolds. The multiple regression might be useful in predicting the mechanical strength at different time point, thus facilitating the selection of appropriate hydrogel for specific tissue engineering applications.

- MVSA precursor conjugated with single or dual peptides supports better survival, attachments, and morphology of embedded cells compared to pure MVSA hydrogel. Besides, peptide conjugated MVSA strands supports better directional neurite growth compared to positive controls. In the future, the peptide conjugated alginate could be used as a potential NGC filler material to regenerate a damaged peripheral nerve.

- Printability results suggest that PCSA precursor demonstrate reasonable printability at a particular range of extrusion pressure and needle speed. Beyond the range PCSA precursor shows poor printability in the fabrication of 3D scaffolds. Besides, the concentration of ionic crosslinker to effect the printability of PCSA precursor, low concentrated ionic crosslinker facilitate better printability compared to higher concentrated crosslinker. Moreover, the bioprinting of simple to complex 3D structure seems possible using PCSA precursor as a bioink. In the future, the PCSA precursor could be used as potential bioink for the fabrication of complex tissue and organ.

6.2 Recommendations for future research

In this dissertation, the flow rate of MVSA precursor has been modeled for 3D bioprinting, the influence of three different ionic crosslinkers on the scaffold bioprinting has been assessed, and the effect of PCSA scaffolds on axon outgrowth has been evaluated. . Close investigations on different issues have further given rise to several issues which might be considered as potential research topics in the future research efforts for better outcome of biofabricated scaffolds. For future research, the recommendations are:

- In this thesis, MVSA precursor was used as a bioink for 3D bioprinting of nerve tissue scaffolds. Lacking cell binding motifs, MVSA precursor was further conjugated with peptide molecules to enhance axon regeneration ability. Although, PCSA scaffolds facilitated directional axon regeneration, peptide conjugation is associated with high expenditure and cytotoxicity caused by coupling agent that needs to be addressed. Addition of protein molecules or ECM component (e.g. collagen, fibrinogen, gelatin, hyaluronic acid, etc.) in the MVSA precursor might be a potential alternative of peptide conjugation. Single or multiple protein molecules could be admixed with MVSA precursor at a certain ratio in the preparation of bio-ink. However, challenges associated with the extrusion and crosslinking of hybrid polymer needs to be taken care of. Besides, alternative hydrogel could be explored for the bioprinting of nerve tissue scaffolds. Recently, poly (ethylene glycol) diacrylate, poly (ethylene glycol) methacrylate, gelatin methacryloyl has been identified as a potential bio-ink in scaffold bioprinting since the polymers demonstrated enhanced printability, structural stability, and cell viability. Besides, several carbohydrate-based polymers have been explored in 3D bioprinting, however, none of them are free from shortcomings. For example, while hyaluronic acid shows a rapid degradation rate, chitosan demonstrates poor mechanical stability. Therefore, it is recommended that hybrid MVSA precursor or alternative hydrogel-based bio-ink could be explored in future studies for nerve tissue regeneration.

- In this thesis, it has been shown that in the bioprinting process Ba^{2+} ions ensure better mechanical strength and structural stability of MVSA scaffolds compared to Ca^{2+} or Zn^{2+} ions, while Ca^{2+} ions keep the incorporated cells more viable in the tissue regeneration process compared to the other ions. However, the combined effect of various crosslinkers

has not been investigated in this dissertation. MVSA precursor could be extruded into mixture of ionic crosslinkers containing different ratio or bioprinted scaffolds could be sequentially dipped into several ionic crosslinkers containing different concentrations. Crosslinking of MVSA precursor either in various crosslinkers sequentially or in composite crosslinkers concurrently might be an effective approach to enhance the mechanical and biological performance of the scaffolds simultaneously. Therefore, in future research the study of printability, structural stability, and biological performance of MVSA precursor extruded into composite or multiple ionic crosslinkers is recommended.

- All the experiments evaluating mechanical strength were conducted in a constant volume of PBS. However, in real scenario, *in vivo* the renewal of the physiologic buffer occurs periodically suggesting the consideration of dynamic behavior of physiologic buffer rather than static behavior. Therefore, in future research, in the assessment of mechanical strength of scaffolds the physiologic buffer might be changed periodically mimicking the *in vivo* condition. Moreover, the *in vitro* assessments of mechanical stability might be further extended to *in vivo* for the better evaluation of mechanical strength of MVSA scaffolds over time.

- In this dissertation, in predicting the mechanical strength of MVSA precursor over time multiple regression equations were derived from experimental data. In future work, the development of model considering the physical mechanism is suggested, thus tuning the physical parameters would be useful to control the structural stability of MVSA scaffolds. Further, the development of models are recommended in the future work taking into account the physical mechanism to predict the scaffold geometry (i.e. pore size and shape, porosity, etc.) with the change of mechanical strength over time. Thus model developed from the understanding of physical mechanism would facilitate the control of structural stability and mechanical strength of MVSA scaffolds in the *in vitro* or *in vivo* culture.

The effect of single and dual peptide conjugated MVSA on neurite growth has been investigated in this study. In particular, 1:2 molar ratio of two different peptides were maintained in the conjugation reaction to prepare the dual peptide conjugated MVSA. This study could be further

extended to investigate the effect of tripeptide conjugated MVSA precursor in the directional growth of neurites. Since ECM protein laminin can influence the attachment and differentiation of neuron cells and the directional growth of neurites, laminin derived peptide IKVAV could be further investigated to study the neurite outgrowth. In particular, neurite outgrowth could be investigated on 3D scaffolds bioprinted with tripeptide (i.e. RGD, YIGSR, and IKVAV) conjugated MVSA precursor. Moreover, to find out optimum amount of peptides, the tripeptide could be conjugated with hydrogel precursor maintaining different weight ratios. Moreover, in the future work it is recommended that rather than keeping 1:2 molar ratio, the RGD and YIGSR peptide molecules could be covalently linked with MVSA molecule maintaining various weight ratios to optimize the effective molar ratio for the better growth of neurites in the *in vitro* culture. Additionally, in future this *in vitro* study could be further extended to *in vivo* studies for the better characterization of PCSA scaffolds in terms of functional PNS regeneration capability. Furthermore, in future research a number of 2D and 3D patterns could be bioprinted to optimize the suitable geometry of scaffolds that would facilitate the outstanding directional growth of neurites. Thus, the recommended future research would be able to incorporate necessary bio-chemical and bio-physical cues within the scaffolds that would facilitate the regeneration of functional nerve after injury.